

DISS. ETH Nr° 18314

**Engineering Quantum Electronic Chips -
Realization and Characterization of
Circuit Quantum Electrodynamics Systems**

A dissertation submitted to

ETH ZÜRICH

for the degree of

DOKTOR DER WISSENSCHAFTEN

presented by

MARTIN VOLKER GÖPPL

DIPLOM-PHYSIKER (UNIV.), TU MÜNCHEN

date of birth

November 10, 1980

citizen of

Bayern, Deutschland

accepted on the recommendation of

Prof. Dr. Andreas Wallraff

Prof. Dr. Per Delsing

2009

Kurzfassung

Im Rahmen der Quantenelektrodynamik in elektronischen Schaltkreisen (*Circuit Quantum Electrodynamics* oder kurz *Circuit QED*) werden einzelne Mikrowellenphotonen mittels koplanaren Wellenleitern an supraleitende *Quantenbits* (kurz *Qubits*) gekoppelt. Hierbei können Kopplungsstärken erreicht werden, welche sich in klassischen Quantenoptiksystemen nur schwer realisieren lassen. Innerhalb dieser Arbeit wurden Circuit QED Systeme entworfen und im Reinraumzentrum FIRST (www.first.ethz.ch) hergestellt. Zu diesem Zweck wurden Dünnschichtprozesse zur Fabrikation mikro- und nanoelektronischer Bauelemente erfolgreich entwickelt und optimiert, was die Durchführung einer Reihe von neuartigen Experimenten ermöglichte.

Supraleitende Qubits bestehen hier aus Aluminium/Aluminiumoxid-Josephson-Tunnelkontakten und werden in koplanare Wellenleiter integriert. Diese Resonatoren werden mittels optischer Lithographie und reaktivem Ionenätzen im Falle von Niob-Strukturen bzw. mittels optischer Lithographie und Elektronenstrahlverdampfung im Falle von Aluminium-Strukturen hergestellt. Mikrowellenresonatoren mit Fundamentalfrequenzen zwischen 2 und 9 GHz und Qualitätsfaktoren im Bereich von einigen hundert bis zu einigen hunderttausend wurden realisiert und bei Temperaturen von 20 mK elektrisch charakterisiert. Transmissionsspektren sind in guter Übereinstimmung mit theoretischen Modellen.

Die Herstellung von Josephson-Tunnelkontakten mit kontrollierten Parametern wie Josephson- und Ladungsenergie ist Voraussetzung zur Realisierung supraleitender Qubits mit definierten intrinsischen Energieniveaus. Insbesondere müssen maximale Qubit-Übergangsfrequenz, Anharmonizität, Ladungsdispersion und Kopplungsstärke zwischen Qubit und Resonator präzise kontrolliert werden, um ein spezifisches Circuit QED Experiment durchführen zu können. Dies erfordert wiederum gut kontrollierbare Fabrikationsprozesse. Josephsonkontakte werden mittels Elektronenstrahl-Lithographie und Schattenbedampfung hergestellt. Prozesse wurden implementiert und Prozessparameter wie Belichtungsdosis und Aluminium-Oxidationszeit kalibriert. Elektrische- und Materialeigenschaften von Josephson-Tunnelkontakten wurden bei Raumtemperatur und Millikelvin-Temperaturen untersucht. Darüber hinaus wurden Resonatoren, deren Resonanzfrequenz mittels eines äusseren Magnetfeldes abstimmbar ist, durch Integration von Josephson-Tunnelkontakten hergestellt.

Circuit QED Systeme mit definierten Eigenschaften wurden erfolgreich hergestellt und charakterisiert. In Hinblick auf eine zukünftige Quantencomputer-Architektur wurde die Kopplung zweier Qubits über einen Mikrowellenresonator in Abhängigkeit der Verstimmung beider Qubit-Frequenzen zur Resonatorresonanz untersucht. Die Kopplungsstärke kann hier unter Einbezug höherer Resonatormoden erklärt werden. Schliesslich wurden Experimente zur spektroskopischen Bestimmung der *Jaynes-Cummings Energieniveaus*, des *Lamb-Shifts* sowie von *Autler-Townes- und Mollow-Übergängen* ermöglicht. In weiteren Experimenten wurden *verschränkte Zwei-Qubit Zustände* erzeugt und charakterisiert.

Abstract

Circuit quantum electrodynamics (circuit QED) studies the strong coupling of microwave photons stored in a transmission line cavity to superconducting qubits on the level of single quanta and realizes coupling strengths which can hardly be achieved in atomic cavity QED systems. Within the scope of this thesis, micro- and nano-fabrication processes for the realization of circuit QED systems have been successfully realized and optimized in the ETH clean room facility FIRST. These achievements allowed to perform a number of new circuit QED experiments.

The circuit QED systems discussed here consist of aluminum/aluminum-oxide Josephson junction qubits integrated into superconducting coplanar waveguide resonators. The physical properties of high quality resonators, made by using optical lithography and reactive ion etching of niobium or evaporation of aluminum thin films were analyzed in detail. In particular, resonators with fundamental frequencies from 2 to 9 GHz and quality factors ranging from a few hundreds to several hundred thousands controlled by appropriately designed input and output coupling capacitors were realized, their microwave transmission spectra were measured at temperatures of 20 mK and well described with theoretical lumped element and distributed element transmission matrix models.

The ability to realize superconducting qubits with precisely controlled properties like Josephson energy and charging energy is essential for defining a certain qubit energy level structure. In particular, the maximum qubit transition frequency, the level of anharmonicity, the charge dispersion and the coupling strength between qubit and cavity must be controlled in order to perform a specific circuit QED experiment. This in turn requires a high level of control over the applied fabrication procedures. Josephson junctions were fabricated by using electron beam lithography and shadow evaporation. Fabrication processes were set up and process parameters like resist exposure dose and junction oxidation time were calibrated. Electrical and material properties of aluminum/aluminum-oxide Josephson junctions like the room temperature tunnel resistance, the current-voltage characteristic at milli-Kelvin temperatures or the resistance alteration with time due to post-oxidation processes (*junction aging*) were studied. The development of tunable coplanar waveguide resonators with integrated direct current superconducting quantum interference devices (DC-SQUIDs) with which the resonator frequency can be varied by an external magnetic flux threading the SQUID loop has been started and transmon type qubits have been designed and fabricated for performing circuit QED experiments.

The ability to realize circuit QED systems with controlled parameters has been demonstrated by fabricating and characterizing circuit QED devices with one or several transmon type qubits integrated into a transmission line cavity. To realize qubit-qubit coupling in quantum computer architectures, the virtual photon exchange between two qubits in a transmission line cavity has been studied in dependence on the detuning of both qubits from the cavity resonance. The qubit-qubit interaction strength is explained by taking into account higher order cavity modes. Furthermore, experiments were enabled where the *Jaynes-Cummings energy ladder*, the *Lamb shift*, the *Mollow triplet* and the *Autler-Townes doublet* were spectroscopically observed in a circuit QED system and where *two-qubit entangled states* were prepared and characterized using *quantum state tomography*.

Contents

1	Introduction	1
2	Coplanar Waveguide Resonators for Circuit QED	5
2.1	Basic Properties of Coplanar Waveguide Resonators	7
2.2	Distributed and Lumped Element Model of a Transmission Line Resonator	12
2.3	Capacitively Coupled Transmission Line Resonators	16
2.4	Transmission Matrix Model and Harmonic Resonator Modes	20
2.5	Power Dependence of Quality Factor	21
2.6	Quantization of the LC Oscillator	26
3	Josephson Junction Devices	29
3.1	Macroscopic Quantum Model and Josephson Junctions	31
3.2	Josephson Voltage State and RCSJ Model	35
3.3	Current Voltage Characteristic of a Josephson Junction	37
3.4	Measurement of the Current Voltage characteristic of a Josephson junction	39
3.5	Superconducting Quantum Interference Devices	42
3.6	DC-SQUIDs and Tunable Resonators	47
3.7	Superconducting Qubits: The Cooper Pair Box	52
3.8	Two Level Approximation and Split Cooper Pair Box	55
3.9	Decoherence in Charge Qubits	58
3.10	Transmon Type Qubits	59
4	Design and Thin Film Fabrication of Coplanar Waveguide Resonators and Qubits	63
4.1	Thin Film Fabrication of Superconducting Transmission Line Resonators	65
4.1.1	Reactive Ion Etching of Magnetron Sputtered Niobium Thin Films	65
4.1.2	Electron Beam Evaporation of Aluminum Films and Lift-Off	68
4.1.3	Characterization of Niobium and Aluminum Thin Films	68
4.1.4	Substrate Materials	72
4.2	Nano-Fabrication of Josephson Junction Devices	74
4.2.1	Basics of the Shadow Evaporation Technique	74
4.2.2	Designing and Optimizing the PMMA Double Layer Resist Structure	78
4.2.3	Electron Beam Lithography	84
4.2.4	Josephson Junction Parameter Control	86
4.2.5	Junction Deposition and Process Monitoring	90
4.2.6	Integration of Multiple Process Steps for Circuit QED Device Fabrication	92
5	Circuit Quantum Electrodynamics Experiments	95
5.1	Jaynes-Cummings Interaction and Cavity-Atom Coupling	97
5.2	Strong Coupling Regime and Vacuum Rabi Splitting	98
5.3	Dispersive Limit and Qubit Readout	100

Contents

5.4	Continuous and Pulsed Qubit Spectroscopy	102
5.5	Measurement Setup for Multi Qubit Experiments	105
5.6	Qubit-Qubit Coupling via Virtual Photons	112
5.7	Jaynes-Cummings Ladder and \sqrt{n} -Nonlinearity	119
5.8	Lamb-Shift	120
5.9	Autler-Townes and Mollow Transitions	120
5.10	Two-Qubit State Preparations and Tomography	121
6	Conclusion	123
A	Device Parameters	125
B	Designs of Fabricated Circuit QED Devices	129
C	Optical Lithography	135
D	Reactiv Ion Etching	141
E	Electron Beam Lithography	143
F	Shadow Evaporation and Oxidation	151
G	Process Receipes for Plassys Evaporator	155
H	Dicing, Mounting and Bonding of Devices	159
I	DC Probing of Josephson Junctions	163
J	Measuring the Current Voltage Characteristic of a Josephson Junction	165
	Bibliography	169
	List of Publications	177
	Acknowledgements	179
	Curriculum Vitae	181

1 Introduction

Quantum mechanics paved the way for a number of pioneering technological breakthroughs since its foundation in the early twentieth century. Techniques to manipulate matter and light were brought to perfection and allowed to build ultra fast and ultra small electronic devices. The invention of transistors, lasers and ultimately the development of integrated circuits finally lead to the triumphal advance of digital computers within the current information age.

Although the mentioned devices make use of quantum mechanical properties, a quantum mechanical machine with pure *macroscopic* quantum variables has not yet come to application. Quantum mechanics was initially developed to describe the behavior of microscopic objects. Indeed, its formalism covers both, microscopic *and* macroscopic systems. This however implies that one should be able to experience quantum mechanical effects also in the macroscopic world. But even the lack of familiarity with effects like entanglement and superposition, which every undergraduate physics student can report on, shows that this is usually not the case.

An explanation why quantum mechanical states do usually not appear in daily life can be given when recognizing decoherence effects in the context of open quantum systems. Macroscopic systems are usually not well isolated from their environment and thus couple to a large number of environmental degrees of freedom. In particular when detecting the state of a quantum system, the system has to interact with a measurement apparatus which in turn couples to the environment. The possible outcomes of a measurement can be statistically described with a density matrix operator having diagonal and off-diagonal elements. Here, off-diagonal elements represent quantum correlations whereas diagonal elements represent classical ones. As pointed out in [Zurek1991], the density matrix of an initially pure state having diagonal and off-diagonal elements evolves now, due to the environmental interaction, into a mixed state density matrix having only diagonal elements. Coherent superpositions are continuously reduced to a mixture of classical states due to the environmentally induced loss of coherence. The time evolution of the density matrix for a particle propagating in and interacting with a scalar field is exemplary given in [Zurek1991]. It is qualitatively shown that the coherence time of such a system scales inversely with the length scale and the relaxation rate of the system.

Macroscopic systems typically exhibit coherence times which are orders of magnitude smaller than its relaxation times and correlated quantum states thus usually collapse instantaneously. Microscopic systems like single ions or atoms however can be isolated well to its environment and coherence times can become large compared to the system relaxation times. Observing quantum states on a macroscopic level would make it necessary to substantially reduce dissipation (leading to smaller relaxation rates) or in other words to substantially reduce decoherence.

In the early eighties, scientists started to use superconducting Josephson junctions for studying quantum effects in macroscopic electronic circuits. It was demonstrated that macroscopic electronic circuits can indeed behave quantum mechanically and effects like macroscopic quantum tunneling and resonance tunneling were successfully observed [Voss1981, Martinis1987, Clarke1988, Rouse1995]. In the nineties, superconducting circuits attracted strongly increased interest when the idea came up that quantum circuits could be used for computation purposes, in particular for realizing quantum bits and quantum mechanical logic gates [Shnirman1997, Mooij1999, Nakamura1999].

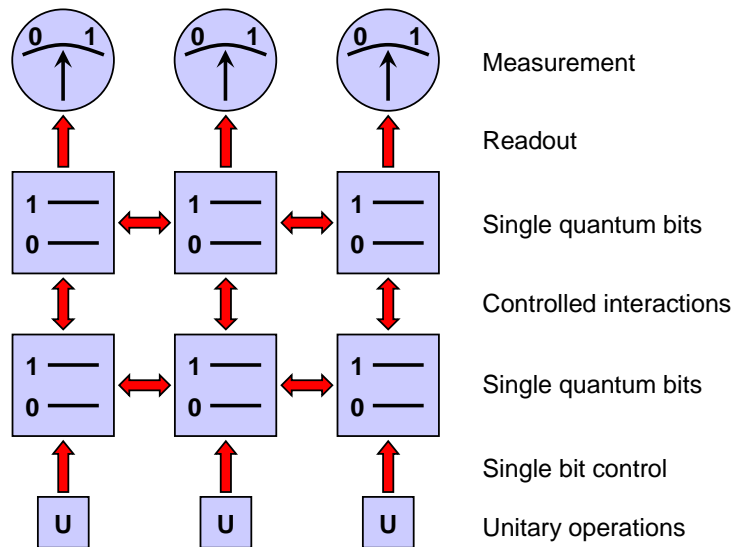


Figure 1.1: Schematic of a quantum information processor.

Several groundbreaking experiments were performed in the following, demonstrating superpositions of macroscopically distinct states, coherent oscillations as well as entangled quantum states of several qubits.

On the theoretical side, Deutsch and Jozsa were the first ones who demonstrated a quantum algorithm that can solve a certain problem more efficiently than a classical algorithm. Yet the most prominent quantum algorithm was discovered by Shor and allows for the efficient factorization of large numbers. This algorithm is particularly interesting since the widely spread RSA encryption codes used for secure communication rely on the computational problem that large numbers even cannot be factorized in adequate times with classical computers. It showed that quantum computers can easily solve certain computational problems which are out of reach of any classical supercomputer. However, the number of discovered quantum algorithms is up to now rather small. Quantum information processors harvest the tremendous capabilities the quantum world offers and have basically the potential to herald a second information age. Unfortunately, the scientific and technological challenge to realize such a device is huge.

In a classical binary computer, a binary digit (bit) forms the fundamental information unit and can adopt two states, usually denoted as zero and one. In a quantum computer, classical bits are replaced by quantum bits (qubits) which can adopt zero and one state, but also linear superpositions of those. A computation is carried out by preparing initial qubit states, subsequently performing coherent interactions between several qubits and reading out the final qubit states, see Fig. 1.1.

In order to treat computational problems, quantum processors use two fundamental principles of quantum mechanics - superposition and entanglement. Superposition offers the possibility to process many states in parallel. A unitary gate operation on a superposition of input states here generates in turn a superposition of output states. Entanglement coherently correlates several qubits and forms the basis for multi bit operations. The entanglement of qubits with photons (flying qubits) further offers the possibility to interconnect distant qubits via a quantum bus. When performing a projective measurement, the manifold of superposition states collapses into a certain single state giving a solution to the computational problem.

Quantum processors profoundly rely on the preservation of quantum coherence during gate operations. If perfect quantum coherence would be required for correctly processing quantum information, it would be technically almost impossible to build a larger scale quantum computer.

Fortunately, this restrictive constraint can be relieved at least partially when using redundancy based quantum error correcting codes [Shor1995, Steane1996]. Using quantum error correction, a small amount of decoherence may occur during operation without the fear of losing the correct result. In detail, a processor has to successfully perform on average 10^4 logic operations without error for quantum error correction codes to be applied [Preskill1998].

Numerous physical systems are studied today in the context of quantum information processing. Systems are based on single atoms in optical lattices [Bloch2008], trapped atomic ions [Blatt2008], semiconductor quantum dots [Hanson2008] or in particular on superconducting circuits [Clarke2008]. Atoms or ions form natural quantum bits since they have identical energy states and since they are well isolated from the environment but they cannot be scaled up easily. Solid state based systems, especially superconducting circuits can be scaled up when using techniques borrowed from integrated circuit technology but couple more strongly to external degrees of freedom which leads to increased loss of quantum coherence. For realizing quantum communication networks, quantum connections between qubits must be established [Schoelkopf2008]. When interconnecting trapped atoms, optical photons can be used to transmit quantum information. Superconducting qubits also couple to photons, but in the microwave regime.

The approach of coupling superconducting qubits to microwave photons is known as *circuit quantum electrodynamics* (circuit QED) in analogy to the field in atomic physics which is called *cavity quantum electrodynamics* (cavity QED). While cavity QED systems use real atoms as qubits, circuit QED systems use superconducting circuits instead, which can be regarded as artificial atoms. Cavity QED studies quantum mechanics on the level of single quanta [Haroche1989, Raimond2001, Mabuchi2002, Walther2006]. The simplest cavity QED system consists of an individual atom which is coupled to the electromagnetic field inside a cavity. The cavity can be realized by a pair of mirrors which continuously reflect photons traveling inside. The atom interacts with the cavity field by exchanging a photon. If the atom is in an excited state, it can decay by emitting a photon into the cavity. If the atom is in its ground state, it can be excited by absorbing a photon from the cavity field. The photon exchange rate of this interaction is proportional both to the dipole moment of the atom and to the cavity's electric field strength. Since cavity as well as atom in any real system also couple to environmental degrees of freedom channels of loss open up leading to a decay of quantum coherence. Coherence loss has to be minimized by isolating the system as well as possible to the environment.

Cavity QED systems have the advantage that high coupling strengths between atom and cavity field can be realized. In this regime of *strong coupling*, cavity and atom states are strongly correlated by coherently and reversibly exchanging a single photon. The effect is known as vacuum Rabi oscillations and takes place when cavity and atom decay rates are sufficiently low compared to the photon exchange rate. Many experiments have been performed in the past using strongly coupled cavity QED systems. In quantum *non demolition* experiments for example, photons in a cavity can be measured without being destroyed [Gleyzes2007, Guerlin2007]. For quantum computing and quantum communication applications, several atoms must be interconnected within a *quantum bus* in order to transmit information via photons. However, the technical challenge to reach sufficient strong coupling for atom photon entanglement as well as to control a large ensemble of atoms is tremendous.

Circuit QED realizes strong coupling in superconducting electronic circuits [Wallraff2004]. A circuit QED system consists of one or several Josephson junction qubits which are integrated into a superconducting transmission line resonator. Josephson junction qubits couple to photons in the microwave regime and can be considered as *artificial atoms* which replace the *real atoms*. The cavity is formed by a transmission line resonator which can be regarded as electromagnetic oscillator

1 Introduction

where photons appear as quantized excitations of the electromagnetic field inside.

In circuit QED systems, the strong coupling regime can be explored in scalable electronic circuits. The systems can be engineered by using well developed micro- and nano-fabrication techniques. In particular, size and shape of the artificial atoms can be lithographically defined to a certain extent so that large dipole coupling strengths can be realized [Devoret2007]. Moreover, the relative coupling between atoms and photons in such systems is much higher than in atomic cavity QED systems which allows to enter new regimes of quantum optics.

Several fruitful experiments with superconducting circuits have been performed within the last few years. Strong coupling with circuit QED was first demonstrated in 2004 [Chiorescu2004, Wallraff2004]. A single artificial atom was used to realize a maser [Astafiev2007]. Further, two experiments simultaneously implemented a quantum bus where a quantum state can be transferred via a microwave photon between two qubits [Majer2007, Sillanpää2007]. All in all, circuit QED devices consisting of a small number of qubits have proven to be controllable. Nevertheless, larger scale systems face significant technological and scientific challenges that prevents them, at least at the current stage, from an industrial application.

This thesis presents the work carried out from April 2006 to April 2009 in the Quantum Device Lab at ETH Zurich [Qudev] which was raised into life only in April 2006.

Chapter 2 concentrates on transmission line resonators which form one essential part of a circuit QED system. It is explained in detail how electrical properties of a coplanar waveguide resonator, a specific type of transmission line resonator, depend on its geometry and can be precisely designed. Furthermore, the dependence of the resonator quality factor on the applied input power is discussed.

In chapter 3 the underlying principles of Josephson junctions which form a second important ingredient of a circuit QED system are discussed. DC-characterizations of Josephson tunnel junctions are presented. Transmission line resonators with integrated DC-SQUIDS are further treated. Such resonators show a magnetic field tunable resonance frequency and can be used for example to tune the cavity in resonance with the qubit instead of tuning the qubit in resonance with the cavity. Finally, the Cooper pair box and the transmon type qubit are discussed.

Chapter 4 describes in detail many aspects of fabricating circuit QED devices. The implementation and optimization of micro and nanofabrication processes in the ETH clean room facility FIRST [FIRST] was a major part of this thesis. The ability of actually realizing circuit QED devices with defined properties is an engineering challenge and essential for performing particular circuit QED experiments. Process calibrations and material characterizations are presented. Chapter 5 explains the principles of qubit manipulation and qubit readout and presents circuit QED characterizations demonstrating the coherent control of such devices. In particular, experiments for studying the coupling of multiple qubits are presented. Finally, chapter 6 summarizes the results obtained within the scope of this thesis and gives an outlook.

2 Coplanar Waveguide Resonators for Circuit QED

Superconducting coplanar waveguide (CPW) resonators find a wide range of applications as radiation detectors in the optical, UV and X-ray frequency range [Mazin2002, Day2003, Zmuidzinas2004, Mazin2008, Vardulakis2008], in parametric amplifiers [Tholén2007, Castellanos2007, Bergeal2008], for magnetic field tunable resonators [Castellanos2007, Palacios2007, Sandberg2008] and in quantum information and quantum optics experiments [Frunzio2005, Göppl2008]. In the context of quantum optics and quantum computation experiments with superconducting circuits, qubits are coherently controlled, they interact with each other and their states are read out. All three tasks - manipulation, mutual interaction and read out - can be handled very efficiently when integrating the qubits into a transmission line resonator [Blais2004]. Such a resonator, which has a function analog to a cavity in cavity QED, thus is an essential ingredient on a circuit QED system. This chapter is devoted to a specific type of transmission line resonator - the coplanar waveguide resonator. While the fabrication aspect of such devices is discussed in detail in chapter 4, this chapter concentrates on the question how geometric design parameters influence the electrical properties of the resonator. Furthermore, the dependence of the resonator's quality factor on the applied input power will briefly be discussed. The chapter closes with the quantum mechanical description of the LC oscillator.

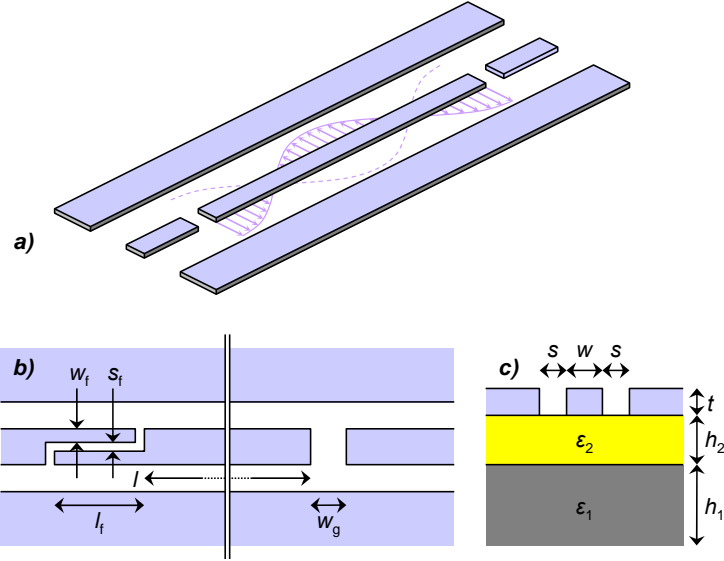


Figure 2.1: (a) Schematic of a coplanar waveguide resonator capacitively coupled to input and output lines. The electric field component (indicated by the purple arrows) is maximal at the ends of the resonator where electrical currents vanish. (b) Top view of a coplanar waveguide resonator with finger capacitors (left hand side) and gap capacitors (right hand side). (c) Cross section of a coplanar waveguide resonator design. Center conductor and lateral ground metallization (blue) on top of a double layer substrate (grey/yellow).

2.1 Basic Properties of Coplanar Waveguide Resonators

Coplanar waveguide resonators have a number of advantageous properties for applications in circuit QED. Coplanar waveguide resonators can easily be designed to operate at frequencies of up to 10 GHz or higher. Their distributed element construction avoids uncontrolled stray inductances and capacitances allowing for better microwave properties than lumped element resonators. In comparison to other distributed element resonators, such as those based on microstrip lines, the impedance of coplanar waveguide resonators can be controlled at different lateral size scales from millimeters down to micrometers not significantly constrained by substrate properties. Their potentially small lateral dimensions allow to realize resonators with extremely large vacuum fields due to electromagnetic zero-point fluctuations [Schoelkopf2008], a key ingredient for realizing strong coupling between photons and qubits in the circuit QED architecture. Moreover, coplanar waveguide resonators with large internal quality factors of typically several hundred thousands are now routinely realized [Frunzio2005, Baselmans2005, Barends2007, O'Connell2008, Göppl2008].

Figure 2.1a shows the schematic of a coplanar waveguide resonator coupled capacitively to input and output ports. Most of the resonator characterizations done within the scope of this thesis have been performed with aluminum structures fabricated on thermally oxidized high resistivity silicon. The results are presented in the following. The planar and cross section geometry of a capacitively coupled coplanar waveguide resonator on a double layer substrate is sketched in Fig. 2.1b and c, respectively. The silicon has a thickness of typically $h_1 = 500 \mu\text{m} \pm 25 \mu\text{m}$ and the silicon oxide layer thickness is about $h_2 = 550 \text{ nm} \pm 50 \text{ nm}$. The substrate is metallized with a $t = 200 \text{ nm} \pm 5 \text{ nm}$ thick layer of aluminum. Resonators were designed with fixed width $w = 10 \mu\text{m}$ and various center conductor lengths l between 8 and 29 mm aiming at fundamental resonance frequencies f_0 between 2 and 9 GHz. The center conductor is separated by a gap of width $s = 6.6 \mu\text{m}$ from the lateral ground planes and is coupled via gap- or finger capacitors to the input and output transmission

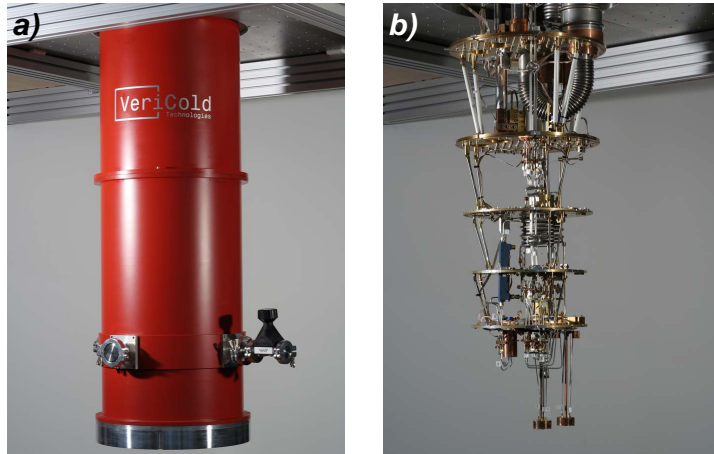


Figure 2.2: Pulse-tube based dilution refrigerator system. a) View on closed system, ready for operation. b) View on opened system showing different temperature stages and mounted sampleholder.

f_0 (GHz)	l (mm)
2.3430	28.44928
3.5199	18.96995
4.6846	14.22000
5.8491	11.37998
7.0162	9.480000
8.1778	8.130000

Table 2.1: Exact values for resonator lengths and resonance frequencies corresponding to the data shown in Fig. 2.5.

lines, see Fig. 2.1. Gap capacitors of widths $w_g = 10$ to $50 \mu\text{m}$ and finger capacitors formed by one-up to 8 pairs of fingers of length $l_f = 100 \mu\text{m}$, width $w_f = 3.3 \mu\text{m}$ and separation $s_f = 3.3 \mu\text{m}$ have been realized.

For determining the electrical resonator parameters, S_{21} transmission measurements have been performed using a *Rhode und Schwarz* 40 GHz vector network analyzer while having the device installed in a pulse-tube based dilution refrigerator system [VeriCold] and cooled down to a temperature of 20 mK. Figure 2.2 shows the pulse-tube based dilution refrigerator and Fig. 2.3 shows the measurement configuration. The vector network analyzer generates a RF signal which is applied via attenuators installed at different temperature stages of the refrigerator to the device under test (DUT). The attenuators stepwise reduce electrical and heat noise which otherwise would be transferred from higher temperature stages to the sample. High Q resonators were measured using a 32 dB high electron mobility transistor (HEMT) amplifier with a noise temperature of < 5 K installed at the 4 K stage of the refrigerator as well as one, respectively two room temperature amplifiers with 35 dB gain each. Low Q resonators were characterized without additional amplifiers since here the resonator transmission is sufficiently high. An additional amplification as used for high Q resonators is thus not necessary for detecting the transmitted signal of low Q devices with sufficient high signal to noise ratio.

A typical transmission spectrum of a weakly coupled ($w_g = 10 \mu\text{m}$) coplanar waveguide resonator of length $l = 14.22$ mm is shown in Fig. 2.4. The spectrum clearly displays a Lorentzian lineshape of width δf centered at the resonance frequency f_0 . Figure 2.5 shows measured resonance frequencies f_0 for resonators of different length l , all coupled via $w_g = 10 \mu\text{m}$ gap capacitors and Tab. 2.1 lists the respective values for l and f_0 . For these small capacitors the coupling induced frequency

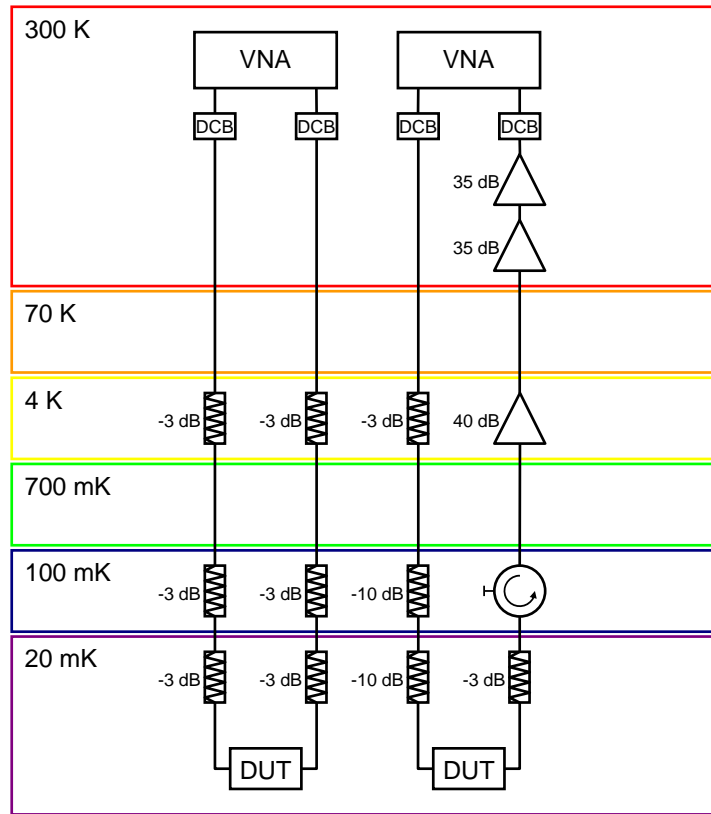


Figure 2.3: Measurement setup for RF-characterization of coplanar waveguide resonators. The device under test (DUT) is mounted at the base plate (20 mK) in a dilution refrigerator and characterized with a vector network analyzer (VNA). An RF signal is applied via a DC block (DCB) and several attenuators at different temperature stages at the resonator's input. The signal is transmitted through the resonator and is detected and analyzed by the vector network analyzer after passing through several attenuators, respectively after passing through an attenuator, a circulator and amplifiers in the output line. The numbers on the left hand side of the graphic indicate the temperatures of individual refrigerator stages.

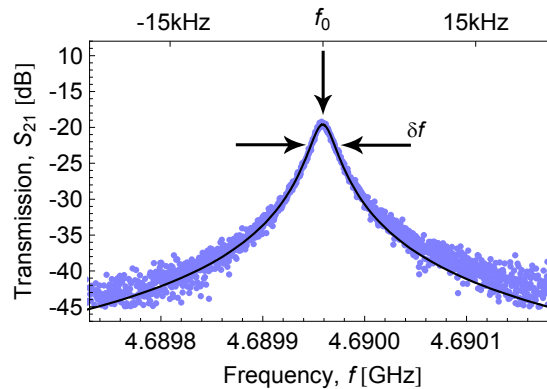


Figure 2.4: Transmission spectrum of a 4.7 GHz resonator (device L in Tab. 2.2). Data points (blue) were fitted (black) with a Lorentzian line.

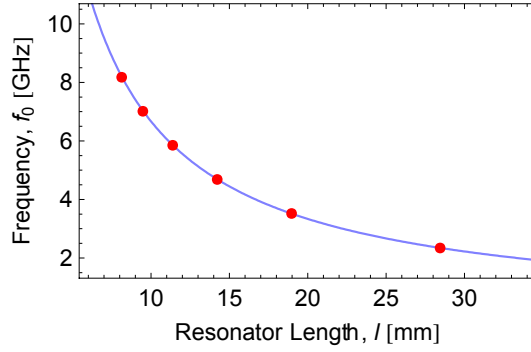


Figure 2.5: Measured f_0 (red points) of resonators with different length l coupled via $w_g = 10 \mu\text{m}$ gap capacitors. The blue line is a fit to the data using Eq. (2.1) with ϵ_{eff} as fit parameter.

shift can be neglected, as discussed in a later section. In this case, the fundamental resonator frequency f_0 is given by

$$\begin{aligned} f_0 &= v_{\text{ph}} \lambda_0^{-1} \\ &= \frac{c}{\sqrt{\epsilon_{\text{eff}}}} \frac{1}{2l}. \end{aligned} \quad (2.1)$$

Here, $v_{\text{ph}} = c/\sqrt{\epsilon_{\text{eff}}}$ is the phase velocity depending on the velocity of light in vacuum c and the effective permittivity ϵ_{eff} of the coplanar waveguide line. The permittivity ϵ_{eff} is a function of the waveguide geometry and the relative permittivities ϵ_1 and ϵ_2 of substrate and the oxide layer, see Fig. 2.1c. Furthermore, $2l = \lambda_0$ is the wavelength of the fundamental resonator mode. The length dependence of the measured resonance frequencies f_0 of our samples is well described by Eq. (2.1) with the effective dielectric constant $\epsilon_{\text{eff}} = 5.05$, see Fig. 2.1c.

The phase velocity of electromagnetic waves propagating along a transmission line depends on the capacitance C_ℓ and inductance L_ℓ per unit length of the line as

$$v_{\text{ph}} = \frac{1}{\sqrt{L_\ell C_\ell}}. \quad (2.2)$$

Using conformal mapping techniques, the geometric contribution to L_ℓ and C_ℓ of a coplanar waveguide line is found to be [Gevorgian1995, Watanabe1994]

$$L_\ell = \frac{\mu_0}{4} \frac{K(k'_0)}{K(k_0)}, \quad (2.3)$$

$$C_\ell = 4\epsilon_0\epsilon_{\text{eff}} \frac{K(k_0)}{K(k'_0)}. \quad (2.4)$$

Here, K denotes the complete elliptic integral of the first kind with the arguments

$$k_0 = \frac{w}{w + 2s}, \quad (2.5)$$

$$k'_0 = \sqrt{1 - k_0^2}. \quad (2.6)$$

For non magnetic substrates ($\mu_{\text{eff}} = 1$) and neglecting kinetic inductance for the moment L_ℓ is determined by the coplanar waveguide geometry only. C_ℓ depends on the geometry and ϵ_{eff} . An analytical expression

$$\epsilon_{\text{eff}} = 1 + \frac{\epsilon_1 - 1}{2} \frac{K(k_1)}{K(k'_1)} \frac{K(k'_0)}{K(k_0)} + \frac{\epsilon_2 - \epsilon_1}{2} \frac{K(k_2)}{K(k'_2)} \frac{K(k'_0)}{K(k_0)} \quad (2.7)$$

with the arguments

$$k_{1,2} = \frac{\sinh\left(\frac{\pi w}{4h_{1,2}}\right)}{\sinh\left[\frac{\pi(2s+w)}{4h_{1,2}}\right]}, \quad (2.8)$$

$$k'_{1,2} = \sqrt{1 - k_{1,2}^2} \quad (2.9)$$

has been deduced from conformal mapping [Gevorgian1995] for coplanar waveguide resonators on double layer substrates. However, the accuracy of these calculations depends sensitively on the ratio between substrate layer thicknesses and the dimensions of the coplanar waveguide resonator cross-section [Chen1997] and does not lead to accurate predictions for our devices. Using Eq. (2.7) we get $\epsilon_{\text{eff}} = 5.85$ for our coplanar waveguide geometry in case of $\epsilon_1 = 11.6$ for Si (see reference [Musil1986]) and $\epsilon_2 = 3.78$ for thermal grown SiO_2 (see reference [Musil1986]), yielding a deviation of about 16% from the measured value 5.05. Therefore, $C_\ell \approx 1.27 \cdot 10^{-10} \text{ Fm}^{-1}$ was calculated using a finite element electrostatic simulation and the values $\epsilon_1 = 11.6$ and $\epsilon_2 = 3.78$ for the coplanar waveguide geometry and substrate. From this calculation we find $\epsilon_{\text{eff}} \approx 5.22$ which deviates only by about 3% from the value extracted from our measurements.

The characteristic impedance of a coplanar waveguide is given by $Z_0 = \sqrt{L_\ell/C_\ell} = 59.7 \Omega$ for our geometry, which deviates from the usually chosen value of 50Ω as the original design was optimized for a different substrate material.

In general, for superconductors, the inductance L_ℓ is given by

$$L_\ell = L_\ell^{\text{m}} + L_\ell^{\text{k}}, \quad (2.10)$$

with the temperature independent geometric (magnetic) inductance L_ℓ^{m} and the temperature dependent kinetic inductance L_ℓ^{k} (see reference [Tinkham1996]). For superconductors, L_ℓ^{k} refers to the inertia of moving Cooper pairs and can contribute significantly to L_ℓ since resistivity is suppressed and thus charge carrier relaxation times are large. According to [Watanabe1994], L_ℓ^{k} is

$$L_\ell^{\text{k}} = \mu_0 \frac{\lambda^2}{wt} g(s, w, t) \quad (2.11)$$

and scales with the geometry factor

$$g(s, w, t) = \frac{1}{2k_0^2 K^2(k_0)} \left(-\ln \frac{t}{4w} - \frac{w}{w+2s} \ln \frac{t}{4(w+2s)} + \frac{2(w+s)}{w+2s} \ln \frac{s}{w+s} \right) \quad (2.12)$$

and $\lambda^2(T)$, where $\lambda(T)$ is the temperature dependent London penetration depth which can be approximated as

$$\lambda(0) = 1.05 \cdot 10^{-3} \sqrt{\frac{\rho(T_c)}{T_c}} \sqrt{\frac{\text{Km}}{\Omega}} \quad (2.13)$$

at zero temperature in the local and dirty limits [Watanabe1994]. In this limit, the mean free path of electrons l_{mf} is much less than the coherence length $\xi_0 = \hbar v_f / \pi \Delta(0)$, where v_f is the Fermi velocity of the electrons and $\Delta(0)$ is the superconducting gap energy at zero temperature [Parks1969]. The clean (nonlocal) limit occurs when l_{mf} is much larger than ξ_0 (see reference [Parks1969]). $T_c = 1.23 \text{ K}$ is the critical temperature of the used thin film aluminum and $\rho(T_c) = 2.06 \cdot 10^{-9} \Omega \text{ m}$ is the normal state resistivity at $T = T_c$. T_c and $\rho(T)$ were determined in a four-point measurement of the resistance of a lithographically patterned Al thin film meander structure from the same substrate in dependence on temperature. The measured residual resistance ratio

ID	Coupling	C_κ (fF)	f_0 (GHz)	Q_L
A	8 + 8 finger	56.4	2.2678	$3.7 \cdot 10^2$
B	7 + 7 finger	48.6	2.2763	$4.9 \cdot 10^2$
C	6 + 6 finger	42.9	2.2848	$7.5 \cdot 10^2$
D	5 + 5 finger	35.4	2.2943	$1.1 \cdot 10^3$
E	4 + 4 finger	26.4	2.3086	$1.7 \cdot 10^3$
F	3 + 3 finger	18.0	2.3164	$3.9 \cdot 10^3$
G	2 + 2 finger	11.3	2.3259	$9.8 \cdot 10^3$
H	1 + 1 finger	3.98	2.3343	$7.5 \cdot 10^4$
I	10 μm gap	0.44	2.3430	$2.0 \cdot 10^5$
J	20 μm gap	0.38	2.3448	$2.0 \cdot 10^5$
K	30 μm gap	0.32	2.3459	$2.3 \cdot 10^5$
L	50 μm gap	0.24	2.3464	$2.3 \cdot 10^5$

Table 2.2: Parameters of coplanar waveguide resonators. C_κ denotes the simulated coupling capacitances, f_0 is the measured resonance frequency and Q_L is the measured quality factor.

($RRR_{300\text{K}/1.3\text{K}}$) is 8.6. Since our measurements were performed at temperatures well below T_c , $\lambda = \lambda(0)$ approximately holds and we find $\lambda(0) \approx 43\text{ nm}$ for our aluminum thin films (compared to a value of 40 nm, given in reference [Poole1995]). Using the above approximation shows that $L_\ell^k \approx 6.43 \cdot 10^{-9}\text{ Hm}^{-1}$ is about two orders of magnitude smaller than $L_\ell^m = 4.53 \cdot 10^{-7}\text{ Hm}^{-1}$ legitimating the assumption $L_\ell \approx L_\ell^m$ made in Eq. (2.3).

2.2 Distributed and Lumped Element Model of a Transmission Line Resonator

The life time τ of photons stored in a cavity is given by the cavity decay rate $\kappa = 1/\tau$ which states how long in average photons are confined in the cavity before they get lost due to resonator leakage or loss and which is given by the quality factor $Q = \omega/\kappa$ of the cavity. The (external) quality factor of a resonator also determines how fast photons can be injected into the cavity when manipulating integrated qubits and measuring their state. Designing circuit QED experiments with a defined κ thus makes it necessary to have accurate control over the cavity Q .

When using capacitively coupled transmission line resonators, photon injection and photon leakage can be controlled by varying the capacitance of the input/output capacitors which couple the resonator to an external transmission line (see Fig. 2.1). In order to gain an intuitive understanding of a capacitively coupled transmission line resonator the device can be modeled by a parallel LCR circuit. This lumped element model of a transmission line provides simple expressions to describe the resonator properties around resonance where $|f - f_0|/f_0 \ll 1$ holds. In order to describe the full transmission spectrum of a resonator, the ABCD matrix model can be used what is discussed in a later section.

To study the effect of the capacitive coupling strength on the microwave properties of coplanar waveguide resonators, twelve 2.3 GHz fundamental frequency devices symmetrically coupled to input/output lines with different gap and finger capacitors have been characterized, see Tab. 2.2 for a list of devices. The measured transmission spectra are shown in Fig. 2.6. The left hand part of Fig. 2.6 depicts spectra of resonators coupled via finger capacitors having eight down to one pairs of fingers (devices A to H). The right hand part of Fig. 2.6 shows those resonators coupled via gap capacitors with gap widths of $w_g = 10, 20, 30$ and $50\ \mu\text{m}$ (devices I to L), respectively. The coupling capacitance continuously decreases from device A to device L. The nominal values for

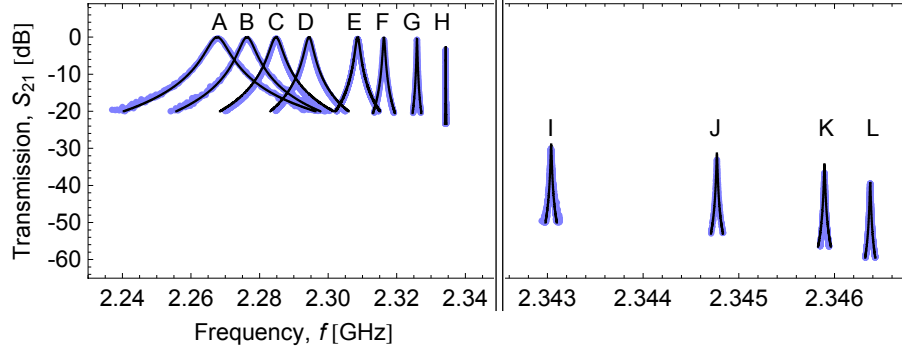


Figure 2.6: S_{21} transmission spectra of 2.3 GHz resonators which are symmetrically coupled to input/output lines. Data points (blue) were fitted (black) with the transmission matrix method, see text.

the coupling capacitance C_κ obtained from electro-static simulations for the investigated substrate properties and geometry are listed in Tab. 2.2. The resonance frequency f_0 and the loaded quality factor $Q_L = f_0/\delta f$ of the respective device is obtained by fitting a Lorentzian line

$$F_{\text{Lor}}(f) = A_0 \frac{\delta f}{(f - f_0)^2 + \delta f^2/4} \quad (2.14)$$

to the data, see Fig. 2.4, where δf is the full width half maximum of the resonance.

With increasing coupling capacitance C_κ , Fig. 2.6 shows a decrease in the measured (loaded) quality factor Q_L and an increase in the peak transmission, as well as a shift of f_0 to lower frequencies. In the following, it is discussed how these characteristic resonator properties can be fully understood and modeled consistently for the full set of data.

A transmission line resonator is a distributed device with voltages and currents varying in magnitude and phase over its length. The distributed element representation of a symmetrically coupled resonator is shown in Fig. 2.7a. R_ℓ , L_ℓ and C_ℓ denote the resistance, inductance and capacitance per unit length, respectively. G_ℓ is the shunt conductance per unit length due to leakage between center conductor and ground and is neglected.

In the following, the impedance of a transmission line resonator is compared to that of a parallel LCR oscillator. By mapping both impedances to each other, one obtains expressions which describe the transmission line resonator in terms of the inductance, the capacitance and the resistance of an equivalent parallel LCR oscillator.

According to reference [Poazar1993] the impedance of a transmission line, terminated with an arbitrary load Z_L at a distance l_L from the input port is given by

$$Z_{\text{TL}} = Z_0 \frac{Z_L + Z_0 \tanh(\gamma l_L)}{Z_0 + Z_L \tanh(\gamma l_L)}. \quad (2.15)$$

Here, Z_0 denotes the characteristic impedance

$$\begin{aligned} Z_0 &= \sqrt{\frac{R_\ell + i\omega L_\ell}{G_\ell + i\omega C_\ell}} \\ &\approx \sqrt{\frac{L_\ell}{C_\ell}} \end{aligned} \quad (2.16)$$

of an infinitely long transmission line with small losses and small leakage. The transmission line's wave propagation coefficient $\gamma = \alpha + i\beta$ is given by the attenuation along the transmission line

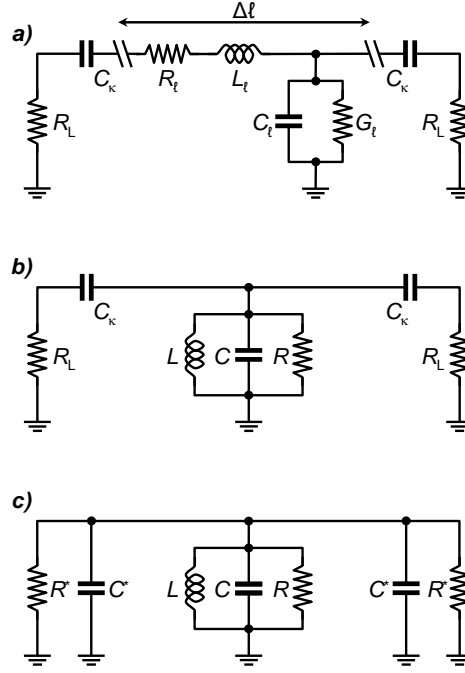


Figure 2.7: (a) Distributed element representation of symmetrically coupled transmission line resonator. (b) Parallel LCR oscillator representation of transmission line resonator. (c) Norton equivalent of symmetrically coupled, parallel LCR oscillator. Symbols are explained in text.

α and the phase propagation of the transmission line $\beta = \omega_n/v_{\text{ph}}$. Here, n denotes the resonator mode number ($n = 1$ for the fundamental mode) and $\omega_n = n\omega_0$ is the angular frequency of the n -th mode ($\omega_0 := \omega_1$ for the fundamental mode). For an open-circuited transmission line resonator ($Z_L \rightarrow \infty$) Eq. (2.15) simplifies to

$$\begin{aligned} Z_{\text{TL}} &= Z_0 \coth(\gamma l) \\ &= Z_0 \frac{1 + i \tan(\beta l) \tanh(\alpha l)}{\tanh(\alpha l) + i \tan(\beta l)}. \end{aligned} \quad (2.17)$$

The wavelength λ_0 of the fundamental resonance with frequency ω_0 is two times the length l of the resonator. When approximating the frequency around the n -th resonance as $\omega = n\omega_0 + \Delta\omega$, one finds

$$\beta l = \pi \left(n + \frac{\Delta\omega}{\omega_0} \right), \quad (2.18)$$

$$\begin{aligned} \tan(\beta l) &= \tan \left(\pi n + \pi \frac{\Delta\omega}{\omega_0} \right) \\ &= \tan \left(\pi \frac{\Delta\omega}{\omega_0} \right) \\ &\approx \pi \frac{\Delta\omega}{\omega_0}, \end{aligned} \quad (2.19)$$

for $\Delta\omega$ being small compared to ω_0 . Using the above approximation and assuming small losses ($\tanh(\alpha l) \approx \alpha l \ll 1$), Eq. (2.17) can be written as

$$Z_{\text{TL}} \approx \frac{Z_0}{\alpha l + i \frac{\pi}{\omega_0} (\omega - \omega_n)}. \quad (2.20)$$

Around resonance, where $\Delta\omega \ll \omega_0$ holds, the properties of a transmission line resonator can be approximated by those of a lumped element parallel LCR oscillator as shown in Fig. 2.7b.

When using Kirchhoff's first and second law, the impedance of a parallel LCR oscillator is found to be

$$Z_{\text{LCR}} = \left(\frac{1}{R} + \frac{1}{i\omega L} + i\omega C \right)^{-1}. \quad (2.21)$$

Around resonance, $\omega = n\omega_0 + \Delta\omega$ and $\Delta\omega \ll \omega$ holds and Eq. (2.21) can be rewritten as

$$\begin{aligned} Z_{\text{LCR}} &\approx \left(\frac{1}{R} + \frac{1 - \Delta\omega/n\omega_0}{in\omega_0 L} + in\omega_0 C + i\Delta\omega C \right)^{-1} \\ &\approx \left(\frac{1}{R} + i \frac{\Delta\omega}{(n\omega_0)^2 L} + i\Delta\omega C \right)^{-1} \\ &\approx \left(\frac{1}{R} + 2i\Delta\omega C \right)^{-1} \\ &\approx \frac{R}{1 + 2i\Delta\omega RC} \\ &= \frac{R}{1 + 2iRC(\omega - \omega_n)}. \end{aligned} \quad (2.22)$$

By means of mapping the two impedances given in Eqs. (2.20) and (2.22) to each other one finds for the characteristic parameters

$$L := L_n = \frac{2L_\ell l}{n^2 \pi^2}, \quad (2.23)$$

$$C = \frac{C_\ell l}{2}, \quad (2.24)$$

$$R = \frac{1}{\alpha l} Z_0. \quad (2.25)$$

As already mentioned, this approximation is only valid around resonance, where $\omega \approx n\omega_0$ holds. The LCR model is useful to get an intuitive picture of the resonator properties. It simplifies analyzing the effect of coupling the resonator to an input/output line on the quality factor and on the resonance frequency as discussed in the next section.

The (internal) quality factor of a resonance circuit is in general defined as ω times the average energy stored in the circuit divided by the energy dissipation per time [Pozar1993]. For the parallel LCR circuit one finds

$$Q_{\text{int}} = \omega_n \frac{W_{\text{el}} + W_{\text{mag}}}{P_{\text{loss}}}. \quad (2.26)$$

In order to calculate W_{el} , W_{mag} and P_{loss} , the time averaged power delivered to a LCR circuit is considered. In case of a harmonic signal applied to the resonator, one finds

$$\begin{aligned} P &= \frac{1}{2} V I^* \\ &= \frac{1}{2} Z_{\text{LCR}} |I|^2 \\ &= \frac{1}{2} \frac{1}{Z_{\text{LCR}}^*} |V|^2, \end{aligned} \quad (2.27)$$

where V is the peak voltage across and I is the total peak current through R , C and L_n . The power dissipated by the resistor is

$$P_{\text{loss}} = \frac{1}{2} \frac{|V|^2}{R}, \quad (2.28)$$

and the average electric and magnetic energy stored in the capacitor respectively inductor is

$$W_{\text{el}} = \frac{1}{4} |V|^2 C \quad (2.29)$$

$$\begin{aligned} W_{\text{mag}} &= \frac{1}{4} |I_L|^2 L_n \\ &= \frac{1}{4} |V|^2 \frac{1}{\omega_n^2 L_n}. \end{aligned} \quad (2.30)$$

The power in Eq. (2.27) can then be rewritten as

$$P = P_{\text{loss}} + 2i\omega(W_{\text{mag}} - W_{\text{el}}). \quad (2.31)$$

Further, for the impedance presented in Eq. (2.21) one finds

$$\begin{aligned} Z_{\text{LCR}} &= 2 \frac{P}{|I_L|^2} \\ &= 2 \frac{P_{\text{loss}} + 2i\omega(W_{\text{mag}} - W_{\text{el}})}{|I_L|^2}. \end{aligned} \quad (2.32)$$

Resonance occurs for $W_{\text{el}} = W_{\text{mag}}$ when average stored electric and magnetic energies are equal. At resonance, one finds $Z = R$ from Eqs. (2.28) and (2.31). Considering Eqs. (2.29) and (2.30), $W_{\text{el}} = W_{\text{mag}}$ implies that the circuit behaves resonant for

$$\omega_n = \frac{1}{\sqrt{L_n C}}. \quad (2.33)$$

Using now Eqs. (2.26, 2.28, 2.29, 2.29, 2.33), one finally finds for the (internal) quality factor of a parallel LCR circuit

$$Q_{\text{int}} = \omega_n R C. \quad (2.34)$$

The internal quality factor describes photon losses of the resonator due to dissipation. In the following section, an external quality factor Q_{ext} will be defined which describes photon losses due to resonator leakage.

2.3 Capacitively Coupled Transmission Line Resonators

When coupling the resonator's input/output lines capacitively to an external load R_L , the quality factor Q_L of the resonator is reduced due to resistive loading, see Figs. 2.7a, b. Additionally, the frequency of the resonator is shifted because of the capacitive loading C_κ of the resonator due to the input/output lines, see Figs. 2.7a, b, as will be shown in this section.

In order to understand the two mentioned effects, the series connection of C_κ and R_L at one output port of the resonator can be transformed into a Norton equivalent parallel connection of a resistor R^* and a capacitor C^* , see Figs. 2.7b, c, with

$$R^* = \frac{1 + \omega_n^2 C_\kappa^2 R_L^2}{\omega_n^2 C_\kappa^2 R_L}, \quad (2.35)$$

$$C^* = \frac{C_\kappa}{1 + \omega_n^2 C_\kappa^2 R_L^2}. \quad (2.36)$$

The small capacitor C_κ transforms the usually $R_L = 50 \Omega$ load into the large impedance $R^* = R_L/k^2$ with $k = \omega_n C_\kappa R_L \ll 1$.

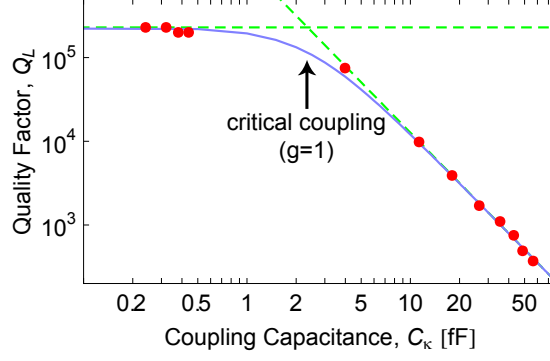


Figure 2.8: Q_L dependence on C_κ . Data points (red) indicate measured Q values. These values are compared to Q_L predictions by the mapped LCR model (blue curve) given by Eqs. (2.35, 2.39, 2.41).

When considering now both, input and output lines, the parallel combinations of the two resistors R^* and the two capacitors C^* have to be taken into account. For symmetric input/output coupling, the loaded quality factor for the parallel combination of R and $R^*/2$ is

$$\begin{aligned} Q_L &= \omega_n^* \frac{C + 2C^*}{1/R + 2/R^*} \\ &\approx \omega_n \frac{C}{1/R + 2/R^*} \end{aligned} \quad (2.37)$$

with the n -th resonance frequency shifted by the capacitive loading due to the parallel combination of C and $2C^*$

$$\omega_n^* = \frac{1}{\sqrt{L_n(C + 2C^*)}}. \quad (2.38)$$

For $\omega_n^* \approx \omega_n$ with $C + 2C^* \approx C$, the Norton equivalent expression for the loaded quality factor Q_L is a parallel combination of the internal and external quality factors

$$\frac{1}{Q_L} = \frac{1}{Q_{\text{int}}} + \frac{1}{Q_{\text{ext}}}, \quad (2.39)$$

with

$$\begin{aligned} Q_{\text{int}} &= \omega_n RC \\ &= \frac{n\pi}{2\alpha l}, \end{aligned} \quad (2.40)$$

$$Q_{\text{ext}} = \frac{\omega_n R^* C}{2}. \quad (2.41)$$

The measured loaded quality factor Q_L for devices A to L is plotted versus the coupling capacitance in Fig. 2.8. Q_L is observed to be constant for small coupling capacitances and decreases for large ones. In the overcoupled regime ($Q_{\text{ext}} \ll Q_{\text{int}}$), Q_L is governed by Q_{ext} which is well approximated by $C/2\omega_n R_L C_\kappa^2$, see sloping dashed line in Fig. 2.8. Thus, in the overcoupled regime the loaded quality factor $Q_L \propto C_\kappa^{-2}$ can be controlled by the choice of the coupling capacitance. In the undercoupled limit ($Q_{\text{ext}} \gg Q_{\text{int}}$) however, Q_L saturates at the internal quality factor $Q_{\text{int}} \approx 2.3 \cdot 10^5$ determined by the intrinsic losses of the resonator, see horizontal dashed line in Fig. 2.8.

Radiation losses are expected to be small in coplanar waveguide resonators [Browne1987], resistive losses are negligible well below the critical temperature T_c of the superconductor [Frunzio2005]

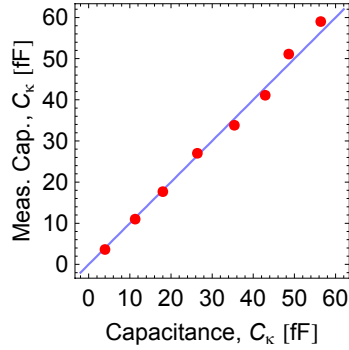


Figure 2.9: Comparison of C_κ values extracted from the Q_L by Eqs. (2.35, 2.39, 2.41) (red points) to the EM-simulated values for C_κ for devices A to H. The blue curve is the line through origin with slope one.

and at frequencies well below the superconducting gap. The internal quality factor of the characterized devices is mainly limited by dielectric losses, as discussed in references [Martinis2005] and [O'Connell2008].

In order to investigate how well the designed values for the coupling capacitances C_κ match the real ones, C_κ has been extracted from the measured loaded quality factors Q_L of the overcoupled devices A to H and the measured value of $Q_{\text{int}} \sim 2.3 \cdot 10^5$ by using Eqs. (2.35, 2.39, 2.41), see Fig. 2.9. Values for C_κ which match the designed value are represented by the blue line in Fig. 2.9. The experimental values of C_κ are in good agreement with the ones found from finite element calculations, listed in Tab. 2.2, with a standard deviation of about 4%.

Over and undercoupled resonators are used for different circuit QED applications. Strongly coupled resonators with accordingly low quality factors are ideal for performing fast measurements on the state of a qubit integrated into the resonator. Undercoupled resonators with large quality factors can be used to store photons in the cavity on a long time scale, with potential use as a quantum memory.

The insertion loss

$$L_0 = -20 \log \left(\frac{g}{g+1} \right) \text{ dB} \quad (2.42)$$

of a resonator, i.e. the deviation of peak transmission from unity, is dependent on the ratio of the internal to the external quality factor which is also called the coupling coefficient $g = Q_{\text{int}}/Q_{\text{ext}}$ (see reference [Pozar1993]). The measured values of L_0 as extracted from Fig. 2.6 are shown in Fig. 2.10. For $g \gg 1$ (large C_κ) the resonator is overcoupled and shows near unit transmission ($L_0 = 0$). Due to the large capacitance input/output coupling, photons can be injected and transmitted easily in this case. The resonator is said to be critically coupled for $g = 1$. For $g \ll 1$ (small C_κ) the resonator is undercoupled and the transmission is significantly reduced, due to the small capacitance input/output coupling. In this case L_0 is well approximated by $-20 \log(2\omega_n Q_{\text{int}} R_L C_\kappa^2 / C)$, see dashed line in Fig. 2.10, as calculated from Eqs. (2.35, 2.41, 2.42). Q_{ext} and Q_{int} can be determined from Q_L and L_0 using Eqs. (2.39) and (2.42), thus allowing to roughly estimate internal losses even of an overcoupled cavity.

For the overcoupled devices A to H, the coupling induced resonator frequency shift as extracted from Fig. 2.6 is in good agreement with calculations based on Eqs. (2.36) and (2.38), see Fig. 2.11. For $C^* \approx C_\kappa$ and $C \gg C_\kappa$, one can Taylor-approximate ω_n^* as $\omega_n(1 - C_\kappa/C)$. As a result, the relative resonator frequency shift is $(\omega_n^* - \omega_n)/\omega_n = -C_\kappa/C$ for symmetric coupling. Figure 2.11 shows the expected linear dependence with a maximum frequency shift of about 3% over a range of 60 fF in C_κ and for $C = 1.82$ pF.

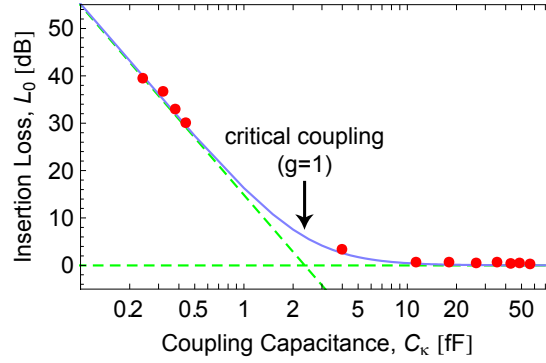


Figure 2.10: Dependence of L_0 on C_κ . Data points (red) show measured L_0 values. The values are compared to the mapped LCR model expectations (blue curve) given by Eqs. (2.35, 2.41, 2.42).

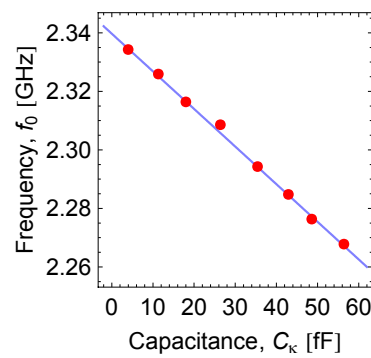


Figure 2.11: Dependence of f_0 on C_κ . The mapped LCR model behavior given by Eqs. (2.36) and (2.38) is shown (blue curve) for resonators coupled via finger capacitors together with the measured values for f_0 (red points).

All in all, it is demonstrated that loaded quality factors and resonance frequencies can be precisely controlled and that the LCR model is in good agreement with measured data. In the case of resonators coupled via finger capacitors, simulated values for C_κ deviate by only about 4%.

2.4 Transmission Matrix Model and Harmonic Resonator Modes

As an alternative method to the LCR model which provides only an accurate description of the resonator near resonance, measured data is analyzed using the transmission matrix method [Pozar1993]. Using this method, the full transmission spectrum of the coplanar waveguide resonator can be calculated. Here, each component of an arbitrary microwave network is described by a 2×2 matrix. The product of the individual 2×2 matrices gives an overall transmission matrix with which the S_{21} transmission of the network can be calculated.

The transmission or ABCD matrix of a symmetrically coupled transmission line resonator is defined by the product of an input-, a transmission-, and an output matrix as

$$\begin{pmatrix} A & B \\ C & D \end{pmatrix} = \begin{pmatrix} 1 & Z_{\text{in}} \\ 0 & 1 \end{pmatrix} \begin{pmatrix} t_{11} & t_{12} \\ t_{21} & t_{22} \end{pmatrix} \begin{pmatrix} 1 & Z_{\text{out}} \\ 0 & 1 \end{pmatrix}, \quad (2.43)$$

with input/output impedances $Z_{\text{in/out}} = 1/i\omega C_\kappa$ and the transmission matrix parameters

$$t_{11} = \cosh((\alpha + i\beta)l), \quad (2.44)$$

$$t_{12} = Z_0 \sinh((\alpha + i\beta)l), \quad (2.45)$$

$$t_{21} = 1/Z_0 \sinh((\alpha + i\beta)l), \quad (2.46)$$

$$t_{22} = \cosh((\alpha + i\beta)l). \quad (2.47)$$

The resonator transmission spectrum is then defined by the ABCD matrix components as

$$S_{21} = \frac{2}{A + B/R_L + CR_L + D}. \quad (2.48)$$

Here, R_L is the load resistance of the external input/output transmission lines, α is determined by Q_{int} and l and β depends on ϵ_{eff} , as discussed before. According to Eqs. (2.3) and (2.4) Z_0 is determined by ϵ_{eff} , w and s . The attenuation constant is $\alpha \sim -72$ dB/m as determined from $Q_{\text{int}} \sim 2.3 \cdot 10^5$.

For gap capacitor coupled devices, the measured data fits very well, see Fig. 2.6, to the transmission spectrum calculated using the ABCD matrix method with $\bar{\epsilon}_{\text{eff}} = 5.05$, already obtained from the measured dependence of f_0 on the resonator length, see Fig. 2.5. For finger capacitor coupled structures however, see Fig. 2.1b, approximately 40% of the length of each $100 \mu\text{m}$ finger has to be added to the length l of the bare resonators in order to obtain good fits to the resonance frequency f_0 . The relatively large finger capacitors have to be considered as distributed element, with voltages and currents varying inside. The actual finger geometry determines the electric field geometry of the finger and leads to the mentioned result which is independent of the number of fingers. The ABCD matrix model describes the full transmission spectra of all measured devices very well with a single set of parameters, see Fig. 2.6.

So far, only the properties of the fundamental resonance frequency of any of the measured resonators is discussed. Superconducting charge qubits like the Cooper pair box or transmon type qubit which are integrated into a coplanar waveguide resonator couple capacitively to the electric field inside the resonator. When using the fundamental ($n = 1$) cavity mode, the electric field is

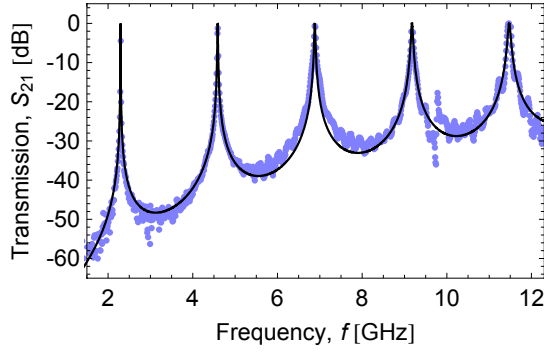


Figure 2.12: S_{21} transmission spectrum of resonator D with fundamental mode and harmonics. The measured data (blue) is compared to the S_{21} spectrum (black) obtained by scattering matrix methods.

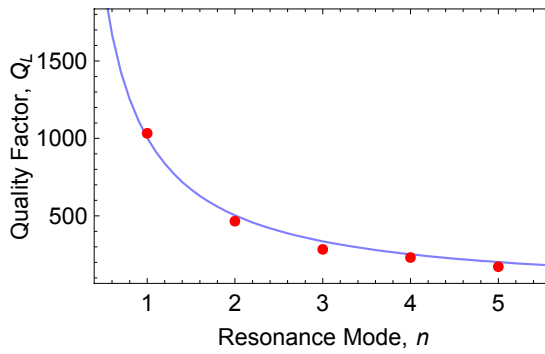


Figure 2.13: Measured Q for the overcoupled resonator D (red points) together with the prediction of the mapped LCR model given by Eqs. (2.35, 2.39, 2.41) (blue curve).

maximal at the resonator ends and for maximum qubit-cavity coupling one would place the qubit close to the resonator ends. Using harmonic modes is especially interesting for accessing integrated qubit structures at cavity positions off from the resonator ends. In general, the field of the n -th harmonic mode has $n - 1$ additional electric field amplitude maxima. In this way, multi qubit structures can be coupled to a single cavity with the same frequency, allowing inter-qubit coupling via the cavity.

A full transmission spectrum of the overcoupled resonator D, including 5 harmonic modes, is shown in Fig. 2.12. The measured spectrum fits well to the ABCD matrix model for the fundamental frequency and also for higher cavity modes, displaying a decrease of the loaded quality factor with harmonic number. The dependence of the measured quality factor Q_L on the mode number n is in agreement with Eqs. (2.35, 2.39, 2.41) and scales approximately as $C/2n\omega_0 R_L C_\kappa^2$, see Fig. 2.13. This result is in particular important when designing circuit QED devices for experiments where higher harmonic modes are used for qubit manipulation and readout.

2.5 Power Dependence of Quality Factor

The measured Q of undercoupled devices can vary strongly with the power applied to the resonator. In the particular measurements of high Q devices presented above, the resonator transmission spectrum loses its Lorentzian shape at drive powers above approximately -70 dBm at the input port of the resonator due to non-linear effects [Abdo2006]. At low drive powers, dielectric resonator losses significantly depend on the photon number inside the cavity [Martinis2005, O'Connell2008],

measured quality factors may be substantially reduced. In the measurements presented above, S_{21} transmission spectra were acquired at power levels chosen to result in the highest measurable quality factors, i.e. at high enough powers to minimize dielectric loss but low enough to avoid non-linearities. This approach has been chosen to be able to focus on geometric properties of the resonators.

Figure 2.14 shows the transmission spectrum of the highly undercoupled resonator K (compare Tab. 2.2) for drive powers at the resonator input ranging between -70 dBm and -40 dBm. Clearly, the transmission spectrum gets non-linear for higher powers. The behavior of a transmission line resonator which is modeled by a parallel LCR circuit, see Fig. 2.7a, b, can be described by its equation of motion. In the following, the linear case is treated before non-linear resonators are considered.

The temporal response of a linear LCR oscillator can be calculated by its equation of motion

$$LC\ddot{I}_L + \frac{L}{R}\dot{I}_L + I_L = 0 \quad (2.49)$$

which is derived by Kirchhoff's first and second law. Here, I_L is the current through the inductor which is found as

$$I_L(t) = I_{L0} \exp[-\delta\omega t] \cos(\tilde{\omega}_r t + \phi_0), \quad (2.50)$$

with $\delta\omega = 1/2RC$ and $\tilde{\omega}_r = \sqrt{1/LC - 1/4R^2C^2}$, in case of an underdamped resonator where $(L/R)^2 - 4LC < 0$ holds. Here, the current amplitude I_{L0} and the phase offset ϕ_0 is determined by the initial conditions. The transmission spectrum of the LCR oscillator is then given by the real part of the Fourier transform of Eq. (2.50). When considering the power transmitted through the resonator which scales quadratic to the transmitted amplitude one finds for the parallel LCR oscillator

$$P(\omega) = P_0 \frac{\delta\omega^2}{(\omega - \tilde{\omega}_r)^2 + \delta\omega^2}. \quad (2.51)$$

A LCR oscillator driven with a harmonic force is in its linear regime described by the equation of motion

$$LC\ddot{I}_L + \frac{L}{R}\dot{I}_L + I_L = I_{D0} \cos(\Omega t) \quad (2.52)$$

where the driving force is modeled by the term $I_{D0} \cos(\Omega t)$. This differential equation is solved by the sum of the homogeneous solution (2.50) and the particular solution

$$I_p(t) = I_{p0} \cos(\Omega t - \phi_p), \quad (2.53)$$

where

$$I_{p0} = \frac{I_{D0}/LC}{\sqrt{(1/LC - \Omega^2)^2 + \Omega^2/R^2C^2}}, \quad (2.54)$$

$$\phi_p = \frac{\Omega/RC}{1/LC - \Omega^2} \quad (2.55)$$

holds.

In order to describe the nonlinear behavior of a parallel LCR oscillator, the equation of motion

$$LC\ddot{I}_L + \frac{L}{R}\dot{I}_L + I_L + pI_L^3 = I_{D0} \cos(\Omega t), \quad (2.56)$$

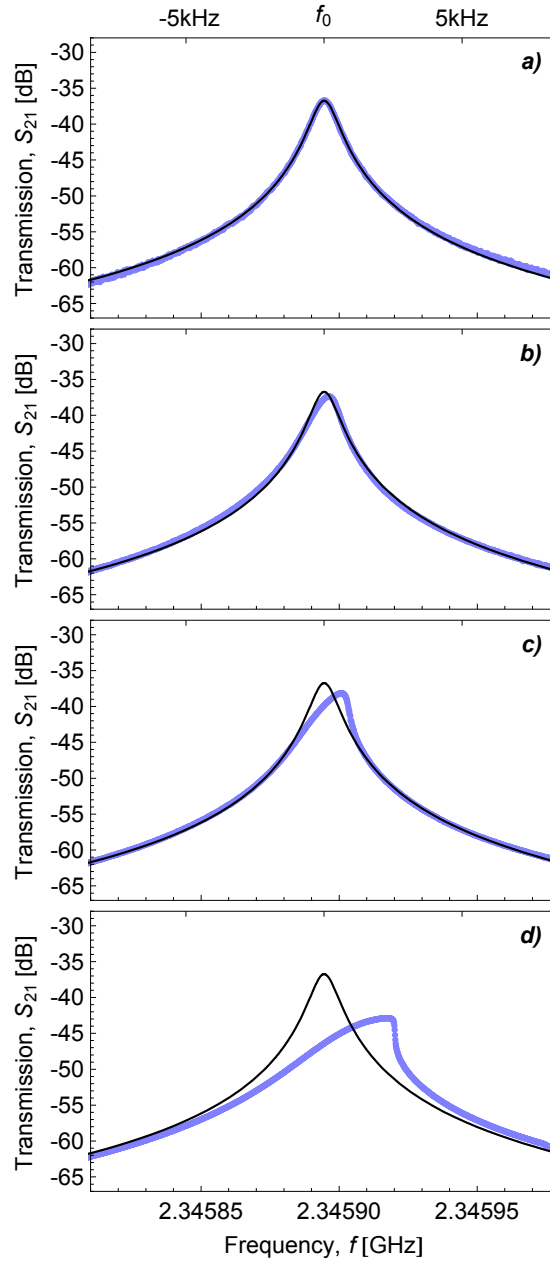


Figure 2.14: Transmission spectrum of resonator K (see Tab. 2.2) in dependence on the power applied to the resonator input port. (a) -70 dBm, (b) -60 dBm, (c) -50 dBm and (d) -40 dBm. The transmission spectrum shown in part a) was fitted with a Lorentzian line (compare Eq. (2.14)). The Lorentz fit from part a) is also depicted in parts b, c and d.

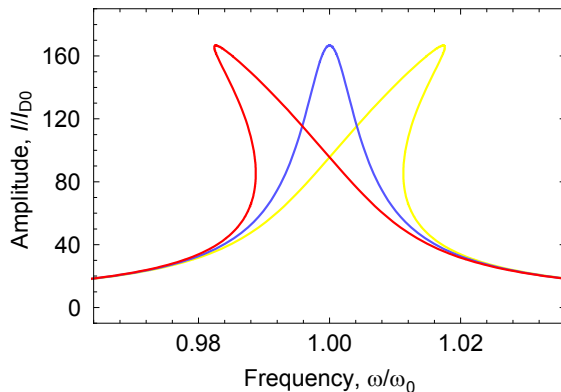


Figure 2.15: Resonance curves for a Duffing oscillator. The blue line shows the linear case for $p = 0$, the red line shows the case for $p < 0$ and the yellow line shows the case for $p > 0$.

is used, where p is a positive or negative parameter describing the degree of nonlinearity. An oscillator modeled by this equation is known as *Duffing oscillator*. Equation (2.56) is solved numerically for $p < 0$, $p = 0$ and $p > 0$ and the corresponding resonance curves are shown in Fig. 2.15. The resonance curve of a linear oscillator (blue line) is not tilted whereas those of a nonlinear oscillator with $p < 0$ (red line) and $p > 0$ (yellow line) are tilted to lower and higher frequencies, respectively.

An example of a Duffing oscillator is a spring with a restoring force

$$F = -qx - px^3, \quad (2.57)$$

where x is the spring elongation and q and p are spring parameters, compare Eq. (2.56). The case $p < 0$ describes a *softening spring* with a spring constant decreasing with elongation x and the case $p > 0$ a *hardening spring* with a spring constant increasing with elongation x . The nonlinear transmission spectrum of the measured coplanar waveguide resonator K, shown in Fig. 2.14, tilts to higher frequencies and thus behaves like a hardening spring.

In order to study the dependence of Q_L on the drive power respectively on the average photon number in the cavity, transmission spectra of resonator K were acquired for an input power range of -115 dBm to -70 dBm. Within this range, the resonator is always operated in its linear regime. The corresponding quality factors are extracted by fitting a Lorentzian line and shown in Fig. 2.16a in dependence on the drive power at the resonator's input port. As already mentioned above, the (internal) quality factor of a resonance circuit is in general defined as ω times the average energy stored in the circuit divided by the energy dissipation per time, see Eq. (2.34). The average energy stored in the resonator is given by $n\hbar\omega$, where n denotes the average photon number inside the cavity. In the steady state, the average energy in the cavity stays constant and thus the power delivered to the resonator minus the transmitted power equals the power which is dissipated inside the cavity and corresponds to the insertion loss. The measured insertion loss L_0 of device K is depicted in Fig. 2.16b for different input powers. For increasing drive power, L_0 decreases and saturates at a value of about 35 dB. For an undercoupled resonator such as device K, $Q_{\text{ext}} \gg Q_{\text{int}}$ and thus $Q_L \approx Q_{\text{int}}$ holds. Further, the transmission is significantly reduced due to the high insertion loss L_0 . In the steady state, the dissipated power in the resonator is thus mainly given by the input power delivered to the resonator and $P_{\text{loss}} \approx P_{\text{in}}$ holds. Using the general definition of the quality factor given above, the average photon number inside the cavity is therefore found

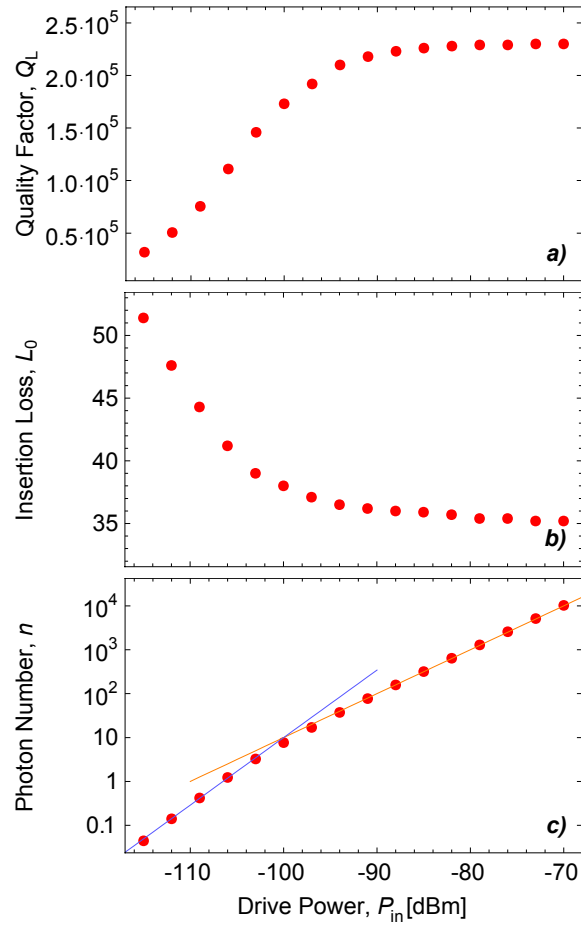


Figure 2.16: (a) Dependence of Q_L on the drive power P_{in} at the resonator input port for resonator K. (b) Dependence of L_0 on the drive power. (c) Average photon number n in dependence on the drive power in a logarithmic scale.

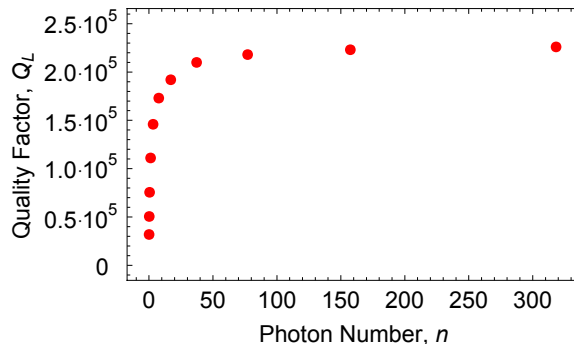


Figure 2.17: Quality factor Q_L of resonator K in dependence on the average photon number n inside the cavity.

as

$$\begin{aligned}
 n &= \frac{P_{\text{loss}} Q_{\text{int}}}{\hbar \omega^2} \\
 &\approx \frac{P_{\text{in}} Q_L}{\hbar \omega^2}.
 \end{aligned} \tag{2.58}$$

Figure 2.16c depicts n in dependence on the drive power P_{in} at the resonator input for device K (see Tab. 2.2). The logarithmic average photon number scales linearly with the logarithmic drive power in two regimes with different slopes. The logarithmic photon number first increases linearly from -115 dBm to approximately -100 dBm. It further increases linearly but less strongly from -100 dBm on. The internal Q can be obtained from the measured Q_L and L_0 using Eqs. (2.39) and (2.42) and P_{out} is given by P_{in} and L_0 . The photon number n calculated by using Q_{int} instead of Q_L and $P_{\text{in}} - P_{\text{out}}$ instead of P_{in} gives only small deviations to the result shown in Fig. 2.16c. The blue and orange lines in Fig. 2.16c,

$$n_{\text{lp}} = 2.42 \cdot 10^{16} (P_{\text{in}}[\text{mW}])^{3/2} \tag{2.59}$$

$$n_{\text{hp}} = 1.00 \cdot 10^{11} P_{\text{in}}[\text{mW}], \tag{2.60}$$

approximate the obtained photon numbers for low and high power regimes. The photon number n scales approximately with P_{in} for low powers and with $P_{\text{in}}^{3/2}$ for high powers. The internal Q thus stays constant for high powers and scales with $P_{\text{in}}^{1/2}$ for low powers, according to Eq. (2.58).

The Q dependence on P_{in} in the low power regime is consistent with the results presented in references [Martinis2005] and [O'Connell2008] where the behavior of the internal quality factor of the characterized devices is modeled by two-level fluctuators in the dielectric. Here, Q_{int} scales with the root mean square electric field component inside the resonator which is proportional to $P_{\text{in}}^{1/2}$. With increasing average photon number in the resonator, the two level fluctuators get saturated and Q_{int} no longer depends on P_{in} but stays constant.

Figure 2.17 additionally depicts the loaded Q of resonator K in dependence on the photon number n inside the transmission line cavity. The quality factor saturates at a photon number between $n = 50$ and 100.

2.6 Quantization of the LC Oscillator

In the previous sections, coplanar waveguide resonators were modeled around resonance as classical LCR oscillators. This classical treatment is especially important and useful when designing

resonator quantities like resonance frequency and input/output coupling strength and last but not least, for gaining an intuitive understanding of such devices. However, when performing quantum optics and quantum computation experiments, single photon interactions between resonator and implemented qubits naturally have to be treated fully quantum mechanically. The quantities of both sub-systems - qubit *and* cavity - have to be expressed in terms of quantum mechanical operators. For a lossless parallel LC circuit with inductance L and capacitance C , the voltage V across inductor and capacitor is given by

$$\begin{aligned} V &= \frac{Q_{\text{el}}}{C} \\ &= -L \frac{\partial I_L}{\partial t}, \end{aligned} \quad (2.61)$$

where Q_{el} is the charge stored on the capacitor and I_L is the current through the inductor. The total energy is the sum of the magnetic and electric contributions and is given by

$$\begin{aligned} E &= \frac{1}{2} L I_L^2 + \frac{1}{2} C V^2 \\ &= \frac{\Phi^2}{2L} + \frac{Q_{\text{el}}^2}{2C}, \end{aligned} \quad (2.62)$$

where $\Phi = L I_L$ is the magnetic flux stored in the inductor. The Hamiltonian is then derived as

$$\hat{H} = \frac{\hat{\Phi}^2}{2L} + \frac{\hat{Q}_{\text{el}}^2}{2C}, \quad (2.63)$$

when replacing the classical variables Φ and Q_{el} by the flux and charge operators $\hat{\Phi}$ and \hat{Q}_{el} . Considering Eqs. (2.61) and (2.63) gives

$$\begin{aligned} \frac{\partial \hat{H}}{\partial \hat{\Phi}} &= \frac{1}{L} \hat{\Phi} \\ &= \dot{\hat{Q}}_{\text{el}}, \end{aligned} \quad (2.64)$$

$$\begin{aligned} \frac{\partial \hat{H}}{\partial \hat{Q}_{\text{el}}} &= \frac{1}{C} \hat{Q}_{\text{el}} \\ &= -\dot{\hat{\Phi}}, \end{aligned} \quad (2.65)$$

showing that $\hat{\Phi}$ and \hat{Q}_{el} can be identified as the generalized canonical position and momentum variables of the system which fulfill the commutator relation

$$[\hat{\Phi}, \hat{Q}_{\text{el}}] = i\hbar \quad (2.66)$$

and which can be expressed as

$$\hat{\Phi} = -i\hbar \frac{\partial}{\partial \hat{Q}_{\text{el}}}, \quad (2.67)$$

$$\hat{Q}_{\text{el}} = i\hbar \frac{\partial}{\partial \hat{\Phi}}. \quad (2.68)$$

A parallel LC oscillator and a mechanical oscillator can be equally described by the same fundamental equations. In the following, this equivalence will be used to describe flux and charge operators in terms of photon creation and annihilation operators.

The Hamiltonian for a particle with mass M and momentum P moving along the X direction in the

2 Coplanar Waveguide Resonators for Circuit QED

potential of a harmonic oscillator with resonance frequency ω_r is given by $\hat{H} = \hat{P}^2/2M + M\omega_r^2\hat{X}^2/2$. A comparison with Eq. (2.63) leads to the mapping $P \rightarrow Q_{\text{el}}$, $X \rightarrow \Phi$ and $\omega_r \rightarrow 1/\sqrt{LC}$ for the different mechanical and electrical oscillator quantities. By analogy to the mechanical oscillator the Hamiltonian of the parallel LC circuit can then be written as

$$\hat{H} = \hbar\omega_r \left(\frac{1}{2} + \hat{a}^\dagger \hat{a} \right) \quad (2.69)$$

in terms of the dimensionless photon creation and annihilation operators

$$\hat{a}^\dagger = \frac{1}{\sqrt{2\hbar\sqrt{L/C}}} \left(\sqrt{\frac{L}{C}} \hat{Q}_{\text{el}} - i\hat{\Phi} \right), \quad (2.70)$$

$$\hat{a} = \frac{1}{\sqrt{2\hbar\sqrt{L/C}}} \left(\sqrt{\frac{L}{C}} \hat{Q}_{\text{el}} + i\hat{\Phi} \right). \quad (2.71)$$

Charge and flux operators can then be rewritten as

$$\hat{\Phi} = \sqrt{\frac{2\sqrt{L/C}}{\hbar}} (\hat{a} - \hat{a}^\dagger), \quad (2.72)$$

$$\hat{Q}_{\text{el}} = \sqrt{\frac{\hbar}{2\sqrt{L/C}}} (\hat{a} + \hat{a}^\dagger). \quad (2.73)$$

Finally, using Eq. (2.61), the voltage operator

$$\hat{V} = \sqrt{\frac{\hbar\omega_r}{2C}} (\hat{a} + \hat{a}^\dagger) \quad (2.74)$$

can be defined. The operator \hat{V} describes a quantum voltage which is generated by the photons inside the cavity.

Usually, quantum mechanical properties cannot be observed in macroscopic electronic circuits. One of the reasons for this is the dissipation of energy due to resistive circuit elements. In order to operate an electronic circuit quantum coherent, it has to be made out of superconducting materials and operated at temperatures below T_c . Circuit QED systems therefore use superconducting cavities and superconducting qubits as discussed in the next chapter.

3 Josephson Junction Devices

Within the last decades, a number of macroscopic quantum devices based on Josephson junctions such as quantum limited amplifiers [Manucharyan2007, Castellanos2008], detectors and magnetometers [Clarke2006] and in particular superconducting qubits [Bouchiat1998, Nakamura1999, vanderWal2000, Martinis2002] has been developed. In a classical electronic circuit, all quantities such as voltages or currents are described by classical variables. In contrast to this, quantum electronic circuits represent physical quantities by quantum mechanical operators. A macroscopic circuit behaves quantum mechanically when single particles act collectively and this way form a macroscopic quantum state. In superconductors, such a macroscopic state is realized by the ensemble of condensed Cooper pairs. Josephson junctions make use of the quantum nature of this condensate and form the building blocks for superconducting quantum bits. Thus, they have to be well understood when designing and operating superconducting qubit devices. The fabrication aspect of Josephson junction circuits is discussed in detail in chapter 4. In this chapter, the underlying principles of Josephson junctions and DC-SQUIDS are introduced. Further, the DC-characterization of a Josephson junction device is presented and coplanar waveguide resonators whose resonance frequency is magnetic field tunable by an integrated DC-SQUID will be treated. The chapter will close with the introduction of the Cooper pair box and the transmon qubit.

3.1 Macroscopic Quantum Model and Josephson Junctions

The fundamental equation with which the behavior of individual particles can be described quantum mechanically is the Schrödinger equation

$$i\hbar \frac{\partial \psi}{\partial t} = \hat{H}\psi, \quad (3.1)$$

where \hbar is the Planck constant divided by 2π , \hat{H} is the Hamilton operator and ψ the wavefunction of the system. Macroscopic systems usually do not behave quantum mechanically since macroscopic quantities like current or voltage sum over a distribution of many different microscopic states whereby the quantum character of individual particles is averaged out. In case of a superconductor however, all particles are described by the same wavefunction and quantum mechanical properties can be observed also on a macroscopic scale.

In superconducting systems, the ensemble of all particles is described by the wave function $\psi(\mathbf{r}, t)$ which depends on the place \mathbf{r} and the time t . The Schrödinger equation (3.1) is solved by

$$\psi(\mathbf{r}, t) = \psi_0(\mathbf{r}, t)e^{i\theta(\mathbf{r}, t)}, \quad (3.2)$$

and the equation of motion for the *macroscopic phase* of the wave function writes as

$$\hbar \frac{\partial}{\partial t} \theta(\mathbf{r}, t) = -E_0, \quad (3.3)$$

where ψ_0 was assumed to be time independent and E_0 is the eigenenergy of the system. In case of fermions, for example electrons in a normal conducting metal, all particles have different energies due to the Pauli exclusion principle. According to Eq. (3.3), also the time evolution of the phase differs from particle to particle in this case and on average the macroscopic phase vanishes. Thus, macroscopic quantum effects are not observed. In superconductors however, electrons condensate to Cooper pairs which are described by Bose-Einstein statistics. All particles have the same energy in the ground state and thus, according to Eq. (3.3), all phases evolve identically in time. In this *phase locked state*, the ensemble of all Cooper pairs is described as *superfluid* by the single wave function

$$\psi(\mathbf{r}, t) = \sqrt{n_s(\mathbf{r}, t)}e^{i\theta(\mathbf{r}, t)}, \quad (3.4)$$

where $n_s(\mathbf{r}, t)$ denotes the local Cooper pair density. A superconducting metal can thus be described by the macroscopic quantum variable $\theta(\mathbf{r}, t)$ and the local charge carrier density $\rho_s(\mathbf{r}, t) = q_s n_s(\mathbf{r}, t)$, where $q_s = 2e$ is the charge of a single Cooper pair.

In the picture of a superfluid of Cooper pairs, a *macroscopic quantum current density* $\mathbf{J}_s(\mathbf{r}, t)$ in an electromagnetic field can be defined as

$$\mathbf{J}_s(\mathbf{r}, t) = q_s \Re \left\{ \psi^* \left(\frac{\hbar}{im_s} \nabla - \frac{q_s}{m_s} \mathbf{A} \right) \psi \right\}, \quad (3.5)$$

where m_s is the Cooper pair mass and \mathbf{A} is the vector potential of the magnetic field. Using Eq. (3.2), one finally arrives in

$$\mathbf{J}_s(\mathbf{r}, t) = q_s n_s(\mathbf{r}, t) \left\{ \frac{\hbar}{m_s} \nabla \theta(\mathbf{r}, t) - \frac{q_s}{m_s} \mathbf{A}(\mathbf{r}, t) \right\}. \quad (3.6)$$

On a macroscopic scale, the collective quantized behavior manifests itself by the dependence of current and voltage on the macroscopic phase $\theta(\mathbf{r}, t)$ which leads to coherent macroscopic

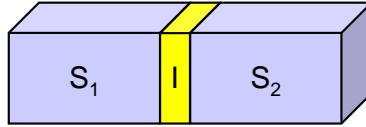


Figure 3.1: Geometry of a Josephson junction which consists of two superconducting electrodes (S₁ and S₂) interrupted by a thin insulating barrier (I).

effects such as flux quantization [London1950, Deaver1961, Doll1961] and the Josephson effect [Josephson1962, Anderson1963].

In its simplest form, a *Josephson tunnel junction* consists of two superconducting electrodes (S₁, S₂) connected via a thin insulating layer (I) as depicted in Fig. 3.1. If the barrier is thin enough, the macroscopic wave functions of both electrodes overlap and form a weakly coupled system. Cooper pairs can tunnel coherently from one side to the other forming a superconducting tunnel current. *Brian Josephson* was the first who presented a theory in 1962 [Josephson1962] describing a superconductor-insulator-superconductor tunnel junction. The first Josephson equation or *current phase relation* [Josephson1962]

$$I_s(t) = I_c \sin \phi(t), \quad (3.7)$$

describes the supercurrent $I_s(t)$ flowing through a Josephson junction. Here I_c is the *critical current*, which is the maximum current that can be carried by the junction as supercurrent. Further, ϕ is the gauge invariant phase difference

$$\phi(\mathbf{r}, t) = \theta_2(\mathbf{r}, t) - \theta_1(\mathbf{r}, t) - \frac{2\pi}{\Phi_0} \int_1^2 dl \mathbf{A}(\mathbf{r}, t), \quad (3.8)$$

which is in general space dependent, where $\theta_1(\mathbf{r}, t)$ and $\theta_2(\mathbf{r}, t)$ are the macroscopic phases in the superconducting electrodes 1 and 2. The vector potential $\mathbf{A}(\mathbf{r}, t)$ accounts for external magnetic fields and has to be integrated from one junction electrode to the other in the direction of the current flow. The *Ambegaokar-Baratoff relation* [Ambegaokar1963]

$$I_c = \frac{\pi \Delta(T)}{2eR_n} \tanh \left(\frac{\Delta(T)}{2k_B T} \right), \quad (3.9)$$

relates the critical current to the temperature dependent BCS energy gap between ground and excited state $\Delta(T)$ and the tunnel resistance in the non superconducting state R_n . Equation (3.9) gives an approximate result for the critical current I_c . The second Josephson equation or *voltage phase relation* gives an expression for the voltage across a Josephson junction and writes [Josephson1962]

$$V(t) = \frac{\Phi_0}{2\pi} \frac{d\phi}{dt}, \quad (3.10)$$

where $\Phi_0 = h/2e$ is the magnetic flux quantum. The first Josephson effect, described by Eq. (3.7) states that the current through a Josephson junction varies sinusoidally with the macroscopic phase difference θ . The second Josephson effect, described by Eq. (3.10), says that a voltage V drops across the junction if the phase difference $\phi(t)$ changes in time. Combining Eqs. (3.7) and (3.10) it follows

$$I_s(t) = I_c \sin \left(\frac{2\pi}{\Phi_0} V \cdot t + \phi_0 \right), \quad (3.11)$$

where the supercurrent oscillates with period $\Phi_0/2\pi$ and frequency V/Φ_0 .

A Josephson junction is characterized in terms of energy by the *Josephson energy* $E_J = \int dt VI_s$ and the *charging energy* $E_C = C_J V^2/2$, where C_J is the junction capacitance. The Josephson energy can be understood as the kinetic energy of the tunneling Cooper pairs, the charging energy can be seen as the potential energy capacitively stored in the junction. Using the first and second Josephson equations, E_J and E_C can be expressed as

$$\begin{aligned} E_J &= \frac{\Phi_0 I_c}{2\pi} (1 - \cos \phi) \\ &= E_{J0} (1 - \cos \phi), \end{aligned} \quad (3.12)$$

$$\begin{aligned} E_C &= \frac{(2e)^2}{2C} N^2 \\ &= E_{C0} N^2. \end{aligned} \quad (3.13)$$

Here $E_{J0} = \Phi_0 I_c / 2\pi$ and $E_{C0} = (2e)^2 / 2C$ holds and N denotes the number of excess Cooper pairs on the Junction electrodes each carrying a charge of $2e$. The inductance of a Josephson junction can be derived when taking the time derivative of Eq. (3.7) and when using Eq. (3.10), leading to

$$\frac{dI_s}{dt} = I_c \frac{2\pi}{\Phi_0} V(t) \cos \phi. \quad (3.14)$$

The non linear *Josephson inductance* can then be defined as

$$\begin{aligned} L_J &= \frac{\Phi_0}{2\pi I_c} \frac{1}{\cos \phi} \\ &= L_c \frac{1}{\cos \phi}, \end{aligned} \quad (3.15)$$

where Eq. (3.7) has been used. Here, $L_{J0} = (\Phi_0 / 2\pi I_{J0})$ is the specific Josephson inductance. When applying the current $I < I_c$ to the Josephson junction, $\cos \phi = \sqrt{1 - I/I_c}$ holds according to Eq. (3.7). Equation (3.15) can thus be rewritten as

$$L_J = \frac{L_c}{\sqrt{1 - (I/I_c)^2}}. \quad (3.16)$$

Until now, the magnitude of the maximum Josephson current I_c was not discussed. This will be done in the following by deriving an expression for the maximum Josephson current density \mathbf{J}_c of a superconductor-insulator-superconductor Josephson tunnel junction with a tunnel barrier of thickness d , compare reference [Gross2003]. Using the *wave matching method*, the Schrödinger equation is solved in three different regions, the two superconducting electrodes and the insulating barrier. Using Eqs. (3.3) and (3.2), the time dependent macroscopic wave function inside the two superconducting electrodes can be written as

$$\psi(\mathbf{r}, t) = \psi_0(\mathbf{r}) e^{-i(E_0/\hbar)t}, \quad (3.17)$$

where ψ_0 is assumed to be time independent. The tunnel barrier is modeled by a potential which has the constant value U_0 inside the barrier, which is zero outside the barrier and for which $U_0 > E_0$ holds. The potential does not change in time, thus the time independent Schrödinger equation

$$-\frac{\hbar^2}{2m_s} \nabla^2 \psi_0(\mathbf{r}) = (E_0 - U_0) \psi_0(\mathbf{r}) \quad (3.18)$$

is considered for the region inside the junction barrier. In case of a homogeneous barrier and homogeneous supercurrent flow along the x -direction, Eq. (3.18) can be solved in one dimension with the function

$$\psi(x) = A \cosh(\kappa_s x) + B \sinh(\kappa_s x), \quad (3.19)$$

where the characteristic decay constant κ_s is given by

$$\kappa_s = \sqrt{\frac{2m_s(U_0 - E_0)}{\hbar^2}}. \quad (3.20)$$

The wave function inside the superconducting electrodes and in particular at $x = \pm d/2$ of the insulating layer is given by Eq. (3.4). The coefficients A and B in Eq. (3.19) are determined by the boundary conditions at $x = \pm d/2$ and given as

$$\psi(-d/2) = \sqrt{n_{s1}} e^{i\theta_1}, \quad (3.21)$$

$$\psi(+d/2) = \sqrt{n_{s2}} e^{i\theta_2}. \quad (3.22)$$

Here, $\sqrt{n_{s1,2}}$ and $\theta_{1,2}$ are magnitude and the phase of the wave function at the boundaries $x = \pm d/2$. These boundary conditions together with Eq. (3.19) finally lead to

$$A = \frac{\sqrt{n_{s1}} e^{i\theta_1} + \sqrt{n_{s2}} e^{i\theta_2}}{2 \cosh\left(\frac{\kappa_s d}{2}\right)}, \quad (3.23)$$

$$B = \frac{\sqrt{n_{s1}} e^{i\theta_1} - \sqrt{n_{s2}} e^{i\theta_2}}{2 \sinh\left(\frac{\kappa_s d}{2}\right)}. \quad (3.24)$$

Using the definition for the quantum current density given in Eq. (3.5), as well as Eq. (3.19), the current density of the Josephson junction

$$\mathbf{J}_s = \frac{q_s}{m_s} \hbar \kappa_s \Im \{A^* B\} \quad (3.25)$$

is obtained. Substituting Eqs. (3.23) and (3.24) into Eq. (3.25) leads to the supercurrent density

$$\mathbf{J}_s = \mathbf{J}_c \sin(\theta_2 - \theta_1), \quad (3.26)$$

with the maximum Josephson current density

$$\begin{aligned} \mathbf{J}_c &= -\frac{q_s \hbar \kappa_s}{m_s} \frac{\sqrt{n_{s1} n_{s2}}}{2 \sinh\left(\frac{\kappa_s d}{2}\right) \cosh\left(\frac{\kappa_s d}{2}\right)} \\ &= -\frac{q_s \hbar \kappa_s}{2m_s} \frac{\sqrt{n_{s1} n_{s2}}}{2 \sinh(\kappa_s d)} \\ &\approx -\frac{q_s \hbar \kappa_s}{2m_s} \sqrt{n_{s1} n_{s2}} e^{-\kappa_s d}. \end{aligned} \quad (3.27)$$

The barrier height U_0 is typically in the order of a few electron volts and the decay length $1/\kappa_s$ is accordingly less than a nanometer [Gross2003]. The thickness d is usually in the order of a few nanometer that $\kappa_s \ll 1$ holds. In this case, the approximation $\sinh(\kappa_s d) \approx \exp(\kappa_s d/2)$, which was used in the last step of Eq. (3.27), is justified.

This result is particular important when fabricating aluminum/aluminum-oxide tunnel junctions, see chapter 4. Here, the oxide layer thickness is used beside the junction area to control the maximum Josephson current. Due to the exponential dependence of \mathbf{J}_c on d , for small thicknesses d already small deviations in the designed oxide layer thickness lead to large deviations in the

aimed critical current density \mathbf{J}_c .

3.2 Josephson Voltage State and RCSJ Model

A Josephson junction can adopt two fundamental states. The junction is said to be in the *zero voltage state* as long as no voltage drops across the junction. This is the case when a DC current, smaller than the critical current I_c is applied to the junction. In case the applied current exceeds I_c , the total current through the Josephson junction can no longer be carried completely as supercurrent. For temperatures above zero, a finite number of Cooper pairs thermally break up into *quasiparticles* which can carry a normal current I_n flowing through the junction. This current $I_n = V/R_J$ is a resistive current where the voltage V drops across the Josephson junction which shows a resistance R_J . The junction is said to be in the *voltage state*.

The junction resistance R_J depends on the temperature and the voltage across the junction. For $T \approx T_c$ nearly all Cooper pairs break up since its binding energy 2Δ is small compared to $k_B T$. The junction then behaves ohmic and R_J is given by the normal junction resistance R_n . In case the junction voltage is higher than the *gap voltage* $V_g = (\Delta_1(T) + \Delta_2(T))/e$, the external source provides enough energy to break up Cooper pairs and R_J is again given by the ohmic resistance R_n . Here, $\Delta_1(T)$ and $\Delta_2(T)$ are the gap energies of the two junction electrode materials. For $|V| < V_g$ and $T \ll T_c$, the energy eV of the external source is not sufficient to break up Cooper pairs and the thermal energy $k_B T$ only evokes a small amount of quasiparticles so that the normal current is very small. In this case, the junction resistance R_J is given by the *sub-gap resistance* $R_{sg}(T)$ which depends on the number of thermally excited quasiparticles. For $T \ll T_c$, one finally finds

$$R_J(V, T) = \begin{cases} R_n & \text{for } V < V_g \\ R_{sg}(T) & \text{for } V \geq V_g \end{cases}. \quad (3.28)$$

In addition to normal and supercurrent, also a displacement current $I_d = C_J(dV/dt)$ can flow through the junction in presence of a time varying voltage. Here, C_J is the intrinsic capacitance of the Josephson junction. Intrinsic current noise of the junction can further be taken into account by including an additional current source with fluctuating current I_f . Using Kirchhoff's rules, the current carried by a Josephson junction in the voltage state writes

$$\begin{aligned} I &= I_s + I_n + I_d + I_f \\ &= I_c \sin \phi + \frac{1}{R_J(V, T)} V + C_J \frac{dV}{dt} + I_f. \end{aligned} \quad (3.29)$$

Here, Eq. (3.7) was used for the supercurrent term. Using Eq. (3.10), the current through a Josephson junction is

$$I = I_c \sin \phi + \frac{1}{R_J(V, T)} \frac{\Phi_0}{2\pi} \frac{d\phi}{dt} + C_J \frac{\phi_0}{2\pi} \frac{d^2\phi}{dt^2} + I_f. \quad (3.30)$$

The capacitance of an ideal Josephson junction can be approximated by

$$C_J = \frac{\epsilon_r \epsilon_0 A}{d}, \quad (3.31)$$

where ϵ_r is the relative dielectric constant of the tunnel barrier of thickness d and area A . According to Eq. (3.29), a Josephson junction can be effectively modeled as the parallel circuit shown in Fig. 3.2. This description is known as the *resistively and capacitively shunted junction*

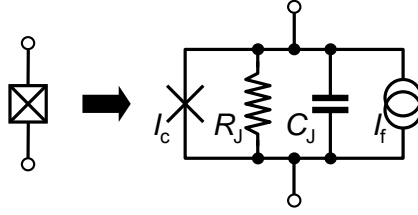


Figure 3.2: RCSJ model of a Josephson junction. The symbol on the left hand side represents a Josephson junction which is characterized by its critical current I_c , its intrinsic resistance R_J and its capacitance C_J (see right hand side). The fluctuating current I_f accounts for intrinsic current noise.

(RCSJ) model. Neglecting the noise current I_f and using Eqs. (3.12) and (3.30), one finds the differential equation

$$C_J \frac{\Phi_0}{2\pi} \frac{d^2\phi}{dt^2} + \frac{1}{R_n} \frac{\Phi_0}{2\pi} \frac{d\phi}{dt} + \frac{d}{d\phi} [E_{J0}(1 - \cos\phi - i\phi)] = 0, \quad (3.32)$$

governing the dynamics of a Josephson junction, where the normalized current $i = I/I_c$ has been introduced. Equation (3.32) can be compared to the equation of motion

$$M \frac{d^2X}{dt^2} + \eta \frac{dX}{dt} + \nabla U = 0. \quad (3.33)$$

of a particle of mass M moving along the coordinate X in a potential U with damping η . Comparing the two Eqs. (3.32) and (3.33), one finds for the potential U which describes the dynamics of the macroscopic phase difference of a Josephson junction

$$U(\phi) = E_{J0}(1 - \cos\phi - i\phi). \quad (3.34)$$

This potential is known as the *tilted washboard* or *Josephson potential*. The mass M of a *phase particle* moving in the Josephson potential, its damping η and the quality factor Q_J of the junction are further defined as

$$M = C_J \frac{\Phi_0}{2\pi}, \quad (3.35)$$

$$\eta = \frac{1}{R_n} \frac{\Phi_0}{2\pi}, \quad (3.36)$$

$$\begin{aligned} Q_J &= \sqrt{\frac{2\pi}{\Phi_0} I_c R_J^2(V, T) C_J} \\ &= \sqrt{\beta_C}, \end{aligned} \quad (3.37)$$

where the *Stewart McCumber parameter* $\beta_C = (2\pi/\Phi_0) I_c R_J^2(V, T) C_J$ was introduced. The parameter β_C describes the damping of a Josephson junction. A highly damped junction has a small Stewart McCumber parameter and accordingly a small Q_J since dissipation is high. A weakly damped junction has a high Stewart McCumber parameter and also a high Q_J since dissipation is low. The dynamics of the phase difference ϕ across a Josephson junction respectively the dynamics of a particle with mass M is illustrated in Fig. 3.3. For $I < I_c$, the phase potential is given by $U(\phi) \approx E_{J0}(1 - \cos\phi)$. The tilt of the potential increases with increasing bias current. For $i \approx 0$

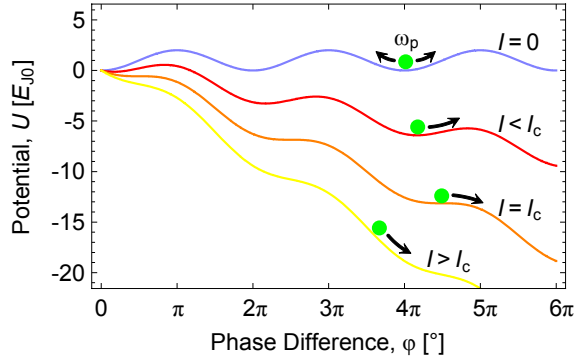


Figure 3.3: Josephson or tilted washboard potential. The potential gets tilted more with larger bias current I , applied to the junction. As far as I reaches the critical current I_c , the local extrema vanish in the potential. When increasing the current from $I < I_c$ to $I > I_c$, the phase particle can no longer be trapped in a potential minimum and starts to escape. This *running state* represents the voltage state of the junction. When decreasing the applied current from $I > I_c$ to $I < I_c$, the phase particle is, in case of strong damping, immediately trapped in a local minimum when the potential minima start to arise. In case of weak damping however, the particle is only trapped for a current I smaller I_c where the arising potential barrier is high enough to compensate the kinetic energy of the running particle.

the height of the local potential barrier is $U_0 \approx E_{J0}$ and the oscillation frequency is

$$\omega_0 = \sqrt{\frac{2\pi I_c}{\Phi_0 C_J}}, \quad (3.38)$$

which is known as the *Josephson plasma frequency*. The nonlinearity of the potential $U(\phi)$ is essential for performing quantum information processing with *superconducting phase qubits*.

The RCSJ model explains the dynamics of a Josephson junction in a simple and demonstrative manner. The above considerations on current biased junctions are especially important for understanding the current voltage characteristic of a Josephson junction what will be treated in the next section. From the measured current voltage characteristic of a fabricated junction, fundamental parameters like the energy gap Δ of the electrode material, the critical current I_c and the normal state resistance R_n of the junction can be extracted and analyzed. This way, properties of fabricated junctions can be monitored in order to guaranty a stable process quality.

3.3 Current Voltage Characteristic of a Josephson Junction

The behavior of a lumped element Josephson junction is described in the RCSJ model by Eq. (3.32). According to Eq. (3.10), the time averaged voltage V_{avg} across a Josephson junction can be written

as

$$\begin{aligned}
 V_{\text{avg}}(t) &= \frac{1}{T} \int_0^T dt V(t) \\
 &= \frac{1}{T} \int_0^T dt \frac{\Phi_0}{2\pi} \frac{d\phi}{dt} \\
 &= \frac{1}{T} \frac{\Phi_0}{2\pi} \int_{\phi(0)}^{\phi(T)} d\phi \\
 &= \frac{1}{T} \frac{\Phi_0}{2\pi} [\phi(T) - \phi(0)] \\
 &= \frac{\Phi_0}{T},
 \end{aligned} \tag{3.39}$$

compare reference [Gross2003]. In the voltage state, $V(t)$ changes in time and according to Eq. (3.10), the Josephson phase ϕ oscillates with time. Therefore, also the Josephson current I_s oscillates with time, see Eq. (3.7). Here, T is the oscillation period of the supercurrent. The last step in Eq. (3.39) follows from the fact that the $\sin \phi$ dependence of the Josephson current has a 2π -periodicity. The oscillation period is then given by Eq. (3.32).

In case of an *underdamped* Josephson junction ($\beta_C \ll 1$) and large bias currents $i = I/I_c \gg 1$, Eq. (3.32) can be solved in order to find the time dependent phase difference as [Clarke2006]

$$\phi(t) = 2 \arctan \left[\sqrt{1 - \frac{1}{i^2}} \tan \left(\frac{t\sqrt{i^2 - 1}}{2\tau_c} \right) + \frac{1}{i} \right], \tag{3.40}$$

with period

$$T = \frac{2\pi\tau_c}{\sqrt{i^2 - 1}}, \tag{3.41}$$

where $\tau_c = 2eI_c R_J(V, T)/\hbar$. The current voltage characteristic for an overdamped Josephson junction in the voltage state is then found with Eq. (3.39) as

$$V_{\text{avg}}(t) = I_c R_J(V, T) \sqrt{\left(\frac{I}{I_c}\right)^2 - 1}, \tag{3.42}$$

see Fig. 3.4a. For a bias current I below the critical current I_c , the current through the junction is completely carried as supercurrent. The washboard potential depicted in Fig. 3.3 is untilted in this case and the phase particle stays in one of the potential minima. According to Eq. (3.10), no voltage drops across the junction for $I < I_c$ since the phase difference ϕ is time independent. The junction is in the zero voltage state. For bias currents I above the critical current I_c , the washboard potential is tilted and the phase particle can leave its potential minimum resulting in a continuously increasing ϕ with time. According to Eq. (3.10), voltage drops across the junction. The Josephson junction is in the voltage state.

The switching from voltage to zero voltage state depends on the damping of the Josephson junction. For overdamped Josephson junctions ($\beta_C \ll 1$), the particle is immediately trapped back in a potential minimum as soon as $I = I_c$ is reached and cannot leave the potential again. For underdamped junctions ($\beta_C \gg 1$) however, the phase particle can escape from a local minimum also for $I < I_c$ due to its kinetic energy. Here, the time evolution of ϕ does not stop immediately at $I = I_c$ and retrapping of the phase particle occurs only for a further lowered current I , the so called *retrapping current* I_r .

For an *underdamped* Josephson junction ($\beta_C \gg 1$), one has to solve Eq. (3.32) numerically. Figure 3.4b shows the current voltage characteristic of an underdamped Josephson junction which is

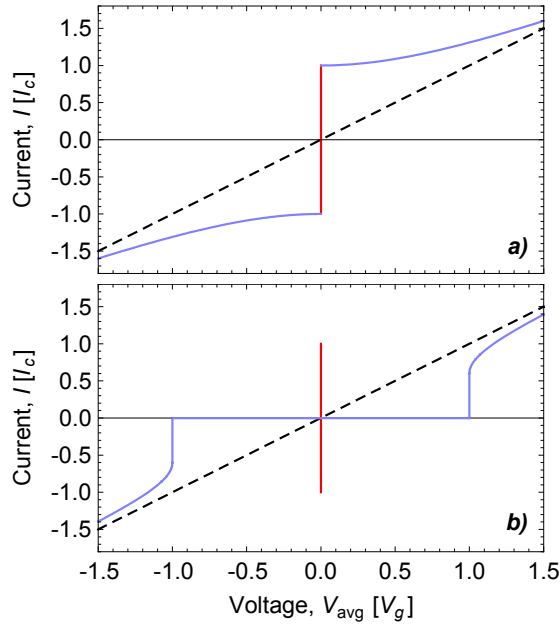


Figure 3.4: a) Current voltage characteristic of an overdamped Josephson junction. The red solid line indicates the current carried by the junction totally as supercurrent, whereas the blue solid line shows the current flowing through the junction, partially as supercurrent and partially as normal current. The black dashed line depicts the ohmic behavior of the normal resistance. b) Current voltage characteristic of an underdamped Josephson junction. Here, the red solid line indicates the supercurrent and the blue solid line shows the quasiparticle current.

relevant for all junctions fabricated within the scope of this thesis.

3.4 Measurement of the Current Voltage characteristic of a Josephson junction

Within the work presented in this thesis, the current voltage characteristic of a fabricated Josephson junction is measured with the setup shown in Fig. 3.5. A Josephson junction or a DC-SQUID is installed inside a dilution refrigerator. In order to perform a four-point measurement, separate cables for current bias and voltage measurement are fed from a *RC-filtered break out box* outside the refrigerator via twisted pairs to the sample. The home-made *bias box*, depicted in Fig. 3.6a, b, applies a DC current through the sample, and measures the voltage across it. In order to control the bias current, a voltage signal is applied to the bias box via the digital to analog and analog to digital converter (DAC/ADC) card *National Instruments BNC-2110*, see Fig. 3.7, which is connected to a personal computer (PC) and controlled by a *LabView* program. The voltage signal applied to the bias box is divided by the resistors R_1 and R_2 and converted to a current with an operational amplifier (OpAmp) inside the box. A bias resistor R_{BS} can be used to control step-wise the coarse range of the applied current which is applied with the break out box to the sample. The voltage across the bias resistor is measured with an operational amplifier and the RC-filtered output signal, which is proportional to the applied current, is determined with the converter card by the computer. The voltage signal across the junction is measured via the break out box, amplified by another operational amplifier in the bias box and RC-filtered. The output signal is digitized in the computer using an analog to digital converter card. Instead of using the converter card and a personal computer for applying signals to the bias box,

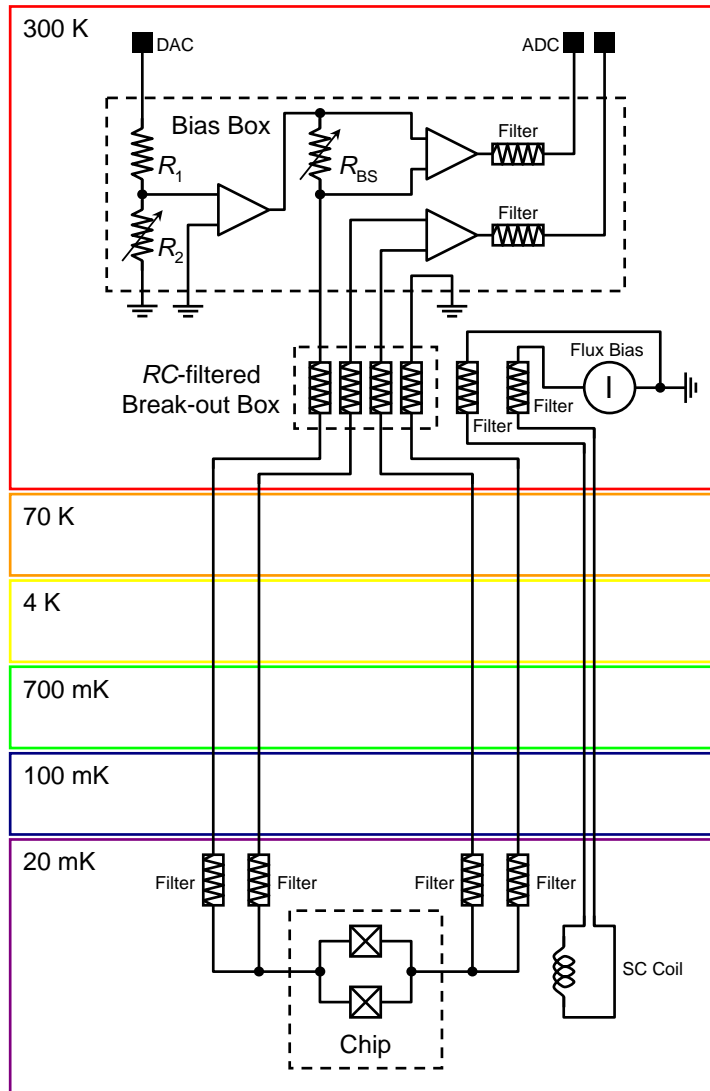


Figure 3.5: Setup for the measurement of the current voltage characteristic of a Josephson junction. The sample is installed at the 20 mK stage of a dilution refrigerator. A four-point resistance measurement is realized with separate feed lines for current bias and voltage determination. See main text for detailed explanation.

3.4 Measurement of the Current Voltage characteristic of a Josephson junction

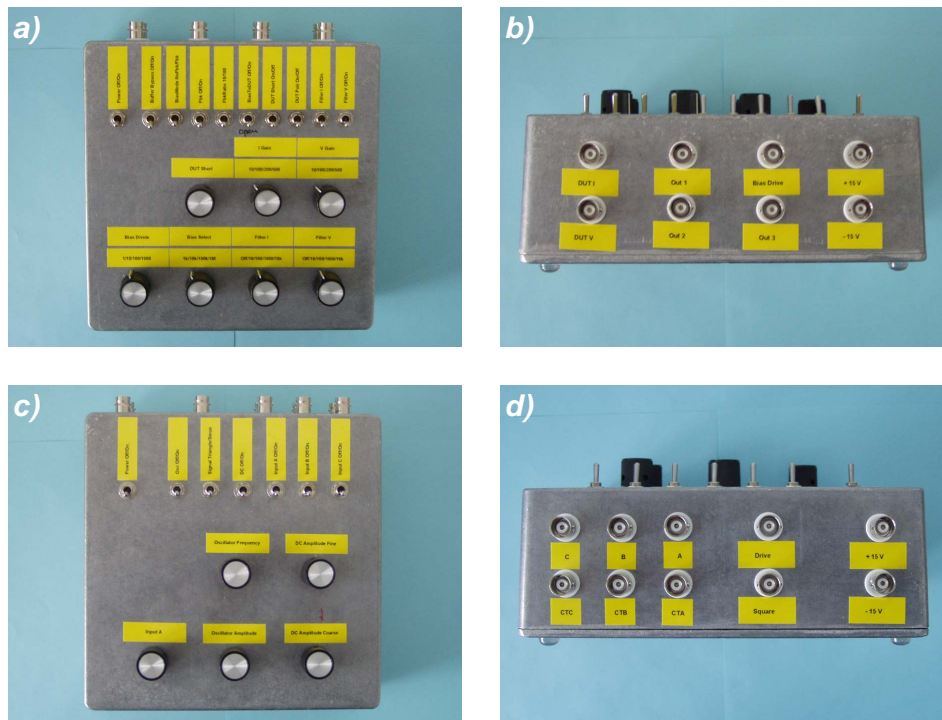


Figure 3.6: Self-made electronic for performing four-point measurements on Josephson junction devices. Top view on bias box (a), view on connectors of bias box (b), top view on adder box (c) and view on connectors of adder box (d).



Figure 3.7: Converter card *National Instruments* BNC-2110, used for applying a bias voltage to the bias box and for reading and digitizing the current and voltage signals from the bias box.

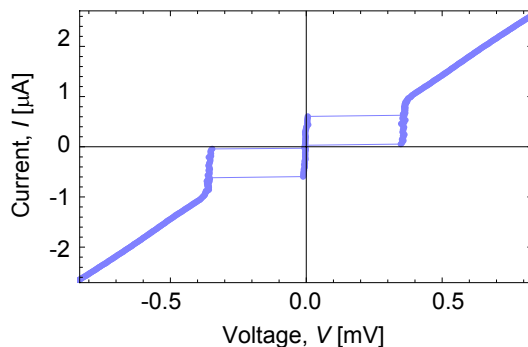


Figure 3.8: Measured current voltage characteristic of a fabricated Josephson junction. The blue solid lines show the switching from the zero voltage state to the voltage state and vice versa.

Critical Current	I_c	6.0×10^{-7} A
Gap voltage	$2\Delta/e$	3.6×10^{-4} V
Normal resistance	R_n	2.8×10^2 Ω

Table 3.1: Josephson junction parameters extracted from the measurement shown in Fig. 3.8.

the home-made *adder box* depicted in Fig. 3.6c, d, can be used for signal generation. The adder box generates sine, triangle and rectangle shaped voltage signals of variable frequency and amplitude which can be applied to the bias box. In addition, arbitrary external generated signals can be applied to the box and are added to the output. Furthermore, a DC-voltage of variable amplitude can be added to the output. The response signals of the bias box can then be displayed on a two-channel oscilloscope.

An additional current source applies a DC-current through a coil underneath the sample to generate a magnetic flux which can be used to reduce the maximum critical current of a DC-SQUID, see next section. A detailed description of the bias box can be found in appendix J.

Figure 3.8 shows the measured current voltage characteristic of a fabricated Josephson junction and Tab. 3.1 lists the parameters, extracted from the measurement. The measured data presented in Fig. 3.8 is corrected for offset voltages. The Josephson junction is measured at a temperature of about 20 mK and has an underdamped current voltage characteristic. The measured gap voltage $V_g = 2\Delta/e$ is close to the value 0.35 mV for aluminum, given in reference [Poole1995]. The extracted $I_c R_n$ product has a value of 1.7×10^{-4} V and is about 38 % smaller than the $I_c R_n$ value estimated from the Ambegaokar-Baratoff relation (3.9). The measured Josephson junction has a size of about $A = 2 \times 0.5 \mu\text{m}^2$ which is the typical size of a SQUID junction used for fabricating frequency tunable SQUID resonators, see later section. The resistance area product of the measured Josephson junction is $\Pi_{RA} = R_n \cdot A = 2.8 \times 10^{-10} \Omega\text{m}^2$ and the critical Josephson current density is $j_c = I_c/A = 60 \text{ A/cm}^2$. The values for Π_{RA} and j_c are typical both for SQUID junctions used for magnetic field tunable resonators and for qubit junctions. Josephson junctions used for qubits have smaller sizes which are typical in the order of $A = 270 \times 200 \text{ nm}^2$, see later sections.

3.5 Superconducting Quantum Interference Devices

A *superconducting quantum interference device* (SQUID) consists of a superconducting loop interrupted by one or more Josephson junctions and converts a magnetic flux into an output voltage. Today, SQUIDs are the most sensitive detectors for magnetic flux available. In the context of the

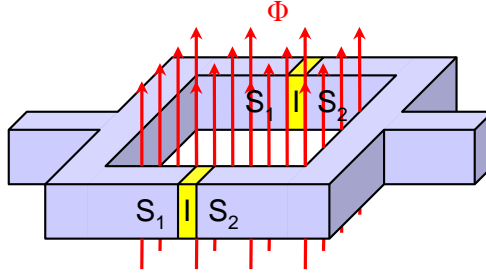


Figure 3.9: Geometry of a direct current superconducting quantum interference device (DC-SQUID) which consists of a superconducting loop, interrupted by two Josephson junctions.

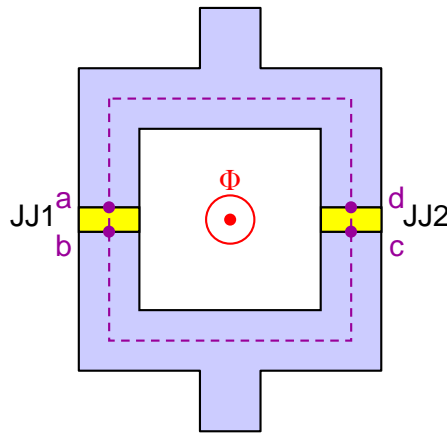


Figure 3.10: Top view of a DC-SQUID consisting of a superconducting loop (blue), interrupted by two Josephson junctions (yellow) (JJ1 and JJ2). The dashed purple line indicates the path for integrating the macroscopic phase gradient.

work presented in this thesis, SQUIDs are important with view to the *split Cooper pair box* as well as the *transmon* qubit, which both incorporate a SQUID type structure in order to magnetically tune the qubit's maximum Josephson energy and which will be considered in a later section.

SQUIDs are based on two quantum mechanical effects, flux quantization [London1950, Deaver1961, Doll1961] and the Josephson effect [Josephson1962, Anderson1963]. Combining two superconducting Josephson junctions in parallel, as shown in Fig. 3.9, forms a SQUID known as the *direct current superconducting quantum interference device* (DC-SQUID). It is named DC-SQUID since it usually operates with a steady bias current. The total current threading the two Josephson junctions of the SQUID is found to be

$$\begin{aligned} I_s &= I_{s1} + I_{s2} \\ &= I_{c1} \sin \phi_1 + I_{c2} \sin \phi_2, \end{aligned} \quad (3.43)$$

when applying Kirchoff's law. In order to derive the maximum critical current of the SQUID in dependence on applied magnetic flux, the gradient of the macroscopic phase is integrated along the path indicated by the purple dashed line shown in Fig. 3.10, compare reference [Gross2003]. The total phase change along the closed contour depicted in Fig. 3.10 is an integer number of 2π .

3 Josephson Junction Devices

Thus, one obtains

$$\begin{aligned}\oint_C dl \nabla \theta &= (\theta_b - \theta_a) + (\theta_c - \theta_b) + (\theta_d - \theta_c) + (\theta_a - \theta_d) \\ &= 2\pi n.\end{aligned}\quad (3.44)$$

Using Eqs. (3.6) and (3.8), one finds for the single phase differences

$$\theta_b - \theta_a = \frac{2\pi}{\Phi_0} \int_a^b dl \mathbf{A} + \phi_1, \quad (3.45)$$

$$\theta_d - \theta_c = \frac{2\pi}{\Phi_0} \int_c^d dl \mathbf{A} - \phi_2, \quad (3.46)$$

$$\begin{aligned}\theta_c - \theta_b &= \int_b^c dl \nabla \theta \\ &= \frac{2\pi}{\Phi_0} \int_b^c dl \Lambda \mathbf{J}_s + \frac{2\pi}{\Phi_0} \int_b^c dl \mathbf{A},\end{aligned}\quad (3.47)$$

$$\begin{aligned}\theta_a - \theta_d &= \int_d^a dl \nabla \theta \\ &= \frac{2\pi}{\Phi_0} \int_a^d dl \Lambda \mathbf{J}_s + \frac{2\pi}{\Phi_0} \int_a^d dl \mathbf{A},\end{aligned}\quad (3.48)$$

where $\Lambda = m_s/(n_s q_s^2)$ is the *London coefficient*. Substituting Eqs. (3.45, 3.46, 3.47, 3.48) into Eq. (3.44) yields

$$\phi_2 - \phi_1 = 2\pi n + \frac{2\pi}{\Phi_0} \oint_C dl \mathbf{A} + \frac{2\pi}{\Phi_0} \int_b^c dl \Lambda \mathbf{J}_s + \frac{2\pi}{\Phi_0} \int_d^a dl \Lambda \mathbf{J}_s. \quad (3.49)$$

According to Stoke's theorem, the integral of \mathbf{A} along the closed contour is equal to the total flux Φ enclosed by it. If the superconducting loop has a thickness that is large compared to the London penetration depth, the integration path can be chosen deep inside the superconducting material. Here, the current density is negligible and the two integrals in Eq. (3.49) involving the current density can be neglected and one finally finds

$$\phi_2 - \phi_1 = 2\pi \left(n + \frac{\Phi}{\Phi_0} \right). \quad (3.50)$$

Using Eq. (3.50), Eq. (3.43) can be rewritten as

$$I_s = I_{c1} \sin \phi_1 + I_{c2} \sin \left(\phi_1 + 2\pi \frac{\Phi}{\Phi_0} \right). \quad (3.51)$$

The maximum supercurrent of the parallel combination of two Josephson junctions which depends on the applied magnetic flux Φ is found by maximizing Eq. (3.51) with respect to ϕ_1 and is given by

$$I_s^{\max} = \sqrt{(I_{c1} - I_{c2})^2 + 4I_{c1}I_{c2} \cos^2 \left(\pi \frac{\Phi}{\Phi_0} \right)}. \quad (3.52)$$

In case of symmetric junctions, where $I_c = I_{c1} = I_{c2}$ holds, Eq. (3.52) simplifies to

$$I_c^{\max} = 2I_c \left| \cos \left(\pi \frac{\Phi}{\Phi_0} \right) \right|. \quad (3.53)$$

The flux dependence of the maximum SQUID supercurrent is depicted in Fig. 3.11 for different

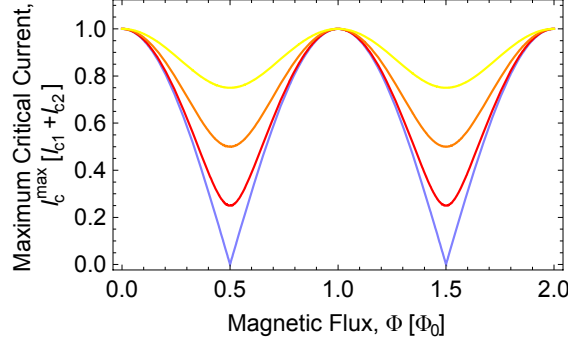


Figure 3.11: Dependence of the maximum critical current I_c^{\max} of a DC-SQUID on the magnetic flux Φ threading the SQUID loop for different junction asymmetries $\zeta = 0$ (blue line), 0.25 (red line), 0.5 (orange line) and 0.75 (yellow line).

relative critical current asymmetries of the individual junctions

$$\zeta = \frac{I_{c1} - I_{c2}}{I_{c1} + I_{c2}}, \quad (3.54)$$

but a constant total critical current $I_{c1} + I_{c2}$. Figure 3.11 shows a decreasing range of current modulation with flux for increasing ζ . A smaller modulation leads to a smaller magnetic flux noise sensitivity of the SQUID. At the extrema of I_c^{\max} , the SQUID is to first order insensitive to flux noise (*sweet spots*).

The flux Φ written down in Eq. (3.11) denotes the total magnetic flux threading the SQUID loop. In general, this flux consists of an external component Φ_{ext} and the flux generated by the finite inductance L_{loop} of the SQUID loop. In the following, an expression for I_c^{\max} in dependence on Φ_{ext} will be derived, compare reference [Gross2003]. The total magnetic flux threading the SQUID loop can be written as

$$\begin{aligned} \Phi &= \Phi_{\text{ext}} + \Phi_{\text{loop}} \\ &= \Phi_{\text{ext}} + L_{\text{loop}} I_{\text{circ}}, \end{aligned} \quad (3.55)$$

where $I_{\text{circ}} = (I_{s1} - I_{s2})/2$ is the average current, circulating in the SQUID loop, compare Fig. 3.10. Thus, using Eqs. (3.7) and (3.50), the total flux Φ can be rewritten as

$$\Phi = \Phi_{\text{ext}} - \frac{L_{\text{loop}}}{2} \left[I_{c1} \sin \phi_1 - I_{c2} \sin \left(\phi_1 + 2\pi \frac{\Phi}{\Phi_0} \right) \right]. \quad (3.56)$$

The behavior of the DC-SQUID is now determined by Eqs. (3.51) and (3.56), which have to be solved self consistently. The maximum current I_c^{\max} of the SQUID has to be found by maximizing Eq. (3.51) with respect to ϕ_1 at a given Φ_{ext} while considering Eq. (3.56). The loop inductance of a typical SQUID structure of size $2 \times 2 \mu\text{m}^2$ is in the order of one pH what corresponds to a flux Φ_{loop} of approximately $10^{-6} \Phi_0$ when assuming the circulating current I_{circ} being close to the critical current $I_c = 10^{-8}$ A of a typical Josephson junction. Thus, Φ_{loop} can usually be neglected that $\Phi \approx \Phi_{\text{ext}}$ holds. Equation (3.52) can then finally be written as

$$I_c^{\max} = \sqrt{(I_{c1} - I_{c2})^2 + 4I_{c1}I_{c2} \cos^2 \left(\pi \frac{\Phi_{\text{ext}}}{\Phi_0} \right)}. \quad (3.57)$$

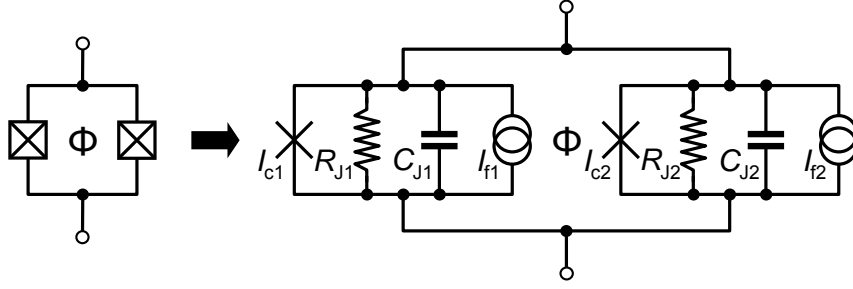


Figure 3.12: DC-SQUID which consists of a superconducting loop interrupted by two Josephson junctions (see left hand side). Lumped element RCSJ model of DC-SQUID (see right hand side).

A DC-SQUID is a device whose maximum critical current is tunable in magnetic flux. In analogy to Eq. (3.16), also the inductance of a DC-SQUID is tunable in flux and given by

$$L_S(\Phi, I) = \frac{\Phi_0}{2\pi} \left[(I_{c1} - I_{c2})^2 + 4I_{c1}I_{c2} \cos^2 \left(\pi \frac{\Phi}{\Phi_0} \right) - I^2 \right]^{-1/2}, \quad (3.58)$$

where I is the bias current, applied to the SQUID and Eq. (3.52) was used. As will be explained in the next section, this characteristic can be used to build resonant circuits, whose impedance and therefore also resonance frequency can be controlled by applying an external magnetic flux.

In terms of the RCSJ model, a DC-SQUID is represented by the lumped element circuit which is shown in Fig. 3.12. The individual Josephson junctions are defined by its critical currents I_{c1} and I_{c2} , its resistances R_{J1} and R_{J2} , as well as by its junction capacitances C_{J1} and C_{J2} . Intrinsic current noise can be taken into account by introducing an additional fluctuating current source. The total critical current of the SQUID is determined by the critical currents of the single junctions as well as by the magnetic flux threading the SQUID loop. The total capacitance of the two junctions connected in parallel is given by

$$C_S = \epsilon_0 \epsilon_r \left(\frac{A_1}{d_1} + \frac{A_2}{d_2} \right), \quad (3.59)$$

with the areas A_1 and A_2 of the single Josephson junctions and the thicknesses d_1 and d_2 denoting the two junction barriers. In the (lumped element) RCSJ model, the total impedance of the SQUID shown in Fig. 3.12 is further given by

$$Z_S(\omega, \Phi) = \frac{i\omega L_S(\Phi) R_S}{R_S + i\omega L_S(\Phi) - \omega^2 L_S(\Phi) C_S R_S}, \quad (3.60)$$

where R_S is defined by the parallel combination of the single junction resistances R_{J1} and R_{J2} by

$$\frac{1}{R_S} = \frac{1}{R_{J1}} + \frac{1}{R_{J2}}. \quad (3.61)$$

The characteristic Josephson energy E_J of a SQUID, which is tunable in flux, is found to be

$$E_J = \sqrt{(E_{J01} - E_{J02})^2 + 4E_{J01}E_{J02} \cos^2 \left(\pi \frac{\Phi}{\Phi_0} \right)}, \quad (3.62)$$

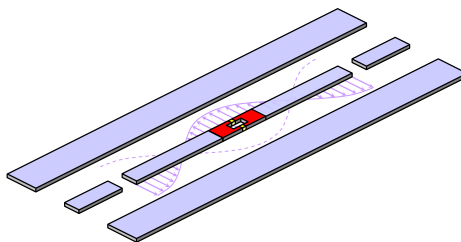


Figure 3.13: Coplanar waveguide resonator with integrated DC-SQUID structure. The purple line indicates the electric field amplitude inside the resonator.

where E_{J01} and E_{J02} are the maximum Josephson energies of the two Josephson junctions forming the SQUID. The total charging energy E_C of a SQUID is finally given by

$$E_C = \frac{(2e)^2}{2C_S} N^2, \quad (3.63)$$

where, N denotes the number of excess Cooper pairs on one electrode of the SQUID.

3.6 DC-SQUIDS and Tunable Resonators

A transmission line resonator whose resonance frequency can be tuned dynamically is realized by integrating a DC-SQUID into a coplanar waveguide resonator, see Fig. 3.13. First experiments with tunable resonator devices have recently been performed and show potential for quantum information applications [Castellanos2007, Palacios2008, Sandberg2008]. Within the scope of this thesis, capacitively coupled $\lambda/2$ wave coplanar waveguide resonators are used in order to perform transmission measurements. When using such devices, the DC-SQUID is positioned at the center of the resonator. For an odd number of resonator modes, the electrical field component at the SQUID position is in this case maximal and the electrical currents at the SQUID position vanish. For an even mode number, however, the current amplitude is maximal at the SQUID position. Tunable resonators can also be realized using other geometries like shorted $\lambda/4$ wave resonators. According to Eqs. (3.58) and (3.60) the impedance of a SQUID can be tuned by using an external magnetic flux. Since the impedance of a resonance circuit determines its resonance frequency, the magnetic flux threading the SQUID loop can be used to control the resonance frequency of the transmission line. The lumped element representation of a transmission line resonator with integrated SQUID is depicted in Fig. 3.14a.

The properties of a DC-SQUID critically depend on the applied bias current. In case the current I which flows through the SQUID is small compared to the critical currents I_{c1} and I_{c2} of the single SQUID junctions, the Josephson junctions show linear behavior. In this case, also the SQUID inductance behaves linearly and the circuit shown in Fig. 3.14a can be modeled by a (harmonic) LCR oscillator with tunable resonance frequency. Here, the presence of the SQUID is taken into account by its inductance $L_S(\Phi)$, connected in series with the inductance L of the transmission line. The equivalent lumped element circuit is shown in Fig. 3.14b. In order to take into account also the resistive and capacitive contributions R^* and C^* when considering the impedance and resonance frequency of the circuit, the series connection of C_κ and R_L can be transformed into a Norton equivalent parallel connection of a resistor R^* and a capacitor C^* , see Fig. 3.14c and

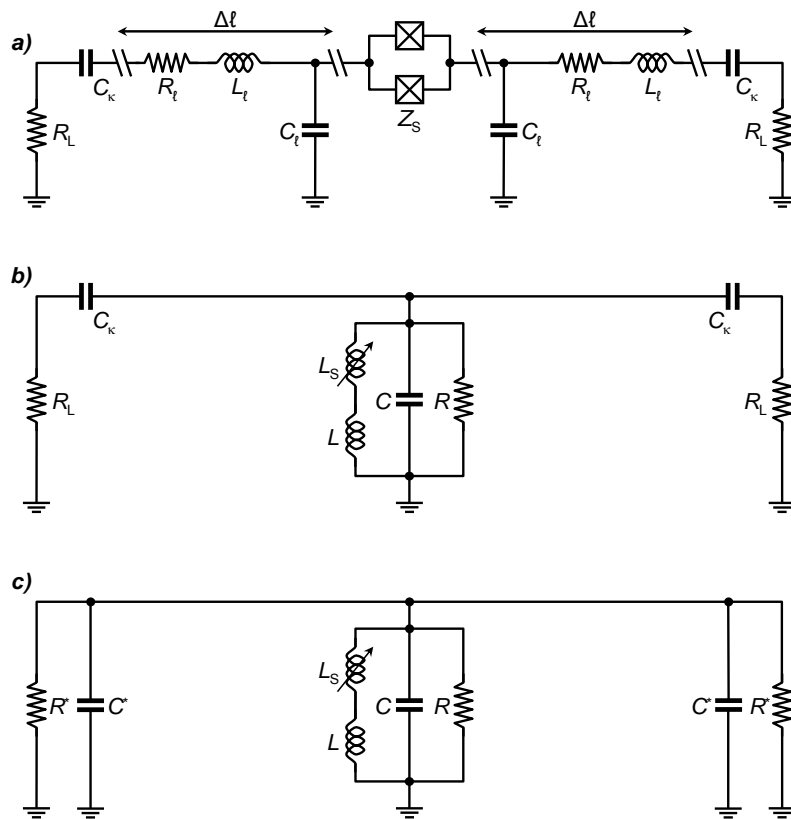


Figure 3.14: a) Distributed element representation of a transmission line resonator with integrated SQUID structure. b) Lumped element representation of the circuit, where the SQUID is taken into account as additional series inductance which is tunable in flux.

compare chapter 2. For the impedance and resonance frequency one finally finds

$$Z(\Phi) = \left(\frac{1}{R} + \frac{2}{R^*} + \frac{1}{i\omega(L + L_S(\Phi))} + i\omega C + 2i\omega C^* \right)^{-1}, \quad (3.64)$$

$$\omega(\Phi) = \frac{1}{\sqrt{(L + L_S(\Phi))(C + 2C^*)}}, \quad (3.65)$$

when neglecting the capacitance C_S of the SQUID junctions.

The lumped element approximation of a tunable SQUID resonator gives an intuitive understanding of the circuit shown in Fig. 3.14a but describes the measured data well only around resonance. In order to model the full resonator transmission spectrum, the scattering matrix model can be applied. The ABCD matrix of a symmetrically coupled transmission line with a DC-SQUID incorporated at the center (see Fig. 3.13) is defined by the product of an input-, a waveguide transmission-, a SQUID transmission-, another waveguide transmission- and an output matrix as

$$\begin{pmatrix} A & B \\ C & D \end{pmatrix} = \begin{pmatrix} 1 & Z_{\text{in}} \\ 0 & 1 \end{pmatrix} \begin{pmatrix} t_{11} & t_{12} \\ t_{21} & t_{22} \end{pmatrix} \begin{pmatrix} 1 & Z_S \\ 0 & 1 \end{pmatrix} \begin{pmatrix} t_{11} & t_{12} \\ t_{21} & t_{22} \end{pmatrix} \begin{pmatrix} 1 & Z_{\text{out}} \\ 0 & 1 \end{pmatrix}, \quad (3.66)$$

with input/output impedances $Z_{\text{in/out}} = 1/i\omega C_\kappa$, where C_κ denotes the input/output coupling capacitor, and the transmission matrix parameters

$$t_{11} = \cosh(\gamma l/2), \quad (3.67)$$

$$t_{12} = Z_0 \sinh(\gamma l/2), \quad (3.68)$$

$$t_{21} = 1/Z_0 \sinh(\gamma l/2), \quad (3.69)$$

$$t_{22} = \cosh(\gamma l/2), \quad (3.70)$$

with the wave propagation coefficient γ , compare chapter 2. The resonator's transmission spectrum is then defined by the ABCD matrix components as

$$S_{21} = \frac{2}{A + B/R_L + CR_L + D}. \quad (3.71)$$

The S_{21} transmission spectrum described by Eq. (3.71) depends on the magnetic flux threading the SQUID loop. Figure 3.15 depicts calculated spectra for two different values of the applied magnetic flux for a $l = 5900 \mu\text{m}$ long coplanar waveguide which has equal geometry parameters as the resonator devices presented in chapter 2. The calculated spectra assume an integrated SQUID structure whose junctions have critical currents of $I_{c1} = 1 \mu\text{A}$ and $I_{c1} = 2 \mu\text{A}$ and $C_\kappa = 10 \text{ fF}$ coupling capacitors to input/output lines. The even resonator modes do not vary with changing magnetic flux since here, the microwave induced current flowing on the waveguide has a node at the resonator's center where the SQUID is positioned. The flux dependent resonance frequency of the circuit, shown in Fig. 3.14a, can be determined by extracting frequencies at which maxima in the transmission amplitude occur, using a numeric routine. Figure 3.16 shows the calculated resonance frequencies versus flux for different junction asymmetries ζ which determines the resonators tuning range. In each case, the resonance frequency is periodic in Φ_0 . For increasing junction asymmetry, the maximum tuning range decreases. For perfectly symmetric junctions for which $\zeta = 0$ holds, unit tuning range is reached. Although the tuning range gets smaller for larger asymmetries, the frequency gradient $df_0/d\Phi$ reduces, thus making the SQUID less sensitive to flux noise. The resonance frequency of the tunable resonator for zero applied flux is higher than the resonance frequency of an equivalent transmission line resonator without integrated SQUID, see

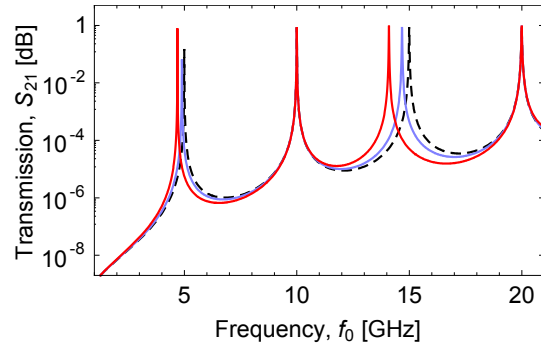


Figure 3.15: Transmission spectrum of a tunable resonator with integrated SQUID structure. The solid blue line shows the resonator transmission for zero flux bias whereas the solid red line indicates the resonator transmission for half a flux quantum threading the SQUID loop. The dashed black line shows the transmission spectrum of the corresponding resonator without incorporated SQUID structure.

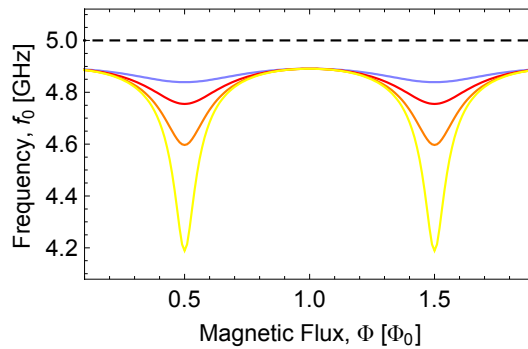


Figure 3.16: Flux dependent resonance frequency f_0 of a tunable resonator for $\zeta = 0.7$ (solid blue line), 0.4 (solid red line), 0.3 (solid orange line) and 0.1 (solid yellow line). The dashed black line shows the flux independent resonance frequency of the corresponding resonator without integrated SQUID structure.

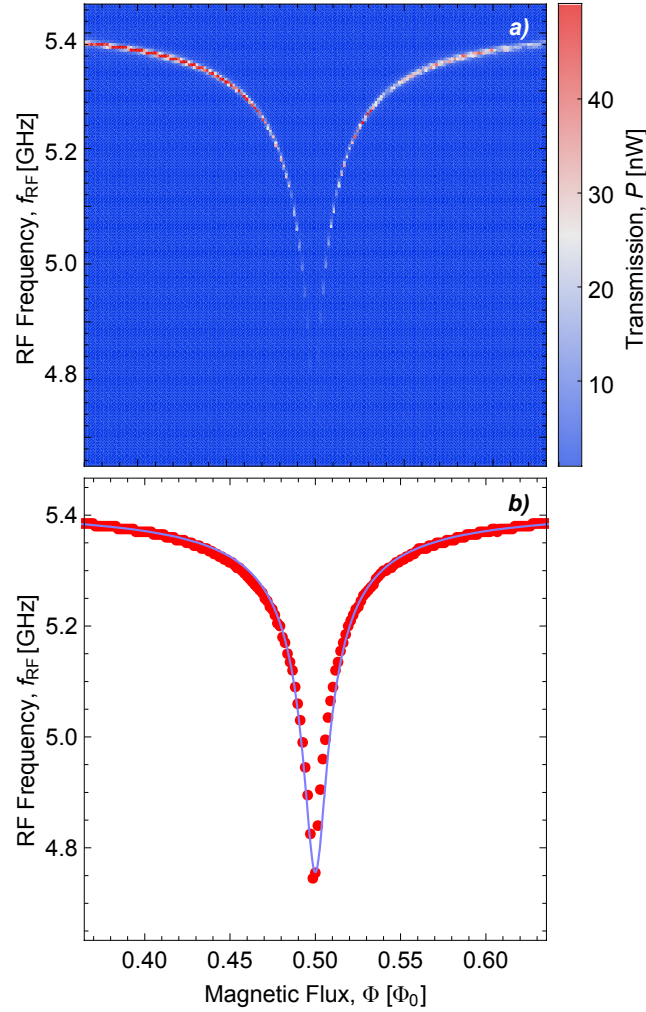


Figure 3.17: a) Transmitted power of a microwave probe signal which is applied to a flux tunable resonator, in dependence on the probe frequency f_{RF} and the applied magnetic flux Φ . b) Resonance frequency extracted from the data shown in part a, in dependence on applied flux, together with a numerical fit obtained by using the ABCD matrix model.

Fig. 3.16. The difference in frequency results from the additional SQUID inductance which is finite, also for zero applied flux. Figure 3.17 shows the measured resonance frequency of a tunable resonator structure in dependence on applied magnetic flux together with a transmission spectrum, numerically evaluated by using the ABCD method. The measured resonance frequency is minimal at $\Phi = 0.5\Phi_0$. The frequency gradient $df_0/d\Phi$ is large for magnetic fluxes close to $\Phi = 0.5\Phi_0$ what leads to a large flux noise sensitivity there. The minimum resonance frequency is $f_r^{\min} = 4.75$ GHz and the maximum frequency is $f_r^{\max} = 5.40$ GHz. The maximum tuning range is accordingly $f_r^{\max} - f_r^{\min} = 650$ MHz what corresponds to a relative tuning range of $(f_r^{\max} - f_r^{\min})/f_r^{\max} = 12\%$. The critical currents of the SQUID junctions are extracted as $I_{c1} = 4.41 \times 10^{-6}$ A and $I_{c2} = 4.56 \times 10^{-6}$ A and the junction asymmetry is $\zeta = 0.02$. Both SQUID junctions are designed with equal areas, but tolerances in the fabrication process lead to the small junction asymmetries. Figure 3.18 shows an optical microscope image of the tuning SQUID which is part of the measured structure.

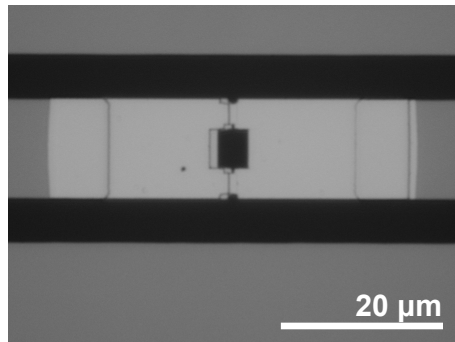


Figure 3.18: Optical microscope image of a fabricated SQUID structure. The coplanar waveguide resonator is made out of niobium while the SQUID consists of aluminum/aluminum-oxide tunnel junctions. Fabrication of such devices is discussed in chapter 4.

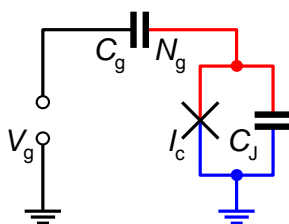


Figure 3.19: Cooper pair box circuit which consists of a serial connection of a single Josephson junction with a gate capacitor. The red part indicates the so-called island, whereas the blue part shows the so-called superconducting reservoir.

3.7 Superconducting Qubits: The Cooper Pair Box

The nonlinearity of a Josephson junction together with its low dissipation renders it a good component for the use in solid state quantum bits (qubits). One can distinguish three different types of Josephson junction qubits according to their relevant degree of freedom: *charge qubits* [Bouchiat1998, Nakamura1999], *flux qubits* [Mooij1999, Friedman2000] and *phase qubits* [Martinis2002]. Within the scope of this thesis, a specific type of superconducting charge qubit, the *Cooper pair box* (CPB), is considered.

The Cooper pair box [Büttiker1987] consists of a Josephson junction and a gate capacitance C_g which are connected in series, as depicted in Fig. 3.19. The electrode of the Josephson junction which is connected to one side of the capacitor is called the *island* (red in Fig. 3.19), whereas the other junction electrode which is connected to ground, is referred to as the *reservoir* (blue in Fig. 3.19). The remaining side of the capacitor is connected to a bias voltage source. In the superconducting state, Cooper pairs of the reservoir can tunnel coherently through the Josephson junction increasing the number of excess Cooper pairs N on the island. In the same way, Cooper pairs can tunnel back from the island to the reservoir decreasing the number of excess Cooper pairs N on the island. An applied gate voltage V_g which acts as control parameter, additionally induces a defined number of polarization charges $N_g = V_g C_g / (2e)$ (taken in units of Cooper pairs) on the capacitor electrodes. The total charge on the island is then given by $2e(N - N_g)$. The gate voltage V_g is used to compensate for offset charges and fluctuations in the number of Cooper pairs on the island.

The Cooper pair box shown in Fig. 3.19 is described by the Hamiltonian

$$\hat{H}_{\text{CPB}} = \hat{H}_{\text{el}} + \hat{H}_{\text{mag}} = E_{\text{C}0} \left(\hat{N} - N_g \right)^2 + E_{\text{J}0} \left(1 - \cos \hat{\phi} \right), \quad (3.72)$$

which consists of an electrostatic and a magnetic part, where $E_{C0} = (2e)^2/2C_\Sigma$ is the characteristic charging energy. Here, the total capacitance C_Σ of the Cooper pair box circuit to ground is written as $C_\Sigma = C_g + C_J + C_s$, taking into account a possible stray capacitance C_s . \hat{N} and $\hat{\phi}$ are the Cooper pair number and phase difference operators which are defined as

$$\hat{N} = i \frac{\partial}{\partial \phi}, \quad (3.73)$$

$$\hat{\phi} = -i \frac{\partial}{\partial N}, \quad (3.74)$$

where N and ϕ are the Cooper pair number and phase expectation values. The operators \hat{N} and $\hat{\phi}$ are conjugate generalized position and momentum operators which obey

$$[\hat{\phi}, \hat{N}] = i. \quad (3.75)$$

The first term of the Hamiltonian written down in Eq. (3.72) is the energy needed to change the number of Cooper pairs N on the island whereas the second term of the Hamiltonian is the energy required to change the phase difference ϕ across the Josephson junction, respectively to move single flux quanta over the junction. The constant term E_{J0} in Eq. (3.72) is not considered in the following since constant terms in the Hamiltonian do not matter for the dynamics.

Charge Basis The electrostatic part \hat{H}_{el} of the Hamiltonian (3.72) can be diagonalized using a discrete charge basis

$$\langle M | N \rangle = \delta_{NM}, \quad \sum_N |N\rangle \langle N| = \hat{1}, \quad \hat{N} |N\rangle = N |N\rangle, \quad (3.76)$$

where N is the number of Cooper pairs on the island. The spectral decomposition of the Hamiltonian (3.72) in the charge basis can be calculated as

$$\hat{H}_{CPB} = \sum_N \left[E_{C0} (\hat{N} - N_g)^2 |N\rangle \langle N| - \frac{E_{J0}}{2} (|N\rangle \langle N+1| + |N+1\rangle \langle N|) \right]. \quad (3.77)$$

The Hamiltonian (3.77) can now be diagonalized using a numeric routine which yields the energy levels as functions of N_g .

Figure 3.20 shows the calculated energy levels of the Cooper pair box as a function of the gate charge N_g , taken in units of Cooper pairs. Figure 3.20a shows the bare electrostatic energy levels when not taking into account the magnetic (tunneling) term of the Hamiltonian (3.72). The energy level structure in Fig. 3.20a is parabolic and periodic in N_g . Energy states are degenerated at points where the energy parabolas cross (*charge degeneracy points*). Figure 3.20b shows the energy levels of the full Cooper pair box Hamiltonian (3.72) where the tunneling term was additionally taken into account. Here, degeneracy disappears due to the perturbation \hat{H}_{mag} and a periodic energy band structure with periodicity $2e$ arises. A certain number of Cooper pairs N on the island defines a specific Cooper pair box state $|N\rangle$. If this number changes from N to $N+1$ due to a tunneling process, the Cooper pair box state also changes from $|N\rangle$ to $|N+1\rangle$. This way, the tunneling interaction leads to superposition states

$$|\psi\rangle_{CPB} = \frac{1}{\sqrt{2}} (|N\rangle \pm |N+1\rangle) \quad (3.78)$$

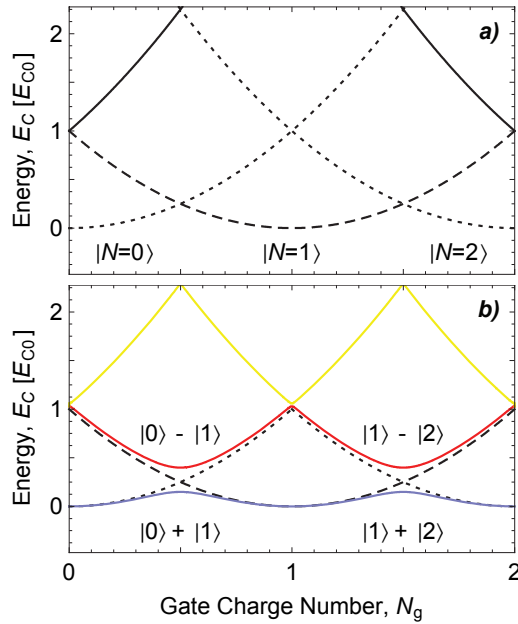


Figure 3.20: a) Normalized eigenenergies of the bare electrostatic Hamiltonian as function of the gate charge number N_g for one additional Cooper pair sitting on the island (black dotted line) and for two (black dashed line) respectively three excess Cooper pairs (black solid line). b) Eigenenergies when additionally taking into account the Josephson tunneling term. The blue, red and yellow line accordingly show the first, second and third resulting energy bands, respectively.

in the energy band structure, see Fig. 3.20b. The lowest two energy bands have now a minimum spacing of E_{J0} . Here it is important to say that the difference between adjacent higher bands is much larger compared to the difference between the lowest two levels. Due to this anharmonic energy band structure, the Cooper pair box can be operated as effective two level system respectively as qubit. The energy level structure and in particular the degree of anharmonicity is determined by the ratio E_{J0}/E_{C0} . In order to see that, the phase representation of the Cooper pair box will be considered.

Phase Basis In the charge basis, the Schrödinger equation which describes the Cooper pair box cannot be solved analytically, since the charge basis is unbound. Using the phase basis in contrast allows for doing this. The phase basis which is continuous and periodic, is given by

$$\langle \phi | \phi' \rangle = \delta(\phi - \phi'), \quad \int d\phi |\phi\rangle \langle \phi| = \hat{1}, \quad \hat{\phi} |\phi\rangle = \phi |\phi\rangle. \quad (3.79)$$

Charge and phase basis are related by Fourier transforms as [Devoret1996]

$$|\phi\rangle = \sum_N e^{i\phi N} |N\rangle, \quad |N\rangle = \int_0^{2\pi} d\phi e^{-i\phi N} |\phi\rangle. \quad (3.80)$$

Equations (3.79) and (3.80) lead to the time independent Schrödinger equation in phase representation

$$\left(E_{C0} \left(i \frac{\partial}{\partial \phi} - N_g \right)^2 \psi_k(\phi) - E_{J0} \cos \phi \right) \psi_k(\phi) = E_k \psi_k(\phi). \quad (3.81)$$

The spectral decomposition of the Hamiltonian is

$$\hat{H}_{\text{CPB}} = E_{\text{C0}} \int_0^{2\pi} d\phi \left(i \frac{\partial}{\partial \phi} - N_{\text{g}} \right)^2 |\phi\rangle \langle \phi| - \frac{E_{\text{J0}}}{2} \int_0^{2\pi} d\phi (e^{i\phi} + e^{-i\phi}) |\phi\rangle \langle \phi|. \quad (3.82)$$

Equation (3.81) is part of the *Mathieu equations* and can be solved analytically [Cottet2002]. After deriving solutions to Eq. (3.81), the energy levels are found as [Koch2007]

$$E_{\text{m}}(N_{\text{g}}) = E_{\text{C0}} M_{\text{A}} (2 [N_{\text{g}} + k(m, N_{\text{g}})]) \left(-\frac{E_{\text{J0}}}{2E_{\text{C0}}} \right), \quad (3.83)$$

where M_{A} is Mathieu's characteristic value and $k(m, N_{\text{g}})$ an eigenvalue sorting function.

A description of the Cooper pair box Hamiltonian in the charge basis offers an intuitive understanding of the Cooper pair box. The phase representation however gives exact results and most calculations can be performed more efficiently.

3.8 Two Level Approximation and Split Cooper Pair Box

Close to the points of avoided crossing, the energy spacing of the lowest two energy bands is small compared to the spacing of higher adjacent bands. The anharmonicity in energy is therefore large and the Cooper pair box can be treated as an effective two level system, respectively as a quantum bit. In the following, the lowest two states of the Cooper pair box are denoted as $\{|\downarrow\rangle, |\uparrow\rangle\}$. In the corresponding two dimensional Hilbert space the Hamiltonian (3.77) writes

$$\hat{H}_{\text{CPB}} = E_{\text{C0}} \left[N_{\text{g}}^2 |\downarrow\rangle \langle \downarrow| + (1 - N_{\text{g}})^2 |\uparrow\rangle \langle \uparrow| \right] - \frac{E_{\text{J0}}}{2} (|\downarrow\rangle \langle \uparrow| + |\uparrow\rangle \langle \downarrow|). \quad (3.84)$$

The state of a qubit can be described by a unit vector on the Bloch sphere, as depicted in Fig. 3.21. In Pauli representation, the two level Hamiltonian of the Cooper pair box writes

$$\hat{H}_{\text{CPB}} = -\frac{E_{\text{C0}}}{2} (1 - N_{\text{g}}) \hat{\sigma}_z - \frac{E_{\text{J0}}}{2} \hat{\sigma}_x. \quad (3.85)$$

Here, the constant term $\bar{E} = \text{Tr}(\hat{H}_{\text{CPB}})$ was not considered. When introducing the mixing angle [Bouchiat1997]

$$\theta_{\text{m}} = \arctan \left(\frac{E_{\text{J0}}}{E_{\text{C0}}(1 - N_{\text{g}})} \right), \quad (3.86)$$

the (symmetric and antisymmetric) eigenfunctions of the Hamiltonian (3.85) can be written as

$$|\psi_{\pm}\rangle = \cos \left(\frac{\theta_{\text{m}}}{2} \right) |\downarrow\rangle \pm \sin \left(\frac{\theta_{\text{m}}}{2} \right) |\uparrow\rangle. \quad (3.87)$$

Here, the ground state is symmetric whereas the excited state is antisymmetric. These two states span the Hilbert-subspace $\{\psi_{-}, \psi_{+}\}$ of the Cooper pair box. The Hamiltonian (3.85) has the same form as the Hamiltonian of a spin-half particle in a magnetic field whose orientation is perpendicular to the z -axis. In this picture, the quantization axis of the qubit is parallel to this field. Rotating the coordinate system around the y -axis by the mixing angle θ_{m} leads to

$$\hat{H}_{\text{CPB}} = \hbar\omega_{\text{a}} \hat{\sigma}_z. \quad (3.88)$$

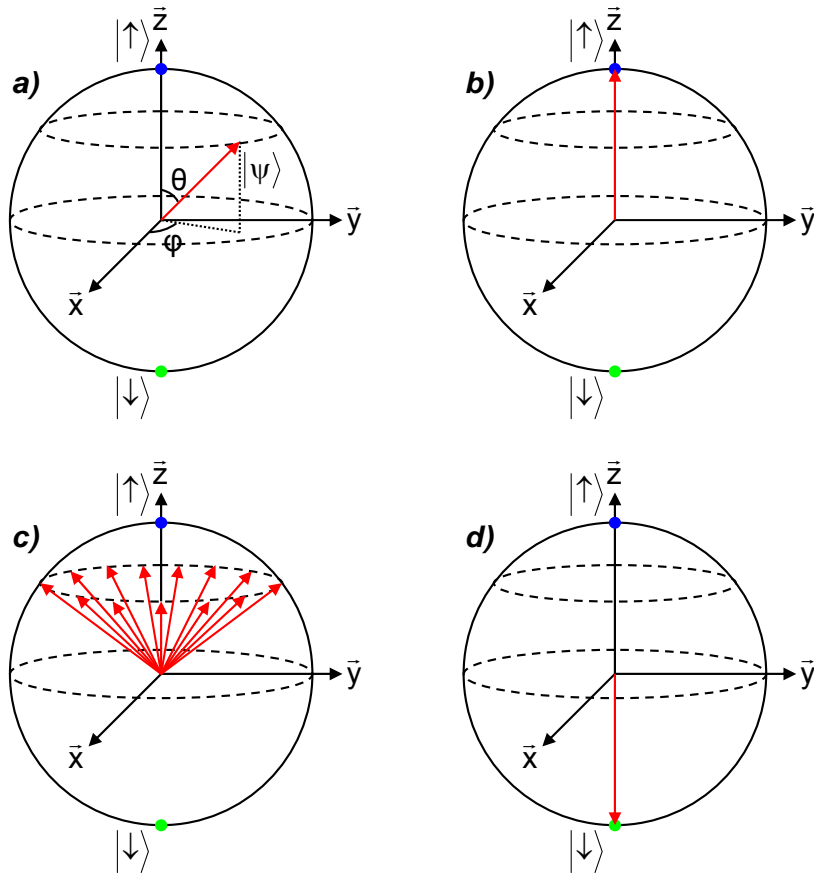


Figure 3.21: Different types of decoherence. a) Initial coherent state of a two level system. b) Excitation of the two-level system from its ground state (see green point) to its excited state (see blue point). c) Dephasing of the two-level system. d) Relaxation from the excited to the ground state.

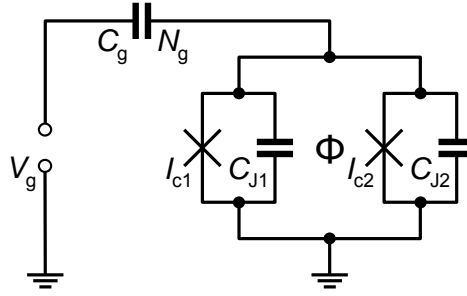


Figure 3.22: Split Cooper pair box circuit, formed by the series connection of a DC-SQUID (instead of a single Josephson junction) and a gate capacitor.

Here, the transition frequency

$$\omega_a = \frac{1}{\hbar} \sqrt{E_{C0}^2 (1 - N_g)^2 + E_{J0}^2} \quad (3.89)$$

was defined. In this *rotated frame*, $|\downarrow\rangle$ and $|\uparrow\rangle$ represent the computational states of the Cooper pair box.

A Cooper pair box can be described as effective two-level system and thus can in principle serve as a qubit. However, a number of other requirements must be fulfilled that a Cooper pair box or in general any physical system can practically be operated as qubit. These fundamental aspects are summarized by the DiVincenzo criteria [DiVincenzo1995]:

1. The system has to provide a well defined two-level quantum system
2. It must be possible to prepare an initial state with sufficient accuracy
3. Long coherence times are needed for quantum error correction
4. There must be a universal set of quantum gates
5. For read-out of the quantum information a quantum measurement is needed
6. There should be the possibility to increase the number of qubits (scalability)

An extension to the *single Cooper pair box*, shown in Fig. 3.19, is the *split Cooper pair box*, where the single Josephson junction is replaced by a DC-SQUID, as depicted in Fig. 3.22. In contrast to the single Cooper pair box, here, the Josephson energy can be tuned by changing the magnetic flux threading the SQUID loop, see Eq. (3.62). The split Cooper pair box can be controlled independently by the gate voltage V_g as well as the external magnetic flux Φ threading the qubit loop. The magnetic flux tunable transition frequency of the split Cooper pair box, compare Eq. (3.89), is then given by

$$\omega_a = \frac{1}{\hbar} \sqrt{E_{C0}^2 (1 - N_g)^2 + (E_{J01} - E_{J02})^2 + 4E_{J01}E_{J02} \cos^2 \left(\pi \frac{\Phi}{\Phi_0} \right)}. \quad (3.90)$$

Figure 3.23 shows an optical microscope image of a fabricated split Cooper pair box structure, integrated into a coplanar waveguide resonator. The big rectangular metal part forms the reservoir and the horizontal aluminum stripe located above forms the island. Reservoir and island are connected via Josephson junctions (see red circles). Fabrication issues are considered in detail in chapter 4.

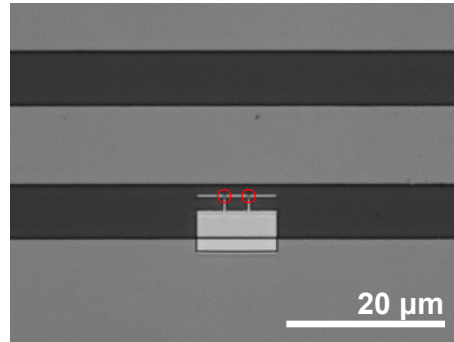


Figure 3.23: Optical microscope image of fabricated split Cooper pair box made out of aluminum (light grey). Red circles indicate Josephson junctions. The Cooper pair box is integrated into the gap (black) of a transmission line resonator made out of niobium (dark grey).

3.9 Decoherence in Charge Qubits

One of the biggest challenges when developing quantum information systems is the suppression of decoherence in qubits. Decoherence results from the entanglement of the quantum system with its environment and causes the qubit to lose its defined quantum state over time. It can be categorized by the two forms *energy relaxation* and *dephasing*.

Energy Relaxation Energy relaxation lets the qubit decay from its excited to its ground state due to the interaction with environmental noise of frequencies close to the qubit transition frequency, see Fig. 3.21d. In this context, T_1 describes the characteristic time over which the qubit undergoes the de-excitation caused by the environmental interaction. This characteristic time is defined as

$$T_1 = \frac{1}{\Gamma_\uparrow}, \quad (3.91)$$

where Γ_\uparrow is the corresponding relaxation rate. Energy relaxation results from the fact that physical systems cannot be perfectly isolated from the environment. The decoherence rate of a quantum system depends on how well it can be decoupled from environmental degrees of freedom.

Dephasing Dephasing refers to the mechanism that lets the qubit accumulate a random phase, see Fig. 3.21c. It is caused by environmental, typically low frequency processes that arbitrarily vary the qubit transition frequency. Dephasing can be divided in different types. Processes which cause the qubit to decay with the rate Γ_1 will also dephase the qubit at a rate $\Gamma_1/2$. Furthermore, fluctuations can occur also on longer timescales from experiment to experiment what is described by the rate Γ_ϕ^* so that the total dephasing rate Γ_2 is then given by

$$\Gamma_2 = \frac{\Gamma_1}{2} + \Gamma_\phi^*. \quad (3.92)$$

In charge qubits, dephasing is mainly caused by the intrinsic low frequency $1/f$ Josephson junction noise. As can be seen from Eq. (3.92), the upper limit for the dephasing time is given by $T_2 = 2T_1$.

3.10 Transmon Type Qubits

One of the biggest challenges towards the realization of large scale quantum information processing with superconducting qubits is the improvement of their coherence times. Superconducting qubits are solid state based systems and thus couple strongly to the environment, which leads to decoherence and dephasing.

The problem mentioned above can be confronted in general with two different strategies. First, one can systematically try to improve the material properties of cavities and Josephson junctions in order to reduce material loss. Second, one can develop cavity and qubit designs, which are less or insensitive to mechanisms which lead to decoherence. The operation of Cooper pair boxes at *sweet spots* where the qubit is in first order insensitive to charge noise is such an example [Vion2002]. Another example is the *transmission line shunted plasma oscillation* or *transmon* type qubit which has been developed [Koch2007, Schreier2008].

The transmon type qubit is based on the Cooper pair box whose energy level anharmonicity and charge dispersion can be controlled by design. The transmon charge dispersion is dramatically reduced compared to the Cooper pair box design in order to create a *permanent sweet spot* for making the qubit insensitive to charge noise. The characteristic Josephson and charging energy E_{J0} and E_{C0} here determine the energy level structure. Both anharmonicity and charge dispersion depend on the ratio of Josephson and charging energy E_{J0}/E_{C0} . A sufficient anharmonicity of the lowest two energy levels is needed in order not to excite higher energy levels when operating the qubit as effective two-level system. Using Eq. (3.83), one can calculate the first three energy levels $m = 0, 1, 2$ of the Cooper pair box Hamiltonian. The levels are shown in Fig. 3.24 for different ratios of E_{J0}/E_{C0} as function of N_g . As can be seen in Fig. 3.24, the energy bands get flatter and flatter with increasing energy ratio E_{J0}/E_{C0} . For an energy ratio $E_{J0}/E_{C0} = 50$, almost no charge dispersion can be recognized and a permanent sweet spot is reached. The charge dispersion of the m -th Cooper pair box level in the limit $E_{J0}/E_{C0} \gg 1$ is approximately given by [Koch2007]

$$\epsilon_m \approx (-1)^m E_{C0} \frac{2^{4m+5}}{m!} \sqrt{\frac{2}{\pi}} \left(\frac{E_{J0}}{2E_{C0}} \right)^{\frac{m}{2} + \frac{3}{4}} e^{-\sqrt{8E_{J0}/E_{C0}}}. \quad (3.93)$$

The charge dispersion exponentially reduces with an increasing ratio E_{J0}/E_{C0} . The reduced charge dispersion makes the transmon which is operated in the regime $E_{J0}/E_{C0} > 1$ nearly insensitive to charge noise in contrast to the Cooper pair box which is operated in the regime $E_{J0}/E_{C0} < 1$. However, the gate voltage V_g respectively the gate charge N_g can no longer be used as control parameter.

In order to reduce the charging energy of the transmon $E_{C0} = e^2/2C_\Sigma$, the total capacitance C_Σ of the structure is increased by adding an additional shunt capacitor C_{sh} . The total capacitance is then $C_\Sigma = C_g + C_J + C_s + C_{sh}$, see Fig. 3.25, where C_g is the gate capacitance, C_J the Josephson capacitance and C_s the stray capacitance. In practice, an additional shunt capacitance is realized by adding large finger type capacitor structures to the device. An optical microscope image of such a transmon structure integrated into a coplanar waveguide resonator is shown in Fig. 3.26.

An energy level ratio E_{J0}/E_{C0} chosen large enough for significantly reducing the transmon charge dispersion leads also to a decreased energy level anharmonicity. The degree of anharmonicity in dependence on the energy ratio E_{J0}/E_{C0} can be analyzed by extending the Josephson cosine potential in the Cooper pair box Hamiltonian (3.72) to fourth order and treating the quadratic

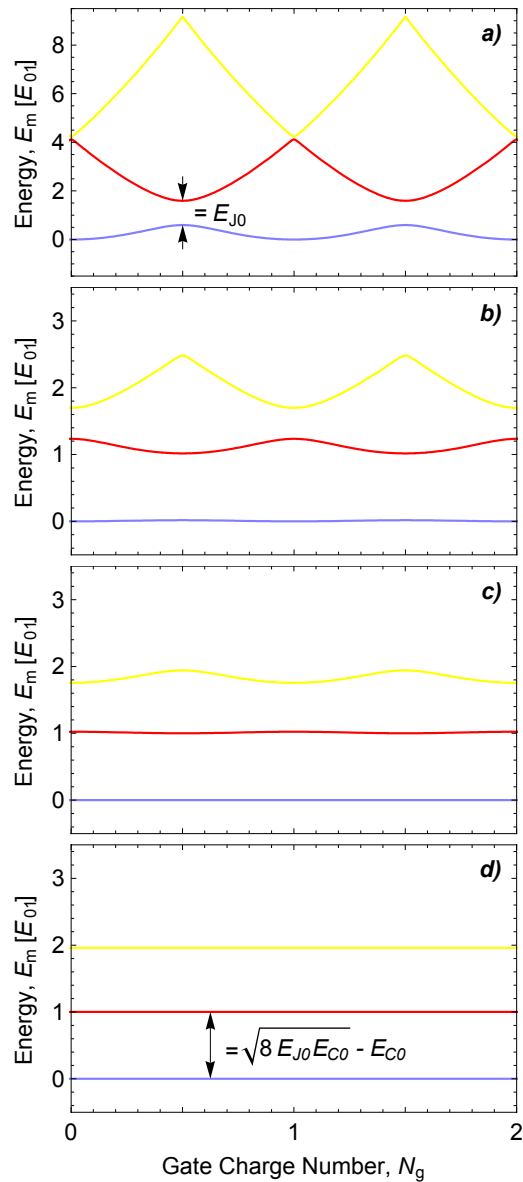


Figure 3.24: Eigenenergies of the Cooper pair box Hamiltonian for different ratios $E_{J0}/E_{C0} = 1$ (a), 5 (b), 10 (c) and 50 (d).

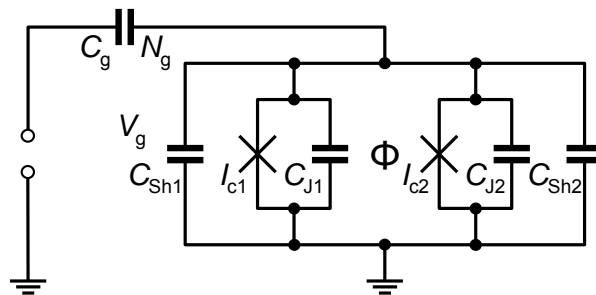


Figure 3.25: Transmon circuit which consists of a split Cooper pair box with additional shunt capacitors connected in parallel.

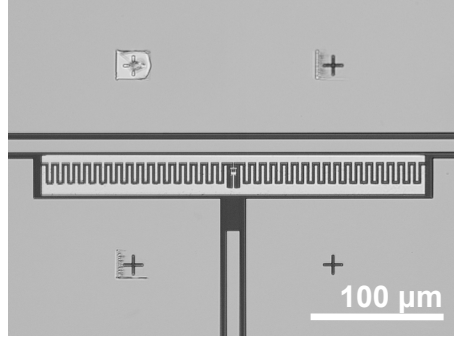


Figure 3.26: Optical microscope image of a transmon qubit integrated into a coplanar waveguide resonator. Its fabrication is considered in detail in chapter 4.

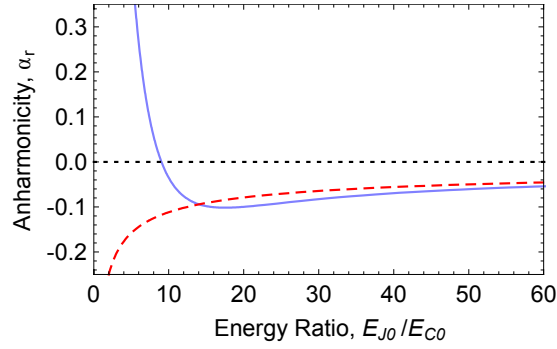


Figure 3.27: Relative anharmonicity α_r of the transmon respectively Cooper pair box energy levels as a function of the ratio E_{J0}/E_{C0} . The blue solid line shows the numerically exact calculation whereas the red dashed line shows the approximate expression according to Eq. (3.96).

term perturbatively. This leads to the approximate eigenenergies

$$E_m \approx -E_{J0} + \sqrt{8E_{J0}E_{C0}} \left(m + \frac{1}{2} \right) - \frac{E_{C0}}{12} (6m^2 + 6m + 3). \quad (3.94)$$

The relative anharmonicity of the first two levels is then defined as

$$\alpha_r = \frac{(E_2 - E_1) - (E_1 - E_0)}{(E_1 - E_0)}. \quad (3.95)$$

The approximate result for E_m given in Eq. (3.94) finally gives

$$\alpha_r \approx - \left(8 \frac{E_{J0}}{E_{C0}} \right)^{-1/2}. \quad (3.96)$$

Equation (3.96) shows that the transmon anharmonicity decreases with a weak power law in the ratio E_{J0}/E_{C0} in contrast to the exponential decrease of the charge dispersion with E_{J0}/E_{C0} . Due to this fact, one can choose values E_{J0}/E_{C0} leading to a drastically reduced charge noise sensitivity but still a sufficient amount of energy level anharmonicity. Figure 3.27 depicts the approximate anharmonicity given in Eq. (3.96) as a function of the energy ratio E_{J0}/E_{C0} together with the values obtained from a numerical exact calculation. The relative anharmonicity is minimal for $E_{J0}/E_{C0} \approx 20$.

A typical single transmon device which was designed and fabricated within the scope of this

3 Josephson Junction Devices

thesis for the experiment reported in reference [Fink2008] has a maximum Josephson energy of $E_{J0} = h \cdot 45$ GHz, a charging energy of $E_{C0} = h \cdot 0.48$ GHz and is integrated into a $f_r = 6.9$ GHz transmission line cavity. The charge dispersion of the first three levels is $\epsilon_0 = h \cdot (2.8 \times 10^{-10}$ GHz), $\epsilon_1 = h \cdot (-3.1 \times 10^{-8}$ GHz) and $\epsilon_2 = h \cdot (1.7 \times 10^{-6}$ GHz). The first three energy levels are $E_0 = h \cdot (-38.5$ GHz), $E_1 = h \cdot (-25.9$ GHz) and $E_2 = h \cdot (-13.7$ GHz) and the relative anharmonicity of the first two levels is $\alpha_r = -0.037$. The transition frequencies between first and second and second and third energy level are accordingly $f_{01} = 12.6$ GHz and $f_{12} = 12.2$ GHz.

The small energy dispersion of the fabricated transmon device makes it to a large degree insensitive to charge noise. In contrast to the Cooper pair box where charge fluctuations and drifts modify the working point of the device in an uncontrolled manner, the transmon avoids this problem by its designed permanent sweet spot. This way, measurements in particular done on a longer time scale are much easier to perform. However, the transmon stability against charge noise is payed off with the absence of the gate voltage as additional control parameter.

4 Design and Thin Film Fabrication of Coplanar Waveguide Resonators and Qubits

This chapter is intended to guide through the complete set of design methods and thin film fabrication techniques used to realize circuit QED devices. A central goal of the author's efforts within the scope of this thesis consisted in the development, implementation and optimization of micro- and nanofabrication processes in the ETH clean room facility FIRST [FIRST]. In particular, optical lithography, reactive ion etching and electron beam evaporation processes were set up for the fabrication of thin film coplanar waveguide resonators and electron beam lithography and shadow evaporation techniques were established for realizing Josephson junction devices. For this purpose, a new electron beam evaporator was acquired, installed and calibrated. The ability of actually realizing circuit QED devices with defined properties is essential for performing particular circuit QED experiments and ultimately, for engineering large scale quantum information systems. All developed processes are explained in detail in this chapter. The reader has to keep in mind that process parameters may usually vary over time due to changing equipment conditions. Consequently, it is necessary to constantly monitor the process quality and to readjust design and fabrication parameters from time to time in order to get reproducible results. In this context, a well thought, fault-tolerant component design can already lead to a better process stability. In the following, processing techniques will be discussed from both, a conceptual as well as from a practical point of view. Photos of machines and instruments presented in this chapter are all taken in the ETH clean room facility FIRST, as long as not stated otherwise.

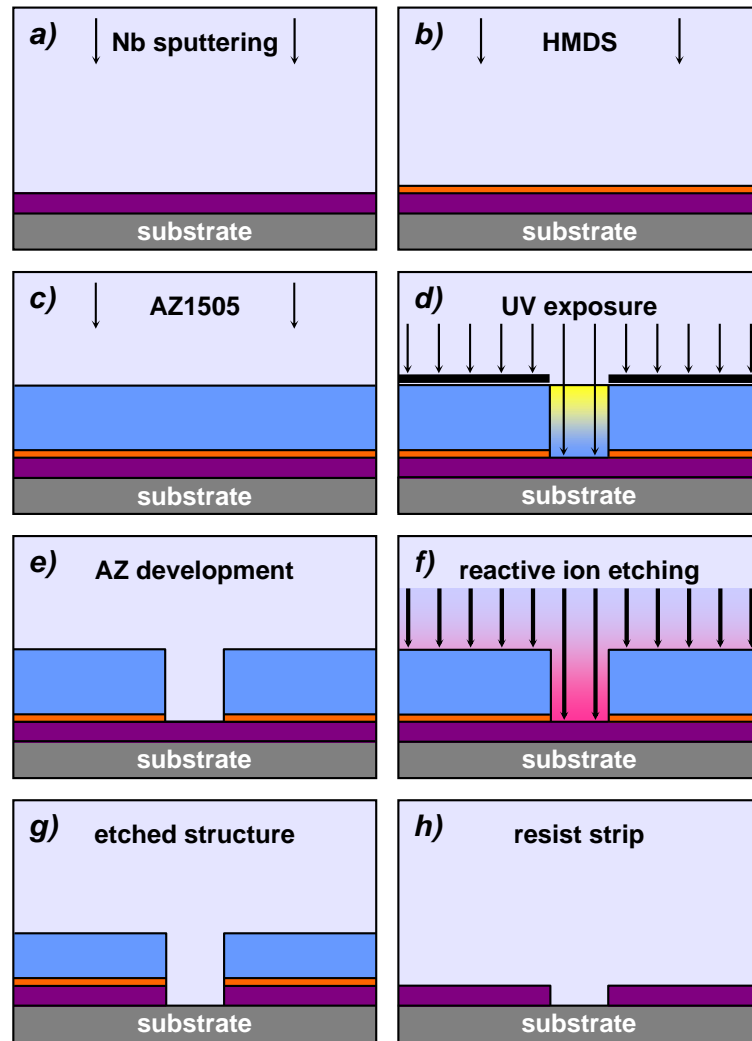


Figure 4.1: Schematic of process chain for fabricating niobium thin film structures using a positive tone resist and reactive ion etching. Single steps are explained in main text.

4.1 Thin Film Fabrication of Superconducting Transmission Line Resonators

Superconducting transmission line resonators are successfully used to address and read out integrated qubits and thus form a major ingredient for a circuit QED architecture. While chapter 2 focuses on resonator modeling and characterization, this section describes the realization of coplanar waveguide resonators. In the context of this thesis, superconducting thin film resonators are either made by reactively etching niobium or by evaporating aluminum thin films. In each case, thermally oxidized high resistivity silicon or sapphire wafers are used as substrate material and optical lithography is used to pattern the device structure.

4.1.1 Reactive Ion Etching of Magnetron Sputtered Niobium Thin Films

The overall process chain for fabricating niobium transmission line resonators is schematically depicted in Fig. 4.1. First of all, a layer of 150 to 200 nm of niobium is magnetron sputtered (see Fig. 4.1a) on a sapphire or thermally oxidized silicon wafer. In order to improve the sticking ability of the photo resist which is spun on top of the wafer surface in a subsequent step, the adhesion

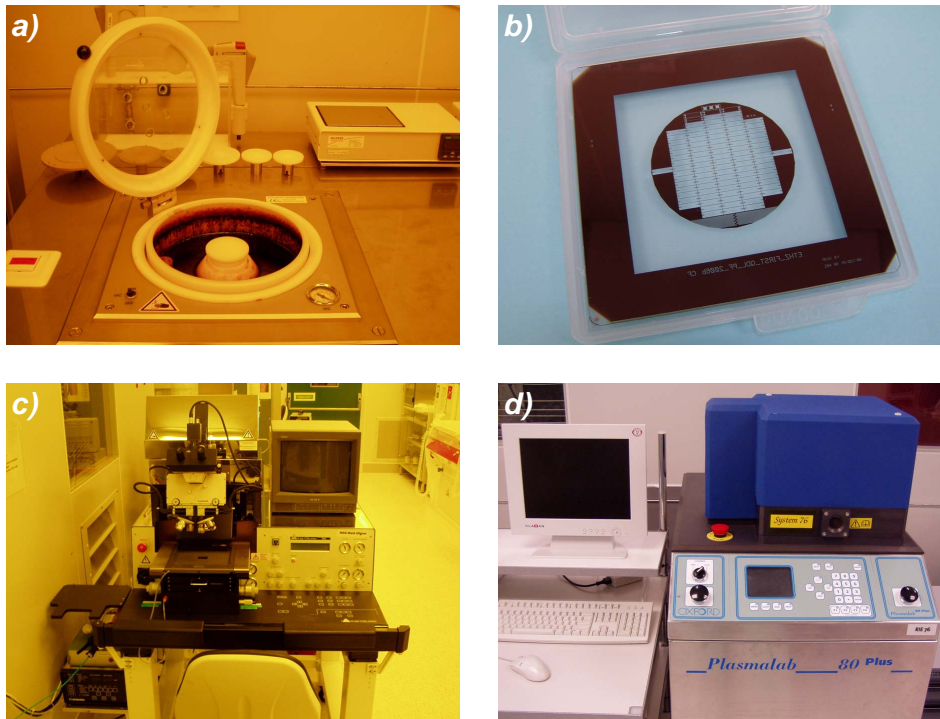


Figure 4.2: a) Resist spinner and hotplates. b) Chromium patterned glass mask carrying resonator structures which is used for UV-exposing photo resist with a mask aligner. c) Mask aligner *Karl Suess MA6* used for UV-exposure of the photo resist. d) Reactive ion etcher *Oxford RIE80* used for etching niobium.

primer hexamethyldisilazane (HMDS) is put onto the niobium sputtered wafer (see Fig. 4.1b). After that, the positive tone resist *Microchemicals AZ1505* is spun onto the wafer (see Fig. 4.1c) and baked out on a hotplate. Figure 4.2a shows a photograph of spinner and hotplates used for resist spinning and bake out. Next, the baked out photo resist is UV-exposed (see Fig. 4.1d) through a chromium patterned glass mask (see Fig. 4.2b) which carries the resonator pattern. Here, the mask aligner *Karl Suess MA6* (see Fig. 4.2c) is used for precisely adjusting the wafer position relative to the photo mask and for UV exposing the resist. In a subsequent step, *Microchemical AZ* developer is used to develop the exposed resist (see Fig. 4.1e). Since AZ1505 is a *positive tone resist*, exposed resist areas will be developed away. Figure 4.3 show an AZ1505 resist structure of a $100\ \mu\text{m}$ wide finger capacitor which is properly exposed (see part a) and developed and which is overdeveloped (see part b). Fingers and gaps between the fingers have nominally the same width of $3.3\ \mu\text{m}$. In case of the too long developed resist structure, the finger width is significantly reduced. The wafer is now ready for etching (see Fig. 4.1f). The niobium is reactively ion etched with an *Oxford RIE80* machine, shown in Fig. 4.2d, in a gas flow of sulphurhexafluoride (SF_6) and argon (Ar). Here, Ar ions physically etch niobium (sputtering) whereas SF_6 radicals chemically remove the metal. Before putting the wafer into the etcher, the process chamber is cleaned by applying an oxygen plasma for about half an hour. During etching of the wafer, the resist acts as sacrificial layer and serves as protection for niobium at places where the metal shall remain on top of the wafer. Only at exposed areas where resist was developed away niobium is attacked by sulphurhexafluoride and argon and removed during the etch process. The resist is also continuously etched and naturally the resist thickness has to be chosen big enough in order not to lose its protection ability after a certain time of etching. A crucial point is to correctly determine the etching endpoint to neither under- nor to overetch the structures. On the one hand, the etching time should be chosen not too short in order

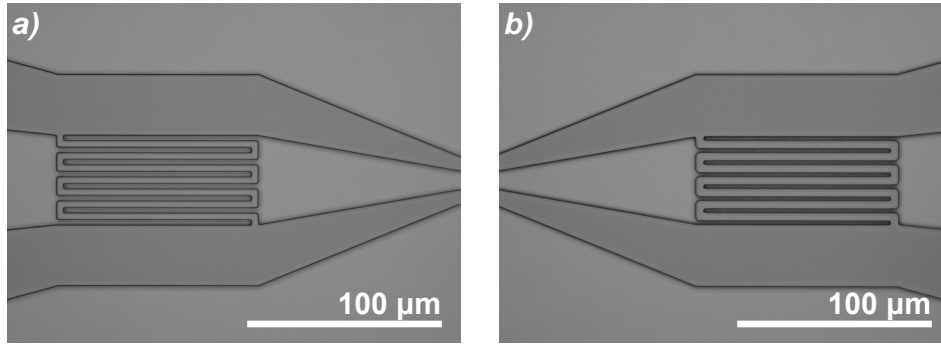


Figure 4.3: a) Positive tone AZ1505 resist structure which is properly exposed and developed. b) Highly overdeveloped AZ1505 resist structure.

Material	Etching Rate
Si	186 nm/sec
SiO ₂	31 nm/sec
Photoresist	85 nm/sec
PMMA resist	121 nm/sec

Table 4.1: Etch rates for different materials when using the *Oxford* RIE80 etcher. The rates were determined for the process parameters listed in appendix D.

to get totally rid of all niobium at places where no niobium shall be left. Otherwise, remaining niobium for example in the gap between center conductor and ground plane of a resonator can lead to a short and thus to malfunctions of the fabricated device. On the other hand, the etching time should not be chosen too long in order to remove as little substrate material as possible when all niobium has been removed. Etching rates were determined for different resists, substrate materials and for niobium, see Tab. 4.1. After having finished the etch process (see Fig. 4.1g), the remaining resist structure is stripped in hot acetone (see Fig. 4.1h). Finally, the two inch wafer is cut into single chips of size $2 \times 7 \text{ mm}^2$, carrying a single transmission line resonator each. Figure 4.4a shows the dicing saw used for this process step. Figure 4.5a shows the scanning electron microscope (SEM) image of a niobium thin film which is only slightly overetched. In contrast, Fig. 4.5b presents the SEM image of a highly overetched niobium thin film. Figures 4.6a to g show a selection of optical microscope images of etched niobium structures. The feature sizes of the

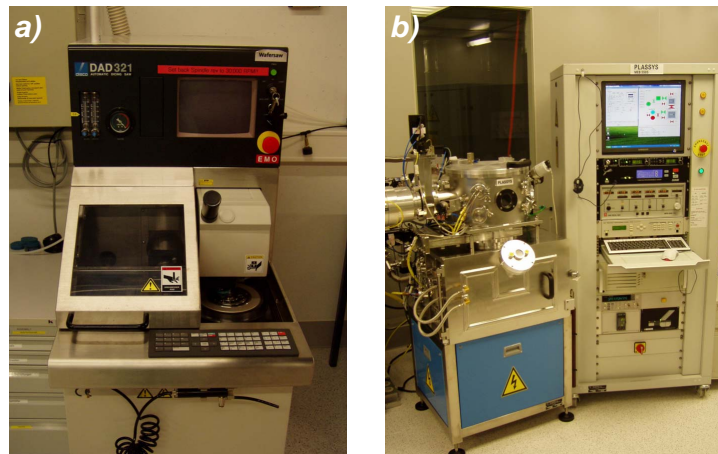


Figure 4.4: a) Dicing saw used for cutting two inch silicon or sapphire wafers into single chips. b) Electron beam evaporator *Plassys* MEB550.

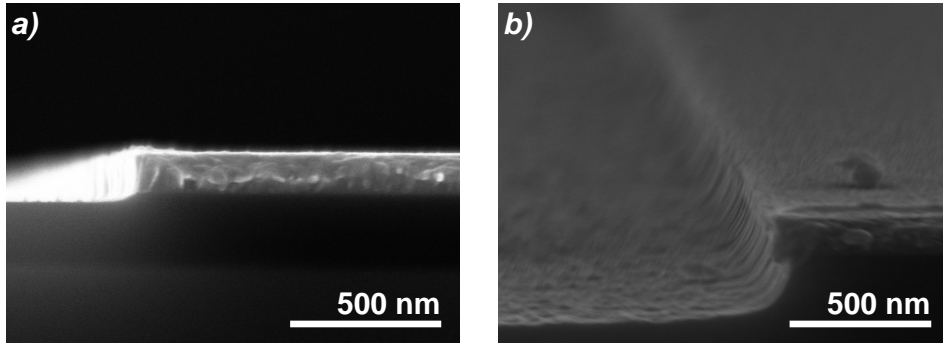


Figure 4.5: SEM images of reactively etched niobium on top of thermally oxidized silicon wafers after resist strip. a) Wafer which is only slightly overetched. b) Highly overetched wafer.

fabricated resonators deviates less than 100 nm from the designed dimensions as determined by SEM inspection indicating a good control over the fabrication process. A detailed process sheet for reactively etching niobium structures can be found in appendix D. Further, process sheets for optical lithography as well as for the wafer dicing procedure can be found in appendix C and H.

4.1.2 Electron Beam Evaporation of Aluminum Films and Lift-Off

Electron beam evaporation of aluminum thin films, together with a lift-off process offers an alternative method for fabricating superconducting transmission line resonators. For the purpose of depositing high quality aluminum, a new electron beam evaporator *Plassys* MEB550, shown in Fig. 4.4b, was installed and calibrated in the ETH clean room facility FIRST as part of the work within the scope of this thesis. Figure 4.7 schematically shows the overall process chain for fabricating aluminum transmission line resonators with a lift-off process. After spinning a layer of HMDS adhesion primer on top of a silicon or sapphire wafer (see Fig. 4.7a), *Microresist* ma-N1410 negative tone resist is spun onto the wafer (see Fig. 4.7b) and baked. The resist is then UV-exposed (see Fig. 4.7c) and developed with *Microresist* maD-533S developer (see Fig. 4.7d). Since ma-N1410 is a *negative tone resist*, regions of the resist which were not exposed, are developed away. The continuous absorption of UV-light from the upper to the lower part of the resist layer results in a typical undercut profile. The undercut profile avoids a metalization of resist side walls during a subsequent aluminum deposition so that metal which covers the resist is not joined to metal which covers the substrate. In this way, the undercut profile separates areas where metal remains on the wafer and those where metal is removed from the wafer and is thus essential for a working lift-off process. The developed resist structure is evaporated with typically 200 nm of aluminum (see Fig. 4.7e) using the electron beam evaporator *Plassys* MEB550. Finally, the resist is stripped in hot acetone (see Fig. 4.7f) and the wafer is cut into single chips. Also this process is documented in detail in appendix C.

4.1.3 Characterization of Niobium and Aluminum Thin Films

Bulk niobium has a critical temperature $T_c \approx 9.2\text{K}$ which is above the temperature of liquid helium. Thus, devices made out of niobium can easily be characterized in a helium dewar. Although the ETH clean room facility FIRST operates a brand new sputtering chamber, all niobium layers used within the scope of this thesis were sputtered either in Prof. Schölkopf's group at Yale University or in Prof. Siegel's group at University of Karlsruhe. The machine installed at FIRST is

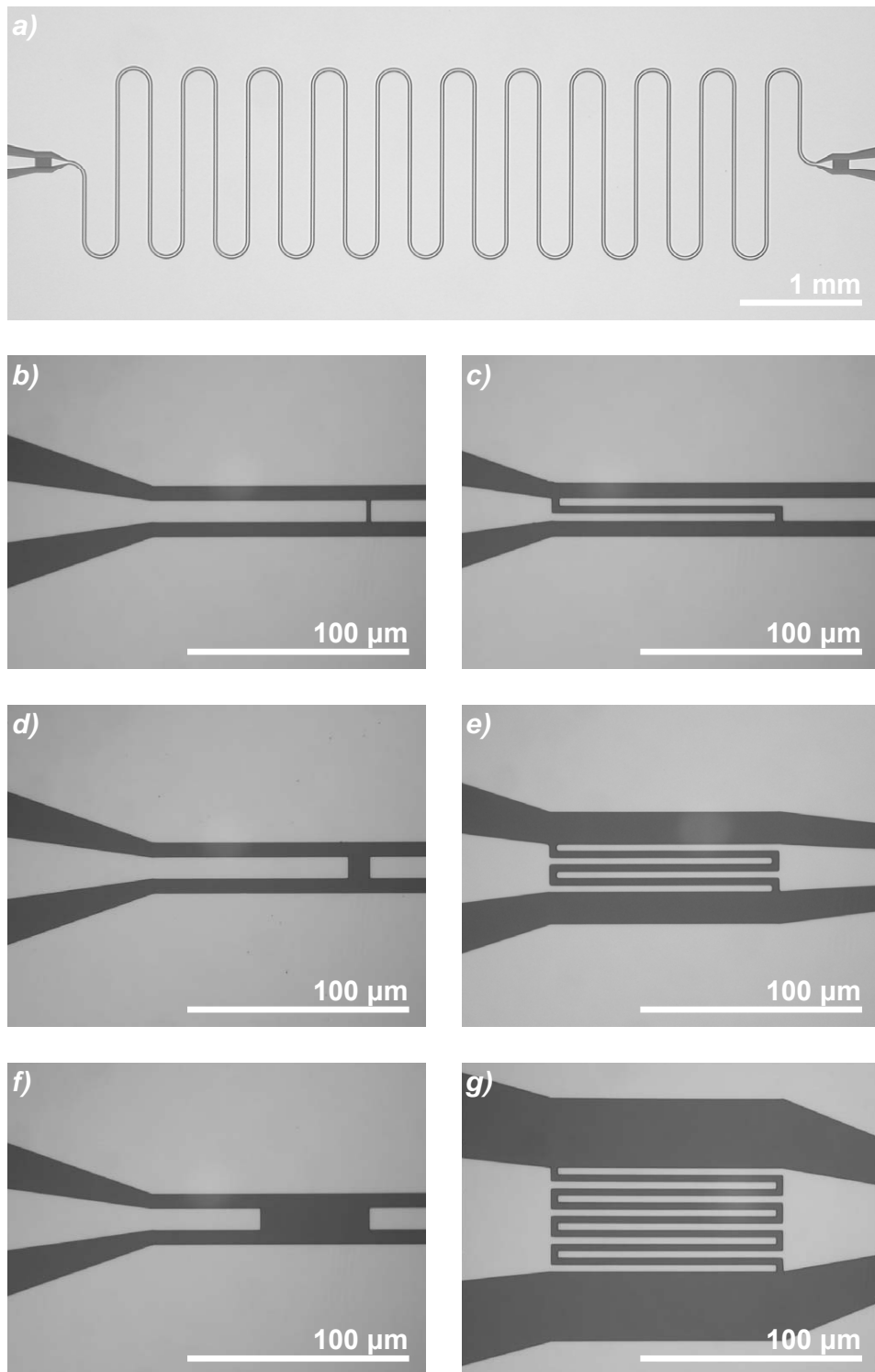


Figure 4.6: Optical microscope images of etched niobium thin film structures. Coplanar waveguide resonator (a), gap capacitors with $2\ \mu\text{m}$ (b), $10\ \mu\text{m}$ (d) and $50\ \mu\text{m}$ (f) gap width and finger capacitors with 2×1 (c), 2×2 (e) and 2×4 (g) $3.3\ \mu\text{m}$ wide, $3.3\ \mu\text{m}$ separated and $100\ \mu\text{m}$ long fingers.

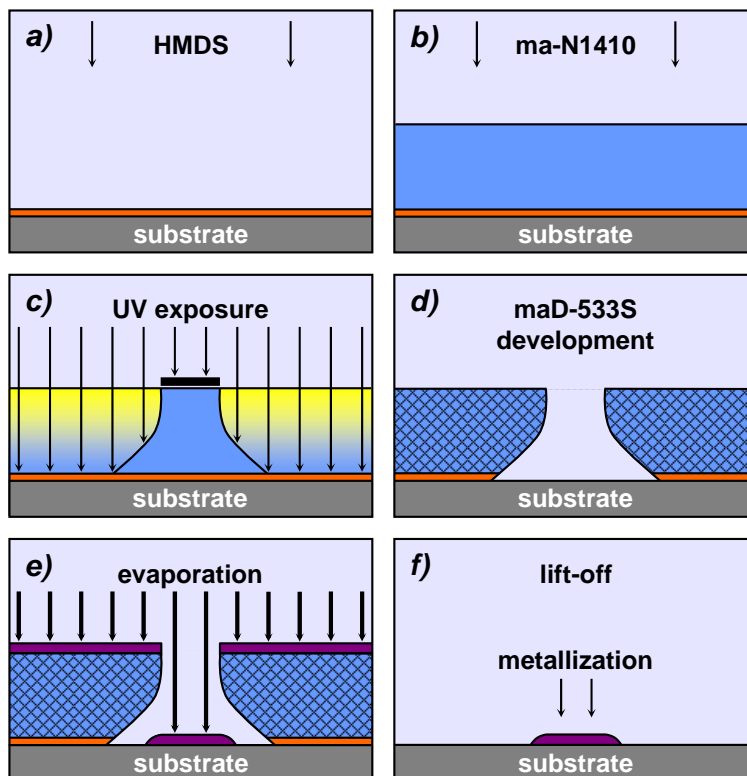


Figure 4.7: Schematic of process chain for fabricating aluminum thin film structures using a negative tone resist and electron beam evaporation. Single steps are explained in main text.

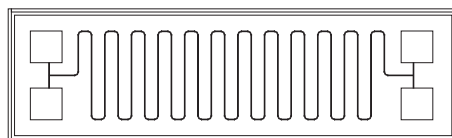


Figure 4.8: Computer aided design (CAD) image of a meander structure used for measuring the resistivity of sputtered niobium thin films in a physical properties measurement system (PPMS). The four contact pads are used for separate current bias and voltage measurement lines (four-point measurement).

also used for sputtering magnetic materials that may contaminate niobium films when depositing them in the same process chamber. Thus, it was decided to outsource this process step, which was possible since the niobium deposition is at the beginning of the process chain when using an etch process. Nevertheless, setting up a niobium sputtering process at ETH remains as a middle term goal. Niobium thin films from both groups were analyzed with a *physical properties measurement system* (PPMS). In such a system, the temperature can be ramped arbitrarily within a certain range while performing a four-point measurement. The niobium thin film deposited at Yale University has a thickness of 190 nm and the niobium thin film deposited at University of Karlsruhe has a thickness of 150 nm. The meander structure shown in Fig. 4.8 was prepared with optical lithography for both materials in order to perform a resistivity four-point measurement while varying the temperature from 300 K down to about 2 K. Figure 4.9 shows the dependence on the resistivity ρ on the temperature for both niobium thin films revealing the values for the critical temperature T_c , for the resistivity ρ_c just above T_c as well as for the *residual resistance ratio* (RRR). The critical temperature T_c is extracted from the measurement data as the temper-

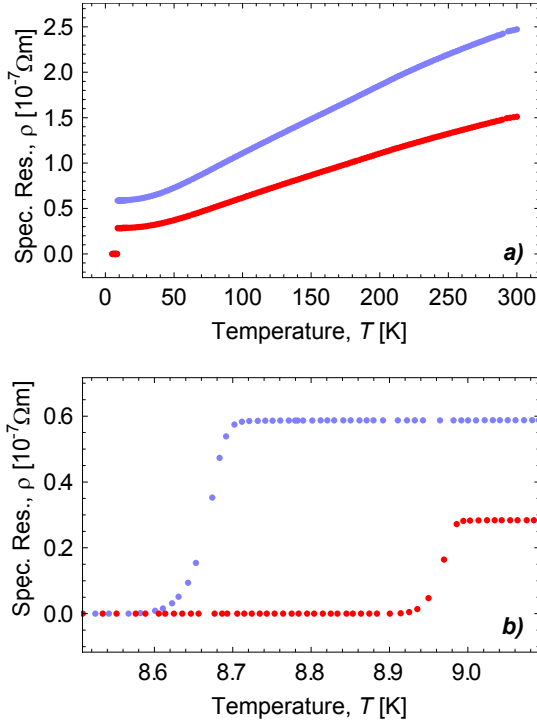


Figure 4.9: a) Resistivity of a 190 nm thin niobium layer (film 1, red) and of a 150 nm thin niobium layer (film 2, blue) in dependence on temperature. b) The same curves close to the critical temperatures T_c of the two thin films.

	Film 1	Film 2	Film 3
T_c	8.97 K	8.67 K	1.23 K
ρ_c	$0.28 \times 10^{-7} \Omega\text{m}$	$0.58 \times 10^{-7} \Omega\text{m}$	$2.06 \times 10^{-9} \Omega\text{m}$
RRR	6.9	4.6	8.6
t	190 nm	150 nm	200 nm

Table 4.2: Measured properties of a niobium layer deposited at Yale University (film 1), a niobium layer deposited at University of Karlsruhe (film 2) and an aluminum layer deposited with the electron beam evaporator *Plassys* MEB550 (film 3).

ature where the interpolated resistivity is half of the resistivity ρ_c just above T_c . The extracted measurement values are listed in Tab. 4.2. The critical temperature T_c of film 1 is smaller than T_c of film 2 and the normal state resistivity ρ for $T > T_c$ of film 1 is smaller than ρ of film 2. Critical temperature T_c and resistivity ρ are higher for thinner films due to stronger surface scattering and for dirtier films due to stronger impurity scattering. Since surface scattering will become significant for film thicknesses in the order of the electron mean free path which is for metals typically in the order of a few nanometers at room temperature and typically an order of magnitude larger at low temperatures, the difference in thickness of film 1 and film 2 does not explain the different values for T_c and ρ and one can conclude that film 1 has less impurities than film 2.

The residual resistance ratio RRR is a measure for the thin film quality and increases with decreasing impurity concentration in the film. Film 1 has a higher RRR than film 2 and thus a smaller impurity concentration. The RRR values for film 1 and 2 compare to measurements of other groups on sputtered thin niobium films [Hammer2007].

Bulk aluminum has a critical temperature $T_c \approx 1.2$ K which is below the temperature of liquid helium. Thus, devices made out of aluminum cannot be characterized simply in a helium dewar. Nevertheless, the advances in cryogenic technology, in particular the development of cryogenic free

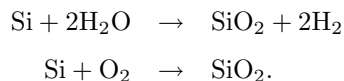
dilution refrigerators [VeriCold], makes low temperatures more or less easily available. In order to characterize aluminum thin films, fabricated with the evaporator *Plassys* MEB550, a four-point measurement is performed on a deposited 200 nm thick aluminum meander structure (see Fig. 4.8). The aluminum meander is installed in a dilution refrigerator and its resistivity in dependence on temperature is measured during warming up the refrigerator. The values for the critical temperature T_c , the resistivity ρ_c just above T_c and the residual resistance ratio RRR are listed also in Tab. 4.2. As already discussed in chapter 2, the temperature dependent London penetration depth $\lambda(T)$ can be approximated as

$$\lambda(0) = 1.05 \cdot 10^{-3} \sqrt{\frac{\rho(T_c)}{T_c}} \sqrt{\frac{\text{Km}}{\Omega}} \quad (4.1)$$

at zero temperature in the local and dirty limits [Watanabe1994]. One finds $\lambda(0) \approx 43$ nm compared to a value of 40 nm, given in reference [Poole1995]. Furthermore, the determined RRR is comparable to the RRR of 200 nm thick aluminum films reported in reference [Mazin2008].

4.1.4 Substrate Materials

Silicon is probably the most studied element and the base material in the integrated circuit industry. It is easy to handle and available in many different configurations. When using silicon as substrate material for circuit QED devices, undoped, high resistivity silicon is used in order to reduce microwave dielectric losses. When fabricating qubits onto a substrate, the isolation between qubit and substrate can be improved by thermally oxidizing the silicon. Thermal oxidation of silicon is usually performed in furnaces at temperatures between 800 and 1200°C, which leads to *high temperature oxide* (HTO). Thermal oxidation can be performed by using either water vapor (steam) or molecular oxygen as an oxidant,



The processes are consequently called either *wet oxidation* or *dry oxidation*. Wet oxidation is preferred for growing thick oxides because of the higher growth rate. However, fast oxidation causes more dangling bonds at the silicon/silicon oxide interface which leads to higher dielectric losses (*dirty interface*). Since there is no oxidation equipment installed at FIRST, silicon wafers are oxidized in Prof. Schölkopf's group at Yale University and also in Prof. Siegel's group at University of Karlsruhe. The thickness of the silicon oxide grown at Yale University is typically in the range of 500 to 600 nm. The thickness of the silicon oxide grown at University of Karlsruhe is typically in the range of 200 to 300 nm. Figure 4.10 shows the SEM imaged cross section of a thermally oxidized silicon wafer and Fig. 4.11a shows the scanning electron microscope *Zeiss* ULTRA55 installed at the ETH clean room facility FIRST which was used for imaging.

Silicon wafers with two inch diameter are bought from *Crystec* [Crystec]. Table 4.3 lists the specified material characteristics. The actual resistivity ρ of the silicon wafers is determined with the *van-der-Pauw method* using the *Accent* HL5500 hall system, shown in Fig. 4.11b. The system further offers the possibility to determine the charge carrier density n , the charge carrier mobility μ and the Hall coefficient R_H . Before doing the measurement, several 6 mm×6 mm square shaped chips cut from different wafers of the same batch are prepared with ohmic contacts on top of their surface by evaporating 200 nm aluminum onto each chip through a mechanical mask. Here, annealing of the metalization was not necessary to get stable ohmic contacts with sufficient small contact

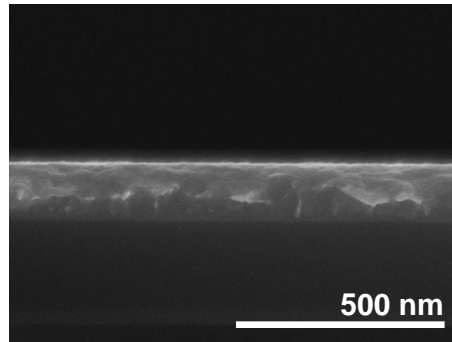


Figure 4.10: SEM image of a cleaved silicon wafer which was thermally oxidized and sputtered with niobium. The cross section shows the pure silicon substrate, thermally oxidized silicon as well as a layer of niobium on top.

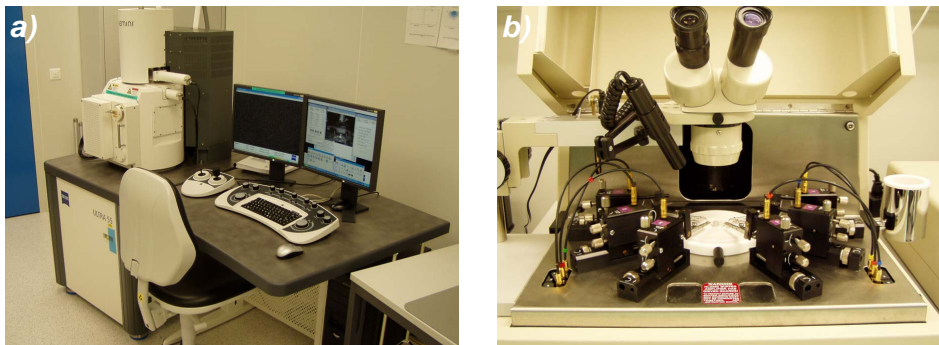


Figure 4.11: a) Scanning electron microscope *Zeiss ULTRA55*. b) Hallmeter *Accent HL5500* used for performing van-der-Pauw measurements.

material	silicon, floating zone
diameter	2 inch
thickness	500 μm
orientation	(100)
dopant	undoped
front side	polished
back side	etched
specific resistance	$> 9000 \Omega\text{cm}$

Table 4.3: Specified material characteristics of high resistivity silicon wafers bought from *Crystec* (batch S4849) and used as substrate material for circuit QED devices.

ρ	$3 \times 10^3 \Omega\text{cm}$
n	$-1.3 \times 10^{12} / \text{cm}^3$
μ	$7.2 \times 10^3 \text{ cm}^2/\text{Vs}$
R_H	$-5.3 \text{ m}^3/\text{C}$

Table 4.4: Measured material characteristics of high resistivity silicon wafers bought from *Crystec* (batch S4849).

material	sapphire, C-plane
diameter	2 inch
thickness	$500 \mu\text{m}$
orientation	C-plane (0001)
primary flat	A-plane
front side	epi-polished
back side	fine ground
TTV	$\leq 10 \mu\text{m}$
flatness	$\leq 5 \mu\text{m}$

Table 4.5: Specified material characteristics of sapphire wafers bought from *Crystec* (batch S4735) and used as substrate material for circuit QED devices.

resistances. Table 4.4 lists values of the measured quantities. The specific resistance ρ is smaller than the specified one. The measured charge carriers are n-type and the charge carrier density n is low as expected. The maximum quality factors, measured for devices which are fabricated on high resistivity silicon wafers are in the range of $Q_L \approx 2.0 \times 10^5$ to 2.5×10^5 .

Instead of thermally oxidized high resistivity silicon wafers, also sapphire wafers are used as substrate for circuit QED devices. Sapphire wafers are also bought from *Crystec*. Table 4.5 lists the specified material characteristics. The thickness of the sapphire and also the silicon wafers is chosen as $500 \mu\text{m}$ to fit the processed chips into a sampleholder printed circuit board of the same thickness. In Tab. 4.5, TTV stands for *total thickness variation* and gives the maximum thickness variation over the wafer surface. Sapphire is nearly a perfect isolator and thus exhibits small microwave dielectric losses with loss tangents typically smaller than 10^{-4} [Crystec]. However, the isolating character of sapphire makes it also harder to perform electron beam lithography on top of the material. Sapphire, which is chemically defined as Al_2O_3 , is an extremely hard material that requires special dicing blades and low dicing speeds when being cut.

4.2 Nano-Fabrication of Josephson Junction Devices

In the following section, fabrication procedures used for realizing nano-scale Josephson junctions, the building blocks for superconducting quantum bits are discussed. A circuit QED system is realized by integrating one or several qubits into a coplanar waveguide resonator. To fabricate Josephson junction devices, such as single junctions, SQUIDs or qubits, electron beam lithography and shadow evaporation is used.

4.2.1 Basics of the Shadow Evaporation Technique

In order to fabricate Josephson junctions with desired feature sizes of about 100 nm the use of appropriate lithographic techniques is necessary. *Electron beam lithography* (EBL) offers an ideal tool to structure devices in this dimension. Feature sizes of 100 nm are not at the limit of the machine's writing resolution which is (dependent on the used resist system) about 5 nm. Electron beam lithography is, as direct writing technique, very flexible and thus well suited for rapidly developing

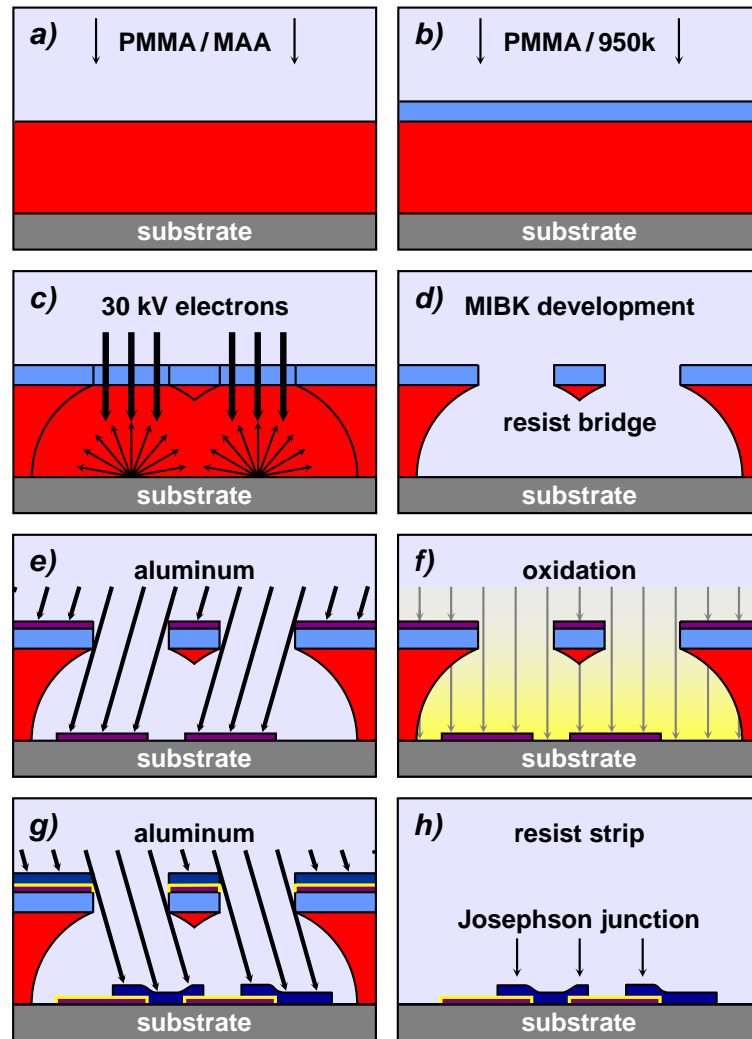


Figure 4.12: Process chain for fabricating aluminum/aluminum oxide tunnel junctions using electron beam lithography and shadow evaporation technique. Single steps are explained in main text.

new device designs. Figure 4.12 depicts the overall process chain for fabricating superconducting tunnel junctions using electron beam lithography and shadow evaporation. First, two layers of *polymethyl-methacrylate* (PMMA) electron beam resist are spun onto the chip and baked out, will say dehydrated on a hotplate. The first layer consists of PMMA/MAA (see Fig. 4.12a) and serves as spacer for the upper resist layer. The second layer consists of PMMA 950k (see Fig. 4.12b) and serves after electron beam exposure and development of the resist as mask layer during a subsequent metal deposition. After resist spinning and bake out, the double layer resist structure is exposed with 30 keV electrons (see Fig. 4.12c) using the electron beam writer *Raith 150*, shown in Fig. 4.13. The lower resist layer is more sensitive to electrons than the upper one. Further, when the electron beam exposes the resist, incoming electrons are backscattered at the wafer surface. The backscattering of electrons together with the different resist sensitivities to electrons leads to a typical undercut structure and to free standing resist bridges after resist development (see Fig. 4.12d). The resist is developed with *methyl-isobutyl-methyl-ketone* (MIBK). After development, the chip is installed at the sampleholder of the electron beam evaporator *Plassys MEB550*. The sampleholder can be tilted by 180 and rotated by 360 degree, see Fig. 4.13b. After mounting the chip in the evaporation chamber of the machine, the sampleholder is rotated to a first position.

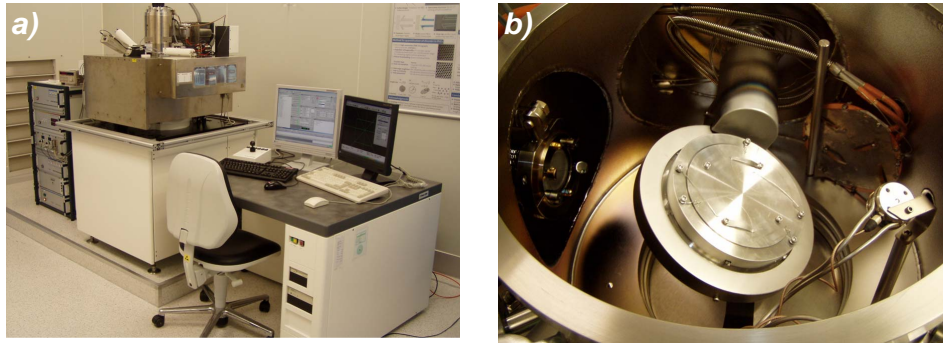


Figure 4.13: a) Electron beam direct writing system *Raith* 150. b) Sample holder which is inside the electron beam evaporator *Plassys* MEB550 and which can be arbitrary tilted and rotated.

The influence of the rotation angles on the junction geometry will be explained in a later section. In that first position, a layer of aluminum is evaporated onto the resist under *a defined angle* to the substrate surface (see Fig. 4.12e). The deposited aluminum layer forms the bottom electrode of the Josephson junction. In a subsequent step, the process chamber is filled with a mixture of oxygen and argon until a defined pressure is reached. The oxygen oxidizes the surface of the aluminum layer resulting in a thin aluminum oxide layer with a thickness on the order of a few nanometer depending on the partial oxygen pressure and the oxidation time (see Fig. 4.12f). The process of aluminum oxidation will be discussed in detail in a later section. Having finished the oxidation, the gas is pumped out of the process chamber and the sampleholder is rotated to a second position. According to that second sampleholder position, another layer of aluminum is evaporated under *a defined angle* to the substrate surface (see Fig. 4.12g). In that way, the upper aluminum film which overlaps the lower aluminum layer forms the top electrode of the Josephson junction. With this technique, a sub-micron scale Josephson junction, consisting of aluminum bottom electrode, a very thin tunnel barrier and aluminum top electrode can be defined in the evaporator process chamber without breaking the vacuum. Not breaking the vacuum is a crucial point in this context since the thickness as well as the quality of the oxide layer sensitively determines Josephson and charging energies of the tunnel junction. Figure 4.12h shows the junction after stripping the resist in hot acetone.

The electron beam evaporator *Plassys* MEB550 was bought for the purpose of fabricating Josephson junction devices. Since the machine was only installed about one and a half year after having started with the work presented in this thesis, junction processing was initially performed using a different system. In order to perform shadow evaporation, the electron beam evaporator *Leybold* UNIVEX450, installed at FIRST, was fitted with a home made sample holder. Figure 4.14a shows the evaporator *Leybold* UNIVEX450, Fig. 4.15 presents the self made sample holder and Fig. 4.14b shows the sample holder installed in the machine and ready for operation.

In contrast to the *Plassys* MEB550 evaporator which provides the possibility to control processes fully automatically, the *Leybold* UNIVEX450 evaporator has to be operated manually. Further, the evaporator *Leybold* UNIVEX450 has no separate load lock. Although the *Plassys* MEB550 electron beam evaporator offers a number of additional features such as an ion milling gun, a cryogenic pump for excellent vacuum conditions, a UV lamp for ozone generation as well as a sample holder which can be heated and cooled, the *Leybold* UNIVEX450 machine is a tested alternative for fabricating working Josephson junction devices. Detailed process sheets for shadow evaporation and oxidation using both, the *Plassys* MEB550 and the *Leybold* UNIVEX450 electron beam evaporator

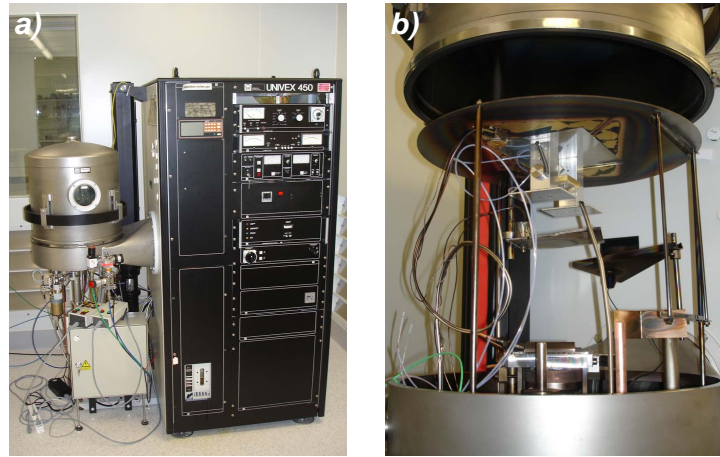


Figure 4.14: a) Electron beam evaporator *Leybold* UNIVEX450. b) Home made sample holder installed in UNIVEX450.

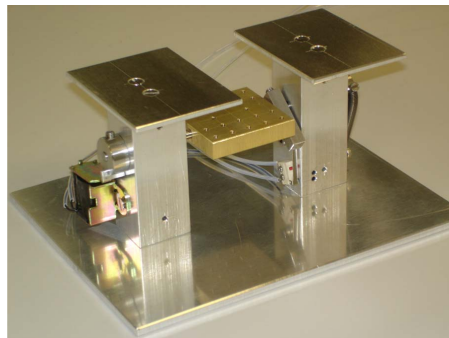


Figure 4.15: Home made sampleholder used for performing shadow evaporation with the electron beam evaporator *Leybold* UNIVEX450. Initial and final sampleholder positions are adjusted manually before starting the process. A mechanical spring rotates the sampleholder from the predefined initial to the predefined final position as soon as an electrical magnet holding the sampleholder in its initial position is released.

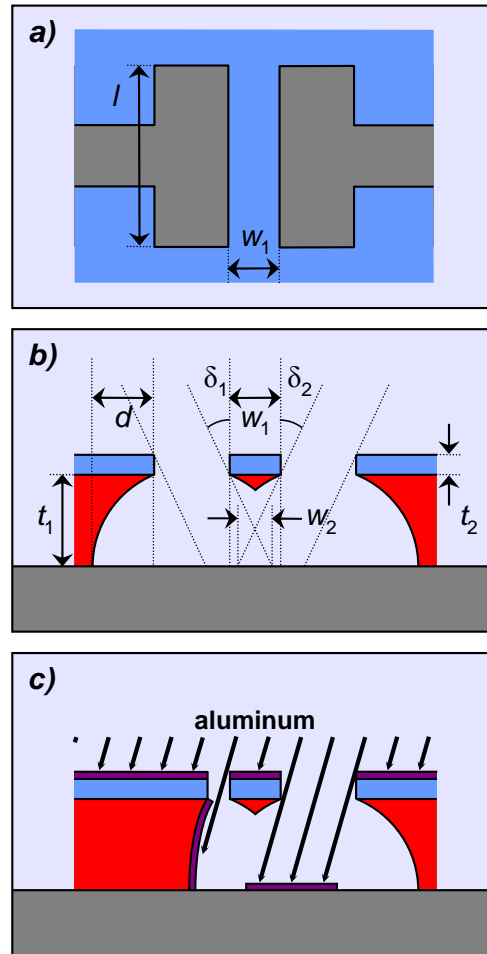


Figure 4.16: a) Top view of a double layer resist profile which is used for fabricating small aluminum/aluminum oxide Josephson junctions. b) Cross section view of the resist profile. The junction width w_2 is determined by the deposition angles δ_1 and δ_2 , as well as by the width w_1 of the resist bridge and by the thickness t_1 of the lower resist layer (see Eq. (4.2)). c) Resist profile for side wall deposition.

can be found in appendix F. Further, recipes for automatic processing using the *Plassys* MEB550 evaporator are listed in appendix G.

4.2.2 Designing and Optimizing the PMMA Double Layer Resist Structure

Fabricating Josephson junction devices using electron beam lithography and shadow evaporation technique exhibits two main challenges. First, a double layer resist structure with free standing resist bridges and a defined undercut profile has to be realized (compare Fig. 4.12) and second, the oxidation process during junction deposition has to be controlled. The oxidation conditions are controlled by using the calibration results of an oxidation series of test Josephson junctions. The double layer resist profile however is controlled by using the calibration results of an exposure dose array.

The geometry of a double layer resist profile used for fabricating tunnel junctions is shown in Fig. 4.16. The lower resist layer (thickness t_1) serves as spacer for the upper resist layer (thickness t_2) which in turn acts as shadow mask during aluminum deposition. The first aluminum layer is deposited under the angle δ_1 , the second one is deposited under the angle δ_2 . Although a free standing resist bridge (width w_1 and length l) is not required for an overlap of the two aluminum

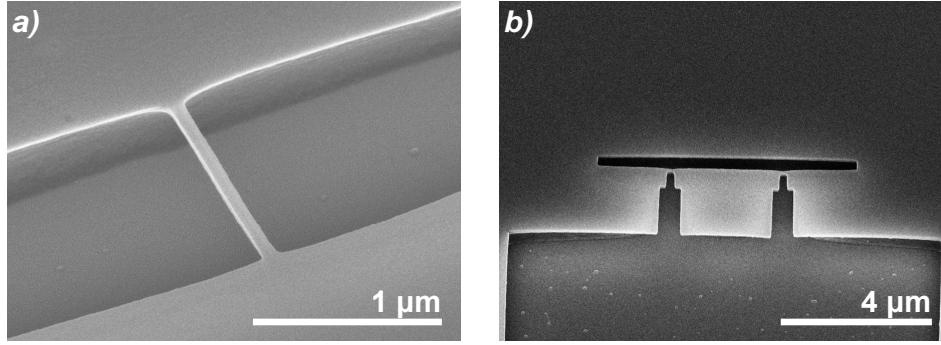


Figure 4.17: a) SEM image of resist structure with free standing resist bridge. b) SEM image of developed Cooper pair box resist structure.

films, it would be impossible to bring up feed lines to the actual Josephson junction without having the bridge. Using Fig. 4.16, the overlap w_2 of the two aluminum films can be determined as

$$\begin{aligned} w_2 &= w_1 - (w_1 - t_1 \tan \delta_1 + w_1 - t_1 \tan \delta_2) \\ &= t_1(\tan \delta_1 + \tan \delta_2) - w_1, \end{aligned} \quad (4.2)$$

which can be approximated in case of small angles δ_1 and δ_2 by

$$w_2 \approx t_1(\delta_1 + \delta_2) - w_1. \quad (4.3)$$

Equations (4.2) and (4.3) show that the overlap w_2 increases with increasing deposition angles δ_1 and δ_2 , with increasing thickness t_1 of the lower resist layer and with decreasing width w_1 of the free standing resist bridge. Naturally, t_1 cannot be increased arbitrarily since higher acceleration voltages V_{acc} are necessary for exposing thicker resist layers and V_{acc} of the used EBL system *Raith 150* is limited to 30 kV. Furthermore, w_1 cannot be decreased arbitrarily since the resist bridge loses mechanical stability and breaks down when decreasing its width too much. The thicknesses t_1 and t_2 can be controlled by varying the rotational speed when spinning the resist layer. Typical geometric parameters are $w_1 = 100$ nm, $t_1 = 660$ nm and $t_2 = 120$ nm. The depth d of the undercut profile can be controlled by varying the exposure dose. A higher dose leads to a deeper undercut, a lower exposure dose results in a steeper resist profile. On the one hand, the undercut profile, schematically depicted in Fig. 4.16, must be deep enough that resist side walls do not get deposited with aluminum during evaporation, in order to realize a working lift-off. On the other hand, the resist profile must be steep enough that the overall resist structure is stable enough not to collapse during evaporation. Figure 4.17a shows the SEM image of a developed resist structure with a free standing resist bridge of only about 50 nm width but with a length of more than 1 μ m. The resist bridge is stable even the resist underneath the bridge is totally removed. Figure 4.17b depicts the SEM image of a developed Cooper pair box resist structure with a deep undercut profile. Clearly one can see the thin top layer resist which starts to bend down under electron beam exposure during SEM inspection.

Appropriate exposure doses for a specific design can be determined in an *exposure dose array*. Within this array, the same structure is exposed several times into a double layer resist with different doses. After evaporation and resist strip, the deposition result can be SEM inspected, junction sizes can be determined and a proper exposure dose can be chosen. An exposure dose chosen too high for example, can lead to a broken resist bridge and finally to a defective junction. Figure 4.18a shows an optical microscope image of the developed resist structure of a DC-SQUID.

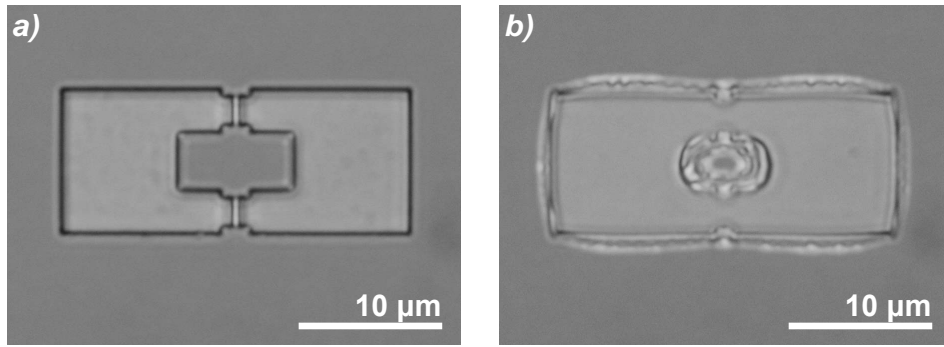


Figure 4.18: a) Optical microscope image of the developed resist structures of a DC-SQUID, exposed with an appropriate dose. b) Optical microscope image of the developed resist structure of an equal design, overexposed with a much too high dose. Due to the overexposure, the resist bridge was completely developed away.

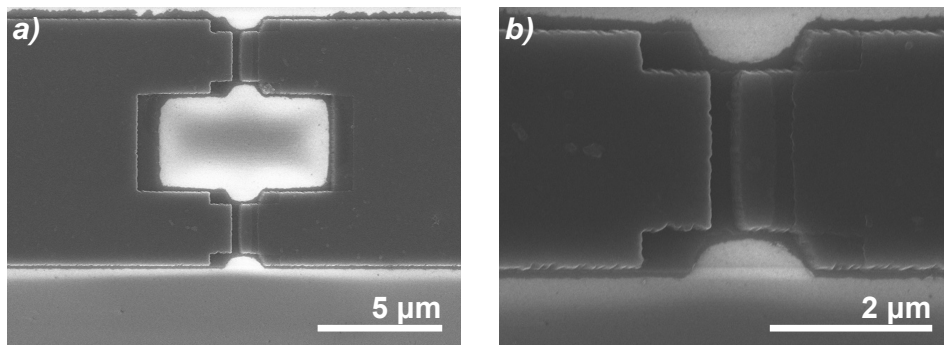


Figure 4.19: a) SEM image of a DC-SQUID, fabricated with shadow evaporation. The developed resist structure of the device is shown in Fig. 4.18. b) SEM image of a single junction of the device shown in part a.

Figure 4.18b further depicts an optical microscope image of the developed resist structure of an identical device geometry but exposed with a too high dose. Figures 4.19a and 4.19b are SEM images of the deposited device whose developed resist structure is shown in Fig. 4.18a. The overlap w_2 of bottom and top aluminum layer which defines the actual Josephson junction area is about $0.5 \mu\text{m}$ and the length l of the junction is $2 \mu\text{m}$. Bottom and top layers are displaced by a distance $t_1(\tan \delta_1 + \tan \delta_2)$ which is here about $0.8 \mu\text{m}$, see Fig. 4.19b. Both evaporation angles δ_1 and δ_2 are 30° so that the thickness of the bottom layer resist can be calculated as $t_1 = 690 \text{ nm}$ what is about 5% thicker than the estimated resist thickness of 660 nm according to the resist spinning speed and the degree of resist dilution. The darker parts around the actual junction boundaries indicate a thin layer of aluminum within the undercut region due to a certain degree of diffusion and scattering of evaporated aluminum particles. Short circuits due to these aluminum layers are not observed. However, it is not clear whether the aluminum layers may badly affect coherence properties of the junction.

When engineering the undercut profile of a double layer resist structure, the concept of *undercut boxes* offers a helpful tool. Within this method, specific resist areas are exposed with an additional dose, chosen slightly below the clearing dose of the top resist layer. The top resist layer thus does not open up, in contrast to the bottom resist layer which is more sensitive to electrons and therefore has a lower clearing dose. Figure 4.20 shows optical microscope images of resist structures after development for two different Cooper pair box and transmon designs where the concept of undercut boxes was applied and of the respective structures after deposition and resist strip. Furthermore,

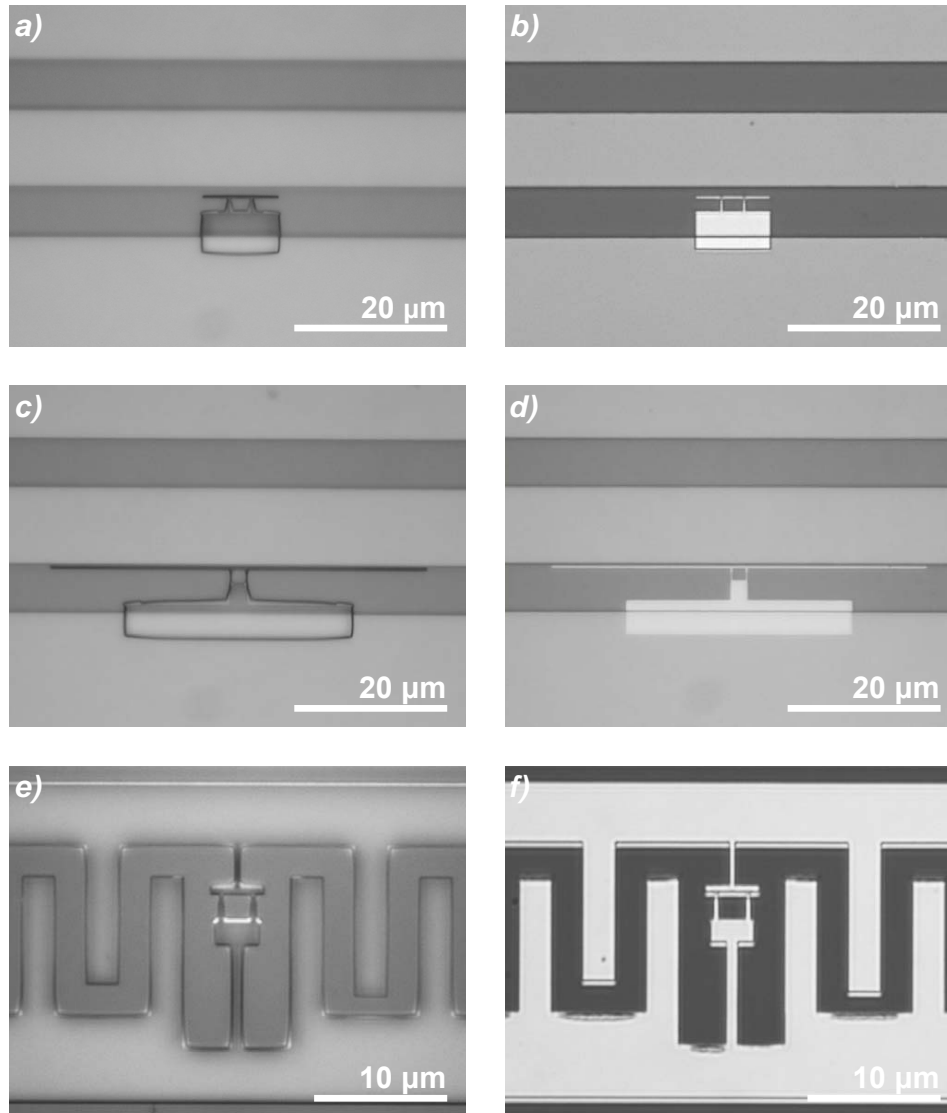


Figure 4.20: Optical microscope images of developed resist structures (left hand side) and of the respective devices after deposition and lift-off (right hand side) for different qubit designs: Cooper pair box with 10 μm long island (a and b), Cooper pair box with 50 μm long island (c and d) and transmon type qubit (e and f).

Fig. 4.21 shows the respective CAD designs of the three qubit types which are shown in Fig. 4.20. Here, the second Cooper pair box was designed with a longer island compared to the island of the first Cooper pair box design in order to achieve a higher cavity-qubit coupling strength g , see chapter 5. Exposure regions in Fig. 4.21 are white, additional exposure regions for undercut boxes are red, resonator metalization and gaps are gray and blue, respectively. Also shown are alignment markers and alignment scan fields for electron beam lithography (yellow and purple, respectively), which will be explained in the next section. The three qubit designs are optimized for evaporation angles of $\delta_1 = 0^\circ$ and $\delta_2 = 30^\circ$ and for typical exposure doses between 300 and 400 $\mu\text{C}/\text{cm}^2$. The additional dose for undercut boxes ranges typically between 50 to 100 $\mu\text{C}/\text{cm}^2$. In the optical microscope images Fig. 4.20a, c, e of the developed qubit resist structures, regions with additional undercut come out lighter than other resist areas, see in particular the central region of the structure shown in Fig. 4.20e. The first Cooper pair box design shown in Fig. 4.21a uses undercut boxes only at the upper and outer edges of the reservoir since these regions get less exposed compared to central regions of the reservoir. Electrons accelerated onto a certain resist area also expose neighboring resist regions which is called *proximity effect*. Undercut boxes close to the island are not present since here a steep resist profile is favored in order to perform a side wall deposition, see later explanation. Due to the additional undercut boxes, the Cooper pair box resist profile is deep enough for a subsequent aluminum evaporation under an angle of 30° what in turn enables a proper lift-off, see Fig. 4.20b. The second Cooper pair box design, see Fig. 4.21b, also uses undercut boxes at the upper and outer edges of the reservoir but also between the two finger-like structures in the upper part of the reservoir since this region is less exposed with proximity electrons than the central regions of the reservoir. Also for this design, a well defined rectangular island is achieved after evaporation and resist strip, see Fig. 4.20d. The transmon design shown in Fig. 4.21c uses undercut boxes also above the island what leads to a shadow structure of the island, see Fig. 4.20f. However, undercut boxes are not used at the bottom parts of the finger capacitor structures although additional undercut is needed here, what leads to a bad lift-off in these regions, see Fig. 4.20f.

The principle of *side wall deposition*, where parts of an aluminum structure are deposited onto a resist side wall and removed during lift-off, see Fig. 4.16c, provides another useful method in the context of resist profile and device design. Here, the steepness of the undercut profile is increased by reducing the exposure dose to a minimum. During a subsequent evaporation, one deposition angle (δ_1 or δ_2 in Fig. 4.16) is chosen large enough that metal is evaporated onto the resist side wall and thus removed when stripping the resist. This way, one can partially avoid the shadow structure when depositing a certain device. Figure 4.22a and 4.22b show SEM images of a Cooper pair box where the principle of side wall deposition was used to avoid the island shadow structure. Here, the island shadow structure is unwanted in order to achieve a defined electrical coupling between island and center conductor.

As already mentioned, electrons accelerated onto a certain resist area also expose neighboring resist regions. Increasing the exposure dose leads to a larger proximity effect and thus to a larger exposed resist area. This in turn causes a bigger junction size after resist development and junction deposition. The size especially of small Josephson junctions can thus be fine-tuned by using slightly higher or lower exposure doses. Detailed process sheets for preparing PMMA double layer resists can be found in appendix E.

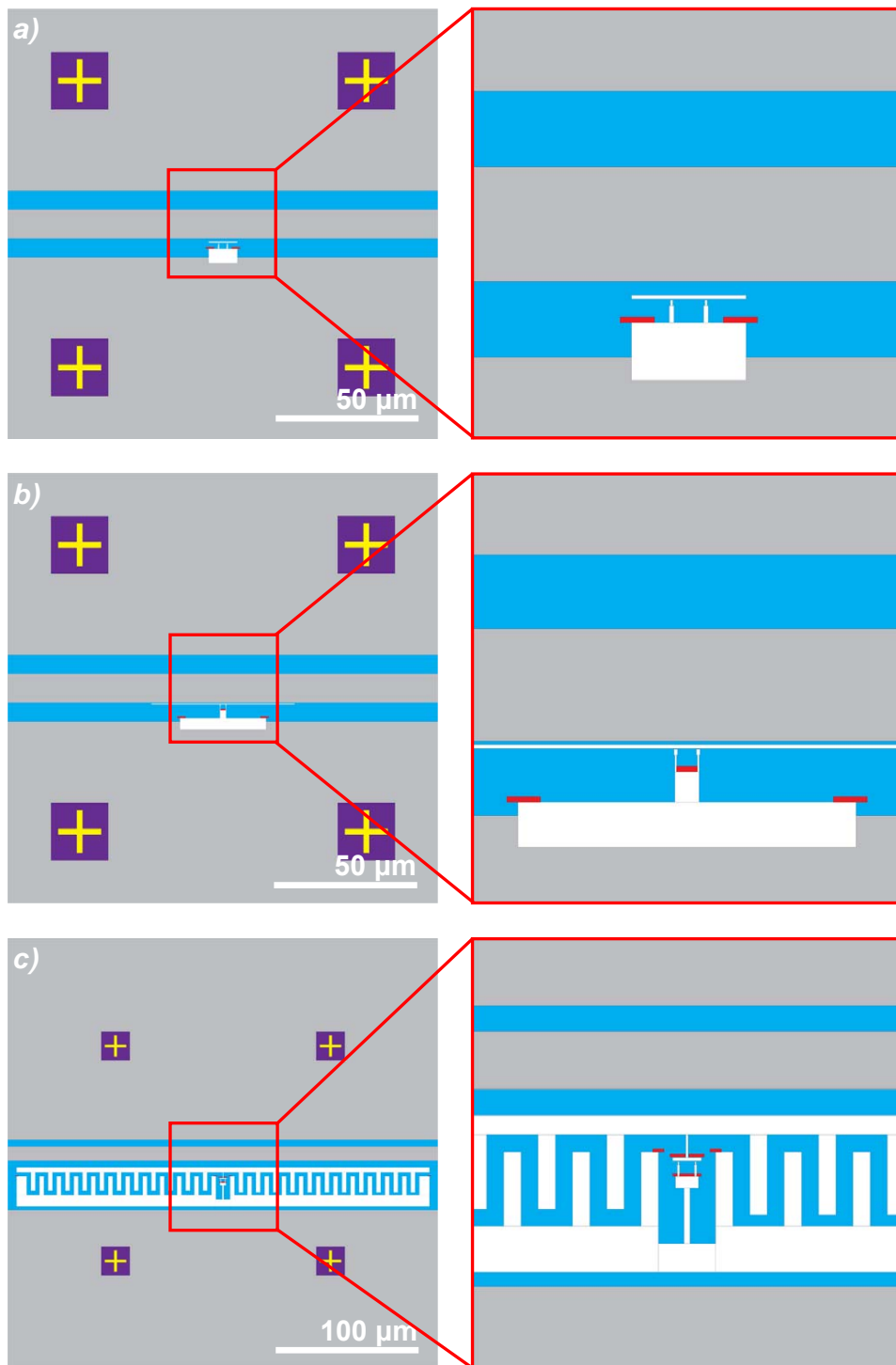


Figure 4.21: CAD designs of the three qubits shown in Fig. 4.20: Cooper pair box with 10 μm long island (a), Cooper pair box with 50 μm long island (b) and transmon type qubit (c).

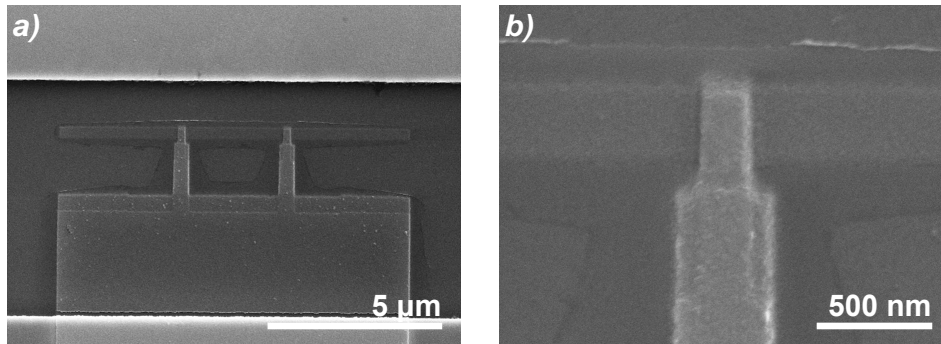


Figure 4.22: a) SEM image of a deposited Cooper pair box. The shadow structure of the island was deposited onto the steep resist side wall and removed during resist strip. b) SEM image of a single Josephson junction of the device shown in part a.

4.2.3 Electron Beam Lithography

In order to transfer the pattern of a nano-scale Josephson junction into a double layer resist structure, electron beam lithography is used. Before doing the actual exposure, the electron beam system has to be calibrated and the resist covered sample has to be aligned to the system coordinates. An electron beam lithography system basically is a combination of a SEM like electron optic and detection system as well as of a fast *pattern generator*. Electrons are generated either by thermionic or field emission sources and accelerated in an electric field through a set of electrostatic and magnetic lenses and apertures. A pattern generator is essentially a fast digital to analog converter, generating the drive currents for magnetic coils which deflect the electron beam. The digital information of the device pattern which gets converted and which is exposed into the resist is stored in a digital pattern file. The two dimensional exposure pattern, generated with a CAD program editor (see Fig. 4.21), is divided into pixels whose size can be chosen in a certain range and affects the resolution of the exposure. The electron beam of the system is focused onto, and scans pixel by pixel the resist surface. A *beam blanker* can rapidly blank the electron beam. In this way, a device pattern can be transferred into the resist by scanning over the resist and partially exposing it.

Electron beam resists are sensitive to deposited electric charge. Due to electron exposure, the resist molecules get split into smaller parts which are removed during development. The total charge Q_{ex} which is deposited onto the resist is given by

$$\begin{aligned} Q_{\text{ex}} &= D_{\text{ex}} A_{\text{ex}} \\ &= I_{\text{EB}} T_{\text{ex}}, \end{aligned} \quad (4.4)$$

where D_{ex} is the exposure dose, A_{ex} is the exposed area, I_{EB} is the electron beam current and T_{ex} is the exposure time. Typical exposure doses for the double layer resist system used within the scope of this thesis are in the order of 300 to 400 $\mu\text{C}/\text{cm}^2$. With a typical pixel size of 100 nm^2 and a typical beam current of 5 pA, the exposure time for a single pixel, which is also called *dwell time*, is in the order of 60 μs . In order to determine the correct exposure dose, the beam current is measured before exposure by focusing the beam into a Faraday cup and measuring the time integrated current.

The electron beam can be deflected with magnetic coils only within a maximum area of 1 $\text{mm} \times 1 \text{mm}$. In order to expose larger structures, the sample has to be exposed and repositioned successively in a process called *stitching*. Repositioning the sample is done by mounting it on a stage which can

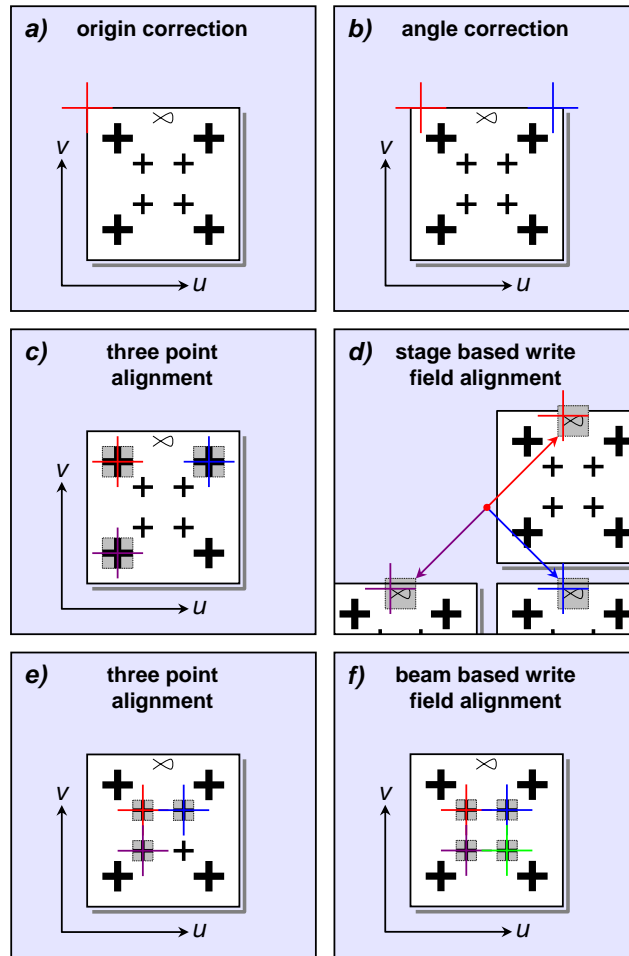


Figure 4.23: Alignment procedure when performing electron beam lithography in order to calibrate sample coordinates and beam optics. Single steps are explained in main text.

be precisely displaced with stepper motors. The stage position is controlled with a laser interferometer (the stage is therefore called *laser stage*) and can be determined with an accuracy of only a few nanometers.

Figure 4.23 shows schematically the procedure of a typical EBL session. First of all, the resist covered sample is mounted onto a sample holder and inserted into the electron beam writer *Raith 150*. Within the following steps, the sample coordinate system (u and v coordinates), which is initially undefined, has to be aligned to the fixed physical coordinate system of the machine (x and y coordinates). In order to be able to coarsely focus onto the resist surface (which is usually very smooth with no features on it), using tweezers, a little scratch is brought onto the resist (see fish-like structure in Fig. 4.23). The coordinate alignment is performed by scanning one edge of the chip which serves as reference. In order to coarsely align sample and machine coordinates (u, v) and (x, y), crosshairs are placed onto the detected reference position what is called *origin correction* (see Fig. 4.23a). Next, an *angle correction* is performed by scanning two positions at the edge of the rectangular chip and using the connection of these points as reference direction (see Fig. 4.23b). For improving the accuracy of the coordinate alignment, a *three point alignment* is performed on a set of predefined alignment markers (see Fig. 4.23c and yellow crosses in Fig. 4.21). Here, the stage subsequently positions each alignment mark, whose coordinates are coarsely known by the system due to the origin and angle correction performed before, under the scan field (see purple area in Fig. 4.21) and the actual position of each cross is detected. Using the detected coordinates

of the three alignment crosses, the coordinate system can be updated. When scanning reference positions on the resist covered wafer, one has always to make sure that the scanning area is small enough and located at an uncritical position since the scanned resist will also be partially exposed during the alignment procedure. When scanning for example the area between ground plane and center conductor of a resonator, metal, evaporated onto the developed resist can remain in the scanned area after stripping the resist and thus can cause an electrical short.

Beside the alignment of sample and machine coordinate system, also the beam itself, respectively the field geometry of the EBL system is calibrated. When using the so called *stage based write field alignment*, the same reference position on top of the sample is scanned from at least three different stage positions using three different beam deflections (see Fig. 4.23d). Here, the stage, which can be positioned very accurately, is used as a reference. The field geometry can now be calibrated by comparing the coordinates of the detected reference points to the nominal stage positions. A write field alignment is usually performed several times with increasing stage displacement and decreasing scan field size which leads to an increasing calibration accuracy.

Before continuing the alignment procedure, the beam is precisely focused onto the resist surface using the *contamination dot technique*. In this technique, the coarsely prefocused electron beam is concentrated onto the resist surface for a certain time. Residual gas molecules are cracked by incoming electrons and the cracked material becomes noticeable as a more or less circular dot with a diameter less than 100 nm. This dot can be used as reference point, lying in the focal plane. After fine focusing onto the resist surface, another three point alignment is performed on a second set of predefined alignment crosses (see Fig. 4.23e). In order to correct for a possible sample tilt, the electron beam is focused onto the resist surface using the contamination dot technique when doing the last three point alignment. This way, the z coordinates of the particular focal points at the three marker positions are determined which defines the focal plane of the resist surface. During exposure, the system automatically corrects the focus when scanning the electron beam over the surface what is known as *automatic focus correction*. The beam current is then measured in order to determine the correct dwell time for a given exposure dose and pixel size (see Eq. 4.4). Next, the inner alignment crosses are scanned in order to perform a final *beam based write field alignment* (see Fig. 4.23f). Here, the sampleholder stays at a fixed position while the scan field is subsequently moved to the positions of the marks by *deflecting the beam*. The mark positions are detected and the coordinate system is finally updated. Now, the stage is not moved any more and the exposure is started.

When performing electron beam lithography on poorly conducting substrates such as sapphire, deposited electrons can charge up the resist which leads to unwanted local beam deflections. In order to avoid these charging effects, a thin layer of typically 5 nm aluminum is evaporated onto the resist surface before exposure. The aluminum layer is chosen thin enough that electrons scatter only slightly at the aluminum layer when exposing the resist. In that case, also the clearing dose of the double layer resist does not change significantly. After having performed an electron beam exposure, the aluminum layer can be removed with sodiumhydroxide solution before continuing with the standard development procedure. Process sheets for performing electron beam lithography on silicon and sapphire substrates can also be found in appendix E.

4.2.4 Josephson Junction Parameter Control

In order to realize a *specific* circuit QED experiment, it is essential to fabricate circuit QED devices with sufficient accuracy, especially with sufficient control over Josephson and charging energy beside the general geometry which controls for example the cavity-qubit coupling strength g . The two

fundamental energies of a Josephson junction are defined as

$$E_{J0} = \frac{\Phi_0 I_c}{2\pi}, \quad (4.5)$$

$$E_{C0} = \frac{(2e)^2}{2C_J} \quad (4.6)$$

and depend both via

$$I_c = j_c A \quad (4.7)$$

$$j_c = -\frac{q_s \hbar \kappa_s}{2m_s} \sqrt{n_{s1} n_{s2}} \exp(-\kappa_s d) \quad (4.8)$$

$$C_J = \epsilon_0 \epsilon_r \frac{A}{d} \quad (4.9)$$

on the tunnel barrier thickness d and the junction area A (compare chapter 3). The junction area A is defined lithographically by varying the exposed resist area and also by varying the exposure dose. Within the scope of this thesis, junction areas ranging from $100 \times 100 \text{ nm}^2$ to $600 \times 1000 \text{ nm}^2$ were fabricated with an accuracy of less than 20 nm. The oxide barrier thickness d is controlled by adjusting the oxidation time and the partial oxygen pressure during oxidation.

In order to calibrate the process of aluminum oxidation, an *oxidation series* is performed, i.e. a set of test junctions with fixed junction area is fabricated under different oxidation conditions and its normal resistivity at room temperature is measured to extract the junction critical current I_c as explained in the following. Within the scope of this thesis, the aluminum bottom electrode in each case is oxidized for a different time but for fixed partial oxygen pressure. Since the final thickness d of the grown aluminum oxide depends on the *product*

$$\Pi_{\text{ox}} = t_{\text{ox}} p_{\text{ox}} \quad (4.10)$$

of oxidation time t_{ox} and oxygen partial pressure p_{ox} , also the pressure p_{ox} can be varied for fixed oxidation time t_{ox} as long as the oxide formation process does not saturate. The critical current of a Josephson junction can be determined by measuring the room temperature tunnel resistance R_n of the junction and using the Ambegaokar-Baratoff relation [Ambegaokar1963]

$$I_c = \frac{\pi \Delta(T)}{2e R_n} \tanh\left(\frac{\Delta(T)}{2k_B T}\right). \quad (4.11)$$

Here, Δ is the superconductor's energy gap and k_B is the Boltzmann constant (compare chapter 3). For $T \rightarrow 0$, Eq. (4.11) simplifies to

$$I_c = \frac{\pi \Delta(0)}{2e R_n}. \quad (4.12)$$

Combining Eqs. (4.5) and (4.12) finally leads to

$$E_{J0} = \frac{\Phi_0 \pi \Delta(0)}{2\pi \cdot 2e R_n}. \quad (4.13)$$

The critical temperature of a 200 nm thin aluminum film, deposited in the evaporator *Plassys* MEB550, has been determined as $T_c = 1.23 \text{ K}$. For $T \ll T_c$ the energy gap at zero temperature is

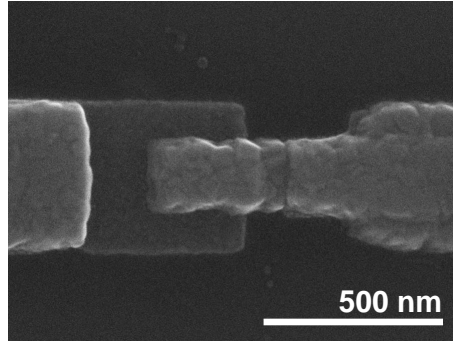


Figure 4.24: SEM image of a typical Josephson test junction, fabricated with electron beam lithography and shadow evaporation and used for oxidation test series. The size of the junction is about $200 \times 270 \text{ nm}^2$.

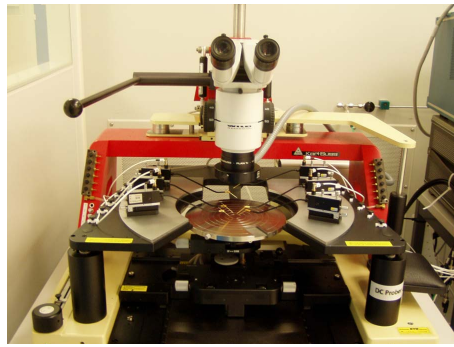


Figure 4.25: DC-Prober *Suess* PM8 used for measuring the room temperature resistance of Josephson test junctions.

given by [Poole1995]

$$\begin{aligned} E_g(0) &= 2\Delta(0) \\ &\approx 3.528 k_B T_c, \end{aligned} \quad (4.14)$$

and an energy gap $2\Delta(0) = 0.374 \text{ meV}$ is found for the deposited aluminum.

A number of test Josephson junctions of size $200 \times 270 \text{ nm}^2$ are fabricated for a fixed oxygen partial pressure of 1 Torr for oxidation times varying between ten seconds and fifteen minutes. Figure 4.24 shows the SEM image of such a test junction.

When performing the junction oxidation, a mixture of 15 % oxygen and 85 % argon is used instead of pure oxygen since due to the smaller oxygen partial pressure longer oxidation times can be chosen when aiming at a certain Josephson current density. This in turn leads to a better accuracy of the oxidation procedure since for example variable gas inlet and gas pump down times lead to smaller relative errors. Further, pure oxygen cannot be used when using oil lubricated vacuum pumps because of the danger of explosion.

All Josephson test junctions have been measured at room temperature six days after fabrication using the DC-prober *Suess* PM8 shown in Fig. 4.25 and the semiconductor characterization system *Keithly* 4200. Figure 4.26 depicts the resistance area product Π_{RA} of measured junction resistance R_n and junction area A in dependence on Π_{ox} , the product of oxygen partial pressure p_{ox} and oxidation time t_{ox} . Each data point represents the mean value of twenty measurements performed on different junctions, which are fabricated on the same chip and nominally identical. The curve in Fig. 4.26 clearly saturates for large values of Π_{ox} . Saturation occurs since the growing oxide layer

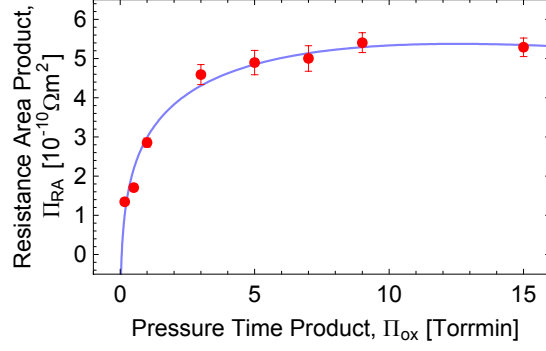


Figure 4.26: Measured resistance area product Π_{RA} of Josephson test junctions which were fabricated for different products Π_{ox} of oxidation time and oxygen partial pressure. The blue line is a fit to the data using the empirical fit function Eq. (4.15). The red error bars indicate the root mean square deviation from the mean value.

passivates the aluminum surface what hinders oxygen molecules to access and further oxidize the aluminum surface. The measured data shown in 4.26 is approximated by the empirical fit function

$$\Pi_{RA}[10^{-10}\Omega m^2] = a + b(\Pi_{ox}[\text{Torrmin}]) + c(\Pi_{ox}[\text{Torrmin}])^{1/6} \quad (4.15)$$

when using the parameters $a = -5.073$, $b = -0.1667$ and $c = 8.226$. The fit function (4.15) here serves as calibration function within the range of the measured data and is not chosen with view to an underlying microscopic model describing the oxidation process. Within the calibration range, the function given in Eq. (4.15) can be used together with Eq. (4.13) to adjust the pressure time product Π_{ox} when aiming at a Josephson junction with a certain Josephson energy. A typical Josephson junction of size $200 \times 270 \text{ nm}^2$ whose oxide barrier was grown in 1 Torr oxygen partial pressure for 5 minutes has a normal state resistance six days after fabrication of about $R_n = 8.8 \text{ k}\Omega$ what corresponds to a Josephson energy of about $E_{J0} = h \cdot 15 \text{ GHz}$.

When choosing a certain oxidation condition for fabricating a Josephson junction, one has to consider junction aging and thus variations of E_{J0} respectively R_n with time. Humidity and oxygen in the air can post oxidize the junction aluminum when storing Josephson junction devices in ambient conditions. Referring to process and design conditions adopted within the scope of this thesis, the initial junction resistance doubles within the first two weeks. The room temperature resistance of the same Josephson test junctions was measured at different times t_a after fabrication. Figure 4.27 shows the resistance area product Π_{RA} for a different time t_a after fabrication. The measured data was fitted with the empirical fit function

$$\Pi_{RA}[10^{-10}\Omega m^2] = d + e(t_a[d]) + f(t_a[d])^{1/6} \quad (4.16)$$

using the parameters $d = -0.1343$, $e = -0.03277$ and $f = 4.090$. Also here, the fit function (4.16) serves as calibration function within the range of the measured data and is not chosen with view to an underlying microscopic model describing the post-oxidation process. The resistance area product of the Josephson test junctions increases by more than 80% within the first week after fabrication and doubles within the first two weeks after fabrication where it finally saturates. After two weeks, the resistance area product of the fabricated test junctions can be controlled with about 10% accuracy. In order to provide Josephson junction devices with defined Josephson energy, the doubling of the resistance has to be taken into account. The junctions should age for at least one week before the device is taken under vacuum for example during the cool down in

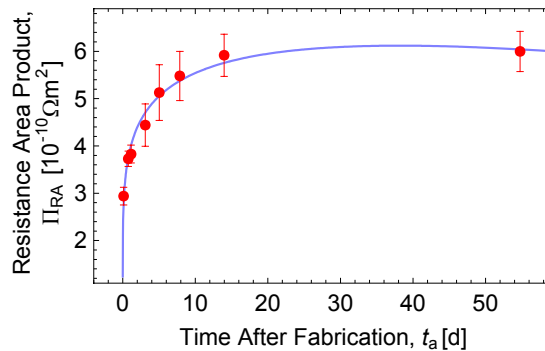


Figure 4.27: Measured resistance area product Π_{RA} of Josephson test junctions at different time t_a after fabrication. Each data point represents the mean value of twenty measurements performed on different junctions, which are fabricated on the same chip and nominally identical. The blue line shows a fit to the data using the empirical fit function given in Eq. (4.16). The red error bars indicate the root mean square deviation from the mean value.

a dilution refrigerator what would interrupt the postoxidation process, before measurement. A detailed description of the evaporation process and oxidation can be found in appendices F and G. The procedure for probing Josephson junctions at room temperature using the DC-prober *Suess* PM8 and the semiconductor characterization system *Keithly* 4200 can be found in appendix I.

4.2.5 Junction Deposition and Process Monitoring

The process conditions during Josephson junction fabrication directly influence the electrical parameters of the device and therefore have to be constantly monitored. In order to reliably fabricate well defined Josephson junction devices it is necessary to recalibrate and to readjust processes once in a while. Figure 4.28 shows a number of important process parameters, automatically tracked during junction deposition using the electron beam evaporator *Plassys* MEB550. Here, p_{LL} is the pressure in the load lock of the evaporator and p_{CH} is the pressure in its main chamber. Furthermore, r_{Al} denotes the aluminum evaporation rate and I_{Em} the emission current of the electron beam source. After loading the sample, the load lock is pumped down first with a rough pump and then with a turbo pump. The transfer valve between load lock and main vacuum chamber is opened and the main chamber is further pumped with a cryogenic pump. The electron beam source is switched on and the emission rate is increased. Having reached a constant evaporation rate, the source shutter is opened in order to perform the first deposition. After having finished the evaporation, the emission current is reduced, the electron beam source is switched off and the transfer valve between load lock and main chamber is closed. The inlet for the argon/oxygen gas is opened until the pressure for oxidation is established. The oxidation of the first aluminum layer is then performed before the load lock is pumped down again and the transfer valve is opened. The electron beam source is switched on again, the deposition rate is increased and the source shutter is opened. Having stabilized the emission rate and having finalized the second evaporation, the emission rate is lowered down and finally the electron beam source is switched off. The inlet for pure oxygen is opened until the pressure for the second oxidation is established. This additional oxidation is performed in order to begin and accelerate the post-oxidation process of the deposited Josephson junction in a defined oxygen atmosphere. After having finished the second oxidation, the load lock is vented and the sample is unloaded.

When fabricating Josephson junction devices which will be used for circuit QED experiments and

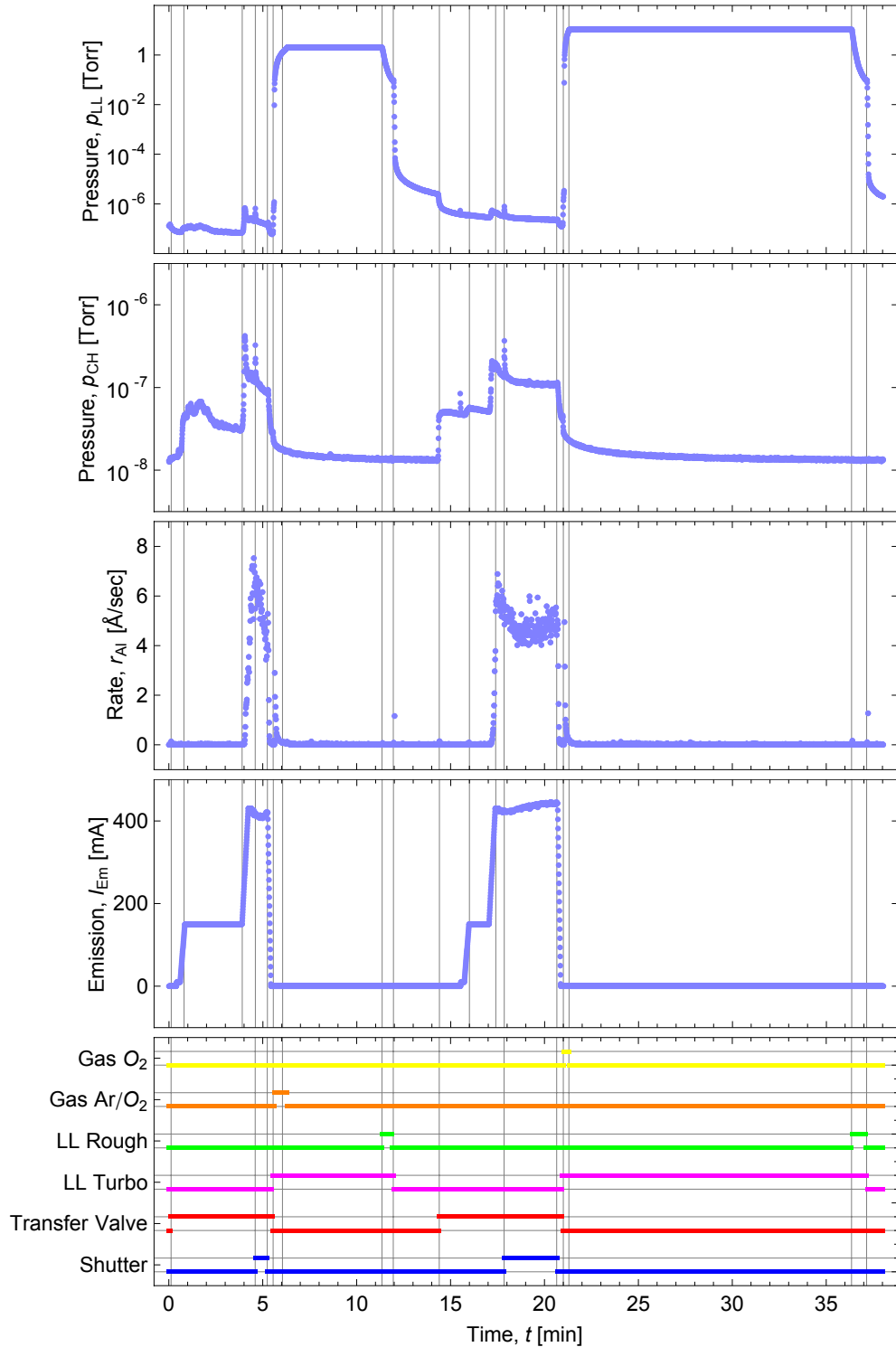


Figure 4.28: Load lock pressure, main chamber pressure, aluminum deposition rate and electron emission current are tracked in dependence on time for a typical tunnel junction deposition process using the electron beam evaporator *Plassys* MEB550. Also shown are digital control signals for the oxygen inlet valve, the oxygen/argon inlet valve, for the load lock rough pump, the load lock turbo pump, the transfer valve between load lock and main chamber and finally for the source shutter. A *high* signal represents an open state for gas inlets, valves and the source shutter, a *low* signal represents a closed state. For rough and turbo pump, a *high* signal represents an on state, whereas a *low* signal represents an off state.

which cannot be electrically accessed directly for probing, it is advisable to fabricate monitor samples in the same deposition process. These samples should then be characterized independently in order to check the process quality.

4.2.6 Integration of Multiple Process Steps for Circuit QED Device Fabrication

The overall process for fabricating circuit QED devices described above consists of two separate parts - the etching or deposition of a resonator structure defined with optical lithography and the deposition of Josephson junction devices which are patterned using electron beam lithography. A set of resonators is simultaneously made on a two inch wafer which is diced into $2 \times 7 \text{ mm}^2$ large chips after fabrication. Electron beam lithography and shadow evaporation is then performed on individual chips each carrying a single resonator structure. In the following, some important aspects of the integration of both processes in order to realize complete circuit QED devices are discussed. Finally, the mounting of the finished chips into high frequency sampleholders is explained.

When designing optical masks for resonator structures used for qubit integration, appropriate alignment marks for performing electron beam lithography have to be integrated into the design. Such alignment crosses, see Fig. 4.21, are typically $15 \times 15 \mu\text{m}$ large and $2 \mu\text{m}$ thick, reliable to fabricate with optical lithography. Since the region around an alignment mark is electron beam exposed during the lithography alignment procedure, the marks should not be placed too close to resonator gap or other critical regions which are sensitive to short circuits after a subsequent metal deposition. The minimal spacing between critical regions and markers is typically in the order of 30 to $50 \mu\text{m}$. Furthermore, alignment crosses should be chosen with standardized shape and standardized spacing to the resonator gaps when designing different resonators in order to avoid alignment errors due to wrongly assumed marker coordinates.

When scanning alignment marks during an electron beam lithography procedure, one has to consider that different materials used for the resonator metalization can exhibit a different detection contrast what makes the process of marker recognition more or less difficult. Here, the alignment procedure is easier to perform on a niobium than on an aluminum resonator metalization. In this context, a coarse set of alignment crosses in addition to a fine one can help a lot during the alignment procedure.

The resist process for performing shadow evaporation was developed on plain silicon or sapphire substrates with no metalization on top. When applying the resist process to $2 \times 7 \text{ mm}^2$ large chips which carry a predefined resonator metalization, resist thicknesses can vary slightly compared to the thicknesses on a plain substrate. Furthermore, the exposure dose can change slightly for example due to varying resist thicknesses. In order to properly define the device structure, it is advisable to perform an additional dose test on a resonator structure where the exposure dose varies within a range of about $\pm 10\%$ with respect to the mean exposure dose before doing the actual sample.

In certain cases, several shadow evaporations have to be performed on the same chip, for example when realizing a tunable SQUID resonator with integrated qubit. Here, evaporation angles, evaporation directions or oxidation conditions can vary for SQUID and qubit fabrication. In order to realize two shadow evaporations on the same chip, one can subsequently define one resist structure for one shadow evaporation within two individual process steps. However, it is also possible to define a single resist structure carrying the pattern of SQUID and qubit and to perform the two evaporations subsequently using an additional coarse mechanical mask covering the appropriate pattern. Such a mask which can be realized for example by a piece of aluminum foil covers the

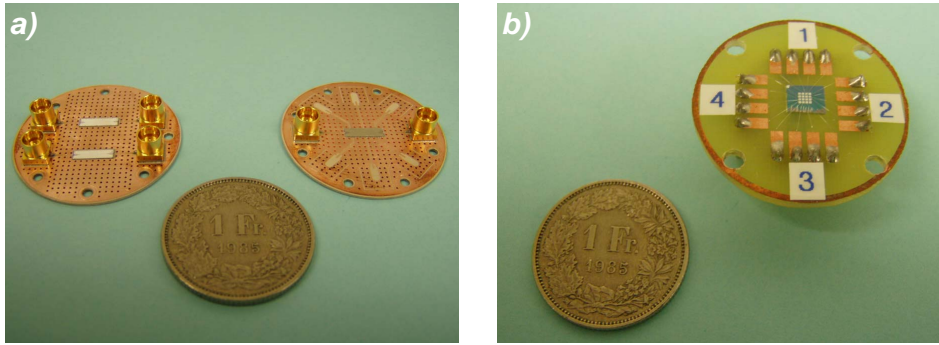


Figure 4.29: a) Circuit QED devices which are mounted onto a high frequency sampleholder. b) Sampleholder used for DC characterizations of Josephson junction devices.



Figure 4.30: Wire bonder *West Bond 747677E* used for device contacting.

qubit resist structure during SQUID deposition and covers the SQUID resist structure during qubit deposition. This way, individual shadow evaporations with different parameters can be performed within a single electron beam lithography step.

The finished circuit QED device is ready to be mounted on a high frequency sampleholder. Figure 4.29a shows the picture of mounted devices. The sampleholder consists of a printed circuit board (PCB) with a high permittivity dielectric ($\epsilon \approx 10$) and a double sided copper metalization. The printed circuit board carries two or several coplanar waveguides in order to high frequency access the mounted device. Vias between top and bottom ground planes improve the microwave frequency properties. Surface mounted microwave connectors are soldered onto the printed circuit board and are connected to coaxial microwave lines. The silicon or sapphire chip is glued with a small amount of PMMA resist into the sampleholder and is properly aligned under a microscope. After the PMMA resist has dried, center conductors and ground planes of the coplanar waveguides on the chip are connected to those on top of the printed circuit board by using the wire bonder *West Bond 747677E* shown in Fig. 4.30. Figure 4.31 shows the optical microscope image of a $2 \times 7 \text{ mm}^2$ large chip mounted on a high frequency sampleholder.

For DC measurements of single Josephson junctions or SQUIDs at low temperatures, the chip which carries the devices is just glued with PMMA resist onto a piece of standard printed circuit board prepared with copper pads. The junctions are contacted with wire bonds to the copper pads on the board. Since the Josephson junctions are directly connected to the bonding tool during the bonding procedure and since they are very sensitive to electrostatic discharge, one has to make sure that bonder as well as the operator are properly grounded. Figure 4.29b shows such a sampleholder with a mounted silicon chip.

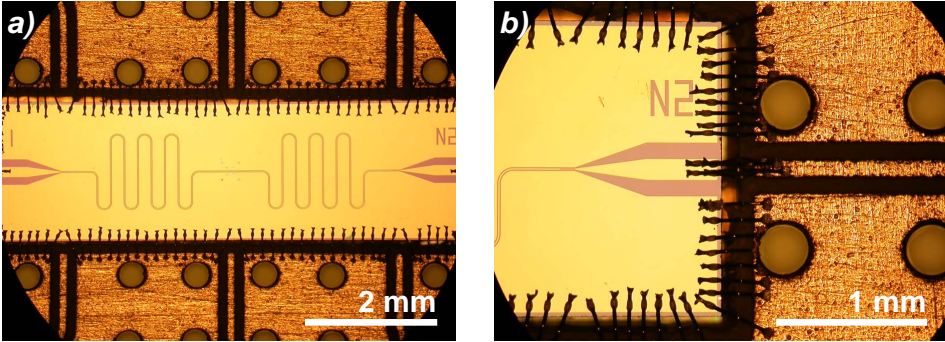


Figure 4.31: a) Optical microscope image of a fabricated chip mounted on a high frequency sampleholder and connected to input/output transmission lines and ground planes with wire bonds. b) Enlarged view of input/output transmission lines and vias of printed circuit board.

5 Circuit Quantum Electrodynamics Experiments

The field of *cavity quantum electrodynamics* (cavity QED) studies the coupling, in particular the *strong coupling* of atoms to cavity modes. This way, the interaction of matter and light can be tested on the level of single quanta.

Recently, strong coupling of an (artificial) atom to a cavity was also realized in superconducting electrical circuits which initiated the new field of *circuit quantum electrodynamics*. Such systems, which exchange microwave instead of optical photons, reach higher relative coupling strengths compared to traditional cavity QED systems and can be easily scaled up. Further, they have the advantage that the coupling can be engineered by lithographically defining the shape and size and therefore the electrical dipole moment of the artificial atom.

Cavity QED and circuit QED can be described equivalently by the same fundamental relations which are presented in the following chapter. The principles of qubit manipulation and qubit readout are explained and circuit QED characterizations done within the scope of this thesis, in particular studies on the qubit-qubit interaction via the exchange of virtual photons, are presented.

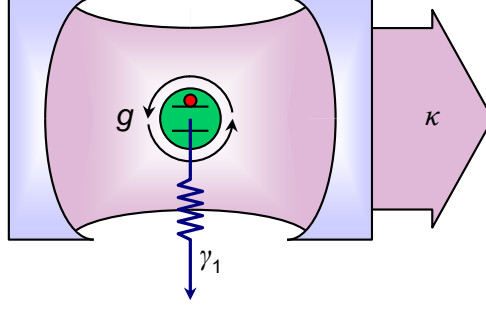


Figure 5.1: Standard representation of a cavity QED system. An atom is coupled with strength g via dipole interaction to a single mode radiation field. The excited atom state decays at a rate γ_1 and the cavity field decays at a rate κ .

5.1 Jaynes-Cummings Interaction and Cavity-Atom Coupling

In its simplest version, a cavity QED system consists of a cavity, realized for example by a set of two mirrors, and an atom placed inside, see Fig. 5.1. The atom can couple to the electromagnetic field inside the cavity via electromagnetic dipole interaction. Photons inside the cavity, which describe discrete cavity field excitations, are confined and bounce back and forth between the two mirrors. This way, photons pass the atom numerous times before they get lost due to imperfect mirrors what leads to a high interaction probability in such systems.

The dynamics of the coherent interaction between cavity field and atom is described by the Jaynes-Cummings Hamiltonian [Jaynes1963]

$$\hat{H}_{\text{JC}} = \hbar\omega_r \left(\hat{a}^\dagger \hat{a} + \frac{1}{2} \right) + \frac{1}{2} \hbar\omega_a \hat{\sigma}^z + \hbar g (\hat{a}^\dagger \hat{\sigma}^- + \hat{a} \hat{\sigma}^+). \quad (5.1)$$

Here, ω_r is the cavity resonance frequency and \hat{a}^\dagger , \hat{a} are photon creation and photon annihilation operators. Furthermore, ω_a is the atom transition frequency, $\hat{\sigma}^z = (|\uparrow\rangle\langle\uparrow| - |\downarrow\rangle\langle\downarrow|)$ is the Pauli z -operator with $|\downarrow\rangle$ and $|\uparrow\rangle$ referring to the ground and excited state of the atom and $\hat{\sigma}^- = |\downarrow\rangle\langle\uparrow|$ and $\hat{\sigma}^+ = |\uparrow\rangle\langle\downarrow|$ are atomic lowering and raising operators describing the transition from excited to ground state and from ground to excited state, respectively. The first term in Eq. (5.1) denotes the energy of the electromagnetic field, where $\hbar\omega_r/2$ describes zero point fluctuations. The second term describes the energy of the atom which is considered as effective two level system. The third term finally denotes the electromagnetic dipole interaction by which the atom can exchange a photon with the cavity field at rate $g/2\pi$, where g is in general defined as $g = \mathbf{d} \cdot \mathbf{E}/\hbar$ with the atom's dipole moment \mathbf{d} and the electric field strength \mathbf{E} .

Beside the coherent atom cavity interaction, decoherence occurs in real systems. As already indicated, the cavity field couples to the continuum and decays at a rate $\kappa = \omega_r/Q$, where Q is the cavity's quality factor. Also the atom usually couples to external degrees of freedom such as resonant electromagnetic fields thus leading beside spontaneous emission to the decay of an excited atom state at the energy decay rate γ_1 .

The cavity QED system schematically depicted in Fig. 5.1 and described by Eq. (5.1) is equivalent to the circuit QED implementation schematically shown in Fig. 5.2. A qubit, here in form of a Cooper pair box, is placed into the center of a coplanar waveguide resonator and couples via its superconducting island capacitively to the waveguide's center conductor [Blais2007]. The center conductor is coupled via finger or gap capacitors, which are equivalent to the mirrors of a cavity QED system, to input and output transmission lines. The coupling between qubit and resonator

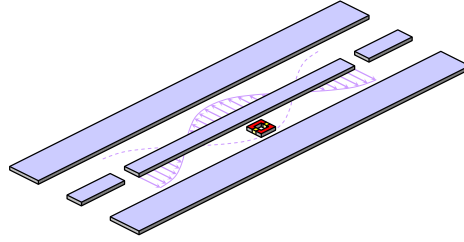


Figure 5.2: Standard representation of a circuit QED system. A superconducting qubit is regarded as artificial atom and integrated into a coplanar waveguide resonator which plays the role of the cavity. The gaps in the waveguide's center conductor act as mirrors for the cavity field.

can be derived when considering the quantum voltage operator

$$\hat{V} = \sqrt{\frac{\hbar\omega_r}{2C}} (\hat{a} + \hat{a}^\dagger), \quad (5.2)$$

where C is the capacitance of the LCR oscillator equivalent to the transmission line resonator of the circuit QED system, compare chapter 2. The quantum voltage $V = Q_{\text{el}}/C$ results from the cavity field and couples to the qubit with a strength determined by C as well as by the gate capacitance C_g and C_Σ . Here, $C_\Sigma = C_g + C_J + C + C_s$ holds, where C_J is the capacitance of the two Josephson junctions and C_s denotes a stray capacitance. The number of Cooper pairs induced by the gate voltage is given by $N_g = V_g C_g / (2e)$ and has to be replaced by $(V_g + V)C_g / (2e)$ due to the additional quantum voltage V . This replacement leads to an additional term (a constant energy offset is here omitted)

$$\hat{H}_{\text{coup}} = 2\hbar g (\hat{a}^\dagger + \hat{a}) \hat{N} \quad (5.3)$$

in the CPB Hamiltonian $E_{C0} (\hat{N} - N_g)^2 + E_{J0} (1 - \cos \hat{\phi})$, derived in chapter 3. The coupling Hamiltonian written in Eq. (5.3) depends on the qubit state as well as on the cavity field. The coupling strength g is further defined as

$$g = \frac{e}{\hbar} \frac{C_g}{C_\Sigma} \sqrt{\frac{\hbar\omega_r}{2C}}. \quad (5.4)$$

At the degeneracy point $N_g = 1/2$, the number operator of the Cooper pairs on the island can be written as $\hat{N} = \hat{\sigma}_x / 2$ and a *rotating wave approximation* can be applied on Eq. (5.3). The approximation neglects the fast oscillating terms $\hat{a}^\dagger \hat{\sigma}^+$ and $\hat{a} \hat{\sigma}^-$ which finally leads to

$$\hat{H}_{\text{coup}} = \hbar g (\hat{a}^\dagger \hat{\sigma}^- + \hat{a} \hat{\sigma}^+), \quad (5.5)$$

the coupling part of the Jaynes-Cummings Hamiltonian stated in Eq. (5.1).

5.2 Strong Coupling Regime and Vacuum Rabi Splitting

The strong coupling regime is achieved when the coupling strength g is large compared to both, the cavity decay rate κ and the energy relaxation rate γ_1 . For zero detuning $\Delta = \omega_a - \omega_r = 0$ between qubit transition and cavity resonance frequency and vanishing coupling strength g , cavity and atom states are degenerate. In case of zero detuning and finite coupling strengths g however, photon number states $|n\rangle$ and atom ground respectively excited state $|\downarrow\rangle, |\uparrow\rangle$ split up into a symmetric and an antisymmetric superposition $(|\downarrow\rangle |n+1\rangle + |\uparrow\rangle |n\rangle) / \sqrt{2}$ and $(|\downarrow\rangle |n+1\rangle - |\uparrow\rangle |n\rangle) / \sqrt{2}$. The

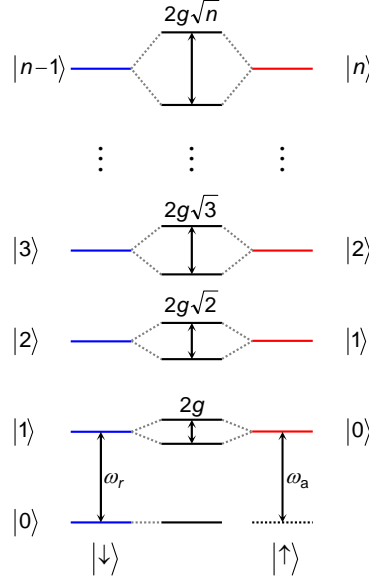


Figure 5.3: Energy states for a qubit in the ground ($|\downarrow\rangle$) and excited state ($|\uparrow\rangle$) and n photons populating the cavity. Blue lines indicate the undressed cavity frequencies and red lines the frequencies of the coupled cavity-qubit states. For zero detuning ($\Delta = 0$), the degenerate states split by $2g\sqrt{n}$.

finite coupling leads to an energy splitting $2g\hbar\sqrt{n}$, see Fig. 5.3. Photon number states and atom ground and excited states are no longer eigenstates of the Hamiltonian (5.1). The atom-cavity superposition state is maximally entangled. The coupling between them is described by the coherent exchange of a *single* photon ($\hat{a}^\dagger\hat{\sigma}^- + \hat{a}\hat{\sigma}^+$), compare Eq. (5.1). The system coherently oscillates with the vacuum Rabi frequency $2g\sqrt{n}$ between the two states $|\uparrow\rangle|0\rangle$ and $|\downarrow\rangle|1\rangle$ with an initially excited atom in a cavity populated with zero photons and a ground state atom in a cavity populated with one photon. The process is called *vacuum Rabi oscillation* [Johansson2006]. In case of $g \gg \kappa, \gamma_1$, a cavity QED system is said to be in the *strong coupling limit* [Wallraff2004] and several Rabi oscillations can occur before a photon inside the cavity decays.

High coupling strengths g in circuit QED systems can be realized by using coplanar waveguide cavities having large electric field strengths \mathbf{E} and by using artificial atoms with large electric dipole moments \mathbf{d} .

Figure 5.4a shows the measurement of a vacuum Rabi mode splitting in a circuit QED system consisting of a single transmon type qubit integrated into a coplanar waveguide resonator. The sample was fabricated within the scope of this thesis, compare sample parameters of transmon device F in appendix A, and was designed for the experiment presented in [Fink2008]. The transition frequency of the qubit $\omega_a \approx \omega_a^{\max} \sqrt{|\cos(\pi\Phi/\Phi_0)|}$ is magnetic flux tuned through the frequency ω_r of the resonator. By applying a probe signal of variable frequency f_{RF} and measuring the transmission spectrum of the cavity, the two superposition states of the system can be detected as cavity resonance peaks. The frequency difference of upper and lower frequency cavity-qubit state is minimal at the degeneracy point and equals $2g/2\pi$ there. A cut of data shown in Fig. 5.4a is shown in Fig. 5.4b for a magnetic flux chosen that the system is tuned close to degeneracy. A coupling strength $g/2\pi = 154$ MHz is extracted from the detected spectroscopy response signal.

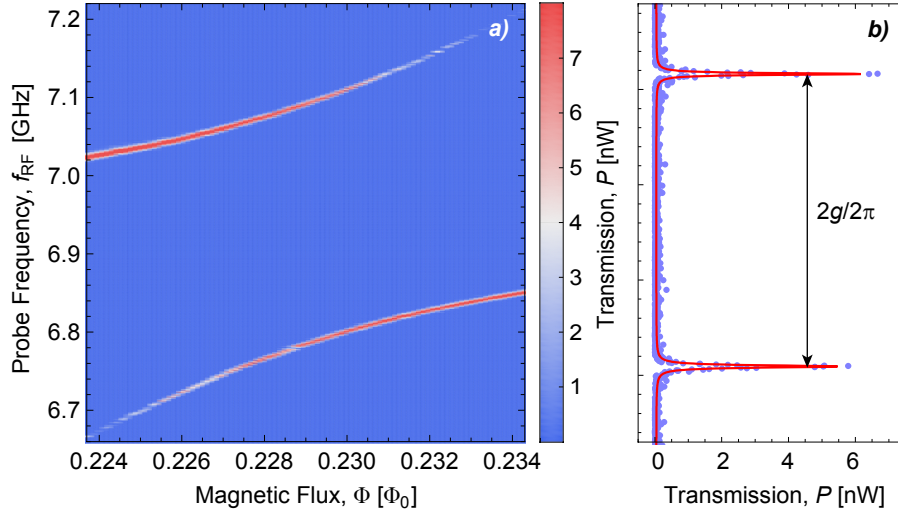


Figure 5.4: a) Measured resonator transmission spectrum versus applied magnetic flux. b) Single frequency-transmission slice of the data shown in part a for a flux which tunes the qubit frequency close to degeneracy. The data (blue) is here fitted (red) with two Lorentzian lines. At degeneracy, both response peaks have the same amplitude.

5.3 Dispersive Limit and Qubit Readout

When regarding the strong coupling regime, one can distinguish two separate limits in dependence on the detuning Δ between cavity and qubit. The system is said to be in the *resonant limit* for $\Delta \rightarrow 0$, as discussed in the previous section. In this case, cavity and qubit are maximally entangled and a vacuum Rabi mode splitting occurs. For $\Delta \gg g$, the system is said to be in the *dispersive regime* where qubit and cavity states no longer split up in superposition states by direct photon exchange. However, dispersive cavity-qubit interactions are observed in form of frequency shifts. In order to describe a circuit QED system in the dispersive regime, the Jaynes-Cummings Hamiltonian (5.1) is transformed as $\hat{U}\hat{H}_{JC}\hat{U}^\dagger$ with

$$\hat{U} = \exp \left[\frac{g}{\Delta} (\hat{a}\hat{\sigma}^+ - \hat{a}^\dagger\hat{\sigma}^-) \right]. \quad (5.6)$$

Expanding the transformed Hamiltonian in g^2/Δ leads to

$$\hat{H}_{DL} \approx \hbar \left(\omega_r + \frac{g^2}{\Delta} \hat{\sigma}^z \right) \hat{a}^\dagger \hat{a} + \frac{\hbar}{2} \left(\omega_a + \frac{g^2}{\Delta} \right) \hat{\sigma}^z. \quad (5.7)$$

For positive detunings Δ , the dispersive atom-cavity interaction shifts the cavity resonance frequency by the amount g^2/Δ in the positive or negative direction, depending on the state of the qubit, see Fig. 5.5. The first term in Eq. (5.7) the Hamiltonian of a harmonic oscillator with resonance frequency

$$\tilde{\omega}_r = \omega_r \pm g^2/\Delta, \quad (5.8)$$

which depends on the qubit state, where ω_r is the bare resonance frequency of the cavity.

The frequency shift denoted in Eq. (5.8) allows for performing a *quantum non demolition* (QND) measurement [Lupascu2007] where the qubit is measured by projecting but not destroying its state. Here, a repeated measurement on the qubit state will give the same result. As pointed out in chapter 2, a coplanar waveguide resonator can be described as a parallel LCR oscillator which

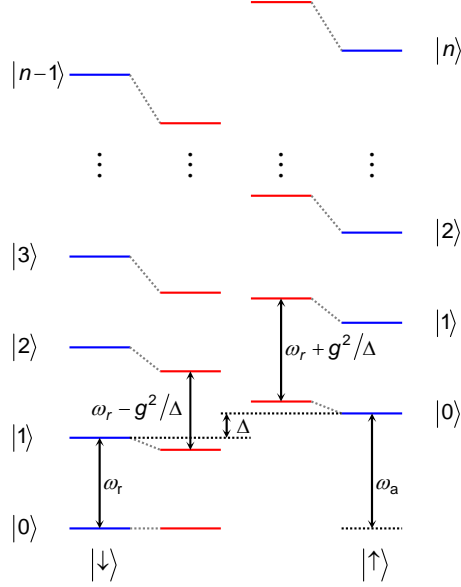


Figure 5.5: In the dispersive limit, cavity modes are shifted in dependence on the qubit state. Blue lines indicate the undressed and red lines the shifted cavity frequencies. A qubit being in its ground state decreases the cavity resonance frequencies by g^2/Δ . A qubit being in its excited state increases the cavity resonance frequencies by g^2/Δ . The levels are shifted by g^2/Δ independent on the mode number n .

has a Lorentzian shaped transmission power spectrum

$$P(\omega) = P_0 \frac{\delta\omega^2}{(\omega - \tilde{\omega}_r)^2 + \delta\omega^2} \quad (5.9)$$

around resonance when driven with microwaves of frequency ω , see Fig. 5.6a. Here, $\tilde{\omega}_r$ is the cavity's effective resonance frequency and $\delta\omega$ is the half width of the Lorentzian line at half of the maximum transmitted power P_0 . When no qubit sits inside the cavity, the Lorentzian shaped transmission spectrum is centered around the bare resonance frequency ω_r . If there is a qubit inside the cavity, the cavity transmission spectrum is shifted to a higher, respectively lower frequency $\tilde{\omega}_r$ by an amount of g^2/Δ when the qubit is in its ground, respectively excited state. When now applying a microwave signal with frequency $\omega_r + g^2/\Delta$, the resonator transmission is low for the qubit being in its ground state and high when the qubit is in its excited state. Likewise when applying a microwave signal with frequency $\omega_r - g^2/\Delta$, the resonator transmission is high for a relaxed qubit and low for an excited qubit. In order to maximize the measurement contrast when determining the qubit state *amplitude sensitive* like described above, the frequency of the microwaves has to be chosen close to $\omega_r \pm g^2/\Delta$, see Fig. 5.6a. The method of *dispersive readout* [Wallraff2005] described above works fine as long as the line width of the Lorentzian shaped transmission peak is on the order of the dispersive shift, $g^2/\Delta > \kappa$.

Beside the amplitude signal also the phase of transmitted microwaves can be detected in order to measure the qubit state. Figure 5.6b shows the frequency dependent phase shift of microwaves transmitted through a transmission line resonator. The acquired phase shift of microwaves transmitted through a parallel LCR oscillator is given by

$$\phi(\omega) = \arctan\left(\frac{\omega - \tilde{\omega}_r}{\delta\omega}\right). \quad (5.10)$$

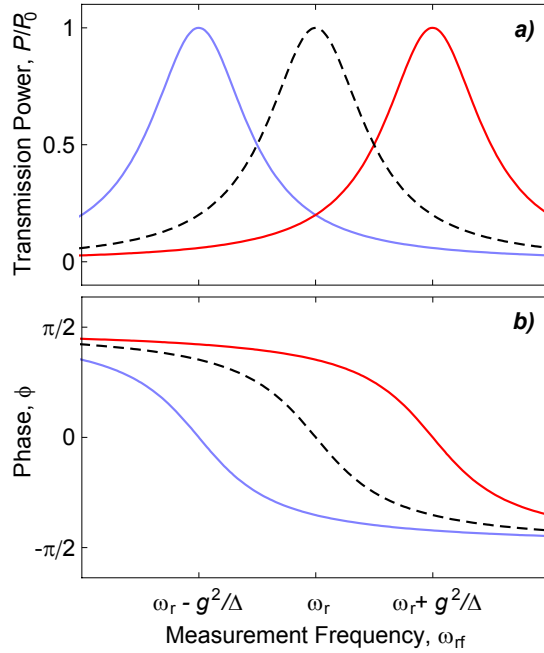


Figure 5.6: a) Transmission power spectrum of a coplanar waveguide resonator with resonance frequency ω_r (black dashed line). The transmission spectrum of an equal resonator with qubit in its ground state (blue solid line) or in its excited state (red solid line). b) Frequency dependent phase shift of a transmitted microwave signal for the case that there is no qubit inside the coplanar waveguide resonator (black dashed line) and for the case that there is a qubit inside being in its ground (blue solid line) or excited state (red solid line).

Off-resonant photons for which $|\omega - \tilde{\omega}_r| \gg 0$ holds, exhibit a phase shift ϕ close to $\pm\pi/2$. Near-resonant photons for which $\omega \approx \tilde{\omega}_r$ holds, have a vanishing phase shift $\phi = 0$. The phase shift spectrum shown in Fig. 5.6b is shifted by g^2/Δ to lower frequencies when the qubit is in its ground state and to higher frequencies when the qubit is in its excited state. The qubit state can be measured *phase sensitive*, when the frequency of the transmitted microwaves is chosen close to the bare resonance ω_r of the transmission line resonator. Here, the measurement contrast between ground state and excited state phase signal is high, see Fig. 5.6b.

In order to illustrate the influence of the cavity field on the qubit state in the dispersive limit, the Hamiltonian (5.7) can be rewritten as

$$\hat{H}_{\text{DL}} \approx \hbar\omega_r \hat{a}^\dagger \hat{a} + \frac{\hbar}{2} \left(\omega_a + \frac{2g^2}{\Delta} \hat{a}^\dagger \hat{a} + \frac{g^2}{\Delta} \right) \hat{\sigma}_z. \quad (5.11)$$

For positive detuning Δ , the qubit transition frequency is increased by the photon number dependent *AC-Stark shift* [Schuster2005] $2g^2 \hat{a}^\dagger \hat{a} / \Delta$ as well as by the constant *Lamb shift* [Lamb1947] g^2 / Δ . The AC-Stark shift can be used to determine the photon number $n = \hat{a}^\dagger \hat{a}$ inside a cavity by measuring the qubit transition frequency $\tilde{\omega}_a$.

5.4 Continuous and Pulsed Qubit Spectroscopy

The dispersive readout of a qubit integrated into a transmission line cavity discussed in the last section forms the basis for the spectroscopic determination of the qubit transition frequency ω_a . Within this concept, a spectroscopy signal with variable frequency ω_{spec} is applied to the trans-

mission line during dispersively measuring the qubit state, as discussed in the following.

When the qubit is initially in its ground state, the transmission amplitude of an applied measurement signal with frequency $\omega_{\text{rf}} = \omega_{\text{r}} + g^2/\Delta$ is low. When applying a constant spectroscopy signal with frequency ω_{spec} in addition to the measurement signal, the qubit is excited when the spectroscopy frequency ω_{spec} matches the qubit transition frequency ω_{a} . The transmission amplitude of the applied measurement signal with frequency $\omega_{\text{rf}} = \omega_{\text{r}} + g^2/\Delta$ changes from low to high according to the qubit transition from the ground to the excited state. This way, the qubit transition frequency can be determined by sweeping the frequency of the spectroscopy signal through resonance with the qubit while dispersively measuring the qubit state.

Within a continuous spectroscopy scheme, a spectroscopy signal is applied to the cavity while measuring the qubit state. Here, photons of the measurement signal which have a frequency $\omega_{\text{rf}} = \omega_{\text{r}} \pm g^2/\Delta$ close to the cavity resonance ω_{r} populate the cavity and thus lead to an AC-stark shifted qubit transition frequency, according to Eq. (5.11). The frequency shift increases with an increasing power P_{rf} of the applied measurement signal. Fluctuations in the number n of photons inside the cavity directly cause fluctuations in the qubit transition frequency ω_{a} . Such fluctuations in ω_{a} in turn lead to dephasing in the qubit state. Further, an additional photon population in the cavity due to the applied measurement signal during spectroscopic excitation can lead to photon number splitting [Schuster2007] in the excited qubit spectrum. The problems mentioned above can be avoided when using a pulsed instead of a continuous spectroscopy concept.

In a pulsed spectroscopy scheme, the measurement signal with frequency ω_{rf} and the spectroscopy signal with frequency ω_{spec} are applied during different periods of time. This way, it is avoided that the cavity is populated with photons of the measurement signal when exciting the qubit with an applied spectroscopy signal. A typical time sequence used for a single pulsed measurement is shown in Fig. 5.7. The qubit is in its ground state. First, the cavity's resonance frequency $\tilde{\omega}_{\text{r}}$ is determined by sweeping the frequency ω_{rf} of the measurement signal and detecting the maximum in the amplitude of the transmitted microwave signal. In the subsequent step of the pulsed measurement procedure, the resonator response is calibrated for the case that the qubit is in its ground state. For this, a measurement signal at frequency $\omega_{\text{rf}} = \tilde{\omega}_{\text{r}}$ is switched on at a time t_3 (see Fig. 5.7a) and the amplitude of the transmitted signal, depicted in Fig. 5.7b, is detected. Next, a measurement signal with frequency $\omega_{\text{rf}} = \tilde{\omega}_{\text{r}}$ is applied again, but additionally to a spectroscopy signal with frequency ω_{spec} which is activated on from the time t_1 until the time t_2 . This pulse is called *saturation pulse* (see Fig. 5.7c) and drives the qubit. If the frequency ω_{spec} of the spectroscopy signal matches the qubit transition frequency ω_{a} , the qubit Rabi oscillates between its ground and excited state and the cavity resonance frequency $\tilde{\omega}_{\text{r}}$ is in average shifted by g^2/Δ . The frequency ω_{rf} does no longer match $\tilde{\omega}_{\text{r}}$ which leads to a resonator response characteristic (see Fig. 5.7d) which is different to the one obtained during calibration (see Fig. 5.7b). In order to compare the cavity response when the qubit is in its excited state (see Fig. 5.7d) to the calibration response when the qubit is in its ground state (compare Fig. 5.7b), the subtraction of the two signals (see Fig. 5.7e) is integrated over time [Bianchetti2009]. Large integration values indicate that ω_{spec} was close to ω_{a} . If ω_{spec} does not match ω_{a} , the transmitted measurement signal has the same shape with or without applying a saturation pulse and the integration value is zero.

The spectroscopic determination of qubit transition frequencies is essential for determining the characteristic qubit energies E_{J0} and E_{C0} . These two energies, together with the cavity's resonance frequency ω_{r} , the cavity's quality factor Q and the coupling strength g are important parameters which have to be known when doing experiments in a circuit QED system. Here, ω_{r} and Q are determined by analyzing the amplitude signal of microwaves transmitted through the cavity. The coupling strength g in turn can be extracted from a vacuum Rabi mode split-

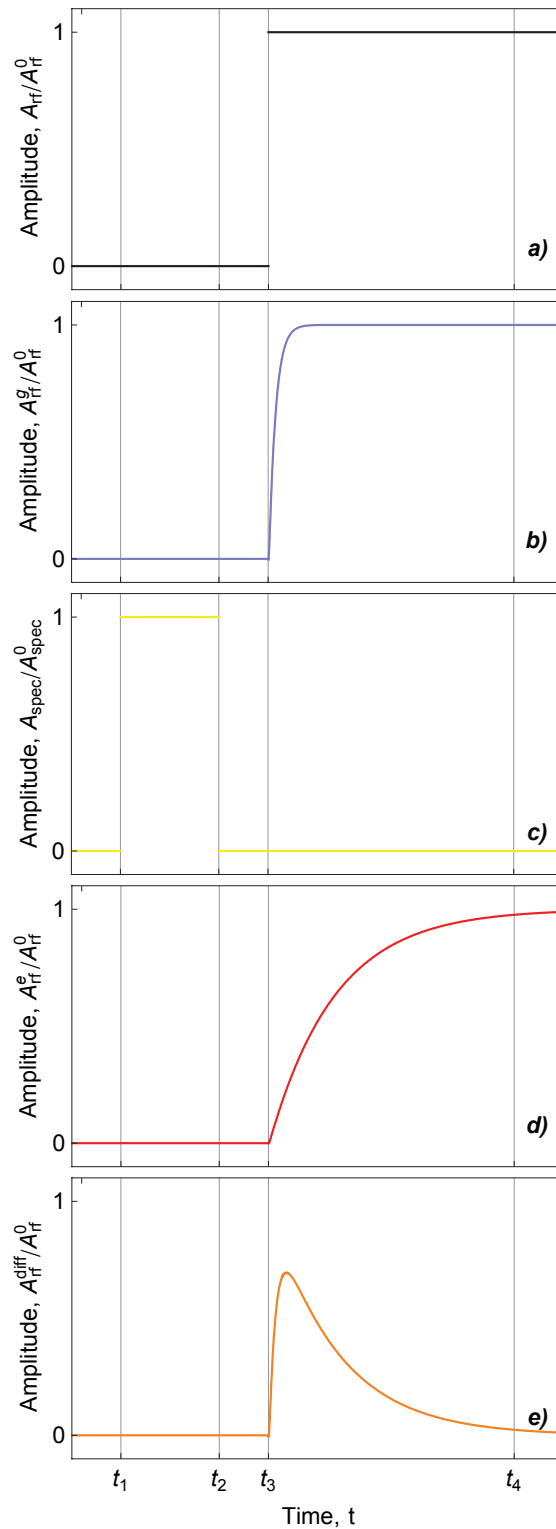


Figure 5.7: Sequence of pulsed spectroscopy measurement scheme. Shown are the time dependent amplitudes of an applied measurement signal A_{rf} (see black line in part a), of the transmitted measurement signal for the qubit being in its ground and excited state A_{rf}^g and A_{rf}^e (see blue and red lines in part b and d), of the spectroscopy pulse A_{spec} (see yellow line in part c) and of the transmitted measurement signal for the qubit being in its ground state minus the transmitted measurement signal for the qubit being in its excited state $A_{\text{rf}}^{\text{diff}} = A_{\text{rf}}^g - A_{\text{rf}}^e$ (see orange line in part e). In each case the amplitudes are normalized to the peak amplitudes A_{rf}^0 respectively A_{spec}^0 .

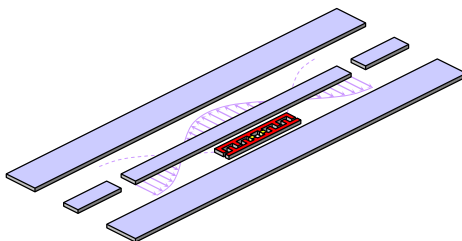


Figure 5.8: Schematic of a circuit QED system consisting of a transmon type qubit integrated into a coplanar waveguide resonator.

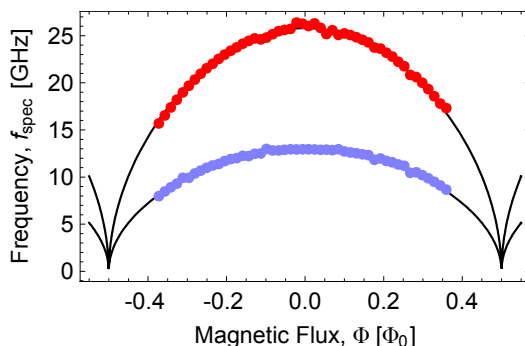


Figure 5.9: Spectroscopic determination of transmon transition frequencies in dependence on the magnetic flux threading the qubit loop. Blue data points represent transitions from E_0 to E_1 whereas red points represent those from E_0 to E_2 . Black solid lines are fits to the measured data.

ting, compare Fig. 5.4. In order to determine E_{J0} and E_{C0} of a transmon type qubit integrated into a coplanar waveguide resonator, see schematic in Fig. 5.8, qubit transition frequencies are spectroscopically measured while sweeping the magnetic field at the qubit position. Figure 5.9 shows the transition frequencies extracted within the measured spectroscopy frequency and magnetic flux range. Blue points correspond to the transition from E_0 to E_1 . The data is fitted with $f_{01} = (E_1 - E_0)/h \approx (\sqrt{8E_J E_C} - E_C)/h$, see chapter 3. The Josephson energy $E_J = E_{J0} \cos(\pi\Phi/\Phi_0)$ here is controlled with the magnetic flux threading the qubit loop. Red points correspond to two-photon excitations from E_0 to E_2 . The data in this case is fitted with $f_{02} = (E_2 - E_0)/h \approx (2\sqrt{8E_J E_C} - 3E_C)/h$, see chapter 3. By fitting both sets of data points using E_{J0} and E_{C0} as fit parameters, the characteristic qubit energies $E_{J0} = h \cdot 53.5$ GHz and $E_{C0} = h \cdot 395$ MHz are determined.

5.5 Measurement Setup for Multi Qubit Experiments

The previous sections explained more from a conceptual point of view how the qubit parameters E_{J0} , E_{C0} and g can be determined using spectroscopy and dispersive readout. This section describes the actual measurement setup used for doing such characterizations, see Fig. 5.10, and in particular for performing multi-qubit experiments, which are treated in the next section.

Low Temperature Setup A circuit QED sample is installed in an *Oxford Instruments* Kelvinox400HA dilution refrigerator. In order to suppress quasi-particle excitations in the superconducting qubit material which would lead to decoherence, the sample is cooled down to a temperature

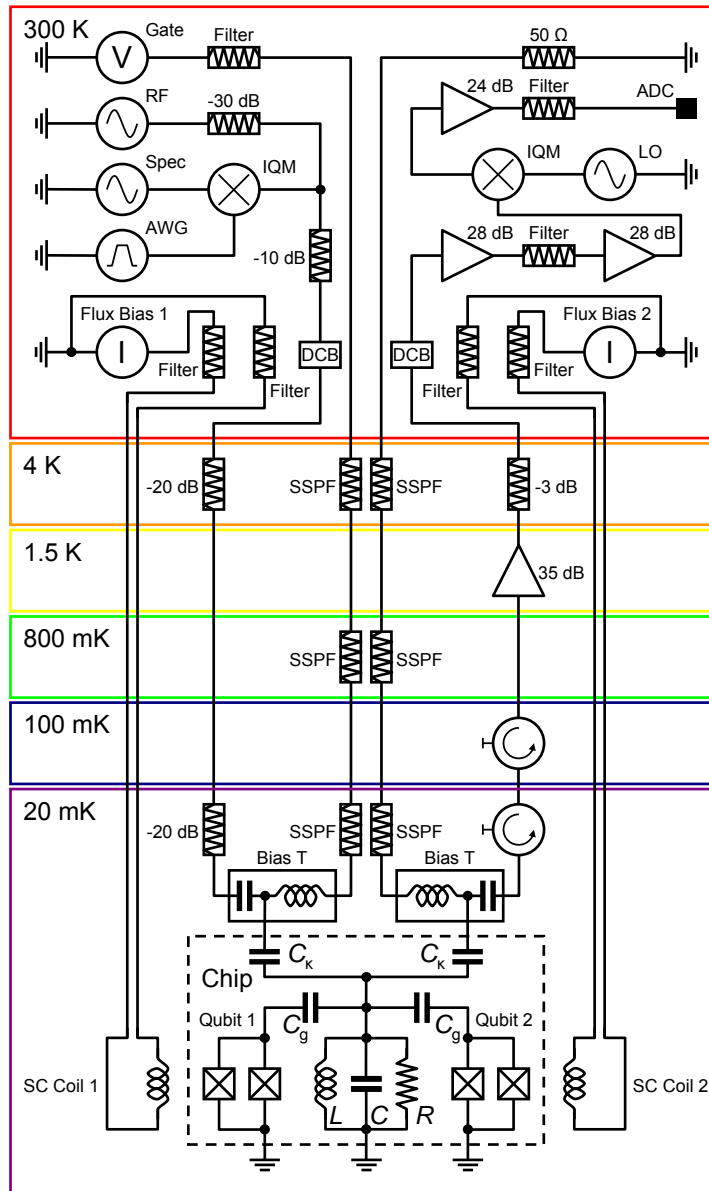


Figure 5.10: Schematic of the measurement setup used for characterizing circuit QED devices. The upper part shows the room temperature setup for generating microwave and DC signals as well as the setup for detecting transmitted RF signals. The lower part shows components installed at different temperature stages of the refrigerator.

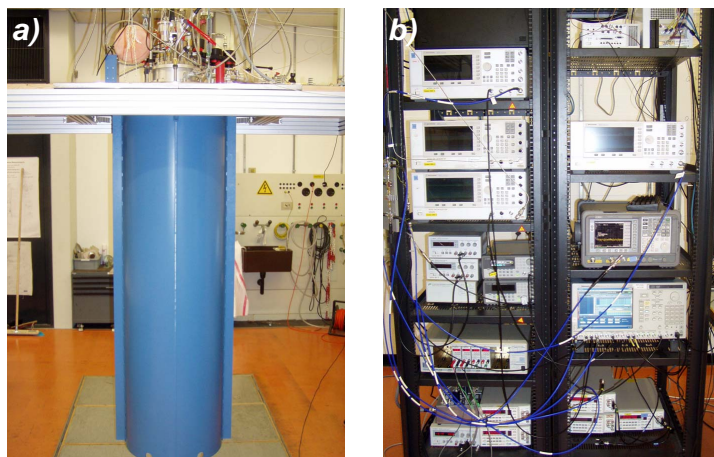


Figure 5.11: a) Photograph of the *Oxford Instruments* Kelvinox400HA dilution refrigerator within the low temperature setup. b) Microwave electronic setup used for signal generation and acquisition.

of about 20 mK which corresponds to an energy far below the gap energy of the superconducting material. The microwave lines which electrically access the sample are fed to the outside via several attenuators, installed at different temperature stages. The attenuators stepwise reduce electrical and thermal noise which otherwise would be transferred from higher temperature stages to the sample. Attenuators of 20 dB each are installed in the input line at the 4 K stage. In the output line two circulators are installed at the 20 mK and 100 mK stage in order to stop the input noise of the amplifier from propagating towards the sample and heating the resonator. A *high electron mobility transistor* (HEMT) is installed at the 1 K stage. The component amplifies the signal transmitted through the sample with 35 dB gain before it is fed through another 3 dB attenuator which is mainly introduced for thermally anchoring the output line. The option of tuning the gate charge N_g is used only when measuring Cooper pair box type qubits which are sensitive to N_g . In order to apply a gate voltage to the qubit via the transmission line, *bias Ts* are installed at the resonator input and output lines. When measuring transmon type qubits, which are insensitive to electrical charge on their island, no gate voltage is used. The DC lines for the bias Ts pass several low pass *stainless steel powder filters* (SSPF) with a cut-off frequency of about 1 MHz which also reduce thermal noise from the outside. A voltage source at room temperature generates the gate voltage for the bias Ts which is low pass filtered and fed to the DC lines. Figure 5.11a shows an image of the *Oxford Instruments* Kelvinox400HA dilution refrigerator.

Microwave Electronic Setup and Signal Generation For spectroscopically determining the state of a qubit, phase coherent microwave signals are synthesized at room temperature with microwave generators and fed via room temperature filters and a *DC-block* to the input ports of the refrigerator, see Fig. 5.10. An *IQ up-converter* offers the possibility to modulate the amplitude (and also the phase) of the spectroscopy signal in order to realize for example a saturation pulse sequence when doing pulsed spectroscopy. The modulation signals for the IQ up-converter are created with an *arbitrary waveform generator* (AWG) which has two analog outputs with 10 bit resolution each. Additional four digital outputs with 1 bit resolution trigger the microwave generators and the *analog to digital converter* (ADC) card which is used for data acquisition. The arbitrary waveform generator has a sampling rate of 1 Gs and thus allows to generate pulse sequences on the nanosecond timescale.

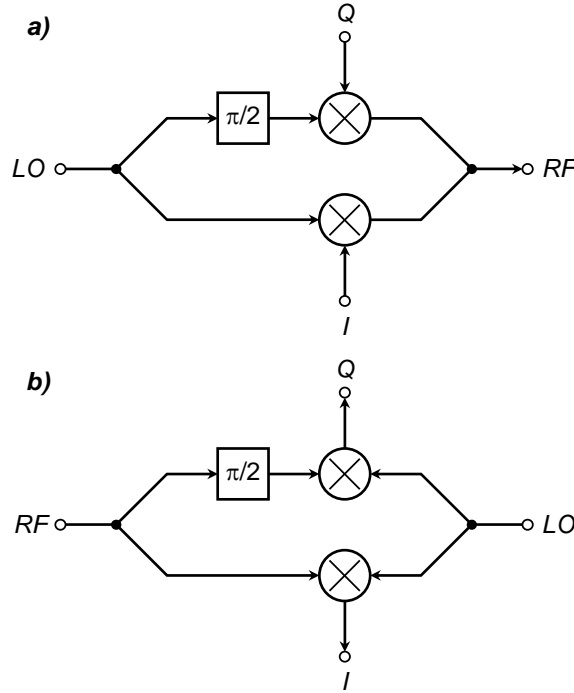


Figure 5.12: a) Schematic of an IQ-up-converter. b) Schematic of an IQ-down-converter. In the up-converter mode, an RF input signal is equally split into two paths. In one path, a 90 degree phase shifter is introduced. The split signals are mixed with the signals of the I and Q input channels and finally added at the RF output port. In the down-converter mode, the RF and LO input signals are also split in two paths. One of the two signals is phase shifted by 90 degrees in one channel. In each path, RF and LO signals are mixed and output at the I and Q ports.

For modulating the spectroscopy signal, two analog output signals of the arbitrary waveform generator are connected to the (intermediate frequency) inputs I and Q of the IQ up-converter, see Fig. 5.12a. The RF spectroscopy input signal is applied to the up-converter's LO input and equally split with a power divider into two signal paths. One of the two signals is directly mixed with the (intermediate frequency) signal applied to the first input I whereas the other one is first shifted in phase by 90 degrees and then mixed with the (intermediate frequency) signal applied to the second input Q of the up-converter. The two paths are finally combined and applied to the up-converter RF output.

A mixer is a non-linear device which multiplies two input signals, in the following a low, respectively intermediate frequency signal $S_{\text{if}}(t)$ with amplitude A_{if} , frequency ω_{if} , phase α_{if} and a high frequency signal of a *local oscillator* $S_{\text{lo}}(t)$ with amplitude A_{lo} , frequency ω_{lo} and phase α_{lo} . The intermediate frequency signal can be used to modulate the carrier signal of the local oscillator. The output signal

$$\begin{aligned}
 S(t) &= S_{\text{if}}(t) \cdot S_{\text{lo}}(t) \\
 &= A_{\text{if}} \cos(\omega_{\text{if}}t + \alpha_{\text{if}}) \cdot A_{\text{lo}} \cos(\omega_{\text{lo}}t + \alpha_{\text{lo}}) \\
 &= \frac{1}{2} A_{\text{if}} A_{\text{lo}} [\cos((\omega_{\text{if}} + \omega_{\text{lo}})t + \alpha_{\text{if}} + \alpha_{\text{lo}}) + \cos((\omega_{\text{if}} - \omega_{\text{lo}})t + \alpha_{\text{if}} - \alpha_{\text{lo}})] \quad (5.12)
 \end{aligned}$$

has two sidebands with frequencies $\omega_{\text{if}} - \omega_{\text{lo}}$ and $\omega_{\text{if}} + \omega_{\text{lo}}$ in its Fourier spectrum. When filtering out one of the two sidebands, either the signal with the difference frequency or that with the sum frequency can be obtained.

As depicted in Fig. 5.12a, an IQ up-converter uses two mixers in addition to a splitter, a phase shifter and a combiner. When applying DC signals to the I and Q input ports, the frequencies $\omega_{\text{if,I}}$, $\omega_{\text{if,Q}}$ and phases $\alpha_{\text{if,I}}$, $\alpha_{\text{if,Q}}$ can be set to zero. In the following, also the phase α_{lo} will be defined as zero. Further, it will be assumed that the sum frequency sideband of both mixers is used only. The harmonic signal $S_{\text{lo}}(t)$ applied to the RF input of the IQ up-converter generates the output signal

$$\begin{aligned}
 S(t) &= \frac{1}{4}A_{\text{if,I}}A_{\text{lo}} \cos(\omega_{\text{lo}}t) + \frac{1}{4}A_{\text{if,Q}}A_{\text{lo}} \cos(\omega_{\text{lo}}t + 90^\circ) \\
 &= \frac{1}{4}A_{\text{if,I}}A_{\text{lo}} \cos(\omega_{\text{lo}}t) - \frac{1}{4}A_{\text{if,Q}}A_{\text{lo}} \sin(\omega_{\text{lo}}t) \\
 &= I \cos(\omega_{\text{lo}}t) - Q \sin(\omega_{\text{lo}}t) \\
 &= A \cos(\omega_{\text{lo}}t) \cos(\alpha) - A \sin(\omega_{\text{lo}}t) \sin(\alpha) \\
 &= A \cos(\omega_{\text{lo}}t + \alpha)
 \end{aligned} \tag{5.13}$$

at the up-converter's RF output port, where $I := A_{\text{if,I}}A_{\text{lo}}/4$ and $Q := A_{\text{if,Q}}A_{\text{lo}}/4$ holds and the amplitude A and the phase α of the output signal are given by

$$A = \sqrt{I^2 + Q^2} \tag{5.14}$$

$$\alpha = \arctan\left(\frac{I}{Q}\right). \tag{5.15}$$

The signal $S(t)$ can be represented according to Eq. (5.13) as vector in the complex plane with real part I and imaginary part Q or equivalently in polar coordinates by a vector with amplitude A and polar angle α . Amplitude and phase of the up-converter output signal can thus be adjusted by varying the voltages at the I and Q input ports. If a voltage $V \neq 0$ is applied to the I input and the Q input is set to $V = 0$, the signal at the up-converter's RF input is simply transmitted in phase. If the input I is set to $V = 0$ and a voltage $V \neq 0$ is applied to the Q input, the RF signal at the up-converter's input is transmitted with 90 degrees phase shift. When the two input ports I and Q are set to ground, no signal is transmitted from the RF input to the RF output. Figure 5.11b shows an image of microwave generators and other instruments which are part of the measurement setup.

When dispersively measuring the state of a qubit which is integrated into a transmission line cavity, the amplitude and phase of a microwave signal transmitted through the cavity is detected. According to the *Nyquist-Shannon theorem*, a signal can be reconstructed correctly only if the sampling rate with which the signal is detected is greater or equal than twice the highest signal frequency. In order to reconstruct a 5 GHz microwave signal, a sampling rate of 10 GHz at minimum would be necessary which is technically hard to achieve and thus expensive. In order to circumvent the direct acquisition of the measurement signal with frequency ω_{rf} , it is first down-converted with an *IQ down-converter* to an intermediate frequency. The signal at the refrigerator output passes a DC-block and a room temperature amplifier before it is mixed in the down-converter with the signal of a local oscillator (LO) with frequency ω_{lo} . The down-converter maps the amplitude and the phase of the RF input signal onto the I and Q ports. In case the frequency ω_{lo} of the local oscillator equals the frequency ω_{rf} of the measurement signal, the intermediate frequency $\omega_{\text{if}} = \omega_{\text{lo}} - \omega_{\text{rf}}$ is zero and the measurement is said to be *homodyne*. If the intermediate frequency $\omega_{\text{if}} = \omega_{\text{lo}} - \omega_{\text{rf}}$ is nonzero, the measurement is said to be *heterodyne*. The I and Q output channels are amplified, low pass filtered and finally digitized with an analog to digital converter having a sampling rate of 1 Gs.

As depicted in Fig. 5.12b, an IQ down-converter uses the same components as an IQ up-converter, compare Fig. 5.12a, but is operated differently. The (high frequency) measurement signal is applied to the down-converter RF input and equally split with a power divider into two signal paths. One of the two signals is directly mixed with the (high frequency) signal of the local oscillator whereas the other one is first shifted in phase by 90 degrees and then mixed with the local oscillator signal applied to the LO input of the down-converter. In the down-converter configuration, the high frequency signals $S_{\text{rf}}(t)$ with amplitude A_{rf} , frequency ω_{rf} , phase α_{rf} and $S_{\text{lo}}(t)$ with amplitude A_{lo} , frequency ω_{lo} and phase α_{lo} are mixed, leading to the signal

$$\begin{aligned} S(t) &= S_{\text{rf}}(t) \cdot S_{\text{lo}}(t) \\ &= A_{\text{rf}} \cos(\omega_{\text{rf}}t + \alpha_{\text{rf}}) \cdot A_{\text{lo}} \cos(\omega_{\text{lo}}t + \alpha_{\text{lo}}) \\ &= \frac{1}{2} A_{\text{rf}} A_{\text{lo}} [\cos((\omega_{\text{rf}} + \omega_{\text{lo}})t + \alpha_{\text{rf}} + \alpha_{\text{lo}}) + \cos((\omega_{\text{rf}} - \omega_{\text{lo}})t + \alpha_{\text{rf}} - \alpha_{\text{lo}})] \end{aligned} \quad (5.16)$$

at the mixer's output. The down-converter now uses the difference frequency sideband only and outputs the corresponding signal to its I and Q ports. Assuming now, that the frequency of the measurement signal is given by $\omega_{\text{rf}} = \omega_{\text{if}} + \omega_{\text{lo}}$, where ω_{if} is the intermediate frequency signal for up-conversion, the signals at the I and Q output ports are given by

$$\begin{aligned} S_{\text{I}}(t) &= \frac{1}{2} A_{\text{rf}} A_{\text{lo}} \cos((\omega_{\text{rf}} - \omega_{\text{lo}})t + \alpha_{\text{rf}} - \alpha_{\text{lo}}) \\ &= \frac{1}{2} A_{\text{rf}} A_{\text{lo}} \cos((\omega_{\text{if}} + \omega_{\text{lo}} - \omega_{\text{lo}})t + \alpha_{\text{rf}} - \alpha_{\text{lo}}) \\ &= \frac{1}{2} A_{\text{rf}} A_{\text{lo}} \cos(\omega_{\text{if}}t + \alpha_{\text{rf}} - \alpha_{\text{lo}}) \end{aligned} \quad (5.17)$$

$$\begin{aligned} S_{\text{Q}}(t) &= \frac{1}{2} A_{\text{rf}} A_{\text{lo}} \cos((\omega_{\text{rf}} - \omega_{\text{lo}})t + \alpha_{\text{rf}} - \alpha_{\text{lo}} + 90^\circ) \\ &= \frac{1}{2} A_{\text{rf}} A_{\text{lo}} \cos((\omega_{\text{if}} + \omega_{\text{lo}} - \omega_{\text{lo}})t + \alpha_{\text{rf}} - \alpha_{\text{lo}} + 90^\circ) \\ &= \frac{1}{2} A_{\text{rf}} A_{\text{lo}} \cos(\omega_{\text{if}}t + \alpha_{\text{rf}} - \alpha_{\text{lo}} + 90^\circ) \\ &= \frac{1}{2} A_{\text{rf}} A_{\text{lo}} \sin(\omega_{\text{if}}t + \alpha_{\text{rf}} - \alpha_{\text{lo}}). \end{aligned} \quad (5.18)$$

Assuming again $\omega_{\text{if}} = 0$ (homodyne up-conversion) and $\alpha_{\text{lo}} = 0$ further leads to

$$S_{\text{I}}(t) = \frac{1}{2} A_{\text{rf}} A_{\text{lo}} \cos(\alpha_{\text{rf}}) \quad (5.19)$$

$$S_{\text{Q}}(t) = \frac{1}{2} A_{\text{rf}} A_{\text{lo}} \sin(\alpha_{\text{rf}}) \quad (5.20)$$

and the amplitude and phase of the down-converted RF signal can be determined by

$$A_{\text{rf}} = \frac{2}{A_{\text{lo}}} \sqrt{S_{\text{I}}^2 + S_{\text{Q}}^2} \quad (5.21)$$

$$\alpha_{\text{rf}} = \arctan\left(\frac{S_{\text{Q}}}{S_{\text{I}}}\right). \quad (5.22)$$

Amplitude and phase of a RF signal can be reconstructed either in a homodyne or a heterodyne configuration. Within a homodyne detection scheme, amplitude and phase can simply be obtained by using Eqs. (5.21) and (5.22). This method has the advantage of a high resolution which is limited only by the bandwidth of the mixers and amplifiers as well as by the sampling rate of the acquisition card. However, real down-converters usually show imperfections in dividing an RF

input signal equally into two branches leading to phase and amplitude imbalances. Furthermore, the DC signals at the I and Q ports are sensitive to $1/f$ noise as well as to voltage drifts.

When choosing a heterodyne detection scheme, an AC instead of a DC signal is generated at the I and Q outputs which has the down-converted intermediate frequency $\omega_{\text{if}} = \omega_{\text{lo}} - \omega_{\text{rf}}$. Choosing ω_{if} high enough avoids $1/f$ noise in the I and Q output signal significantly. Performing heterodyne detection offers the possibility of either using both channels, I and Q, or using only one channel, for example I, to reconstruct the phase and amplitude. In the last mentioned case, the digitized signal of one channel is sampled over one full period and digitally down-converted from the intermediate frequency ω_{if} to a DC signal. This method is here referred to as *digital homodyne* detection scheme. Phase and amplitude imbalances can be avoided within this procedure.

Individual B-Field Control In order to individually control the magnetic flux bias of single qubits in a multi-qubit circuit QED device, magnetic coils close underneath the sample are used, see Fig. 5.10. The coils are made from superconducting Nb-Ti alloy wires, are installed underneath the sample and are voltage biased. The bias lines are RC filtered at room temperature. In case of two magnetic coils flux biasing two qubits, the influence of the voltage biases on the magnetic fluxes threading the individual qubits are described by the matrix equation

$$\begin{pmatrix} \Phi_a \\ \Phi_b \end{pmatrix} = \begin{pmatrix} \Phi_a^0 \\ \Phi_b^0 \end{pmatrix} + \begin{pmatrix} A & B \\ C & D \end{pmatrix} \begin{pmatrix} V_1 \\ V_2 \end{pmatrix}. \quad (5.23)$$

Here Φ_a and Φ_b are the magnetic fluxes threading qubit loop a respectively qubit loop b, Φ_a^0 and Φ_b^0 are offset fluxes at the positions of qubit a respectively qubit b and V_1 and V_2 are bias voltages for coil 1 respectively coil 2. The offset fluxes Φ_a^0 and Φ_b^0 can be determined by applying a certain flux and measuring the transition frequencies of both qubits. A voltage bias here is used instead of a current bias due to the room temperature RC low pass filters in the bias lines. The matrix elements A , B , C and D are defined as

$$A = 1/\Gamma_{a,1}, \quad (5.24)$$

$$B = 1/\Gamma_{a,2}, \quad (5.25)$$

$$C = 1/\Gamma_{b,1}, \quad (5.26)$$

$$D = 1/\Gamma_{b,2}. \quad (5.27)$$

Here, $\Gamma_{a,1}$ and $\Gamma_{a,2}$ are the voltages per magnetic flux threading qubit a and generated by coil 1 respectively coil 2. Accordingly, $\Gamma_{b,1}$ and $\Gamma_{b,2}$ are the voltages per magnetic flux threading qubit b and generated by coil 1 respectively coil 2. The constants $\Gamma_{a,1}$, $\Gamma_{a,2}$, $\Gamma_{b,1}$ and $\Gamma_{b,2}$ are determined by doing separate B -field sweeps with the two coils and spectroscopically measuring the positions of the two qubits. Within this flux control, one can tune qubit a and qubit b independently to two individual positions. In general when doing experiments with k individual qubits, k magnetic coils have to be used for flux bias. However, due to the finite inductance of the coils, only slow flux sweeps can be performed and also the number of coils is limited to the available space underneath the sample. In order to realize fast flux tuning in order to do gate operations, local flux lines have to be integrated directly on chip.

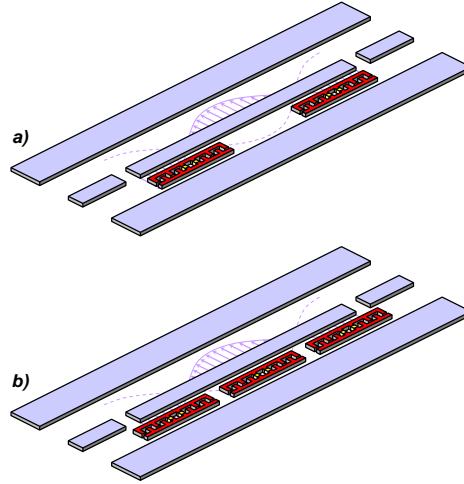


Figure 5.13: Schematic of coplanar waveguide resonator with a) two and b) three integrated transmon type qubit structures.

	Sample 1	Sample 2
f_{r1}	6.44 GHz	3.34 GHz
E_{C0}^a/h	232 MHz	148 MHz
E_{C0}^b/h	233 MHz	153 MHz
E_{J0}^a/h	35 GHz	409 GHz
E_{J0}^b/h	38 GHz	375 GHz
g_0^a	133 MHz	43 MHz
g_0^b	134 MHz	42 MHz

Table 5.1: Parameters of the two characterized samples. f_{r1} denotes the fundamental resonance frequency of the coplanar waveguide resonator, E_{C0}^a and E_{C0}^b the charging energy, E_{J0}^a and E_{J0}^b the maximum Josephson energy and finally g_0^a and g_0^b the coupling strength of the left and right qubit to the fundamental cavity mode.

5.6 Qubit-Qubit Coupling via Virtual Photons

One possible realization of a practical quantum computer architecture couples distant qubits via a cavity in order to perform gate operations. Understanding the coupling of two or several individual qubits is essential for effectively designing and controlling multi-qubit interactions. In this section, the photon exchange between two superconducting qubits integrated into a transmission line cavity is studied in dependence on the detuning of both qubits from the cavity resonance [Göppl2009]. Most features of the qubit-qubit coupling can be explained by considering higher order cavity modes.

The interaction of two qubits integrated into a cavity was studied in two separate samples. In the first sample, two transmon type qubits are placed at the two ends of a coplanar waveguide resonator, see Fig. 5.13a. The transition frequencies $\omega_{a,b} \approx \omega_{a,b}^{\max} \sqrt{|\cos(\pi\Phi/\Phi_0)|}$ of qubit a and b can be controlled independently using two miniature coils mounted underneath the sample. The cavity consists of an aluminum coplanar waveguide resonator on a sapphire substrate [Göppl2008]. The most important parameters of the sample are listed in Tab. 5.1. The sample was fabricated within the scope of this thesis, compare sample parameters of transmon device H in appendix A, and used also for the experiment presented in [Fragner2008]. In the experiment presented in the following, the two qubits are tuned into mutual resonance for a different detuning of the qubits from the cavity resonance and their frequencies are spectroscopically detected in order to extract the frequency dependent qubit-qubit coupling strength. For the measurement, one qubit

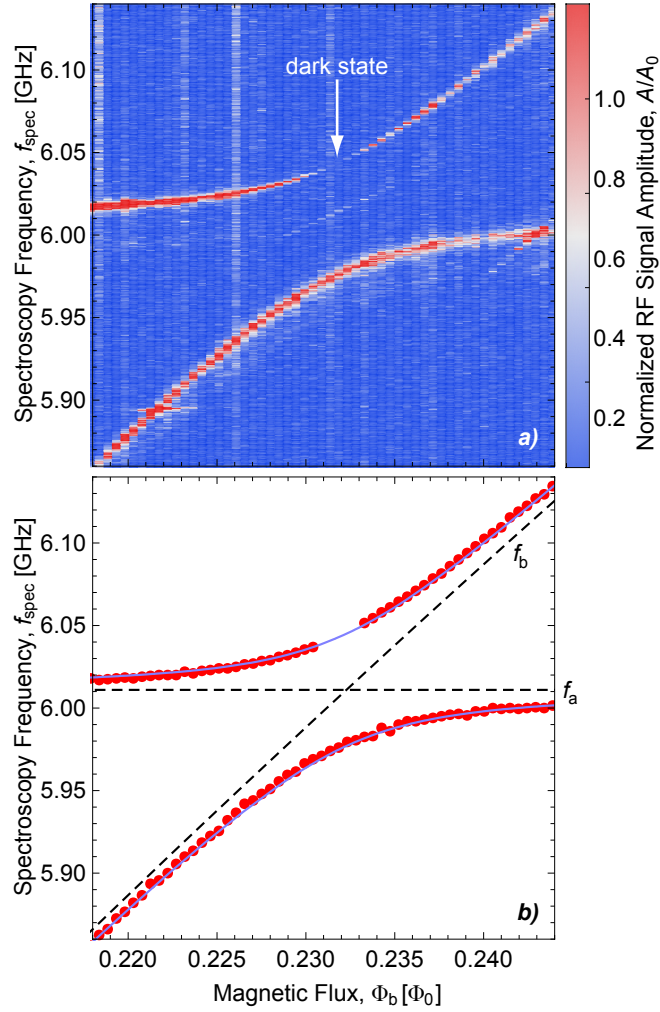


Figure 5.14: a) RF measurement signal in dependence on the frequency ω_{spec} of the applied saturation pulse signal and the tuned magnetic flux. Qubit a has now a fixed transition frequency above the fundamental cavity mode, qubit b is tuned through resonance with qubit a. b) Extracted frequencies of the spectroscopy signal depicted in part c) at maximum transmission power. The data points (red) were fitted with Eq. (5.28) (blue solid line) to extract the minimum splitting. Also shown are the two single qubit lines for zero coupling (dashed black lines).

is first tuned to a fixed transition frequency ω_a . The other qubit is then tuned with magnetic flux such that its transition frequency ω_b crosses the fixed transition frequency of the first qubit. To determine the qubit transition frequencies, a spectroscopy pulse (saturation pulse) with frequency ω_{spec} is applied to the qubit followed by a measurement pulse applied to the cavity to dispersively measure the qubit state. The measurement pulse is separated in time from the saturation pulse and does not populate the cavity during qubit excitation (pulsed spectroscopy scheme). This way, photon number splitting [Schuster2007] in the qubit spectrum is avoided. Figure 5.14a shows the spectroscopy response for the fixed qubit at a frequency of $f_a \approx 6$ GHz which is below the fundamental cavity mode whereas Fig. 5.15a shows the spectroscopy response for the fixed qubit at a frequency of $f_a \approx 7$ GHz which is above the fundamental cavity mode.

Close to the degeneracy point where $\omega_a = \omega_b$ holds, an anticrossing of the two qubits is observed. Here, the single qubit eigenstates $|\downarrow\uparrow\rangle$ with qubit a being in the ground state and qubit b being in the excited state and $|\uparrow\downarrow\rangle$ with qubit a being in the excited state and qubit b being in the ground

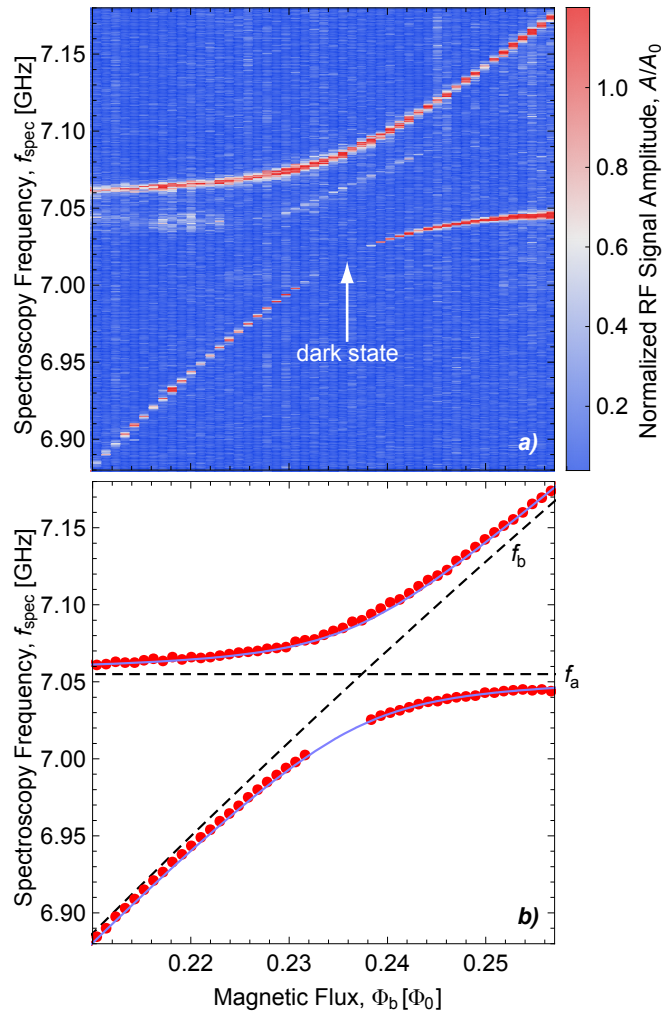


Figure 5.15: a) RF measurement signal in dependence on the frequency ω_{spec} of the applied saturation pulse signal and the tuned magnetic flux. Qubit a has now a fixed transition frequency above the fundamental cavity mode, qubit b is tuned through resonance with qubit a. b) Extracted frequencies of the spectroscopy signal depicted in part c at maximum transmission power. The data points (red) were fitted with Eq. (5.28) (blue solid line) to extract the minimum splitting. Also shown are the two single qubit lines for zero coupling (dashed black lines).

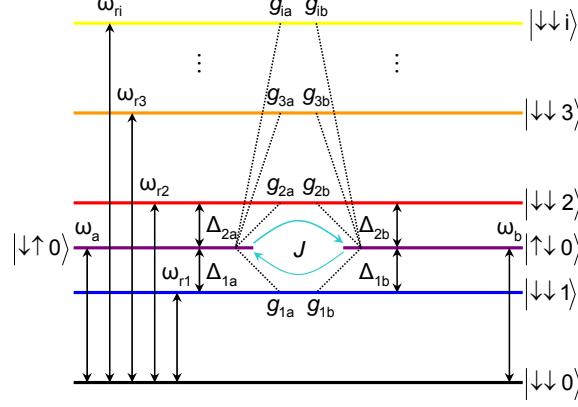


Figure 5.16: Energy diagram and coupling scheme for two qubits with transition frequencies ω_a and ω_b coupled to a transmission line cavity. J depends on the detunings Δ_{ij} and the coupling strengths g_{ij} .

state split up in a symmetric triplet state $|\downarrow\uparrow\rangle + |\uparrow\downarrow\rangle$ and an antisymmetric singlet state $|\downarrow\uparrow\rangle - |\uparrow\downarrow\rangle$ due to virtual photon induced coupling as observed first in reference [Majer2007], compare in Fig. 5.16. Close to the degeneracy point, the spectroscopy line which corresponds to the triplet state disappears, see Fig. 5.14a and Fig. 5.15a. This dark state is observed for the qubit line which corresponds to the symmetric triplet state due to destructive interference [Majer2007]. In the dispersive limit, the spectroscopic excitation is of the form $\sigma_a^x g_{ia} / \Delta_{ia} - \sigma_b^x g_{ib} / \Delta_{ib}$. Here, g_{ij} is the coupling strength between cavity mode i and qubit j with transition frequency ω_j , where i is an integer number and $j = a, b$. Further, $\Delta_{ij} = \omega_j - \omega_{ri}$ is the detuning in frequency of cavity mode i from qubit j . Such an asymmetric signal cannot drive any transitions to the symmetric state which remains dark as a result.

When the qubits are tuned below the resonator (negative detuning), the higher frequency coupled qubit state is the (symmetric) triplet state and the lower frequency qubit state the (antisymmetric) singlet state. When the qubits are tuned above the resonator however, the higher frequency state is the singlet state and the lower frequency state the triplet state. Changing a negative to a positive detuning thus will also bring the dark state from the higher frequency to the lower frequency virtually coupled qubit state and vice versa.

The flux dependent coupled qubit transition frequencies were extracted from data like the one shown in Fig. 5.14a and Fig. 5.15a and fitted to

$$\omega_{a,b} = \frac{1}{2}(\omega_a + \omega_b) \pm \frac{1}{2}\sqrt{(\omega_a - \omega_b)^2 + (2\pi S)^2}, \quad (5.28)$$

where S is the splitting due to the exchange interaction, see Fig. 5.14b and Fig. 5.15b. Here, ω_a and S are used as fit parameters. The calculated uncoupled qubit states are shown in Fig. 5.14b and Fig. 5.15b as dashed lines. Qubit-qubit splittings are determined for different detunings $\Delta = \omega_a - \omega_r = \omega_b - \omega_r$, the data is shown in Fig. 5.17, together with the cavity's transmission spectrum. For qubit transition frequencies closer to the cavity fundamental resonance, the splitting increases. In the dispersive limit where the qubits are tuned far off the cavity's resonance, the maximum qubit-qubit splitting is given by $g_{1a}g_{1b}(\Delta_{1a}^{-1} + \Delta_{1b}^{-1})$ [Majer2007] when taking into account only the fundamental resonator mode. This theoretical splitting, which is symmetric for negative and positive detunings, is depicted in Fig. 5.17a by the black dashed line. Surprisingly, the measured data does not fit to this line and is not symmetric around the fundamental mode. For negative detunings, measured splittings are larger and for positive detunings they are smaller than the

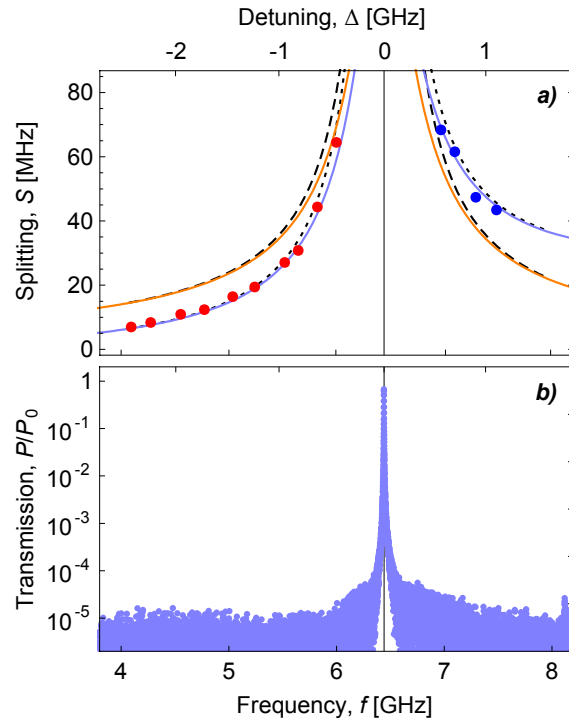


Figure 5.17: a) The red and blue points show the minimal qubit-qubit splittings extracted from a fit to the pulsed spectroscopy measurement versus detuning, using Eq. 5.28. Red points indicate a dark state appearing in the higher frequency coupled qubit state whereas blue points indicate a dark state showing up in the lower frequency coupled qubit state. The black solid vertical line indicates the cavity's fundamental resonance. The black dashed line gives the theoretical splitting evaluated by using Eq. (5.29), taking into account only the fundamental mode $i_{\max} = 1$ whereas the black dotted line represents the case where the fundamental mode as well as the first harmonic mode $i_{\max} = 2$ is considered. The orange solid line depicts the theoretical splitting obtained when numerically evaluating the Hamiltonian given in Eq. (5.30) for $i_{\max} = 1$ and the blue solid line shows the theoretical splitting for $i_{\max} = 2$. b) Normalized transmission power spectrum of the coplanar waveguide resonator.

simple single-mode coupling description.

However, the data can be approximated better when taking into account also harmonic modes. As depicted in Fig. 5.16, the qubits couple not only to the fundamental resonator mode with frequency ω_{r1} but also to higher harmonics with frequency ω_{ri} . For an arbitrary number of resonator modes, the exchange interaction between the two qubits can be approximated in the dispersive limit by

$$J = \sum_{i=1}^{i_{\max}} \frac{g_{ia}g_{ib}}{2} \left(\frac{1}{\Delta_{ia}} + \frac{1}{\Delta_{ib}} \right), \quad (5.29)$$

where i_{\max} is the maximum mode number considered and the minimum qubit-qubit splitting is given by $2J$. The black dotted line takes $i_{\max} = 2$ modes into account and describes the measured data well. Furthermore, when assuming an even number of modes maximally taken into account, $i_{\max} = 2k$, where k is a natural number, the measured data is described well by Eq. 5.29 in the dispersive limit. However, this is not the case for an odd number of modes maximally taken into account, $i_{\max} = 2k + 1$. This observation can currently not be explained.

In order to describe the qubit-qubit coupling not only in the dispersive limit, the generalized Jaynes-Cummings Hamiltonian is solved numerically in the following. The circuit QED system consisting of two qubits coupled to a cavity is described by the generalized Jaynes-Cummings Hamiltonian in the rotating wave approximation as

$$\hat{H}_{JC} = \sum_{i=1}^{i_{\max}} \sum_{j=a,b} \left[\hbar\omega_{ri}\hat{a}_i^\dagger\hat{a}_i + \frac{1}{2}\hbar\omega_j\hat{\sigma}_j^z + \hbar g_{ij} \left(\hat{a}_i^\dagger\hat{\sigma}_j^- + \hat{a}_i\hat{\sigma}_j^+ \right) \right], \quad (5.30)$$

where the index i sums over the number of cavity modes and the index $j = a, b$ sums over the number of qubits. The first term in the Hamiltonian describes the modes of the cavity to which the qubits couple, the second term the qubits itself and the third term the coupling of the qubits to the cavity modes. The energy eigenstates of the Hamilton have been determined for varying qubit frequencies $\omega_a = \omega_b$ by numerically evaluating Eq. (5.30). The frequency dependent, theoretical qubit-qubit splitting which is given by $2J$ is then determined by minimizing the difference of the two lowest energy levels and is shown in Fig. 5.17a for the lowest one and two cavity modes, taken into account.

For large detunings, the curve obtained in the dispersive approximation Eq. (5.29) fits well to the one obtained from the full Hamiltonian (5.30) when taking into account the same number of cavity modes. For small detunings however, where the dispersive approximation is no longer valid, the two curves increasingly disperse with decreasing detuning. When considering more than two resonator modes ($i_{\max} > 2$) (not depicted in Fig. 5.17a) the curves show an alternating behavior where all curves with an odd number of cavity modes up from the fundamental one lie close to the curve using only the fundamental mode, and all curves with an even number of cavity modes up from the fundamental lie close to the one using the fundamental and first harmonic mode. The series described in Eq. (5.29) (dispersive limit) does not converge for $i_{\max} \rightarrow \infty$. Instead, the series alternates between two limit values

$$J_{\text{even}} = \lim_{k \rightarrow \infty} \sum_{i=1}^{2k} \frac{g_{ia}g_{ib}}{2} \left(\frac{1}{\Delta_{ia}} + \frac{1}{\Delta_{ib}} \right) \quad (5.31)$$

$$J_{\text{odd}} = \lim_{k \rightarrow \infty} \sum_{i=1}^{2k+1} \frac{g_{ia}g_{ib}}{2} \left(\frac{1}{\Delta_{ia}} + \frac{1}{\Delta_{ib}} \right), \quad (5.32)$$

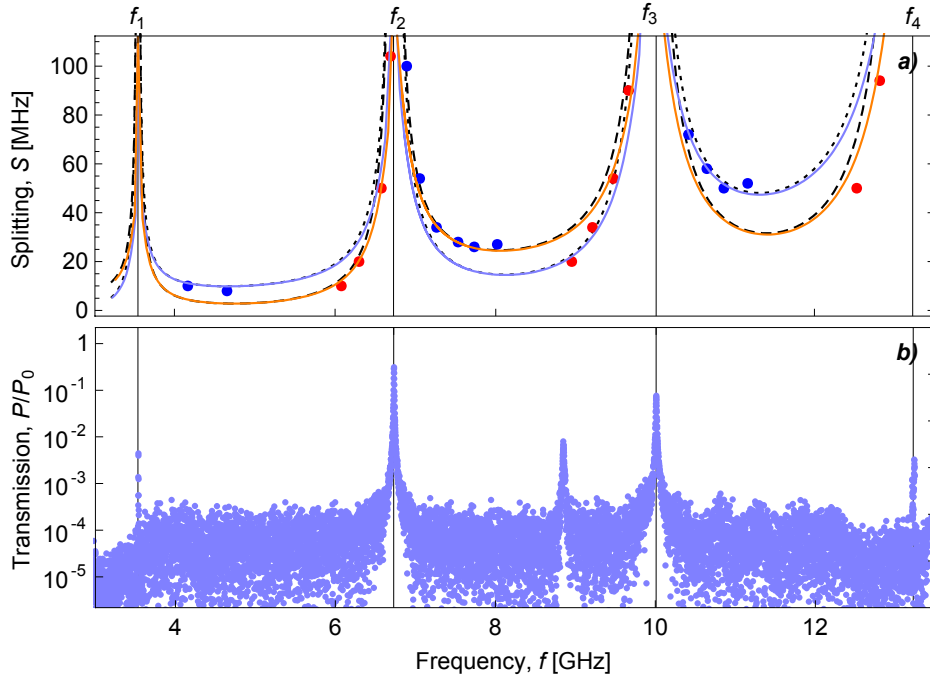


Figure 5.18: a) The red and blue points show the qubit-qubit splittings S extracted from a pulsed spectroscopy measurement. Red points indicate a dark state appearing in the higher frequency coupled qubit state whereas blue points indicate a dark state showing up in the lower frequency coupled qubit state. The black solid vertical lines indicate the cavity's fundamental and harmonic resonances. The black dashed line gives the theoretical splitting evaluated by using Eq. (5.29), taking into account the first four resonator modes $i_{\max} = 4$ whereas the black dotted line represents the case where the first five resonator modes $i_{\max} = 5$ were considered. The blue solid line depicts the theoretical splitting obtained when numerically evaluating the Hamiltonian given in Eq. (5.30) for $i_{\max} = 4$ and the orange solid line shows the theoretical splitting for $i_{\max} = 5$. b) Normalized transmission power spectrum of the coplanar waveguide resonator.

for infinite mode number. A natural cut-off i_{cut} for the maximum mode number i_{\max} is expected for example by the superconducting energy gap Δ of the metalization of the superconducting transmission line cavity and given is by

$$i_{\text{cut}} = \frac{\Delta}{\hbar\omega_{r0}}. \quad (5.33)$$

The measurements and analysis presented above were performed also for a second sample, whose parameters are also listed in Tab. 5.1. In this sample, three transmon type qubits are integrated into a coplanar waveguide resonator where the flux at the three qubit positions is controlled independently with three coils. Here, the frequency of the qubit placed at the center of the waveguide was tuned to close zero in all experiments so that the sample effectively behaves as two qubit device. The main difference to the first sample is the much higher maximal qubit transition frequency $\omega_{a,b}^{\max}$ of both qubits. This makes it possible to tune the qubits to positions in the vicinity of the fundamental but also higher resonator modes when characterizing the frequency dependent qubit-qubit splitting. In this way, the influence of higher harmonic modes on the qubit-qubit interaction can be studied. Figure 5.18 shows the measured qubit-qubit splittings for different transition frequencies of the fixed qubit, together with the cavity's transmission spectrum. Also

here, the experimental data was compared to theory curves derived by numerically solving the Hamiltonian (5.30) as well as obtained in case of the dispersive limit using Eq. (5.29). Again, the measured splitting increases for qubit transition frequencies close to a cavity mode since here the detuning to the respective mode is small and the splitting depends inversely on the detuning, compare Eq. (5.29). Moreover, the splitting in general increases with increasing qubit frequency f . This is because the coupling strength g_{ij} between cavity mode i and qubit j itself scales with the square root of the mode number i [Koch2007] and thus increases with increasing f . In addition, the detuning to higher cavity modes i decreases with increasing f which further increases the splitting, according to Eq. (5.29). The theory curves show an alternating behavior for an odd and even number of modes i_{\max} considered as discussed before. However, the measured splittings show a discontinuity between two modes and do not match to a single curve describing the splitting for either an odd or an even mode. Moreover, the extracted splittings close to an even mode number (first harmonic, third harmonic,...) can be described by theory curves using an odd number of cavity modes and the splittings close to an odd mode number (fundamental, second harmonic,...) can be described by theory using an even number of cavity modes.

The measured splittings are independent of the cavity mode which was used for determining the qubit states with a transmitted RF signal. Further, it was not possible to resolve a qubit-qubit splitting at equal detunings from two cavity modes. Considering qubit-qubit splittings in the vicinity of an arbitrary resonator mode, one can again observe that the dark state switches from the higher to the lower frequency coupled qubit state when tuning the qubits from below to above the respective resonator mode. Between two adjacent cavity modes the dark state switches back from the lower to the upper frequency coupled qubit state when going to higher frequencies.

In summary, the frequency dependent qubit-qubit interaction via a transmission line cavity was measured and analyzed for two samples. It was shown that the splitting behavior around a cavity mode can be described considering higher modes.

5.7 Jaynes-Cummings Ladder and \sqrt{n} -Nonlinearity

The work presented in this thesis allowed for performing several new circuit QED experiments within the Quantum Device Lab at ETH Zurich. In particular, circuit QED devices were designed and fabricated for the experiments presented in references [Fink2008, Fragner2008, Baur2009, Filipp2009, Leek2009], which are discussed in this and the next sections.

In order to prove that a circuit QED system, which here consists of a single transmon type qubit coupled to a transmission line cavity, is quantum mechanical in nature, the Jaynes-Cummings energy ladder was spectroscopically probed within the experiment described in reference [Fink2008]. Although the observation of the vacuum Rabi mode splitting is used to investigate the interaction of matter and light on the level of single quanta, this effect in principle can be explained classically as the normal mode splitting of two coupled linear oscillators [Zhu1990]. The observation of the scaling of the resonant photon-atom coupling strength g with the square root of the photon number n in the cavity however is sufficient to prove the quantum mechanical nature of such a system [Carmichael1996].

In the actual experiment, this nonlinearity is observed by exciting the system into one of the first energy doublet states $(|g\rangle|1\rangle + |e\rangle|0\rangle)/\sqrt{2}$ or $(|g\rangle|1\rangle - |e\rangle|0\rangle)/\sqrt{2}$, compare Fig. 5.3, with a pump microwave signal and then probing the transitions into one of the second energy doublet states $(|g\rangle|2\rangle + |e\rangle|1\rangle)/\sqrt{2}$ or $(|g\rangle|2\rangle - |e\rangle|1\rangle)/\sqrt{2}$, see Fig. 5.3, by measuring the cavity transmission. Here, $|g\rangle$ and $|e\rangle$ refer to qubit ground and excited state.

The whole procedure explained above is performed for different detunings of the qubit from the

cavity which are controlled by the magnetic flux of a miniature coil mounted underneath the sample. Reference [Fink2008] gives a detailed report on the measurement setup and the obtained results.

5.8 Lamb-Shift

Electromagnetic vacuum field fluctuations which permanently create and annihilate virtual energy quanta are of pure quantum mechanical nature and manifest itself in effects like the *Purcell-effect* [Purcell1946] or the *Lamb-shift* [Lamb1947], as discussed here.

The Lamb shifted transition frequencies of a transmon type qubit which is integrated into a transmission line cavity are spectroscopically determined for different detunings from the cavity [Fragner2008]. Since the observed Lamb shift of the qubit transition frequency is about 1.4% of the bare qubit transition frequency in the characterized sample, the parameters of the used device such as the flux dependent Josephson energy E_J , the charging energy E_{C0} as well as the coupling constant g have to be determined very precisely. The dressed transition frequency from qubit ground to qubit excited state is spectroscopically determined for different magnetic flux controlled detunings. Here, the Lamb shift is clearly observed as the difference of the measured frequencies to the bare qubit frequency which results from the qubit interaction with the vacuum field of the cavity.

In the dispersive limit, the qubit frequency is renormalized by the Lamb shift g^2/Δ and the photon number dependent AC-stark shift $2g^2\hat{a}^\dagger\hat{a}/\Delta$, compare Eq. (5.11). In order to check whether the observed shifts in the qubit transition frequency indeed results from vacuum fluctuations of the radiation field and not from an AC-stark effect by residual photons in the cavity, the cavity was populated with additional photons in order to observe photon number splitting [Schuster2007]. For a certain photon number, a Lamb shifted qubit frequency is then again clearly observed which confirms the above results. Reference [Fragner2008] reports in detail on the measurement.

5.9 Autler-Townes and Mollow Transitions

Another experiment which was enabled by the work presented in this thesis is the spectroscopic measurement of the *Autler-Townes doublet* [Autler1955] and the *Mollow triplet* [Mollow1969] in a circuit QED system [Baur2009].

A transmon type qubit integrated into a transmission line cavity is strongly driven with monochromatic microwaves such that the qubit Rabi oscillates between its ground and its excited state. The strong coherent drive leads to two frequency sidebands which are offset by the Rabi frequency from the main qubit transition frequency and which can spectroscopically be determined. When the drive is on resonance with the qubit, the bare states $|g, n\rangle$ and $|e, n-1\rangle$ with the qubit in the ground state $|g\rangle$ and n photons in the cavity, respectively the qubit in the first excited state $|e\rangle$ and $n-1$ photons in the cavity split up into the symmetric and antisymmetric superpositions $|\pm, n\rangle = |g, n\rangle \pm |e, n-1\rangle$ due to the qubit-cavity dipole coupling. The sideband transitions $|-, n\rangle \rightarrow |+, n+1\rangle$ as well as $|+, n\rangle \rightarrow |-, n+1\rangle$ together with the transition $|-, n\rangle \rightarrow |-, n+1\rangle$ respectively $|+, n\rangle \rightarrow |+, n+1\rangle$ can now be spectroscopically resolved as the Mollow triplet. The Autler-Townes doublet furthermore appears due to the transitions $|-, n+1\rangle \rightarrow |f, n+1\rangle$ and $|+, n+1\rangle \rightarrow |f, n+1\rangle$ into the third qubit level $|f\rangle$.

In the experiment, the qubit is strongly detuned from the resonator and strongly driven to induce the transition from qubit ground to qubit excited state. The qubit spectrum is subsequently probed

using a weak spectroscopy tone which is swept over a wide frequency range including frequencies which correspond to transitions from the first into the second respectively from the first into the third qubit level. The qubit drive and probe procedure is repeated for different drive powers. For drive powers above a certain threshold, peaks which correspond to the Autler-Townes doublet and the Mollow triplet emerge, see reference [Baur2009].

5.10 Two-Qubit State Preparations and Tomography

The experiments presented in references [Filipp2009] and [Leek2009] demonstrate the controlled preparation of two-qubit states as well as their characterization using quantum state tomography. Two transmon type qubits are integrated into a transmission line cavity and can be driven with individual gate lines.

The work which is reported in reference [Leek2009] makes use of sideband transitions in order to couple two qubits via a transmission line cavity. Here, the blue sideband transition $|g, 0\rangle \rightarrow |e, 1\rangle$ is driven in a two-photon process since the single photon process is forbidden to first order. The drive amplitude for sideband transitions has to be large since qubit and resonator are far detuned. Direct qubit and sideband transitions can be performed by using individual transmission lines which couple capacitively and individually to each qubit, see Fig. 3.26.

In the experiment, qubit-qubit entangled states are generated by applying a sequence of pulses on the system which is initially in the ground state $|g, g, 0\rangle$. A resonant π -pulse is first applied to qubit b, generating the state $|g, e, 0\rangle$. A $\pi/2$ -pulse is then applied on the blue sideband of qubit a which generates the entangled state $(|g, e, 0\rangle + e^{i\Phi} |e, e, 1\rangle)/\sqrt{2}$. The qubit-resonator entanglement is then transferred to qubit-qubit entanglement with a π -pulse on the blue sideband of qubit b, which generates the Bell state $(|g, e\rangle + e^{i\phi} |e, g\rangle)/\sqrt{2}$ and returns the resonator to its ground state. An additional resonant π -pulse can be applied to qubit a to generate the Bell state $(|g, g\rangle + e^{-i\phi} |e, e\rangle)/\sqrt{2}$. The Phase ϕ here depends on the phase difference between the two blue sideband pulses.

The two-qubit state is fully reconstructed by using state tomography. For this, the pulse sequence described above is carried out 16 times with different combinations of additional final single qubit rotations (identity, $\pi_x/2$, $\pi_y/2$ and π_x) on each qubit. The state of both qubits is then dispersively measured by transmitting a microwave pulse with a frequency close to the transmission line resonance where the resonator frequency is shifted by an amount which depends on the four two-qubit states $|g, g\rangle$, $|g, e\rangle$, $|e, g\rangle$ and $|e, e\rangle$ [Majer2007]. Reference [Leek2009] describes in detail the state preparation and reference [Filipp2009] reports on state tomography procedures.

6 Conclusion

Circuit quantum electrodynamics offers a powerful tool to study fundamental interactions between matter and light on the level of single energy quanta using superconducting electronic circuits. Quantum optics experiments can be performed in coupling regimes which are hardly accessible by atomic cavity quantum electrodynamics systems. Furthermore, circuit QED systems consisting of superconducting tunnel junctions and coplanar transmission line cavities can be realized by using well established micro- and nano-fabrication techniques and thus can be scaled up easily. Single or multiple qubits integrated into a transmission line cavity can be controlled and read out with microwaves applied to the transmission line. Distant qubits can be entangled via the cavity which is in particular interesting for a future quantum computing architecture.

The work conducted within the scope of this thesis established essential preconditions for performing a number of new circuit QED experiments within the Quantum Device Lab at ETH Zurich. Circuit QED devices were designed and fabricated in the ETH clean room FIRST and characterized at low temperatures. In particular, the virtual photon exchange between transmon type qubits via a transmission line cavity was studied in dependence on the detuning of both qubits from the cavity resonance. Here, the qubit-qubit interaction strength is explained by taking higher order cavity modes into account. Considerable contributions were also made to experiments probing the Jaynes-Cummings energy ladder spectroscopically and observing the Lamb shift in a circuit QED system. Furthermore, experiments were enabled where Autler-Townes and Mollow transitions were spectroscopically probed in a circuit QED system and where two-qubit entangled states were prepared and characterized using quantum state tomography.

The work presented here is an essential part of setting up the Quantum Device Lab at ETH Zurich which was founded only three years ago. A complete set of micro- and nano-fabrication processes for realizing tunable and fixed frequency superconducting transmission line resonators as well as Josephson junction qubits was successfully implemented and optimized in the ETH clean room facility FIRST from scratch. Materials were carefully characterized, process parameters were calibrated and precise processing descriptions were developed. An electron-beam evaporator, already existing in FIRST was upgraded with home-made equipment in order to fabricate Josephson junctions using the shadow evaporation technique. First Cooper pair box devices thus could be realized in FIRST and characterized at low temperatures already less than one year after lab foundation. A new electron beam evaporator was installed in FIRST for the special purpose of performing shadow evaporation. Also this machine was tested, processes were precisely calibrated and documented. Josephson tunnel junctions were characterized at room and at low temperatures and important parameters were analyzed. First tunable SQUID resonators were fabricated and tested. Transmon type qubits were designed and integrated into aluminum or niobium transmission line cavities on silicon or sapphire substrates and successfully characterized. The geometric properties of coplanar waveguide resonators were studied in the context of circuit QED and it was shown that electrical parameters can be precisely controlled and well described with theoretical lumped element and distributed element transmission matrix models. Fully functional circuit quantum electrodynamics systems were successfully realized from scratch and their operation was demonstrated which enabled to perform a number of new experiments.

6 Conclusion

The field of circuit quantum electrodynamics is quite young and part of basic research. Circuit QED systems recently gained much interest since in comparison to atomic cavity QED systems very strong couplings between an (artificial) atom and a cavity can be realized. Furthermore, circuit QED systems are potential useful for performing controlled quantum interactions between distant qubits which make these systems in principal interesting for quantum computer applications.

However, systems with only a small number of coupled qubits seem to be technologically feasible within the next years due to the fragility of the systems quantum states. Industrial products are not available until now, in contrast to the field of quantum cryptography where applications are ready to enter the commercial market. In order to push the field of quantum computation from basic to an industrial relevant applied research, a middle term goal must be the development of small applications on the long way to a large scale quantum information processor.

Semiconductor industry developed within the last fifty years to a 260 billion dollar business which is able to fabricate more than two billion transistors on a single chip. This was possible only since from begin on, sideproducts reached the market whose revenues in turn could be invested in research and the development of next generation devices. In this context, the combination of basic and applied research turned out to be especially fruitful.

Although basic research on quantum information systems is essential for gaining more understanding on quantum systems, it would be risky for the emerging field of quantum information processing to loose sight of practical applications. Moreover, it would be a pity not to harness the potential of quantum information systems for technological purposes by concentrating exclusively on fundamental objectives.

A Device Parameters

The following tables list the parameters of the circuit QED devices realized within the scope of this thesis. Table 1 gives a coarse description of qubit and resonator, where FM stands for fundamental mode and HM for harmonic mode. For all resonators, the number of the used optical mask is listed in brackets. Table 2 lists the resonator frequency f_0 , the quality factor Q , the maximum Josephson energy E_{J0} , the charging energy E_{C0} and the coupling constant g . Table 3 specifies the used substrate material and the metallization. Table 4 lists the spacing w_1 between island and resonator center conductor as well as the island length l_1 for Cooper pair box devices and further the width and spacing w_2 and the length l_2 of the finger capacitor structures of transmon devices. Table 5 specifies the sizes A_{JJ1} and A_{JJ2} of the two Josephson junctions of the qubit as well as the qubit loop size A_{Loop1} . Table 6 lists the sizes A_{JJ3} and A_{JJ4} of the two Josephson junctions forming the SQUID which is part of the resonator as well as the SQUID loop size A_{Loop2} in case of tunable resonator structures. Table 7 further gives the evaporation angles θ_1 , θ_2 and layer thicknesses d_1 , d_2 for the first respectively the second aluminum deposition of the qubits. Table 8 lists the oxidation times t_1 , t_2 , the oxidation pressures p_1 , p_2 and the gas mixtures for top and bottom layer oxidations of the qubit junctions. Table 9 gives the evaporation angles θ_3 , θ_4 and layer thicknesses d_3 , d_4 for the first respectively the second aluminum deposition of the SQUIDS in case of tunable resonator devices. Table 10 finally lists the oxidation times t_3 , t_4 , the oxidation pressures p_3 , p_3 and the gas mixtures for top and bottom layer oxidations of the SQUID junctions.

Properties of Qubit Devices 1				
ID	Qubit	Resonator	Measured	Cryostat
A	CPB, Single	HM, 1+1 finger, N2(M1)	08/13/2007	OXFORD
B	CPB, Single	HM, 1+1 finger, N2(M1)	08/21/2007	OXFORD
C	CPB, Single	HM, 1+1 finger, N2(M1)	10/10/2007	OXFORD
D	CPB, Single	HM, 1+1 finger, N2(M1)	10/26/2007	OXFORD
E	CPB, Single	HM, 1+1 finger, N2(M1)	11/12/2007	OXFORD
F	TRM, Single	FM, 1+1 finger, I2(M2)	11/28/2007	OXFORD
G	TRM, Double	HM, 2+2 finger, K6(M3)	02/21/2008	OXFORD
H	TRM, Double	FM, 1+1 finger, E3(M3)	03/26/2008	OXFORD
I	TRM, Single	HM, 1+1 finger, SQUID, L3(M4)	06/11/2008	VERICOLD
J	TRM, Single	HM, 1+1 finger, SQUID, M1(M4)	07/27/2008	VERICOLD

Properties of Qubit Devices 2					
ID	f_0 [GHz]	Q	E_{J0} [GHz]	E_{C0} [GHz]	g [MHz]
A	6.9	$1.0 \cdot 10^4$	6.2	2.4	5.3
B	6.9	$3.0 \cdot 10^2$	n.m.	n.m.	n.m.
C	6.9	$4.9 \cdot 10^3$	13	1.9	19
D	6.9	$1.5 \cdot 10^4$	22	1.9	9
E	6.9	$1.1 \cdot 10^4$	6.0	2.1	10
F	6.9	$8.8 \cdot 10^3$	45	0.48	150
G	6.5	$9.2 \cdot 10^2$	75/130	0.22/0.24	94/92
H	6.4	$4.1 \cdot 10^3$	35/38	0.23/0.23	133/134
I	-	-	n.m.	n.m.	n.m.
J	-	-	n.m.	n.m.	n.m.

A Device Parameters

Properties of Qubit Devices 3				
ID	Substrate	Metallization	Fabricated	Machine
A	Si/SiO _x	Nb	08/09/2007	LEYBOLD
B	Si/SiO _x	Nb	08/20/2007	LEYBOLD
C	Si/SiO _x	Nb	10/02/2007	PLASSYS
D	Si/SiO _x	Nb	10/02/2007	PLASSYS
E	Si/SiO _x	Nb	10/23/2007	PLASSYS
F	Si/SiO _x	Nb	11/26/2007	PLASSYS
G	Sapphire	Nb	02/16/2008	PLASSYS
H	Sapphire	Nb	03/06/2008	PLASSYS
I	Sapphire	Nb	05/28/2008	PLASSYS
J	Sapphire	Nb	07/10/2008	PLASSYS

Properties of Qubit Devices 4				
ID	w_1 [nm]	l_1 [μ m]	w_2 [μ m]	l_2 [μ m]
A	1100	10	-	-
B	300	50	-	-
C	300	50	-	-
D	1100	50	-	-
E	700	50	-	-
F	-	-	3	13
G	-	-	2	14
H	-	-	2	14
I	-	-	3	13
J	-	-	3	13

Properties of Qubit Devices 5			
ID	A_{JJ1} [nm ²]	A_{JJ2} [nm ²]	A_{Loop1} [μ m ²]
A	200×300	200×300	5
B	200×300	200×300	3
C	200×300	200×300	3
D	200×300	200×300	3
E	200×300	200×300	3
F	200×300	200×300	6
G	200×300	200×300	6
H	200×300	200×300	6
I	200×300	200×300	6
J	200×300	200×300	6

Properties of Qubit Devices 6			
ID	A_{JJ3} [nm ²]	A_{JJ4} [nm ²]	A_{Loop2} [μ m ²]
A	-	-	-
B	-	-	-
C	-	-	-
D	-	-	-
E	-	-	-
F	-	-	-
G	-	-	-
H	-	-	-
I	800×2000	800×3000	30
J	800×2000	800×2000	15

Properties of Qubit Devices 7				
ID	d_1 [nm]	θ_1 [°]	d_2 [nm]	θ_2 [°]
A	20	0	60	30
B	20	0	60	30
C	15	0	60	30
D	15	0	60	30
E	15	0	60	30
F	30	0	100	30

To be continued on next page...

ID	d_1 [nm]	θ_1 [°]	d_2 [nm]	θ_2 [°]
G	20	0	80	30
H	20	0	80	30
I	20	0	80	30
J	20	0	80	30

Properties of Qubit Devices 8						
ID	t_1 [sec]	p_1 [Torr]	gas ₁	t_2 [sec]	p_2 [Torr]	gas ₂
A	180	15	15%O ₂ /85%Ar	15	15	15%O ₂ /85%Ar
B	180	15	15%O ₂ /85%Ar	15	15	15%O ₂ /85%Ar
C	300	10	100%O ₂	15	10	100%O ₂
D	300	10	100%O ₂	15	10	100%O ₂
E	300	10	100%O ₂	15	10	100%O ₂
F	80	1	15%O ₂ /85%Ar	15	10	100%O ₂
G	80	1	15%O ₂ /85%Ar	15	10	100%O ₂
H	300	1	15%O ₂ /85%Ar	15	10	100%O ₂
I	300	1	15%O ₂ /85%Ar	15	10	100%O ₂
J	300	1	15%O ₂ /85%Ar	15	10	100%O ₂

Properties of Qubit Devices 9				
ID	d_3 [nm]	θ_3 [°]	d_4 [nm]	θ_4 [°]
A	-	-	-	-
B	-	-	-	-
C	-	-	-	-
D	-	-	-	-
E	-	-	-	-
F	-	-	-	-
G	-	-	-	-
H	-	-	-	-
I	30	-30	150	+30
J	30	-30	150	+30

Properties of Qubit Devices 10						
ID	t_3 [sec]	p_3 [Torr]	gas ₃	t_4 [sec]	p_4 [Torr]	gas ₄
A	-	-	-	-	-	-
B	-	-	-	-	-	-
C	-	-	-	-	-	-
D	-	-	-	-	-	-
E	-	-	-	-	-	-
F	-	-	-	-	-	-
G	-	-	-	-	-	-
H	-	-	-	-	-	-
I	80	1	15%O ₂ /85%Ar	15	10	100%O ₂
J	80	1	15%O ₂ /85%Ar	15	10	100%O ₂

B Designs of Fabricated Circuit QED Devices

Devices

In the following, computer aided designs (CAD) of fabricated Cooper pair box and transmon type qubits which are used for electron beam exposure are presented. Shown are the main and also additional undercut exposure regions. One can also see center conductor and gaps between centerconductor and groundplane of the coplanar waveguide resonators. Further, alignment crosses and scan fields for mark detection during electron beam calibration are shown.

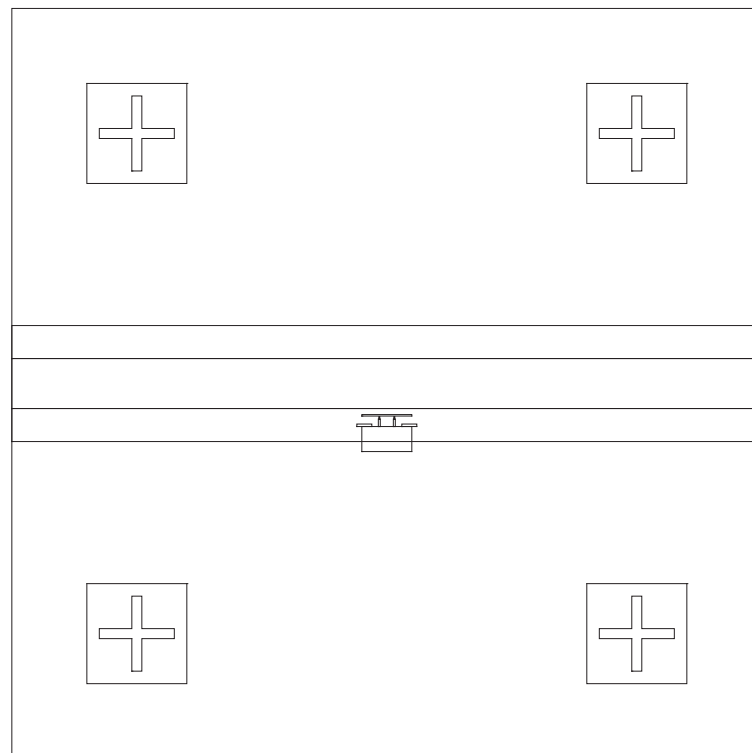


Figure B.1: Computer aided design (CAD) image of the Cooper pair box qubit which is part of device A.

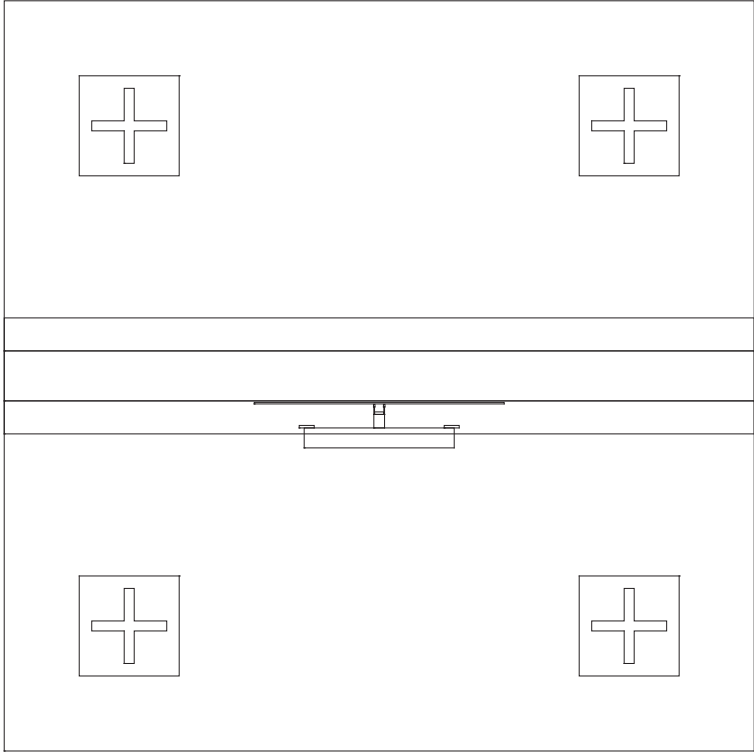


Figure B.2: Computer aided design (CAD) image of the Cooper pair box qubit which is part of device B.

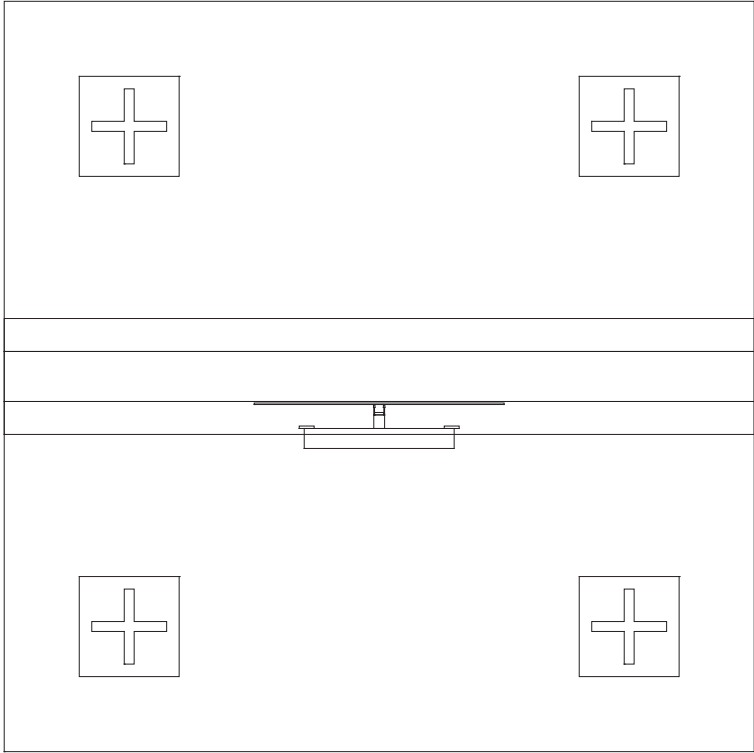


Figure B.3: Computer aided design (CAD) image of the Cooper pair box qubit which is part of device C.

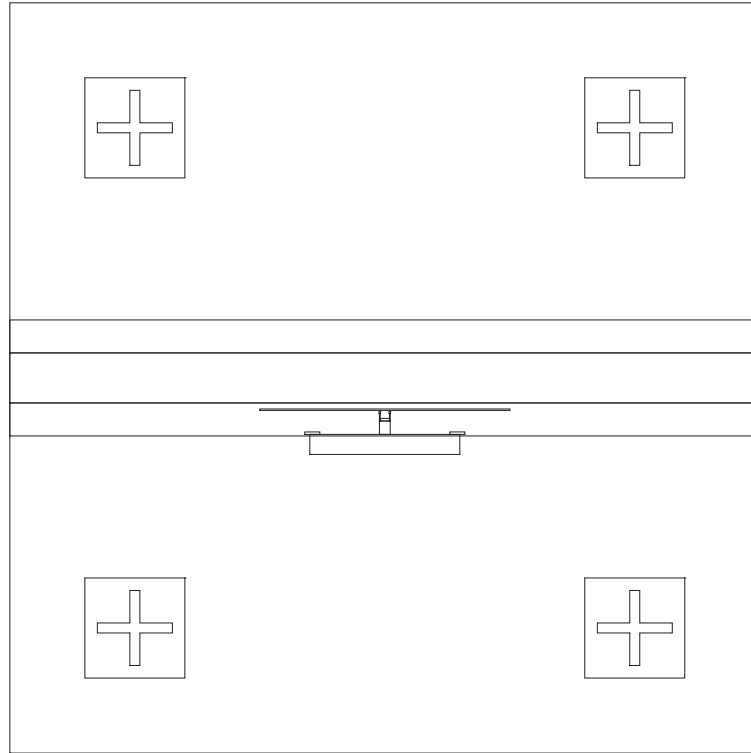


Figure B.4: Computer aided design (CAD) image of the Cooper pair box qubit which is part of device D.

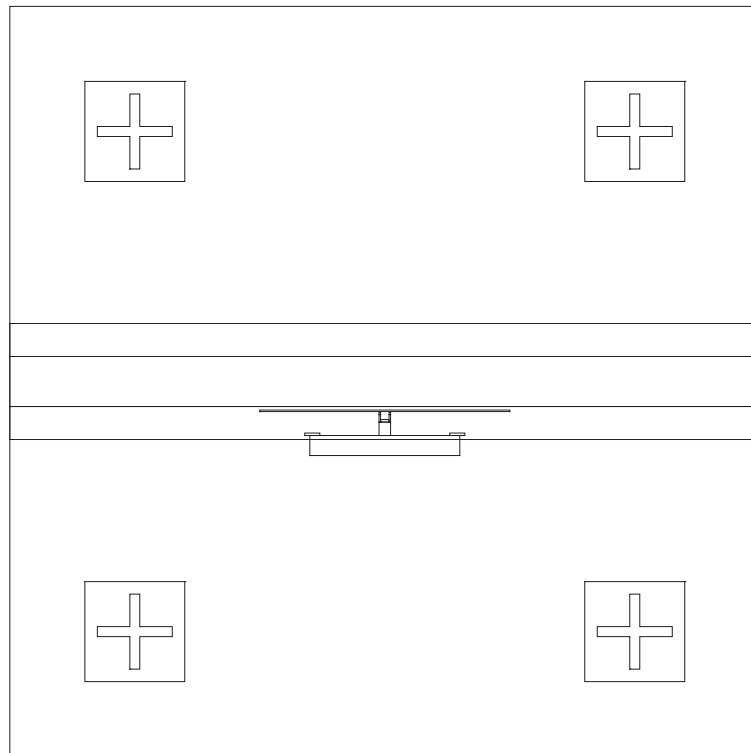


Figure B.5: Computer aided design (CAD) image of the Cooper pair box qubit which is part of device E.

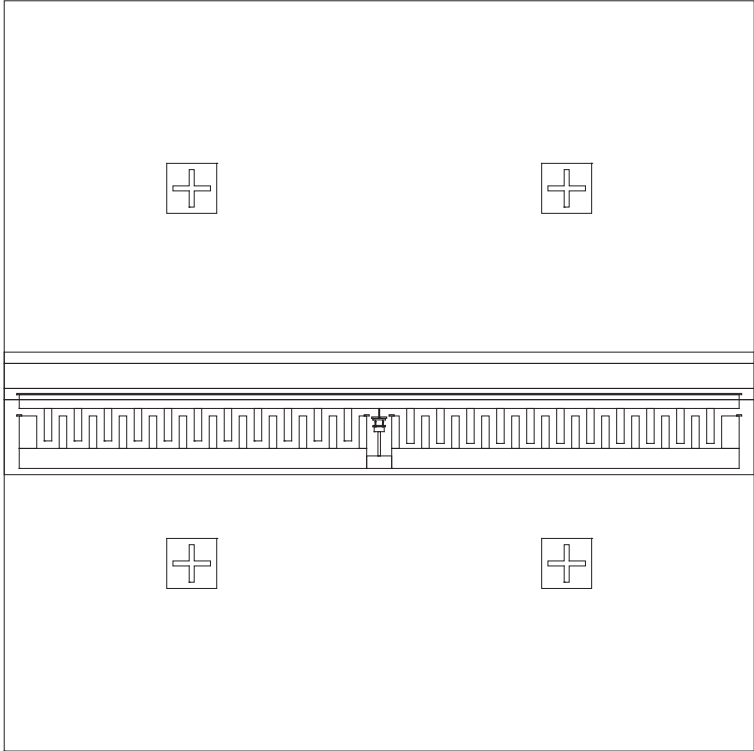


Figure B.6: Computer aided design (CAD) image of the transmon type qubit which is part of device F.

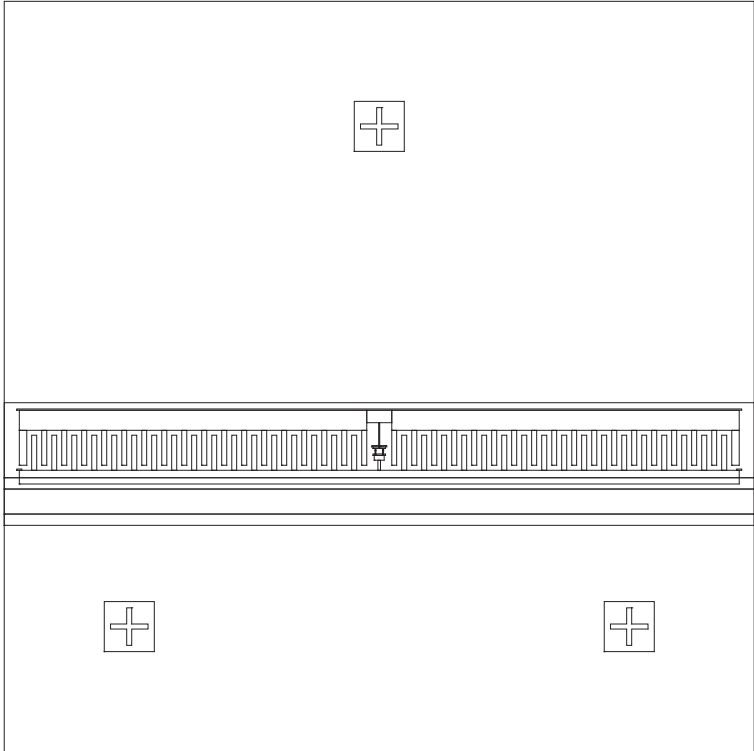


Figure B.7: Computer aided design (CAD) image of the first transmon type qubit which is part of device G.

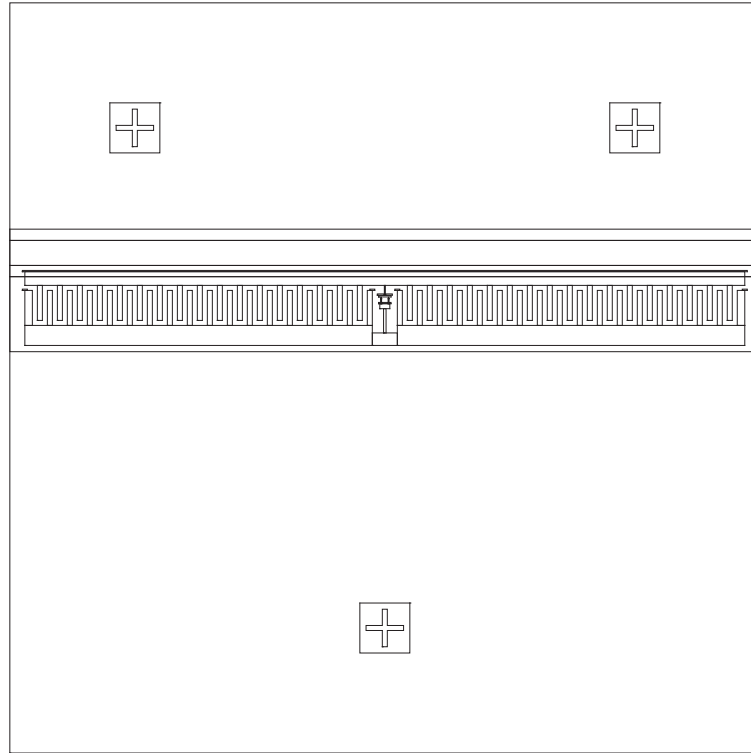


Figure B.8: Computer aided design (CAD) image of the second transmon type qubit which is part of device G.

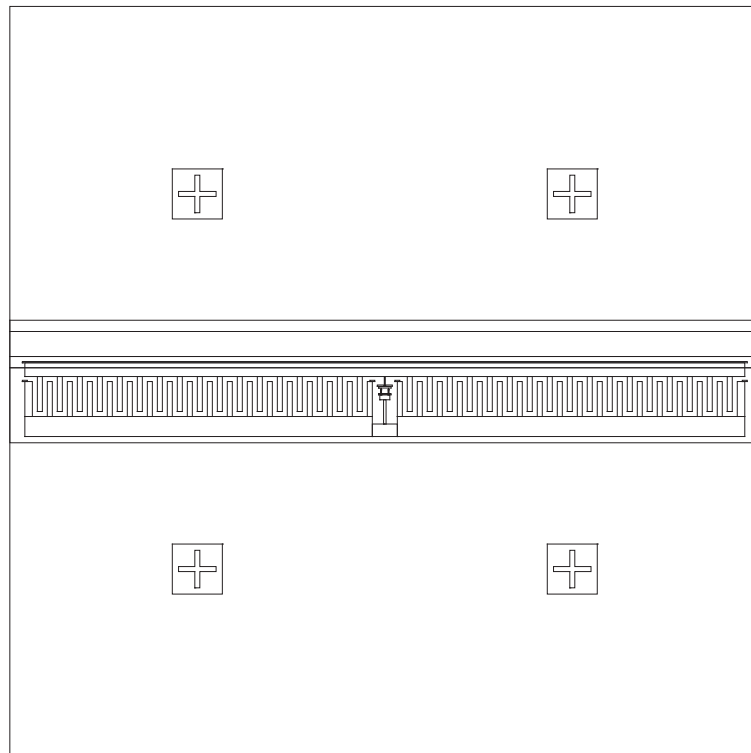


Figure B.9: Computer aided design (CAD) image of the two transmon type qubit which is part of device H.

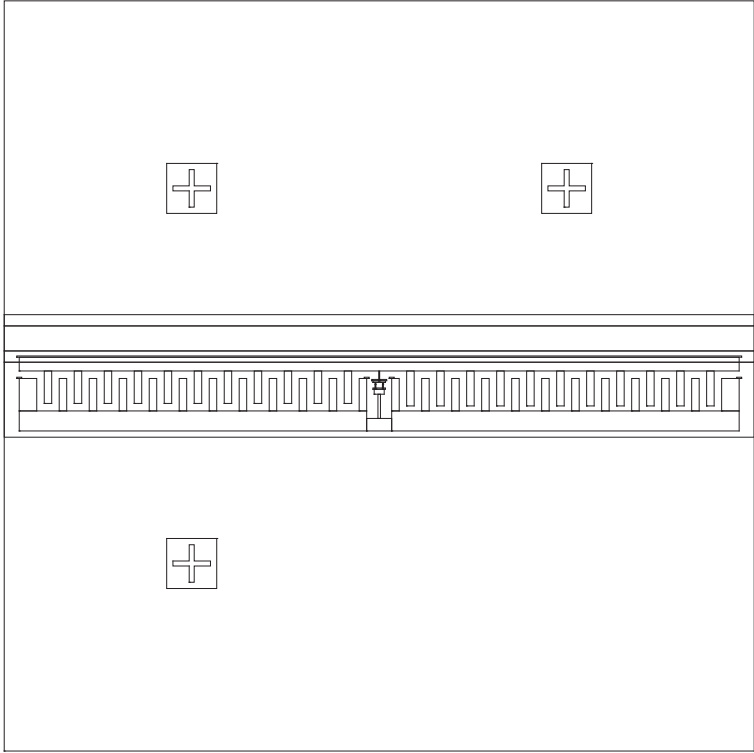


Figure B.10: Computer aided design (CAD) image of the transmon type qubit which is part of device I.

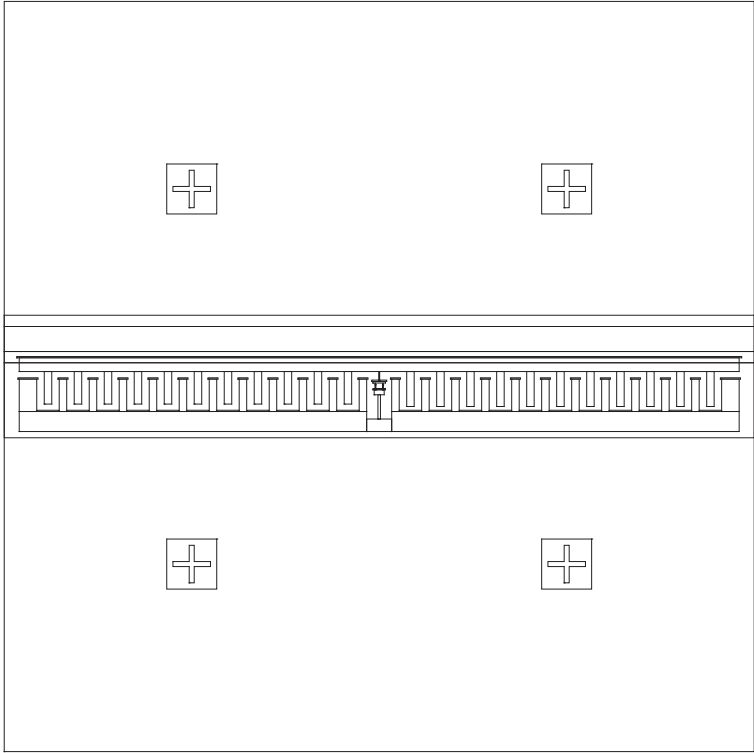


Figure B.11: Computer aided design (CAD) image of the transmon type qubit which is part of device J.

C Optical Lithography

maN-405 Negativ Resist Process for Etching		
Process step	Description	Comments
Cleaning of wafer	<p>Sonicate wafer in acetone for 2 minutes at power 2 in 40 kHz ultrasonic bath</p> <p>Sonicate wafer in acetone for 2 minutes at power 2 in 40 kHz ultrasonic bath</p> <p>Sonicate wafer in isopropanol for 2 minutes at power 2 in 40 kHz ultrasonic bath</p> <p>Sonicate wafer in water for 2 minutes at power 2 in 40 kHz ultrasonic bath</p> <p>blow dry wafer with nitrogene</p>	
Dehydration of wafer	<p>Bake wafer on hotplate at 200 °C for 10 minutes</p> <p>Cooldown wafer for 5 minutes</p>	
Resist spinning and bake out	<p>Spin maN-405 resist with 3000 rpm and acceleration 8 for 60 seconds</p> <p>Remove backside resist with acetone</p> <p>Remove edge bead carfully with acetone</p> <p>Bake wafer on hotplate at 95 °C for 60 seconds</p> <p>Remove edge bead carfully with acetone again</p>	<p>Clean new pipette carefully with nitrogene gun then cover wafer totally with resist, wait 10 seconds and start spinning</p>
UV exposure with mask aligner Karl Suss MA6	<p>Clean mask in mask cleaner with acetone, isopropanol and water</p> <p>Start up maskaligner, wait at least 20 minutes for warm up, perform intensity test with 365 nm intensity meter and calculate the exposure time</p> <p>maN-405 resist needs a dose of 350 mJ/cm² at 365 nm</p> <p>Check MA6 parameters:</p> <p>Gap: 20 μm WEC offset: 0 WEC type: cont Exposure type: vac</p>	<p>Typical UV lamp intensities of 4 to 6 mW/cm² at 365 nm are measured</p>
To be continued on next page...		

C Optical Lithography

Process step	Description	Comments
	<p>PreVac: 5 sec FullVac: 15 sec PurgeVac: 10 sec</p> <p>Mount mask on maskholder, blow off mask and load mask</p> <p>Mount wafer on chuck, blow off wafer and load wafer</p> <p>Perform mask alignment procedure</p> <p>Perform alignment check before exposure</p> <p>Expose structures with calculated exposure time</p>	<p>Check critical structures for dust particles or scratches</p>
<p>Development of maN-405 resist</p>	<p>Develop wafer in maD-332 S for 1 minute</p> <p>Stop developer in water for 1 minute</p> <p>Change bath and stop developer again in water for another minute</p> <p>Blow dry wafer with nitrogene</p> <p>Check development process under microscope</p> <p>Develop wafer in maD-332 S typically for another 20 seconds</p> <p>Stop developer in water for 1 minute</p> <p>Change bath and stop developer again in water for another minute</p> <p>Blow dry wafer with nitrogene</p>	<p>Development process has to be controlled by eye, development times can vary</p> <p>Development process has to be controlled by eye, development times can vary</p>
<p>Resist strip procedure after etching</p>	<p>Sonicate wafer in acetone for 5 minutes at 50 °C at power 2 in 40 kHz ultrasonic bath</p> <p>Sonicate wafer in acetone for 5 minutes at 50 °C at power 2 in 40 kHz ultrasonic bath</p> <p>Sonicate wafer in NMP for 5 minutes at 50 °C at power 2 in 40 kHz ultrasonic bath</p> <p>Sonicate wafer in acetone for 5 minutes at 50 °C at power 2 in 40 kHz ultrasonic bath</p> <p>Sonicate wafer in isopropanol for 5 minutes at 50 °C at power 2 in 40 kHz ultrasonic bath</p> <p>blow dry wafer with nitrogene</p>	<p>Check applicability of resist strip procedure always with view to individual device structure, if necessary use of ultrasonic bath has to be reduced</p>

AZ1505 Positive Resist Process for Etching		
Process step	Description	Comments
Cleaning of wafer	<p>Sonicate wafer in acetone for 2 minutes at power 2 in 40 kHz ultrasonic bath</p> <p>Sonicate wafer in acetone for 2 minutes at power 2 in 40 kHz ultrasonic bath</p> <p>Sonicate wafer in isopropanol for 2 minutes at power 2 in 40 kHz ultrasonic bath</p> <p>Sonicate wafer in water for 2 minutes at power 2 in 40 kHz ultrasonic bath</p> <p>blow dry wafer with nitrogene</p>	
Dehydration of wafer	<p>Bake wafer on hotplate at 200 °C for 10 minutes</p> <p>Cooldown wafer for 5 minutes</p>	
Resist spinning and bake out	<p>Spin HMDS adhesion primer with 4000 rpm and acceleration 8 for 60 seconds</p> <p>Spin AZ1505 resist with 4000 rpm and acceleration 8 for 60 seconds</p> <p>Remove backside resist with acetone</p> <p>Remove edge bead carfully with acetone</p> <p>Bake wafer on hotplate at 100 °C for 60 seconds</p> <p>Remove edge bead carfully with acetone again</p>	<p>Clean new pipette carefully with nitrogene gun then cover wafer totally with resist, wait 10 seconds and start spinning</p> <p>Clean new pipette carefully with nitrogene gun then cover wafer totally with resist, wait 10 seconds and start spinning</p>
UV exposure with mask aligner Karl Suss MA6	<p>Clean mask in mask cleaner with acetone, isopropanol and water</p> <p>Start up maskaligner, wait at least 20 minutes for warm up, perform intensity test with 405 nm intensity meter and calculate the exposure time</p> <p>AZ1505 resist needs a dose of 130 mJ/cm² at 405 nm</p> <p>Check MA6 parameters:</p> <p>Gap: 20 μm WEC offset: 0 WEC type: cont Exposure type: vac PreVac: 5 sec FullVac: 15 sec PurgeVac: 10 sec</p> <p>Mount mask on maskholder, blow off mask and load mask</p>	<p>Typical UV lamp intensities of 8 to 10 mW/cm² at 405 nm are measured</p>

To be continued on next page...

Process step	Description	Comments
	<p>Mount wafer on chuck, blow off wafer and load wafer</p> <p>Perform mask alignment procedure</p> <p>Perform alignment check before exposure</p> <p>Expose structures with calculated exposure time</p>	<p>Check critical structures for dust particles or scratches</p>
Development of AZ1505 resist	<p>Develop wafer in a mixture of 25 ml AZ developer and 75ml water for 75 seconds</p> <p>Stop developer in water for 1 minute</p> <p>Change bath and stop developer again in water for another minute</p> <p>Blow dry wafer with nitrogene</p> <p>Check development process under microscope</p>	<p>Development process has to be controlled by eye, development times can vary</p>
Resist strip procedure after etching	<p>Sonicate wafer in acetone for 5 minutes at 50 °C at power 2 in 40 kHz ultrasonic bath</p> <p>Sonicate wafer in acetone for 5 minutes at 50 °C at power 2 in 40 kHz ultrasonic bath</p> <p>Sonicate wafer in NMP for 5 minutes at 50 °C at power 2 in 40 kHz ultrasonic bath</p> <p>Sonicate wafer in acetone for 5 minutes at 50 °C at power 2 in 40 kHz ultrasonic bath</p> <p>Sonicate wafer in isopropanol for 5 minutes at 50 °C at power 2 in 40 kHz ultrasonic bath</p> <p>blow dry wafer with nitrogene</p>	<p>Check applicability of resist strip procedure always with view to individual device structure, if necessary use of ultrasonic bath has to be reduced</p>

maN-1410 Negativ Resist Process for Metal Evaporation		
Process step	Description	Comments
Cleaning of wafer	<p>Sonicate wafer in acetone for 2 minutes at power 2 in 40 kHz ultrasonic bath</p> <p>Sonicate wafer in acetone for 2 minutes at power 2 in 40 kHz ultrasonic bath</p> <p>Sonicate wafer in isopropanol for 2 minutes at power 2 in 40 kHz ultrasonic bath</p> <p>Sonicate wafer in water for 2 minutes at power 2 in 40 kHz ultrasonic bath</p> <p>blow dry wafer with nitrogene</p>	
To be continued on next page...		

Process step	Description	Comments
Dehydration of wafer	Bake wafer on hotplate at 200 °C for 10 minutes Cooldown wafer for 5 minutes	
Resist spinning and bake out	Spin HMDS adhesion primer with 3000 rpm and acceleration 8 for 60 seconds Spin maN-1410 resist with 3000 rpm and acceleration 8 for 60 seconds Remove backside resist with acetone Remove edge bead carefully with acetone Bake wafer on hotplate at 100 °C for 90 seconds Remove edge bead carefully with acetone again	Clean new pipette carefully with nitrogen gun then cover wafer totally with resist, wait 10 seconds and start spinning Clean new pipette carefully with nitrogen gun then cover wafer totally with resist, wait 10 seconds and start spinning
UV exposure with mask aligner Karl Suss MA6	Clean mask in mask cleaner with acetone, isopropanol and water Start up maskaligner, wait at least 20 minutes for warm up, perform intensity test with 365 nm intensity meter and calculate the exposure time maN-1410 resist needs a dose of 450 mJ/cm ² at 365 nm Check MA6 parameters: Gap: 20 μm WEC offset: 0 WEC type: cont Exposure type: vac PreVac: 5 sec FullVac: 15 sec PurgeVac: 10 sec Mount mask on maskholder, blow off mask and load mask Mount wafer on chuck, blow off wafer and load wafer Perform mask alignment procedure Perform alignment check before exposure Expose structures with calculated exposure time	Typical UV lamp intensities of 4 to 6 mW/cm ² at 365 nm are measured Check critical structures for dust particles or scratches
Development of maN-1410 resist	Develop wafer in maD-533 S for 1 minute	Development process has to be controlled by eye, development times can vary
To be continued on next page...		

C Optical Lithography

Process step	Description	Comments
	<p>Stop developer in water for 1 minute</p> <p>Change bath and stop developer again in water for another minute</p> <p>Blow dry wafer with nitrogene</p> <p>Check development process under microscope</p> <p>Develop wafer in maD-533 S typically for another 30 seconds</p> <p>Stop developer in water for 1 minute</p> <p>Change bath and stop developer again in water for another minute</p> <p>Blow dry wafer with nitrogene</p>	<p>Development process has to be controlled by eye, development times can vary</p>
<p>Resist strip procedure after metallization</p>	<p>Sonicate wafer in acetone for 5 minutes at 50 °C at power 2 in 40 kHz ultrasonic bath</p> <p>Sonicate wafer in acetone for 5 minutes at 50 °C at power 2 in 40 kHz ultrasonic bath</p> <p>Sonicate wafer in NMP for 5 minutes at 50 °C at power 2 in 40 kHz ultrasonic bath</p> <p>Sonicate wafer in acetone for 5 minutes at 50 °C at power 2 in 40 kHz ultrasonic bath</p> <p>Sonicate wafer in isopropanol for 5 minutes at 50 °C at power 2 in 40 kHz ultrasonic bath</p> <p>blow dry wafer with nitrogene</p>	<p>Check applicability of resist strip procedure always with view to individual device structure, if necessary use of ultrasonic bath has to be reduced</p>

D Reactiv Ion Etching

Etching Procedure for Niobium Thin Films		
Process step	Description	Comments
Machine preparations	<p>Switch on "Mains" of heater chiller in grey room, check proper cooling water flow and temperature</p> <p>Switch on RF generator in machine cabinet</p> <p>Use the following machine adjustments:</p> <p>Preset: Local Tune: Auto Meter select: CapPos AC: On Pressure controller: Remote AC line: On Meter: Forward RF Power: Remote Power Adjust: 0</p>	<p>If cooling water does not flow, try several times switching "Cooling" on or off; temperature must be stabilized around 20 °C</p>
Cleaning procedure	<p>Vent chamber and clean chamber with iso-propanol</p> <p>Pump down chamber and start the cleaning process:</p> <p>Base pressure: 9×10^{-5} mbar O₂ flow: 100 sccm RF Power: 150 W Process pressure: 1.3×10^{-2} mbar Temperature: 10 °C Time: 30 minutes</p>	
Etching procedure	<p>Load niobium test sample and perform etch check</p> <p>Use the following parameters for niobium etching</p> <p>Base pressure: 9×10^{-5} mbar Ar flow: 10 sccm SF₆ flow: 20 sccm RF Power: 100 W Process pressure: 1.3×10^{-2} mbar Temperature: 17 °C</p> <p>The following etch rates were determined:</p> <p>Si: 186 nm/sec SiO₂: 31 nm/sec Nb: 85 nm/sec</p>	<p>Check process conditions during etching and write down protocol</p> <p>Always over-etch structures slightly if possible to make sure the full removal of niobium</p>
To be continued on next page...		

D Reactive Ion Etching

Process step	Description	Comments
	<p>maN-405 resist: 83 nm/sec PMMA resist: 121 nm/sec</p> <p>Check etching result after cleaning of test sample under microscope and SEM</p> <p>Load niobium wafer and etch under same process conditions</p> <p>Unload and clean wafer</p>	<p>Check process conditions during etching and write down protocol</p>

E Electron Beam Lithography

PMMA Double Layer Resist Process for Silicon Wafers		
Process step	Description	Comments
Cleaning of wafer	<p>Sonicate wafer in acetone for 2 minutes at power 2 in 40 kHz ultrasonic bath</p> <p>Sonicate wafer in acetone for 2 minutes at power 2 in 40 kHz ultrasonic bath</p> <p>Sonicate wafer in isopropanol for 2 minutes at power 2 in 40 kHz ultrasonic bath</p> <p>blow dry wafer with nitrogene</p>	
Dehydration of wafer	<p>Bake wafer on hotplate at 120 °C for 5 minutes</p> <p>Cooldown wafer for 5 minutes</p>	
Resist spinning and bake out	<p>Spin pure PMMA/MAA resist with 3000 rpm and acceleration 8 for 60 seconds (corresponds to a resist thickness of approximately 660 nm)</p> <p>Remove backside resist with acetone</p> <p>Bake wafer on hotplate at 180 °C for 5 minutes</p> <p>Wait 5 minutes for cooldown of wafer</p> <p>Spin 1:1 PMMA 950k:C-Thinner resist with 3000 rpm and acceleration 8 for 60 seconds (corresponds to a resist thickness of approximately 120 nm)</p> <p>Remove backside resist with acetone</p> <p>Bake wafer on hotplate at 180 °C for 30 minutes</p>	<p>Clean new pipette carefully with nitrogene gun then cover chip totally with resist, wait 10 seconds and start spinning (spinner cover is open)</p> <p>Clean new pipette carefully with nitrogene gun then cover chip totally with resist, wait 10 seconds and start spinning (spinner cover is open)</p>
Electron beam exposure of double layer resist	<p>Use 30 kV electrons for electron beam lithography (EBL) exposue</p> <p>The following doses are typically used for qubit structures:</p> <p>Large structures: 300 to 350 $\mu\text{C}/\text{cm}^2$</p> <p>Small structures: 350 to 400 $\mu\text{C}/\text{cm}^2$</p> <p>Undercut boxes: 50 to 100 $\mu\text{C}/\text{cm}^2$</p>	
To be continued on next page...		

Process step	Description	Comments
Development of PMMA resist	Develop sample in 1:3 MIBK:IPA for 50 seconds	Variations of development time in order of seconds should not be critical for the process
	Rinse wafer in isopropanol for 10 seconds	Variations of development time in order of seconds should not be critical for the process
	Blow dry wafer with nitrogene	
Resist strip procedure after metal evaporation	Strip resist in acetone at 50 °C for 2 hours	Prepare sample in vertical position on aluminum block
	Rinse sample with acetone	
	Clean sample in acetone at 50 °C for 5 minutes	
	Apply ultrasonic agitation in 40 kHz bath at power 1 for 30 seconds	
	Rinse sample with acetone	
	Clean sample in isopropanol for 5 minutes	
	Blow dry sample with nitrogen	

PMMA Double Layer Resist Process for Sapphire Wafers		
Process step	Description	Comments
Cleaning of wafer	Sonicate wafer in acetone for 2 minutes at power 2 in 40 kHz ultrasonic bath	
	Sonicate wafer in acetone for 2 minutes at power 2 in 40 kHz ultrasonic bath	
	Sonicate wafer in isopropanol for 2 minutes at power 2 in 40 kHz ultrasonic bath	
	blow dry wafer with nitrogene	
Dehydration of wafer	Bake wafer on hotplate at 120 °C for 5 minutes	
	Cooldown wafer for 5 minutes	
Resist spinning and bake out	Spin pure PMMA/MAA resist with 3000 rpm and acceleration 8 for 60 seconds (corresponds to a resist thickness of approximately 640 nm)	Clean new pipette carefully with nitrogene gun then cover chip totally with resist, wait 10 seconds and start spinning (spinner cover is open)
	Remove backside resist with acetone	
	Bake wafer on hotplate at 180 °C for 5 minutes	
	Wait 5 minutes for cooldown of wafer	
To be continued on next page...		

Process step	Description	Comments
	<p>Spin 1:1 PMMA 950k:C-Thinner resist with 3000 rpm and acceleration 8 for 60 seconds (corresponds to a resist thickness of approximately 120 nm)</p> <p>Remove backside resist with acetone</p> <p>Bake wafer on hotplate at 180 °C for 30 minutes</p>	Clean new pipette carefully with nitrogen gun then cover chip totally with resist, wait 10 seconds and start spinning (spinner cover is open)
Evaporation of discharge layer	Evaporate a layer of 5 nm aluminum on top of double layer resist	Metal layer should not be thinner than 3 nm and thicker than 10 nm
Electron beam exposure of double layer resist	<p>Use 30 kV electrons for electron beam lithography (EBL) exposure</p> <p>The following doses are typically used for qubit structures:</p> <p>Large structures: 300 to 350 $\mu\text{C}/\text{cm}^2$ Small structures: 350 to 400 $\mu\text{C}/\text{cm}^2$ Undercut boxes: 50 to 100 $\mu\text{C}/\text{cm}^2$</p>	
Development of PMMA resist	<p>Remove aluminum top layer in 10% NaOH for 50 seconds</p> <p>Rinse wafer in water for 10 seconds</p> <p>Develop sample in 1:3 MIBK:IPA for 50 seconds</p> <p>Rinse wafer in isopropanol for 10 seconds</p> <p>Blow dry wafer with nitrogen</p>	<p>Variations of development time in order of seconds should not be critical for the process</p> <p>Variations of development time in order of seconds should not be critical for the process</p> <p>Variations of development time in order of seconds should not be critical for the process</p> <p>Variations of development time in order of seconds should not be critical for the process</p>
Resist strip procedure after metal evaporation	<p>Strip resist in acetone at 50 °C for 2 hours</p> <p>Rinse sample with acetone</p> <p>Clean sample in acetone at 50 °C for 5 minutes</p> <p>Rinse sample with acetone</p> <p>Clean sample in isopropanol for 5 minutes</p> <p>Blow dry sample with nitrogen</p>	Prepare sample in vertical position on aluminum block

ZEP520A Single Layer Resist Process for Silicon Wafers

Process step	Description	Comments
To be continued on next page...		

Process step	Description	Comments
Cleaning of wafer	<p>Sonicate wafer in acetone for 2 minutes at power 2 in 40 kHz ultrasonic bath</p> <p>Sonicate wafer in acetone for 2 minutes at power 2 in 40 kHz ultrasonic bath</p> <p>Sonicate wafer in isopropanol for 2 minutes at power 2 in 40 kHz ultrasonic bath</p> <p>Blow dry wafer with nitrogene</p>	
Dehydration of wafer	<p>Bake wafer on hotplate at 120 °C for 5 minutes</p> <p>Cooldown wafer for 5 minutes</p>	
Resist spinning and bake out	<p>Spin pure ZEP520A resist with 6000 rpm and acceleration 8 for 60 seconds (corresponds to a resist thickness of approximately 300 nm)</p> <p>Remove backside resist with acetone</p> <p>Bake wafer on hotplate at 200 °C for 2 minutes</p>	Clean new pipette carefully with nitrogene gun then cover chip totally with resist, wait 10 seconds and start spinning (spinner cover is open)
Electron beam exposure of single layer resist	<p>Use 30 kV electrons for electron beam lithography (EBL) exposue</p> <p>Clearing dose of 300 nm thick ZEP520A at 30 kV is typically around $60\mu\text{C}/\text{cm}^2$</p>	
Development of ZEP520A resist	<p>Develop wafer in pure n-Amylacetate for 60 seconds</p> <p>Rinse wafer in 9:1 MIBK:IPA for 10 seconds</p> <p>Blow dry wafer with nitrogene</p>	<p>Variations of development time in order of seconds should not be critical for the process</p> <p>Variations of development time in order of seconds should not be critical for the process</p>
Resist strip procedure after metal evaporation or etching	<p>Strip resist in acetone at 50 °C for 2 hours</p> <p>Rinse sample with acetone</p> <p>Strip resist in NMP at 50 °C for 30 minutes</p> <p>Apply ultrasonic agitation in 40 kHz bath at power 1 for 30 seconds</p> <p>Rinse sample with acetone</p> <p>Clean sample in acetone at 50 °C for 5 minutes</p> <p>Rinse sample with acetone</p> <p>Clean sample in isopropanol for 5 minutes</p>	Prepare sample in vertical position on aluminum block
To be continued on next page...		

Process step	Description	Comments
	Blow dry sample with nitrogen	

Electron Beam Exposure with RAITH 150 System		
Process step	Description	Comments
Loading procedure	<p>Clean metal contacts on sample holder with isopropanol and nitrogen gun</p> <p>Mount sample on wafer holder</p> <p>Mount alignment chip with predefined marker pattern on wafer holder or scratch sample in a corner</p> <p>Log onto RAITH computer, start LEO- and RAITH software</p> <p>Choose your project</p> <p>Press "load sample"</p> <p>When loading is finished press "drive stage to home position" and "reset coordinate system"</p>	<p>Cleaning of contacts avoids current fluctuations while measuring the beam current</p> <p>Alignment chip must have same thickness as sample chip</p> <p>LEO software must be started before to avoid communication problems</p> <p>Loading takes about 11 minutes</p>
High voltage start up	<p>Set EHT to 21 kV and aperture size to 10, 30 or 120 μm and wait 5 minutes</p> <p>Set EHT to 25 kV and aperture size to 10, 30 or 120 μm and wait 5 minutes</p> <p>Set EHT to 30 kV and aperture size to 10 or 30 μm and wait at least 10 to 15 minutes</p> <p>Use predefined values for stigmation and aperture settings</p>	<p>Use 10 μm aperture to write fine structures and 30 or 120 μm aperture to write coarse structures</p>
File preparation	<p>Set up and save your position list</p> <p>Check the structures to expose</p>	<p>Check especially position, layer and dose factor</p> <p>Structure files should not be prepared on machine to avoid scheduling conflicts</p>
Alignment procedure	<p>Type "18.5z" in menu of stage control</p> <p>Choose "SE2" as detector in LEO software</p> <p>Set correct write field size and magnification</p> <p>Drive to Faraday cup and correct user position</p> <p>Check stability of beam current</p>	<p>Stage moves upwards</p> <p>Use 300 μm as write field size for qubit structures</p> <p>If beam current is not stable unload sample and clean sample-holder again</p>
To be continued on next page...		

Process step	Description	Comments
	<p>Perform origin correction on upper left corner of sample after choosing the right magnification</p> <p>Perform angle correction on upper left and upper right corner of sample after choosing the right magnification</p> <p>Disable automatic focus correction</p> <p>Perform coarse 3-point alignment on the outer set of alignment crosses of the chip</p> <p>Use contamination dot technique to focus in center of 100 μm alignment crosses</p> <p>Perform stigmatism correction on contamination dot</p> <p>Perform aperture correction by wobbling focus</p> <p>Drive to alignment chip with marker structure or to the scratch on the wafer made before loading to perform write field alignment</p> <p>Perform 3-point alignment on the inner set of alignment crosses of the chip</p>	<p>The crosshair position depends on the magnification</p> <p>The crosshair position depends on the magnification</p> <p>The crosshair position depends on the magnification</p> <p>Focus coarse on edge of alignment crosses first, final dots should be approximately 20 to 30 nm in size</p> <p>Use focus control to round the detector picture of the dot and then sharpen the picture in x- and y-direction with stigmator control</p> <p>Start with small wobble amplitude of 5% and go up to 15 or 20%</p> <p>Start with field size 40 μm, go down to 5 μm and repeat alignment procedure for 2 μm field size at least three times</p> <p>The crosshair position depends on the magnification</p>
<p>Setting up the exposure parameters and starting the writing procedure</p>	<p>Set correct write field size and magnification</p> <p>Set correct step size</p> <p>Drive to Faraday cup and perform dwell time correction</p> <p>Press the dwell time button in the calculator menu to set the right dwell time</p> <p>Use the following advanced details parameters in the calculator menu:</p> <p> Loops: 1 Exposure raster: fixed Area mode: meander Scan direction: auto Settling time: auto Flyback: auto Advanced: dynamic compensation off</p> <p>Drive to write field center, open position list and start scan</p>	<p>Use 300 μm as write field size for qubit structures</p> <p>Use typically a step size of 8 nm (corresponds to 10 pixels) for the 10 μm aperture</p> <p>The measured beam current should be in the order of 30 to 35 pA for the 10 μm aperture</p> <p>The dwell time should not be lower than approximately 1 μs, the beam speed should not be significant higher than 10 mm/s otherwise choose larger step size</p>
<p>To be continued on next page...</p>		

Process step	Description	Comments
	Perform 3 subsequent manual mark scans	For Manual marks, layer 63 is used in the design file
Unloading procedure	Drive back to Faraday cup and press "Un- load sample" Take off chip from sample holder Log off from RAITH- and LEO software Log off from RAITH computer	Unloading takes about 11 minutes

F Shadow Evaporation and Oxidation

Evaporation and Oxidation with LEYBOLD Evaporator		
Process step	Description	Comments
Sampleholder preadjustments and machine preparations	<p>Clean vacuum chamber carefully with vacuum cleaner and acetone</p> <p>Check 0°- and 30° position of tiltable sampleholder</p> <p>Mount sample as well as monitor sample with clips and screws on sampleholder at correct position</p> <p>Build in sampleholder and check position</p> <p>Connect electrical lines to feed throughs of vacuum chamber</p> <p>Build in shutter and check shutter mechanism</p> <p>Build in sheet metal for source protection</p> <p>Build in graphite liner with sufficient aluminum</p> <p>Build in chimney metal sheet</p> <p>Close shutter</p> <p>Build in protection glass</p> <p>Clean sealing of vacuum chamber with isopropanol</p> <p>Close vacuum chamber</p> <p>Pump down vacuum chamber until pressure is lower than 2×10^{-7} mbar</p> <p>Prepare electrical lines, power supply and lock switch for electrical tilt mechanism</p>	
Shadow evaporation and oxidation	<p>Check Inficon adjustments for density of aluminum $\rho = 2.7 \text{ g/cm}^3$, bulk module $\xi = 1.080$ and tooling factor $TF = 100\%$</p> <p>Open cooling water for electron beam source and switch on electron beam source</p> <p>Soak aluminum by increasing the emission current within 3 min to a rate of approximately 1 \AA/sec</p>	<p>The measured thickness the Inficon displays is higher than the actual thickness by a factor of approximately 1.6 with a tooling factor of 100% due to the position of the sampleholder</p>
To be continued on next page...		

F Shadow Evaporation and Oxidation

Process step	Description	Comments
	<p>Hold rate at 1 Å/sec for two more minutes</p> <p>Increase rate up to 5-7 Å/sec within 1 min for preevaporation (shutter is closed)</p> <p>If rate is constant open shutter and press "zero" at Inficon simultaneously</p> <p>Control emission current for constant rate</p> <p>Evaporate first aluminum layer</p> <p>Close shutter, reduce emission current and switch off electron beam source</p> <p>Wait 45 sec, switch off rough- and turbopump and let carefully 15%O₂ / 85%Ar gas mixture flow into vacuum chamber</p> <p>After 1 min pressure increased to 4 mbar</p> <p>Wait further 30 sec and let carefully 15%O₂ / 85%Ar gas mixture flow into vacuum chamber</p> <p>After 2 min pressure increased to 20 mbar</p> <p>Wait for finishing the oxidation at a pressure of 20 mbar</p> <p>Start roughpump when having finished the oxidation</p> <p>Start turbopump when pressure increased up to 1 mbar</p> <p>Pump down for 6 min</p> <p>Tilt sampleholder to 30° position with electrical tilt mechanism</p> <p>When pressure is lower than 10⁻⁵ mbar start electron beam source</p> <p>Increase emission current for a rate of 1 Å/sec within 3 min</p> <p>After 6 min of pump down establish a rate of 5-7 Å/sec</p> <p>When rate is constant, open shutter and press "zero" at Inficon simultaneously</p> <p>Control emission current for constant rate</p> <p>Evaporate second aluminum layer</p> <p>Close shutter, reduce emission current and switch off electron beam source</p> <p>Wait 45 sec, switch off rough- and turbopump and let carefully 15%O₂ / 85%Ar gas mixture flow into vacuum chamber</p> <p>After 1 min pressure increased to 2 mbar</p>	<p>Pressure during evaporation is about 10⁻⁶ mbar</p> <p>Do not use pure oxygen for oxidation when using oil smeared rough pumps</p> <p>Pressure during evaporation is around 10⁻⁶ mbar</p>
To be continued on next page...		

Process step	Description	Comments
	<p>Wait further 30sec and let carefully 15%O₂ / 85%Ar gas mixture flow in vacuum chamber</p> <p>After 2 min pressure increased to 10 mbar</p> <p>After 3 min pressure increased to 20 mbar</p> <p>Let gas mixture flow for 6 min (working pressure is 0.5 bar)</p> <p>After 30 min vent vacuum chamber</p>	
Unloading sample	Take out sampleholder, unmount sample and pump down chamber again	

Evaporation and Oxidation with PLASSYS Evaporator		
Process step	Description	Comments
Loading of sample	<p>Vent chamber and mount sample as well as monitor sample on sample holder</p> <p>Rotate the sampleholder with motion controller to achive a sample orientation parallel to the tilt axes and check position of sample</p> <p>Blow off sample with nitrogene, close- and pump down chamber</p>	Position samples parallel to each other
Shadow evaporation and oxidation	<p>Preadjust position of oxygen inlet needle valve for oxygen doping during first evaporation (needle valve should be opened by approximately 90°)</p> <p>Switch on HV source and beam sweep controller</p> <p>Use the following beam sweep parameters for aluminum:</p> <p>Pattern: 34 + line Gain: 20 Speed: 40 Spin: 60 Profile: 8 Position X: 6 Position Y: 0</p> <p>Log onto DALEK software, check the log file path, load and run the predefined recipe</p> <p>Wait until evaporation procedure is finished</p> <p>Switch off HV source and beam sweep controller and vent load lock</p> <p>Unmount sample and pump down load lock again</p>	<p>Open main chamber valve and carefully adjust position of needle valve</p> <p>Position of beam my vary and has to be adapted</p> <p>Supervise the running process all the time and interact if necessary</p>

G Process Recipes for Plassys Evaporator

Process Recipe for Ion Gun Milling Procedure				
Recipe Step	Par 1	Par 2	Par 3	Comment
Step 1	Root\ Chamber pump	0.0nm	0:00	Sub-process
Step 2	Root\ Load lock pump	0.0nm	0:00	Sub-process
Step 3	Root\ Etch 300V 10mA	0.0nm	3:00	Sub-process
Step 4	Root\ Chamber pump	0.0nm	0:00	Sub-process
Step 5	Root\ Load lock pump	0.0nm	0:00	Sub-process

Process Recipe for SQUID Fabrication				
Recipe Step	Par 1	Par 2	Par 3	Comment
Step 1	Root\ Chamber pump	0.0nm	0:00	Sub-process
Step 2	Root\ Load lock pump	0.0nm	0:00	Sub-process
Step 3	Root\ Al-pure 1nm/s -30°	30.0nm	0:00	Sub-process
Step 4	Root\ Oxid 15%O2 1Torr	0.0nm	1:20	Sub-process
Step 5	Root\ Al-pure 1nm/s +30°	150.0nm	0:00	Sub-process
Step 6	Root\ Oxid 100%O2 10Torr	0.0nm	15:00	Sub-process
Step 7	Root\ Chamber pump	0.0nm	0:00	Sub-process
Step 8	Root\ Load lock pump	0.0nm	0:00	Sub-process

Process Recipe for QUBIT Fabrication				
Recipe Step	Par 1	Par 2	Par 3	Comment
Step 1	Root\ Chamber pump	0.0nm	0:00	Sub-process
Step 2	Root\ Load lock pump	0.0nm	0:00	Sub-process
Step 3	Root\ Al-pure 0.5nm/s 0°	20.0nm	0:00	Sub-process
Step 4	Root\ Oxid 15%O2 1Torr	0.0nm	5:00	Sub-process
Step 5	Root\ Al-pure 0.5nm/s 30°	80.0nm	0:00	Sub-process
Step 6	Root\ Oxid 100%O2 10Torr	0.0nm	15:00	Sub-process
Step 7	Root\ Chamber pump	0.0nm	0:00	Sub-process
Step 8	Root\ Load lock pump	0.0nm	0:00	Sub-process

Sub-Process Chamber Pump				
Recipe Step	Par 1	Par 2	Par 3	Comment
Chamber pump	2.00e-007 Torr	25:00		Pump chamber

Sub-Process Load Lock Pump				
Recipe Step	Par 1	Par 2	Par 3	Comment
Load lock pump	2.00e-006 Torr	25:00		Pump load lock

Sub-Process Etch 300V 10mA				
Recipe Step	Par 1	Par 2	Par 3	Comment
Load lock process	5.00e-006 Torr	15:00		Load lock process
Process chamber	5.00e-007 Torr	10:00		Process chamber
Wait	0:10			Wait this time before the next step
Load lock process	5.00e-007 Torr	15:00		Load lock process
Subst. holder pos.	Etch	-30.0°		Position substrate holder
Gas	3.5 sccm	0:00		Ion gun gas
To be continued on next page...				

G Process Recipes for Plassys Evaporator

Receipe Step	Par 1	Par 2	Par 3	Comment
Wait	0:15			Wait this time before the next step
Source shutter	Closed			Move source shutter
Substrate shutter	IG close/EG open			Move substrate shutter
Rotate planetary	10°/s			Rotate the planetary
Ion source	On			Start ion gun discharge
Wait	0:10			Wait this time before the next step
Ion beam	10.0 mA	300 V	250 V	Ion beam on
Substrate shutter	EG Close/IG open			Move substrate shutter
Wait in the process				Parameterised wait
Ion beam	0.0 mA	0 V	0 V	Ion beam off
Rotate planetary	0°/s			Rotate the planetary
Wait	0:02			Wait this time before the next step
Ion source	Off			End ion gun discharge
Wait	0:05			Wait this time before the next step
Gas	0.0 sccm	0:00		Ion gun gas
Position planetary	Zero	0.0°		Position the planetary
Load lock process	5.00e-006 Torr	10:00		Load lock process

Sub-Process Al_pure 1nm/s -30°				
Receipe Step	Par 1	Par 2	Par 3	Comment
Process chamber	5.00e-007 Torr	30:00		Process chamber
Load lock process	5.00e-007 Torr	20:00		Load lock process
Wait	0:05			Wait this time before the next step
Substrate shutter	EG close/IG open			Move substrate shutter
Subst. holder pos.	Deposit	-30.0°		Position substrate holder
Material select	Al_pure			E gun crucible selection
Source shutter	Open			Move source shutter
E gun emission	0.010 A	0:00		Set the emission current
Wait	0:10			Wait this time before the next step
E gun emission	0.150 A	0:15		Set the emission current
Ramp wait all				Wait for ramp to be finished
Wait	2:00			Wait this time before the next step
Operator requested	Please check the beam			Enter the message to be displayed
E gun emission	0.500 A	0:20		Set the emission current
Wait	0:10			Wait this time before the next step
Rate control	1.00 nm/s	2:00		Set the evaporation rate
Wait	0:10			Wait this time before the next step
Substrate shutter	IG close/EG open			Move substrate shutter
Zero thickness				Set the thickness at zero
Thickness process				Thickness value in the process
Substrate shutter	EG close/IG open			Move substrate shutter
E gun emission	0.000 A	0:10		Set the emission current
Ramp wait all				Wait for ramp to be finished
Wait	0:05			Wait this time before the next step

Sub-Process Al_pure 1nm/s +30°				
Receipe Step	Par 1	Par 2	Par 3	Comment
Process chamber	5.00e-007 Torr	30:00		Process chamber
Load lock process	5.00e-007 Torr	20:00		Load lock process
Wait	0:05			Wait this time before the next step
Substrate shutter	EG close/IG open			Move substrate shutter
Subst. holder pos.	Deposit	30.0°		Position substrate holder
Material select	Al_pure			E gun crucible selection
Source shutter	Open			Move source shutter
E gun emission	0.010 A	0:00		Set the emission current
Wait	0:10			Wait this time before the next step
E gun emission	0.150 A	0:15		Set the emission current
Ramp wait all				Wait for ramp to be finished
Wait	2:00			Wait this time before the next step
Operator requested	Please check the beam			Enter the message to be displayed
E gun emission	0.500 A	0:20		Set the emission current
Wait	0:10			Wait this time before the next step
Rate control	1.00 nm/s	2:00		Set the evaporation rate

To be continued on next page...

Recipe Step	Par 1	Par 2	Par 3	Comment
Wait	0:10			Wait this time before the next step
Substrate shutter	IG close/EG open			Move substrate shutter
Zero thickness				Set the thickness at zero
Thickness process				Thickness value in the process
Substrate shutter	EG close/IG open			Move substrate shutter
E gun emission	0.000 A	0:10		Set the emission current
Ramp wait all				Wait for ramp to be finished
Wait	0:05			Wait this time before the next step

Sub-Process Al_pure 0.5nm/s 0°				
Recipe Step	Par 1	Par 2	Par 3	Comment
Process chamber	5.00e-007 Torr	30:00		Process chamber
Load lock process	5.00e-007 Torr	20:00		Load lock process
Wait	0:05			Wait this time before the next step
Substrate shutter	EG close/IG open			Move substrate shutter
Subst. holder pos.	Deposit	0°		Position substrate holder
Material select	Al_pure			E gun crucible selection
Source shutter	Open			Move source shutter
E gun emission	0.010 A	0:00		Set the emission current
Wait	0:10			Wait this time before the next step
E gun emission	0.150 A	0:15		Set the emission current
Ramp wait all				Wait for ramp to be finished
Wait	2:00			Wait this time before the next step
Operator requested	Please check the beam			Enter the message to be displayed
E gun emission	0.500 A	0:20		Set the emission current
Wait	0:10			Wait this time before the next step
Rate control	0.50 nm/s	2:00		Set the evaporation rate
Wait	0:10			Wait this time before the next step
Substrate shutter	IG close/EG open			Move substrate shutter
Zero thickness				Set the thickness at zero
Thickness process				Thickness value in the process
Substrate shutter	EG close/IG open			Move substrate shutter
E gun emission	0.000 A	0:10		Set the emission current
Ramp wait all				Wait for ramp to be finished
Wait	0:05			Wait this time before the next step

Sub-Process Al_pure 0.5nm/s 30°				
Recipe Step	Par 1	Par 2	Par 3	Comment
Process chamber	5.00e-007 Torr	30:00		Process chamber
Load lock process	5.00e-007 Torr	20:00		Load lock process
Wait	0:05			Wait this time before the next step
Substrate shutter	EG close/IG open			Move substrate shutter
Subst. holder pos.	Deposit	30.0°		Position substrate holder
Material select	Al_pure			E gun crucible selection
Source shutter	Open			Move source shutter
E gun emission	0.010 A	0:00		Set the emission current
Wait	0:10			Wait this time before the next step
E gun emission	0.150 A	0:15		Set the emission current
Ramp wait all				Wait for ramp to be finished
Wait	2:00			Wait this time before the next step
Operator requested	Please check the beam			Enter the message to be displayed
E gun emission	0.500 A	0:20		Set the emission current
Wait	0:10			Wait this time before the next step
Rate control	0.50 nm/s	2:00		Set the evaporation rate
Wait	0:10			Wait this time before the next step
Substrate shutter	IG close/EG open			Move substrate shutter
Zero thickness				Set the thickness at zero
Thickness process				Thickness value in the process
Substrate shutter	EG close/IG open			Move substrate shutter
E gun emission	0.000 A	0:10		Set the emission current
Ramp wait all				Wait for ramp to be finished
Wait	0:05			Wait this time before the next step

G Process Receipes for Plassys Evaporator

Sub-Process Oxid 15%O2 1Torr				
Receipe Step	Par 1	Par 2	Par 3	Comment
Static oxidation	1.0 Torr	ArO2		Static oxidation
Wait in the process				Parameterised wait
Load lock pump	2.00e-006 Torr	20:00		Pump load lock

Sub-Process Oxid 100%O2 10Torr				
Receipe Step	Par 1	Par 2	Par 3	Comment
Static oxidation	10.0 Torr	O2		Static oxidation
Wait in the process				Parameterised wait
Load lock pump	2.00e-006 Torr	20:00		Pump load lock

H Dicing, Mounting and Bonding of Devices

Dicing of Silicon Wafers with Wafer Saw		
Process step	Description	Comments
Resist coverage for wafer protection	Spin maN-415 resist with 3000 rpm and acceleration 8 for 60 seconds	Clean new pipette carefully with nitrogene gun then cover wafer totally with resist and start spinning
	Remove backside resist with acetone	
	Bake wafer on hotplate at 95 °C for 90 seconds	
Substrate and machine preparation	Mount wafer on blue tape, in case of small substrates heat blue tape at 60 °C on hotplate for 10 minutes before	
	Mount ring with blue tape on chuck	
	Open valves for water and pressurized air	
	Start machine with key switch	
Initialization and cutting procedure	<p>Press "SYS INIT" to initialize the machine</p> <p>Choose the right cutting program in "DEVICE DATA LIST"</p> <p>Use the following cutting parameters:</p> <p>Unit: mm Cut mode: A Cut shape: ROUND Spindle rev: 30000 Work thickness: 0.3 mm Tape thickness: 0.07 mm Blade hight: 0.04 mm Auto setup: yes RND work size: 55 mm Feed speed: 2 mm/sec Y Index CH1: 7.1 mm Y Index CH2: 2.1 mm Theta adjustment CH1: 50% Theta adjustment CH2: 50%</p> <p>Press "SPNDL" to start the blade rotation</p> <p>Press "CT/VAC" to start chuck vacuum</p> <p>Press "SETUP", "ENTER", "ENTER" to start the non contact setup</p> <p>Wait 30 minutes for a better cutting accuracy</p>	Press "ENTER" again when noncontact setup is finished
To be continued on next page...		

Process step	Description	Comments
	<p>Select the "SEMI AUTOMATIC PROCEDURE"</p> <p>Align the first cutting path</p> <p>Check the defined cutting paths with the "INDEX" function</p> <p>Check the number of cuts, choose "REAR" as cutting direction to go from the front to the rear of the wafer and press "START/STOP"</p> <p>Press "START/STOP" during first cut and check the cutting path</p> <p>Press "START/STOP" again to continue cutting</p> <p>Rotate substrate by 90° with the "INDEX" function</p> <p>Align the second cutting path</p> <p>Check the defined cutting paths with the "INDEX" function</p> <p>Check the number of cuts, choose "REAR" as cutting direction to go from the front to the rear of the wafer and press "START/STOP"</p> <p>Press "START/STOP" during first cut and check the cutting path</p> <p>Press "START/STOP" again to continue cutting</p>	
Cleaning procedure for diced chips	<p>Dunk chip up side down in acetone for 1 minute</p> <p>Sonicate wafer in acetone for 15 minutes at 50 °C at power 2 in 40 kHz ultrasonic bath</p> <p>Sonicate wafer in acetone for 15 minutes at 50 °C at power 2 in 40 kHz ultrasonic bath</p> <p>Sonicate wafer in isopropanol for 5 minutes at 50 °C at power 2 in 40 kHz ultrasonic bath</p> <p>blow dry wafer with nitrogene</p>	Coarse dirt should fall off immediately

Mounting of Chips on DC Measurement PCBs		
Process step	Description	Comments
Cleaning of PCB	<p>Clean copper pads carfully with fiberglass pen</p> <p>Clean copper pads with 50% citric acid, acetone and isopropanol</p>	
Cleaning and mounting of chip	Clean chip with acetone and isopropanol	
To be continued on next page...		

Process step	Description	Comments
	Glue chip on PCB with a small amount of PMMA resist	

Mounting of Chips on Microwave PCBs		
Process step	Description	Comments
Cleaning of PCB	<p>Clean PCB with fiberglass pen</p> <p>Sonicate wafer in 50% citric acid for 5 minutes at power 5 in 40 kHz ultrasonic bath</p> <p>Sonicate wafer in isopropanol for 5 minutes at power 5 in 40 kHz ultrasonic bath</p> <p>Blow dry wafer with nitrogen</p>	Do not use acetone to clean PCB to preserve the dielectric of the SMP connectors
Mounting of chip	<p>Take a small amount of PMMA onto the sampleholder and carefully place the chip</p> <p>Align the chip and press it slightly into the sampleholder with plastic tweezers</p> <p>PMMA must dry approximately 30 minutes before bonding</p>	

Bonding of Chips with Hard Aluminum Wire		
Process step	Description	Comments
Preparation of chips and PCBs	<p>Clean PCBs carefully with fiberglass pen, citric acid and isopropanol</p> <p>Clean chips carefully with acetone and isopropanol before</p>	
Cleaning of bonding tool	<p>Sonicate tool in acetone for 5 minutes at power 9 in 40 kHz ultrasonic bath</p> <p>Sonicate tool in isopropanol for 5 minutes at power 9 in 40 kHz ultrasonic bath</p> <p>Blow dry tool with nitrogen</p>	Use teflon vessel for cleaning to avoid damage
Bonding procedure	<p>Place first bond on chip and second bond on copper pad</p> <p>Use the following bonding parameters:</p> <p>Power 1: 340 Power 2: 340 Time 1: 30 Time 2: 30 Force 1: LOW Force 2: HIGH Loop height: 10(254μm) Pull: 30 Tail: 50 Dual force: ON</p>	
To be continued on next page...		

H Dicing, Mounting and Bonding of Devices

Process step	Description	Comments
	US power: 150 US power switch: LOW Tool heat: 4 No sample heat	

Bonding of Chips with Soft Aluminum Wire		
Process step	Description	Comments
Preparation of chips and PCBs	Clean PCBs carefully with fiberglass pen, citric acid and isopropanol before Clean chips carefully with acetone and isopropanol before	
Cleaning of bonding tool	Sonicate tool in acetone for 5 minutes at power 9 in 40 kHz ultrasonic bath Sonicate tool in isopropanol for 5 minutes at power 9 in 40 kHz ultrasonic bath Blow dry tool with nitrogen	Use teflon vessel for cleaning to avoid damage
Bonding procedure	Place first bond on chip and second bond on copper Use the following bonding parameters: Power 1: 160 Power 2: 160 Time 1: 70 Time 2: 30 Force 1: LOW Force 2: HIGH Loop height: 10(254 μ m) Pull: 30 Tail: 50 Dual force: ON US power: 150 US power switch: LOW Tool heat: 0 No sample heat	

I DC Probing of Josephson Junctions

DC Probing with Keithly 4200 Semiconductor Characterization System		
Process step	Description	Comments
Preparation of probing station	<p>Connect protective earth of Keithly system to cable box ground of probing station</p> <p>Connect SMU 1 of Keithly system to first needle</p> <p>Connect SMU 2 of Keithly system to second needle</p> <p>Use microscope to correctly place needles onto the contact pads</p>	Use as short cable connections as possible and drill cables to avoid stray field induction
Measuring procedure	<p>Use the intensity knob to reduce the light intensity to zero when measuring</p> <p>Perform linear current sweep</p> <p>Use the following parameters:</p> <p>Speed: quiet Start current: 1×10^{-8} A Stop current: 6×10^{-8} A Step: 2×10^{-9} A Points: 26 Source range: 100 nA Compliance: 50 mV Voltage range: 200 mV Measure current and voltage</p>	Switching off the power supply may destroy the sample due to magnetic stray fields or spikes on ground line

J Measuring the Current Voltage Characteristic of a Josephson Junction

4-Point Characterization with Bias Box and NI BNC-2110 Card		
Process step	Description	Comments
Grounding and cable connections	<p>Do not separately ground the cryo to avoid ground loops</p> <p>Switch the analog inputs of the NI BNC-2110 card to "ground reference source GS" (no ground connection of input shields)</p> <p>Connect the shield of the bias box to the shield of the cable box</p> <p>4 twisted pairs go directly to the sub-D connectors of the cable box (each contains 2 twisted pairs)</p> <p>8 twisted pairs go to the isolated BNC connectors of the cable box over a symmetric lowpass filter (each filter contains 4 $100\ \Omega$ resistors and a $100\ \text{nF}$ capacitor), the switches connect the twisted pairs either to the BNC connectors or to ground</p> <p>Connect "Analog Output 1" of the NI BNC-2110 card to "bias drive" of the bias box</p> <p>Connect "Analog In 1" of the NI BNC-2110 card to "DUT I" of the bias box</p> <p>Connect "Analog In 2" of the NI BNC-2110 card to "DUT V" of the bias box</p> <p>Connect "Out 2" of the bias box to the BNC connector of the cable box which supplies the current</p> <p>Connect "Out 3" of the bias box to the BNC connector of the cable box which measures voltage</p>	<p>Ground is supplied by the NI BNC-2110 card (the analog output shield is connected to protective earth)</p> <p>The Lemo connector connects the shield of the cable box with the cryo housing</p> <p>Use as short cable connections as possible</p>
Measurement with bias box	<p>Short the twisted pairs to ground with the ground switch of the cable box</p> <p>Use the following bias box adjustments:</p> <p>Filter I: On Filter I frequency: 16 Hz</p>	<p>Adapt the corresponding adjustments in the LABVIEW box control software</p>
To be continued on next page...		

J Measuring the Current Voltage Characteristic of a Josephson Junction

Process step	Description	Comments
	<p>Filter V: On Filter V frequency: 16 Hz DUT poti: Off DUT short: Off Bias to DUT: Off Buffer bypass: Off Bias mode: No feedback Feedback: Off Bias divide: 1000 Bias select: 1M I gain: 500 V gain: 500</p> <p>Use the following software adjustments:</p> <p>Number of points: 100 Start voltage NI BNC-2110 card: 0V End voltage NI BNC-2110 card: 5V Waiting time: 100-1000 ms Number of measurements: 100</p> <p>Switch off "Short to ground" at cable box</p> <p>Start measurement</p> <p>Switch on "Short to ground" at cable box when measurement finished</p>	

4-Point Characterization with Bias Box, Adder Box and an Oscilloscope		
Process step	Description	Comments
Grounding and cable connections	<p>Ground the cryo with a single ground line</p> <p>Connect the shield of the bias box and the adder box to the shield of the cable box</p> <p>4 twisted pairs go directly to the sub-D connectors of the cable box (each contains 2 twisted pairs)</p> <p>8 twisted pairs go to the isolated BNC connectors of the cable box over a symmetric lowpass filter (each filter contains 4 100 Ω resistors and a 100 nF capacitor), the switches connect the twisted pairs either to the BNC connectors or to ground</p> <p>Connect "Drive" of the adder box to "bias drive" of the bias box</p> <p>Connect "DUT I" of the bias box to one channel of the oscilloscope</p> <p>Connect "DUT V" of the bias box to the other channel of the oscilloscope</p> <p>Connect "Out 2" of the bias box to the BNC connector of the cable box which supplies the current</p> <p>Connect "Out 3" of the bias box to the BNC connector of the cable box which measures voltage</p>	<p>The Lemo connector connects the shield of the cable box with the cryo housing</p> <p>Use as short cable connections as possible</p>
To be continued on next page...		

Process step	Description	Comments
<p>Measurement with bias box and adder box</p>	<p>Short the twisted pairs to ground with the ground switch of the cable box</p> <p>Use the following bias box adjustments:</p> <p>Filter I: On Filter I frequency: 16 Hz Filter V: On Filter V frequency: 16 Hz DUT poti: Off DUT short: Off Bias to DUT: Off Buffer bypass: Off Bias mode: No feedback Feedback: Off Bias divide: 1000 Bias select: 1M I gain: 500 V gain: 500</p> <p>Use the following adder box adjustments:</p> <p>Oscillator: On Signal: Triangle DC: Off Input A: Off Input B: Off Input C: Off</p> <p>Switch off "Short to ground" at cable box</p> <p>Adjust frequency and amplitude at adder box</p> <p>Switch on "Short to ground" at cable box when measurement finished</p>	<p>Adapt the corresponding adjustments in the LABVIEW box control software</p>

Bibliography

- [Abdo2006] Abdo, B., Segev, E., Shtempluck, O. and Buks, E. (2006). Nonlinear dynamics in the resonance lineshape of NbN superconducting resonators. *Physical Review B*, 73:11.
- [Ambegaokar1963] Ambegaokar, V. and Baratoff, A. (1963). Tunneling between superconductors. *Physical Review Letters*, 10:486.
- [Anderson1963] Anderson, P. and Rowell, J. (1963). Probable observation of the Josephson superconducting tunneling effect. *Physical Review Letters*, 10:230.
- [Astafiev2007] Astafiev, O., Inomata, K., Niskanen, A. O., Yamamoto, T., Pashkin, Y. A., Nakamura, Y. and Tsai, J. S. (2007). Single artificial-atom lasing. *Nature*, 449(7162):588.
- [Autler1955] Autler, S. H. and Townes, C. H. (1955). Stark effect in rapidly varying fields. *Physical Review*, 100:703.
- [Barends2007] Barends, R., Baselmans, J., Hovenier, J., Gao, J., Yates, S., Klapwijk, T. and Hoevers, H. (2007). Niobium and tantalum high Q resonators for photon detectors. *IEEE Transactions on Applied Superconductivity*, 17(2):263.
- [Baselmans2005] Baselmans, J., Barends, R., Hovenier, J., Gao, J., Hoevers, H., de Korte, P. and Klapwijk, T. (2005). High Q niobium superconducting resonators for use as kinetic inductance sensing elements. *Bulletin de la Société Royale des Sciences de Liège*, 74:5.
- [Baur2009] Baur, M., Filipp, S., Bianchetti, R., Fink, J. M., Göppl, M., Leek, P. J., Steffen, L., Blais, A. and Wallraff, A. (2008). Dynamics of dispersive read-out in circuit quantum electrodynamics. *arXiv:0812.4384*.
- [Bergeal2008] Bergeal, N., Vijay, R., Manucharyan, V. E., Siddiqi, I., Schoelkopf, R. J., Girvin, S. M. and Devoret, M. H. (2008). Analog information processing at the quantum limit with a Josephson ring modulator. *arXiv:0805.3452*
- [Bianchetti2009] Bianchetti, R. et al. (2009). Dynamics of dispersive single qubit read-out in circuits. *In preparation*.
- [Blais2007] Blais, A., Gambetta, J., Wallraff, A., Schuster, D. I., Girvin, S. M., Devoret, M. H. and Schoelkopf, R. J. (2007). Quantum-information processing with circuit quantum electrodynamics. *Physical Review A*, 75(3):032329.
- [Blais2004] Blais, A., Huang, R.-S., Wallraff, A., Girvin, S. M. and Schoelkopf, R. J. (2004). Cavity quantum electrodynamics for superconducting electrical circuits: An architecture for quantum computation. *Physical Review A*, 69(6):062320.
- [Blatt2008] Blatt, R. and Wineland, D. (2008). Entangled states of trapped atomic ions. *Nature*, 453(7198):1008.
- [Bloch2008] Bloch, I. (2008). Quantum coherence and entanglement with ultracold atoms in optical lattices. *Nature*, 453(7198):1016.

Bibliography

- [Bouchiat1997] Bouchiat, V. (1997). *Quantum fluctuations of the charge in single electron and single Cooper pair devices*. PhD thesis, Universit'e Paris VI, CEA-Saclay.
- [Bouchiat1998] Bouchiat, V., Vion, D., Joyez, P., Esteve, D. and Devoret, M. H. (1998). Quantum coherence with a single Cooper pair. *Physica Scripta*, T76:165.
- [Browne1987] Browne, J. (1987). Broadband amps sport coplanar waveguide. *Microwaves RF*, 26(2):131.
- [Büttiker1987] Büttiker, M. (1987). Zero-current persistent potential drop across small-capacitance Josephson junctions. *Physical Review B*, 36:3548.
- [Carmichael1996] Carmichael, H. J., Kochan, P. and Sanders, B. C. (1996). Photon correlation spectroscopy. *Physical Review Letters*, 77(4):631.
- [Castellanos2008] Castellanos-Beltran, M. A., Irwin, K. D., Hilton, G. C., Vale, L. R. and Lehnert, K. W. (2008). Amplification and squeezing of quantum noise with a tunable Josephson metamaterial. *arXiv:0806.0659v1*.
- [Castellanos2007] Castellanos-Beltran, M. A. and Lehnert, K. W. (2007). Widely tunable parametric amplifier based on a superconducting quantum interference device array resonator. *Applied Physics Letters*, 91(8):083509.
- [Chen1997] Chen, E. and Chou, S. (1997). Characteristics of coplanar transmission lines on multilayer substrates: Modeling and experiments. *IEEE Transactions on Microwave Theory and Techniques*, 45(6):939.
- [Chiorescu2004] Chiorescu, I., Bertet, P., Semba, K., Nakamura, Y., Harmans, C. J. P. M. and Mooij, J. E. (2004). Coherent dynamics of a flux qubit coupled to a harmonic oscillator. *Nature*, 431:159.
- [Clarke1988] Clarke, J., Cleland, A. N., Devoret, M. H., Esteve, D. and Martinis, J. M. (1988). Quantum mechanics of a macroscopic variable: The phase difference of a Josephson junction. *Science*, 239(4843):992.
- [Clarke2006] Clarke, J. and Braginsky, A. (2006). *The SQUID handbook*. Wiley-VCH.
- [Clarke2008] Clarke, J. and Wilhelm, F. K. (2008). Superconducting quantum bits. *Nature*, 453(7198):1031.
- [Cottet2002] Cottet, A., Vion, D., Aassime, A., Joyez, P., Esteve, D. and Devoret, M. H. (2002). Implementation of a combined charge-phase quantum bit in a superconducting circuit. *Physica C*, 367(1-4):197.
- [Day2003] Day, P. K., LeDuc, H. G., Mazin, B. A., Vayonakis, A. and Zmuidzinas, J. (2003). A broadband superconducting detector suitable for use in large arrays. *Nature*, 425(6960):817.
- [Deaver1961] Deaver, B. and Fairbank, W. (1961). Experimental evidence for quantized flux in superconducting cylinders. *Physical Review Letters*, 7:43.
- [Devoret1996] Devoret, M. (1996). *Quantum fluctuations*. Elsevier, Amsterdam.
- [Devoret2007] Devoret, M., Girvin, S. and Schoelkopf, R. (2007). Circuit-qed: How strong can the coupling between a Josephson junction atom and a transmission line resonator be? *Annalen der Physik*, 16(10-11):767.

- [DiVincenzo1995] Di Vincenzo, D. (1995). Quantum computation. *Science*, 270:255.
- [Doll1961] Doll, R. and Nabauer, M. (1961). Experimental proof of magnetic flux quantization in a superconducting ring. *Physical Review Letters*, 7:51.
- [Filipp2009] Filipp, S., Maurer, P., Leek, P. J., Baur, M., Bianchetti, R., Fink, J. M., Göppl, M., Steffen, L., Gambetta, J. M., Blais, A. and Wallraff, A. (2008). Two-qubit state tomography using a joint dispersive read-out. *arXiv:0812.2485*.
- [Fink2008] Fink, J. M., Göppl, M., Baur, M., Bianchetti, R., Leek, P. J., Blais, A. and Wallraff, A. (2008). Climbing the Jaynes-Cummings ladder and observing its nonlinearity in a cavity QED system. *Nature*, 454(7202):315.
- [FIRST] www.first.ethz.ch.
- [Fragner2008] Fragner, A., Göppl, M., Fink, J. M., Baur, M., Bianchetti, R., Leek, P., Blais, A. and Wallraff, A. (2008). Resolving vacuum fluctuations in an electrical circuit by measuring the lamb shift. *Science*, 322(5906):1357.
- [Friedman2000] Friedman, J. R., Patel, V., Chen, W., Tolpygo, S. K. and Lukens, J. E. (2000). Quantum superposition of distinct macroscopic states. *Nature*, 406(6791):43.
- [Frunzio2005] Frunzio, L., Wallraff, A., Schuster, D., Majer, J. and Schoelkopf, R. (2005). Fabrication and characterization of superconducting circuit QED devices for quantum computation. *IEEE Transactions On Applied Superconductivity*, 15(2):860.
- [Gevorgian1995] Gevorgian, S., Linnér, L. J. P. and Kollberg, E. L. (1995). CAD models for shielded multilayered CPW. *IEEE Transactions on Microwave Theory and Techniques*, 43(2):772.
- [Gleyzes2007] Gleyzes, S., Kuhr, S., Guerlin, C., Bernu, J., Deleglise, S., Busk Hoff, U., Brune, M., Raimond, J.-M. and Haroche, S. (2007). Quantum jumps of light recording the birth and death of a photon in a cavity. *Nature*, 446(7133):297.
- [Göppl2008] Göppl, M., Fragner, A., Baur, M., Bianchetti, R., Filipp, S., Fink, J. M., Leek, P. J., Puebla, G., Steffen, L., and Wallraff, A. (2008). Coplanar waveguide resonators for circuit quantum electrodynamics. *Journal of Applied Physics*, 104:1113904.
- [Göppl2009] Göppl, M., Filipp, S., Baur, M., Bianchetti, R., Fink, J. M., Leek, P. J., Steffen, L., Blais, A. and Wallraff, A. (2008). Qubit-qubit interaction by exchange of virtual photons via multiple cavity modes. *In preparation*.
- [Gross2003] Gross, R. and Marx, A. (2003). *Applied Superconductivity*, Lecture Notes.
- [Guerlin2007] Guerlin, C., Bernu, J., Deleglise, S., Sayrin, C., Gleyzes, S., Kuhr, S., Brune, M., Raimond, J.-M. and Haroche, S. (2007). Progressive field-state collapse and quantum non-demolition photon counting. *Nature*, 448(7156):889.
- [Hammer2007] Hammer, G., Wuensch, S., Roesch, M., Ilin, K., Crocoll, E. and Siegel, M. (2007). Superconducting coplanar waveguide resonators for detector applications. *Superconducting Science and Technology*, 20:408.
- [Hanson2008] Hanson, R. and Awschalom, D. D. (2008). Coherent manipulation of single spins in semiconductors. *Nature*, 453(7198):1043.

Bibliography

- [Haroche1989] Haroche, S. and Kleppner, D. (1989). Cavity quantum electrodynamics. *Physics Today*, 24.
- [Houck2007] Houck, A., Schuster, D., Gambetta, J., Schreier, J., Johnson, B., Chow, J., Frunzio, L., Majer, J., Devoret, M., Girvin, S. and Schoelkopf, R. (2007). Generating single microwave photons in a circuit. *Nature*, 449:328.
- [Jaynes1963] Jaynes, E. and Cummings, F. (Jan. 1963). Comparison of quantum and semiclassical radiation theories with application to the beam maser. *Proceedings of the IEEE*, 51(1):89.
- [Johansson2006] Johansson, J., Saito, S., Meno, T., Nakano, H., Ueda, M., Semba, K. and Takayanagi, H. (2006). Vacuum Rabi oscillations in a macroscopic superconducting qubit LC oscillator system. *Physical Review Letters*, 96(12):127006.
- [Josephson1962] Josephson, B. D. (1962). Possible new effects in superconductive tunnelling. *Physics Letters*, 1(7):251.
- [Koch2007] Koch, J., Yu, T. M., Gambetta, J., Houck, A. A., Schuster, D. I., Majer, J., Blais, A., Devoret, M. H., Girvin, S. M. and Schoelkopf, R. J. (2007). Charge-insensitive qubit design derived from the Cooper pair box. *Physical Review A*, 76(4):042319.
- [Lamb1947] Lamb, W. E. and Retherford, R. (1947). Fine structure of the hydrogen atom by a microwave method. *Physical Review*, 72:241.
- [Leek2009] Leek, P. J., Filipp, S., Maurer, P., Baur, M., Bianchetti, R., Fink, J. M., Göppl, M., Steffen, L. and Wallraff, A. (2008). Using sideband transitions for two-qubit operations in superconducting circuits. *arXiv:0812.2678*.
- [London1950] London, F. (1950). *Superfluids*. Wiley, New York.
- [Lupascu2007] Lupascu, A., Saito, S., Picot, T., de Groot, P. C., Harmans, C. J. P. M., and Mooij, J. E. (2007). Quantum non-demolition measurement of a superconducting two-level system. *Nature Physics*, 3(2):119.
- [Mabuchi2002] Mabuchi, H. and Doherty, A. C. (2002). Cavity quantum electrodynamics: Coherence in context. *Science*, 298(5597):1372.
- [Majer2007] Majer, J., Chow, J. M., Gambetta, J. M., Koch, J., Johnson, B. R., Schreier, J. A., Frunzio, L., Schuster, D. I., Houck, A. A., Wallraff, A., Blais, A., Devoret, M. H., Girvin, S. M. and Schoelkopf, R. J. (2007). Coupling superconducting qubits via a cavity bus. *Nature*, 449(7161):443.
- [Manucharyan2007] Manucharyan, V. E., Boaknin, E., Metcalfe, M., Vijay, R., Siddiqi, I. and Devoret, M. (2007). Microwave bifurcation of a Josephson junction: Embedding-circuit requirements. *Physical Review B*, 76:014524.
- [Martinis2005] Martinis, J. M., Cooper, K. B., McDermott, R., Steffen, M., Ansmann, M., Osborn, K. D., Cicak, K., Oh, S., Pappas, D. P., Simmonds, R. W. and Yu, C. C. (2005). Decoherence in Josephson qubits from dielectric loss. *Physical Review Letters*, 95:210503.
- [Martinis1987] Martinis, J. M., Devoret, M. H. and Clarke, J. (1987). Experimental tests for the quantum behavior of a macroscopic degree of freedom: The phase difference across a Josephson junction. *Physical Review B*, 35(10):4682.

- [Martinis2002] Martinis, J. M., Nam, S., Aumentado, J. and Urbina, C. (2002). Rabi oscillations in a large Josephson-junction qubit. *Physical Review Letters*, 89(11):117901.
- [Mazin2002] Mazin, B. A., Day, P. K., LeDuc, H. G., Vayonakis, A. and Zmuidzinas, J. (2002). Superconducting kinetic inductance photon detectors. *2002 Proceedings SPIE*, 4849:283.
- [Mazin2008] Mazin, B. A., Eckart, M. E., Bumble, B., Golwala, S., Day, P., Gao, J. and Zmuidzinas, J. (2008). Optical/UV and X-ray microwave kinetic inductance strip detectors. *Journal of Low Temperature Physics*, 151:537.
- [Mollow1969] Mollow, B. R. (1969). Power spectrum of light scattered by two-level systems. *Physical Review*, 188:1969.
- [Mooij1999] Mooij, J. E., Orlando, T. P., Levitov, L., Lin Tian, van der Wal, Caspar H. and Lloyd, S. (1999). Josephson persistent-current qubit. *Science*, 285(5430):1036.
- [Musil1986] Musil, J. (1986). *Microwave Measurements of Complex Permittivity by Free Space Methods and their Applications*. Elsevier, Amsterdam.
- [Nakamura1999] Nakamura, Y., Pashkin, Y. A. and Tsai, J. S. (1999). Coherent control of macroscopic quantum states in a single-Cooper-pair box. *Nature*, 398(6730):786.
- [O'Connell2008] O'Connell, A. D., Ansmann, M., Bialczak, R. C., Hofheinz, M., Katz, N., Lucero, E., McKenney, C., Neeley, M., Wang, H., Weig, E. M., Cleland, A. N. and Martinis, J. M. (2008). Microwave dielectric loss at single photon energies and millikelvin temperatures. *Applied Physics Letters*, 92(11):112903.
- [Palacios2007] Palacios-Laloy, A., Nguyen, F., Mallet, F., Bertet, P., Vion, D. and Esteve, D. (2007). Tunable resonators for quantum circuits. *arXiv:0712.0221v1*.
- [Palacios2008] Palacios-Laloy, A., Nguyen, F., Mallet, F., Bertet, P., Vion, D. and Esteve, D. (2008). Tunable resonators for quantum circuits. *Journal of Low Temperature Physics*, 151(3):1034.
- [Parks1969] Parks, R. (1969). *Superconductivity Vol.2* Marcel Dekker, Inc., New York.
- [Poole1995] Poole, C. P. (1995). *Superconductivity*. Academic Press Inc.
- [Pozar1993] Pozar, D. M. (1993). *Microwave Engineering*. Addison-Wesley Publishing Company.
- [Preskill1998] Preskill, J. (1998). *Proceedings of the Royal Society A*, 454:385.
- [Purcell1946] Purcell, E. M. (1946). Spontaneous emission probabilities at radio frequencies. *Physical Review*, 69:681.
- [Raimond2001] Raimond, J. M., Brune, M. and Haroche, S. (2001). Manipulating quantum entanglement with atoms and photons in a cavity. *Review of Modern Physics*, 73(3):565.
- [Rouse1995] Rouse, R., Han, S. and Lukens, J. E. (1995). Observation of resonant tunneling between macroscopically distinct quantum levels. *Physical Review Letters*, 75:1614.
- [Sandberg2008] Sandberg, M., Wilson, C. M., Persson, F., Bauch, T., Johansson, G., Shumeiko, V., Duty, T. and Delsing, P. (2008). Tuning the field in a microwave resonator faster than the photon lifetime. *Applied Physics Letters*, 92(20):203501.

Bibliography

- [Schoelkopf2008] Schoelkopf, R. and Girvin, S. (2008). Wiring up quantum systems. *Nature*, 451:664.
- [Schreier2008] Schreier, J., Houck, A., Koch, J., Schuster, D. I., Johnson, B., Chow, J., Gambetta, J., Majer, J., Frunzio, L., Devoret, M., Girvin, S. and Schoelkopf, R. (2008). Suppressing charge noise decoherence in superconducting charge qubits. *Physical Review B*, 77:180502.
- [Schuster2007] Schuster, D. I., Houck, A. A., Schreier, J. A., Wallraff, A., Gambetta, J. M., Blais, A., Frunzio, L., Majer, J., Johnson, B., Devoret, M. H., Girvin, S. M. and Schoelkopf, R. J. (2007). Resolving photon number states in a superconducting circuit. *Nature*, 445(7127):515.
- [Schuster2005] Schuster, D. I., Wallraff, A., Blais, A., Frunzio, L., Huang, R.-S., Majer, J., Girvin, S. M. and Schoelkopf, R. J. (2005). AC Stark shift and dephasing of a superconducting qubit strongly coupled to a cavity field. *Physical Review Letters*, 94(12):123602.
- [Shnirman1997] Shnirman, A., Schön, G. and Hermon, Z. (1997). Quantum manipulations of small Josephson junctions. *Physical Review Letters*, 79(12):2371.
- [Shor1995] Shor, P. W. (1995). *Physical Review A*, 52:R2493.
- [Sillanpää2007] Sillanpää, M. A., Park, J. I. and Simmonds, R. W. (2007). Coherent quantum state storage and transfer between two phase qubits via a resonant cavity. *Nature*, 449(7161):438.
- [Steane1996] Steane, A. M. (1996). *Physical Review Letters*, 77:793.
- [Tholén2007] Tholén, E., Ergül, A., Doherty, E., Weber, F., Grégis, F. and Haviland, D. (2007). Nonlinearities and parametric amplification in superconducting coplanar waveguide resonators. *Applied Physics Letters*, 90:253509.
- [Tinkham1996] Tinkham, M. (1996). *Introduction to Superconductivity*. McGraw-Hill International Editions.
- [vanderWal2000] van der Wal, C. H., ter Haar, A. C. J., Wilhelm, F. K., Schouten, R. N., Harmans, C. J. P. M., Orlando, T. P., Lloyd, S. and Mooij, J. E. (2000). Quantum superposition of macroscopic persistent-current states. *Science*, 290(5492):773.
- [Vardoulakis2008] Vardoulakis, G., Withington, S., Goldie, D. J. and Glowacka, D. M. (2008). Superconducting kinetic inductance detectors for astrophysics. *Measurement Science and Technology*, 19:015509.
- [Vion2002] Vion, D., Aassime, A., Cottet, A., Joyez, P., Pothier, H., Urbina, C., Esteve, D. and Devoret, M. H. (2002). Manipulating the quantum state of an electrical circuit. *Science*, 296:886.
- [Voss1981] Voss, R. F. and Webb, R. A. (1981). Macroscopic quantum tunneling in 1- μm Nb Josephson junctions. *Physical Review Letters*, 47:265.
- [Wallraff2004] Wallraff, A., Schuster, D. I., Blais, A., Frunzio, L., Huang, R. S., Majer, J., Kumar, S., Girvin, S. M. and Schoelkopf, R. J. (2004). Strong coupling of a single photon to a superconducting qubit using circuit quantum electrodynamics. *Nature*, 431:162.
- [Wallraff2005] Wallraff, A., Schuster, D. I., Blais, A., Frunzio, L., Majer, J., Girvin, S. M. and Schoelkopf, R. J. (2005). Approaching unit visibility for control of a superconducting qubit with dispersive readout. *Physical Review Letters*, 95:060501.

- [Walther2006] Walther, H., Varcoe, B. T. H., Englert, B.G. and Becker, T. (2006). Cavity quantum electrodynamics. *Reports on Progress in Physics*, 69(5):1325.
- [Watanabe1994] Watanabe, K., Yoshida, K., Aoki, T. and Kohjiro, S. (1994). Kinetic inductance of superconducting coplanar waveguides. *Japanese Journal of Applied Physics*, 33:5708.
- [Crystec] www.crystec.de.
- [Qudev] www.qudev.ethz.ch.
- [VeriCold] www.vericold.com.
- [Zhu1990] Zhu, Y., Gauthier, D. J., Morin, S. E., Wu, Q., Carmichael, H. J. and Mossberg, T. W. (1990). Vacuum Rabi splitting as a feature of linear-dispersion theory: Analysis and experimental observations. *Physical Review Letters*, 64(21):2499.
- [Zmuidzinas2004] Zmuidzinas, J. and Richards, P. L. (2004). Superconducting detectors and mixers for millimeter and submillimeter astrophysics. *Proceedings of the IEEE*, 92(10):1597.
- [Zurek1991] Zurek, W. H. (1991). Decoherence and the transition from quantum to classical. *Physics Today*, 23:36.

Bibliography

List of Publications

Published

Göppl, M., Fragner, A., Baur, M., Bianchetti, R., Filipp, S., Fink, J. M., Leek, P. J., Puebla, G., Steffen, L., and Wallraff, A. (2008). Coplanar waveguide resonators for circuit quantum electrodynamics. *Journal of Applied Physics*, 104:1113904.

Fragner, A., **Göppl, M.**, Fink, J. M., Baur, M., Bianchetti, R., Leek, P., Blais, A. and Wallraff, A. (2008). Resolving vacuum fluctuations in an electrical circuit by measuring the lamb shift. *Science*, 322(5906):1357.

Fink, J. M., **Göppl, M.**, Baur, M., Bianchetti, R., Leek, P. J., Blais, A. and Wallraff, A. (2008). Climbing the Jaynes-Cummings ladder and observing its nonlinearity in a cavity QED system. *Nature*, 454(7202):315.

Leek, P. J., Fink, J. M., Blais, A., Bianchetti, R., **Göppl, M.**, Gambetta, J. M., Schuster, D. I., Frunzio, L., Schoelkopf, R. J. and Wallraff, A. (2007). Observation of Berry's phase in a solid-state qubit. *Science*, 318(5858):1889.

Submitted

Filipp, S., Maurer, P., Leek, P. J., Baur, M., Bianchetti, R., Fink, J. M., **Göppl, M.**, Steffen, L., Gambetta, J. M., Blais, A. and Wallraff, A. (2009). Two-qubit state tomography using a joint dispersive read-out. *arXiv:0812.2485*.

Leek, P. J., Filipp, S., Maurer, P., Baur, M., Bianchetti, R., Fink, J. M., **Göppl, M.**, Steffen, L. and Wallraff, A. (2009). Using sideband transitions for two-qubit operations in superconducting circuits. *arXiv:0812.2678*.

Baur, M., Filipp, S., Bianchetti, R., Fink, J. M., **Göppl, M.**, Leek, P. J., Steffen, L., Blais, A. and Wallraff, A. (2009). Measurement of Autler-Townes and Mollow transitions in a strongly driven superconducting qubit. *arXiv:0812.4384*.

In Preparation

Göppl, M., Filipp, S., Baur, M., Bianchetti, R., Fink, J. M., Leek, P. J., Steffen, L., Blais, A. and Wallraff, A. (2009). Qubit-qubit interaction by exchange of virtual photons via multiple cavity modes.

Bianchetti, R., Filipp, S., Baur, M., Fink, J. M., **Göppl, M.**, Leek, P. J., Steffen, L., Blais, A. and Wallraff, A. (2009). Dynamics of dispersive read-out in circuit quantum electrodynamics.

Fink, J. M., Bianchetti, R., Baur, **Göppl, M.**, Steffen, Filipp, S., Leek, P. J., Blais, A. and Wallraff, A. (2009). Collective qubit states and the Tavis-Cummings model in circuit QED. *arXiv:0812.2651*.

Acknowledgements

I would like to thank Prof. Dr. Andreas Wallraff for giving me the opportunity to conduct my PhD thesis within the newly founded Quantum Device Lab at ETH Zurich. The participation in building up a new laboratory from scratch is for sure an instructional and exciting experience offering diverse challenges with which one is confronted. Furthermore, I always appreciated the possibility to openly discuss also controversial perceptions.

I would also like to thank Prof. Dr. Per Delsing from Chalmers University for co-supervising my thesis and for coming from Gothenburg to Zurich for my final PhD examination. Hopefully, Zurich is not too rainy and cloudy at the begin of April. I would be glad if the presented thesis could offer some useful information also for the work going on at Chalmers.

Thanks to Bertram Batlogg who gave me the possibility to use his physical property measurement system for thin film characterizations and who agreed in participating in my final examination.

A notably part of my time during the last three years I spent in the ETH clean room facility FIRST which could not be operated without the excellent help of the FIRST operation and the FIRST technician team. In particular, many thanks to Dr. Otte Homan, who supported me all time with his well-founded knowledge on thin film physics and micro-fabrication technology and with his refreshing Dutch sense of humor. Also thanks to all the nice people from other groups working in FIRST, especially Andreas Alt from the Bolognesi connection.

Thanks are given to people in the Quantum Device Lab for starting up the cavity QED project. Sincere thanks to Romeo Bianchetti and Matthias Baur who helped me a lot to cope with diverse Mathematica and LabView challenges and who brought me to jump down from Ticino dams and to dive to the bottom of ice cold Swiss lakes. Thanks also to Wolf Wüster who helped to bring the bias box into operation, to Hans-Rudi Äschbach who showed me how to mechanically construct precise workpieces and who also pointed out to me the best places to hike in Switzerland and last but not least to Gaby Strahm who never forgot my birthday.

Curriculum Vitae

Personal Data

Name: Martin Göppl
Date of birth: November 10, 1980
Place of birth: Weiden Opf. (Germany)

University

04/2006 - 03/2009 PhD Studies, Physics Department, ETH Zurich, Switzerland
05/2005 - 04/2006 Studies of Physics, TU Munich, Germany
10/2003 - 04/2005 Studies of Physics, University of Bayreuth, Germany

Community Service

09/2000 - 07/2001 Bavarian Red Cross Weiden, Germany

Education

09/1991 - 07/2000 Kepler-Gymnasium Weiden, Germany

